

See discussions, stats, and author profiles for this publication at: <https://www.researchgate.net/publication/343494070>

Polymer-Derived Heteroatom-Doped Porous Carbon Materials

Article in *Chemical Reviews* · August 2020

DOI: 10.1021/acs.chemrev.0c00080

CITATIONS

128

READS

838

9 authors, including:



Hong Wang

Montgomery College

617 PUBLICATIONS 16,630 CITATIONS

[SEE PROFILE](#)



Yan Lu

Helmholtz-Zentrum Berlin

181 PUBLICATIONS 10,447 CITATIONS

[SEE PROFILE](#)



Miao Zhang

Stockholm University

56 PUBLICATIONS 3,795 CITATIONS

[SEE PROFILE](#)

Some of the authors of this publication are also working on these related projects:



Molecular Phylogenetics and Biogeography of the tribe Gaultherieae [View project](#)



Evolution of Angiosperms Pollen [View project](#)

1 Polymer-Derived Heteroatom-Doped Porous Carbon Materials

2 Hong Wang,* Yue Shao, Shilin Mei, Yan Lu, Miao Zhang, Jian-ke Sun, Krzysztof Matyjaszewski,
3 Markus Antonietti, and Jiayin Yuan*



Cite This: <https://dx.doi.org/10.1021/acs.chemrev.0c00080>



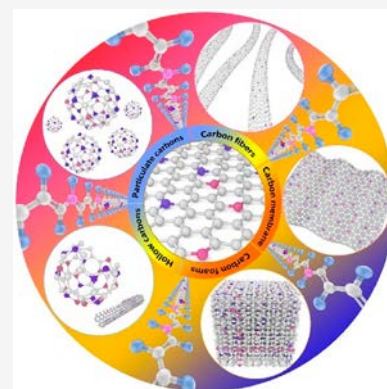
Read Online

ACCESS |

Metrics & More

Article Recommendations

4 **ABSTRACT:** Heteroatom-doped porous carbon materials (HPCMs) have found extensive
5 applications in adsorption/separation, organic catalysis, sensing, and energy conversion/
6 storage. The judicious choice of carbon precursors is crucial for the manufacture of HPCMs
7 with specific usages and maximization of their functions. In this regard, polymers as
8 precursors have demonstrated great promise because of their versatile molecular and
9 nanoscale structures, modulatable chemical composition, and rich processing techniques to
10 generate textures that, in combination with proper solid-state chemistry, can be maintained
11 throughout carbonization. This Review comprehensively surveys the progress in polymer-
12 derived functional HPCMs in terms of how to produce and control their porosities,
13 heteroatom doping effects, and morphologies and their related use. First, we summarize and
14 discuss synthetic approaches, including hard and soft templating methods as well as direct
15 synthesis strategies employing polymers to control the pores and/or heteroatoms in
16 HPCMs. Second, we summarize the heteroatom doping effects on the thermal stability,
17 electronic and optical properties, and surface chemistry of HPCMs. Specifically, the
18 heteroatom doping effect, which involves both single-type heteroatom doping and codoping of two or more types of heteroatoms
19 into the carbon network, is discussed. Considering the significance of the morphologies of HPCMs in their application spectrum,
20 potential choices of suitable polymeric precursors and strategies to precisely regulate the morphologies of HPCMs are presented.
21 Finally, we provide our perspective on how to predefine the structures of HPCMs by using polymers to realize their potential
22 applications in the current fields of energy generation/conversion and environmental remediation. We believe that these analyses
23 and deductions are valuable for a systematic understanding of polymer-derived carbon materials and will serve as a source of
24 inspiration for the design of future HPCMs.



25 CONTENTS

27	1. Introduction to Heteroatom-Doped Porous Carbon Materials	B
28		
29	2. Synthetic Approaches	C
30	2.1. Template Methods	C
31	2.1.1. Inorganic Nanostructures as Templates	C
32	2.1.2. Polymer Nanostructures as Sacrificial Templates	E
33	2.1.3. Polymer/Inorganic Hybrids as Templates	I
34	2.2. Direct Synthesis	J
35	2.2.1. Direct Carbonization of Heteroatom-Rich Polymers	K
36	2.2.2. Carbonization of Heteroatom-Free Polymers with Heteroatom-Rich Coreactants	O
37	3. Heteroatom Doping Effect on Porous Carbons	P
38	3.1. Characterization of Heteroatom-Doped Porous Carbons	P
39	3.2. Molecular Doping Effect of Heteroatoms on Porous Carbon	R
40	3.3. N-Doped Porous Carbons	S
41		
42		
43		
44		
45		
46		
47		

3.3.1. Bulk Doping	S 48
3.3.2. Surface Doping	W 49
3.4. Non-Nitrogen-Atom (B, S, Se, and P)-Doped Porous Carbons	X 51
3.4.1. B Doping	Y 52
3.4.2. S Doping	Z 53
3.4.3. P Doping	AA 54
3.5. Codoping Effect of Heteroatoms on Porous Carbons	AC 56
3.5.1. N, B Codoping	AC 57
3.5.2. N, S Codoping	AD 58
3.5.3. N, Se Codoping	AD 59
3.5.4. N, P Codoping	AE 60
3.5.5. Ternary Doping by Three Types of Heteroatoms	AE 62

Received: January 30, 2020

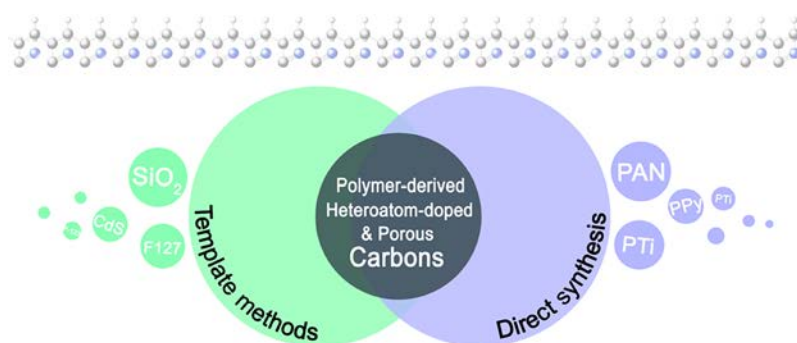


Figure 1. Schematic illustration of two general routes for synthesizing polymer-derived HPCMs.

63	4. Morphological Control of Porous Carbons	AF
64	4.1. Heteroatom-Doped Porous Carbon Particles	AF
65	4.1.1. Carbon Quantum Dots (CQDs)	AG
66	4.1.2. Porous Carbon Spheres	AH
67	4.1.3. Hollow Porous Particles and Anisotropic/Asymmetric Porous Carbon Particles	AI
68	4.2. Heteroatom-Doped Porous Carbon Fibers and Tubes	AI
69	4.2.1. Porous Carbon Fibers	AI
70	4.2.2. Porous Carbon Tubes	AJ
71	4.3. Heteroatom-Doped Porous Carbon Thin Films and Membranes	AK
72	4.4. Heteroatom-Doped Porous Carbon Foams and Monoliths	AL
73	5. Pore Engineering in Heteroatom-Doped Carbons Derived from Polymers	AM
74	5.1. Control of Microporosity	AM
75	5.1.1. Activation Approach to Construct Microporous Structures	AM
76	5.1.2. Utilization of the Polymeric Structure and Composition to Construct Microporous Structures	AN
77	5.2. Control of Mesoporosity	AP
78	5.3. Control of Macroporosity	AQ
79	6. Conclusion	AS
80	Author Information	AS
81	Corresponding Authors	AS
82	Authors	AT
83	Notes	AT
84	Biographies	AT
85	Acknowledgments	AU
86	References	AU

1. INTRODUCTION TO HETEROATOM-DOPED POROUS CARBON MATERIALS

Carbon materials are ubiquitous in our daily life. In retrospect, charcoal, a biomass-derived material, was utilized as medicine in ancient Greek times to relieve dysentery-like diseases, which, as we now understand, functions through the adsorption of bacteria and bacterial metabolites by nanostructured carbons. This guest molecule adsorption property was also used in the early 1900s in the form of filters in respirators for the prevention of toxicant poisoning. Currently, carbon materials are broadly used as adsorbents, supports, and even metal-free catalysts to address pressing global challenges, including, but not limited to, energy and environmental issues. Carbon is of

rich abundance in nature, relatively low cost, and comparably high chemical and thermal stability. It possesses a tunable surface area and multiple structural forms at the atomic/nanoscale that define an unusually broad range of physicochemical properties to satisfy diverse applications. As the sixth element in the periodic table, carbon is sometimes referred to as an all-purpose material, even exceeding “quintessence” (the metaphoric fifth element) of alchemy.

The porous state of carbons no doubt profoundly impacts their properties and functions. Equipping carbons with pores of different sizes and shapes lowers their apparent density and expands their surface area to accelerate interfacial energy and mass transfer, a step that is crucial and decisive in many surface-related physical and chemical processes. The topic of porous carbons is particularly “fueled” by the recent trend to replace fossil fuels with affordable clean energy in the next few generations, as defined in the Sustainable Development Goal 7 (SDG7) by the United Nations. The concept of hierarchical structure of carbons in terms of pore sizes ranging from micro- to meso- and macropores is well developed in the porous carbon community, since it balances both a high density of and a low diffusion resistance toward active sites. The macropores are literally transport highways, while the micro- and mesopores provide a large specific surface area bearing active sites for heterogeneous reactions.

Equally important is the effect of heteroatom doping of carbon materials with nonmetals, e.g., nitrogen (N), phosphorus (P), boron (B), sulfur (S), and selenium (Se).¹ These types of atoms can be solely or jointly incorporated into a carbon framework via either carbonization of heteroatom-rich precursors or chemical postmodification of parental porous carbons. Heteroatoms in turn can tailor the physicochemical properties of carbons and endow carbons with fascinating properties. Not only the electronegativity but also the charge density and size of heteroatoms are vital to the properties of porous carbons. Different types of heteroatoms, or even the same type of heteroatom in a different bond configuration, can impart carbons with distinctively different properties. Considering the potential of heteroatom-doped porous carbon materials (HPCMs) as metal-free catalysts that can replace costly noble/transition metal-based catalysts, as already observed for a number of key applications, and that are stable even under harsh conditions, i.e., at high temperatures, under sulfur species and carbon monoxide atmospheres, or in strong acid and alkali solutions, their research horizon has been significantly and will be further broadened in both academia and industry. HPCMs are discussed in reference to applications such as electrochemical devices, catalysts, fire-

156 retardant materials, seawater desalination devices, and many
157 more.

158 In this context, the judicious choice of carbon precursors is
159 of tremendous significance, among which polymers stand out
160 due to the availability of a myriad of macromolecular and self-
161 assembled (nano)structures, tunable chemical compositions,
162 and versatile processing techniques. HPCMs in different forms
163 have been produced through the rational choice of polymers,
164 including spheres, fibers, thin films/membranes, foams,
165 monoliths, and their hollow counterparts (Figure 1). The
166 polymers are chosen from either biopolymers or synthetic
167 polymers, ranging from traditional polyacrylonitrile (PAN) and
168 conjugated polymers to the recently emerging well-carbon-
169 izable polymers, e.g., poly(ionic liquid)s (PILs) or polydop-
170 amine.

171 In the ongoing search for carbon (nano)materials exhibiting
172 unconventional properties and important applications, studies
173 of polymer-derived porous carbons in well-defined shapes
174 doped by heteroatoms are a fast-growing focus area. Previous
175 reviews and perspective articles in this area targeted the specific
176 aspects of heteroatom doping effects, energy conversion/
177 storage applications, and/or carbonization mechanisms.^{2–7} In
178 terms of polymer-derived HPCMs, there are only a few solid
179 conclusions in the literature. With the ongoing advancement in
180 polymer nanomaterials, we believe that polymers are excellent
181 candidates for producing carbon materials with diverse
182 morphologies. These polymers can be first processed into
183 complicated structures and then build up selective porous
184 networks via intrinsic phase separation. At the same time, with
185 the aid of heteroatoms, the electronic structures of HPCMs
186 can be rationally tailored for designated applications. The
187 current review attempts to survey the progress in the entire
188 field in a comparative fashion and discusses the state-of-the-art
189 understanding of common denominators of these advances.
190 We highlight the impacts of preformed polymer structures and
191 the freedom in the choice of processing strategies on the
192 production of carbons with diverse morphologies and tunable
193 nanostructures and the related physiochemical properties and
194 functions. We also share our views on challenges and
195 opportunities for the synthesis and application of polymer-
196 derived HPCMs. This Review aims to give comprehensive
197 summaries of polymer-derived HPCMs based on their
198 synthesis, morphology, heteroatom doping, and porosity. To
199 be more focused in its content, it will not cover the
200 development of metal atom doping, and interested readers
201 can refer to other recent reviews.^{2,3}

2. SYNTHETIC APPROACHES

202 Heteroatom-doped porous carbons can be prepared by
203 pyrolysis of heteroatom-rich polymers as precursors or by
204 subjecting preformed porous carbons to postsynthetic treat-
205 ment with heteroatom-containing precursors.^{4–8} The former
206 can homogeneously add heteroatoms into the entire porous
207 carbon matrix, whereas the latter mostly loads heteroatoms
208 only onto the carbon surface. Sometimes both methods are
209 combined to maximize the heteroatom loading. Each synthetic
210 route may generate porous carbons in structures with distinct
211 strengths and specific weaknesses.^{9–11} In this section, the
212 synthetic methods for polymer-derived HPCMs are systemati-
213 cally discussed. Two main strategies, including template and
214 direct synthesis, are summarized in Figure 1. These strategies
215 are detailed with a variety of examples in the following section.

2.1. Template Methods

216 Hard and soft template strategies are the most mature and
217 widely used methods for preparing HPCMs with diverse pore
218 structures from polymers (Figure 2). Hard templates are solid

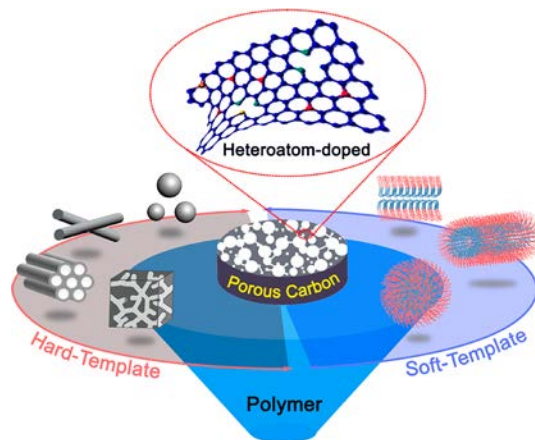


Figure 2. Schematic illustration of hard and soft templates for the synthesis of HPCMs from polymers.

219 compounds with pores or high surface areas, including zeolites
220 and mesoporous silicas, as well as colloidal particles and their
221 assemblies. Soft templates are organic nanostructures built up
222 from micelles of ionic or nonionic surfactants, assemblies of
223 block copolymers, liquid crystalline phases, soft droplets,
224 biopolymers, or vesicles.^{12–15} Despite the significant progress
225 made thus far, precise control of the structure and morphology
226 at low cost remains a persistent topic. To tailor the
227 morphologies of porous carbons, a straightforward method is
228 to adopt templates of the corresponding morphologies.

229 **2.1.1. Inorganic Nanostructures as Templates.** Utiliz-
230 ing inorganic nanostructures as templates for the synthesis of
231 well-defined porous carbons is one of the most straightforward
232 and popular methods. After infiltrating the template with a
233 heteroatom-containing polymer or *in situ* polymerization of the
234 monomer, followed by carbonization and template removal by
235 appropriate chemicals, HPCMs that are an inverse replica of
236 the original template will be obtained. Owing to the rapid
237 synthetic progress of porous inorganic nanostructures, a variety
238 of inorganic templates have been employed to produce carbons
239 with well-defined pores. This approach involves templating
240 with metal nanoparticles, silica nanoparticles or their opal
241 crystals, silica gels, aluminosilicates, silica carbide, and
242 nanostructured metal oxides, such as anodic alumina, calcium
243 carbonate, and zinc oxide, which can be easily removed by a
244 weakly alkaline or acid solution or vaporization.^{16–23} Novel
245 morphologies are accessible for porous carbon materials with
246 such appropriate inorganic templates. Ideally, the template
247 must be chemically inert to carbon and carbon precursors,
248 thermally stable, and equipped with a chemical trigger for
249 removal to leave pores behind in the template. It is worthwhile
250 noting that the pore size of the resulting porous carbons is not
251 always the same as that of the original templates because the
252 carbonaceous material can shrink under further thermal
253 processing at elevated temperatures.

254 Since the templating concept was demonstrated in 1982,
255 colloidal silica particles and silica gels have been explored and
256 widely adopted as molds for porous carbons.²⁴ Hyeon's group
257 pioneered the synthesis of mesoporous carbon using colloidal

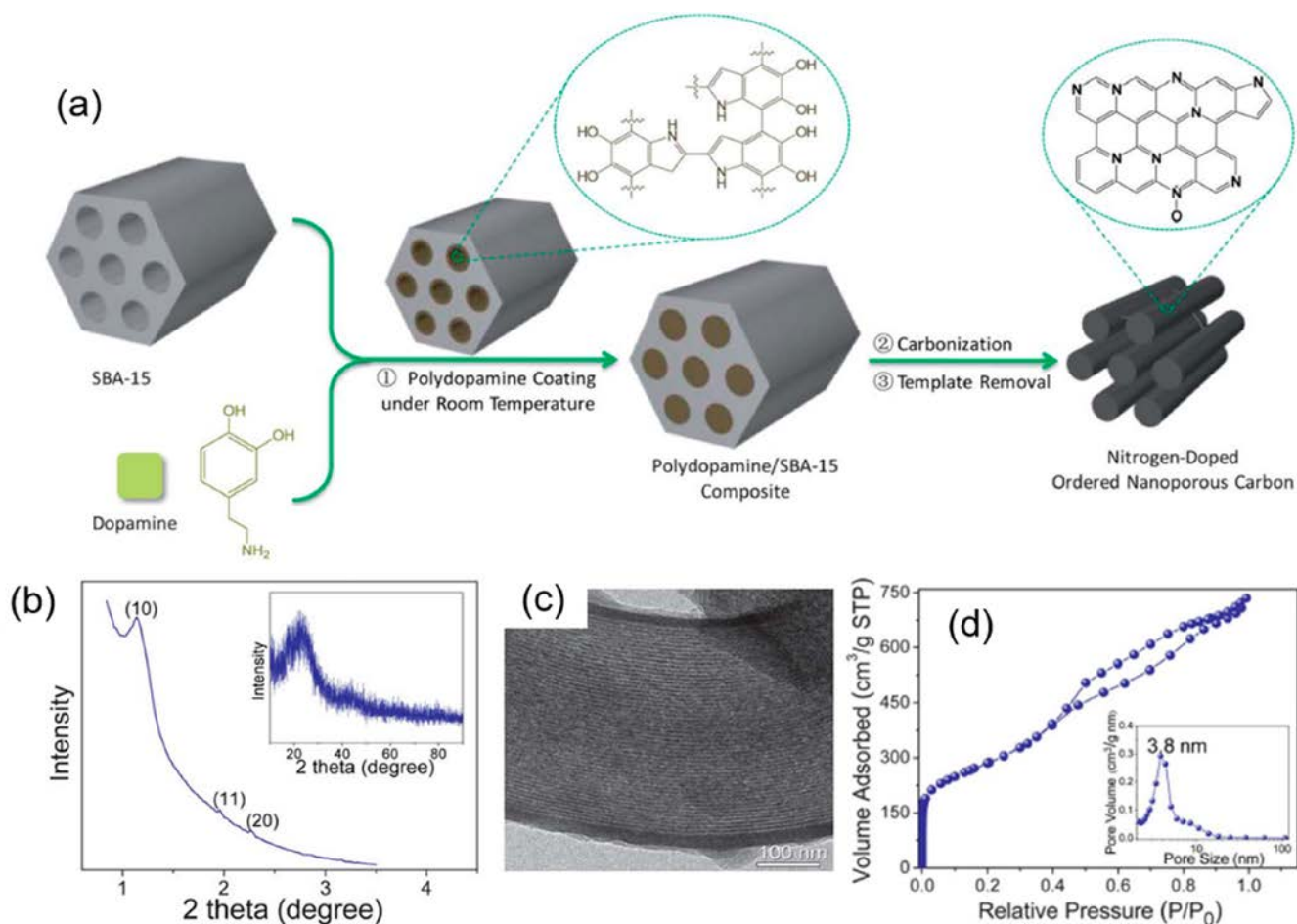


Figure 3. (a) Schematic illustration of the polydopamine-coating-directed synthesis of NONCs. (b) Low-angle XRD pattern and wide-angle XRD pattern (inset) of the NONC. (c) TEM image of the NONC. (d) N_2 sorption isotherms of the NONC and its pore size distribution. Reproduced with permission from ref 30. Copyright 2013 Royal Society of Chemistry.

258 silica particles as hard templates.^{25,26} It was found that the pore
 259 size distribution of the carbon was significantly affected by the
 260 silica/polymer ratio. Stein's group further demonstrated the
 261 preparation of porous carbon with a periodic array of
 262 macropores, which was defined as three-dimensionally ordered
 263 macroporous carbon.²⁷ The pore size distribution of carbons
 264 templated by silica particles of a uniform size is not necessarily
 265 narrow, suggesting that carbon is not always a true replica of
 266 voids in silica nanoparticles. To minimize irregular agglomeration
 267 of silica particles, which produces nonuniform voids, the
 268 surfactant cetyltrimethylammonium bromide (CTAB) was
 269 used to stabilize silica particles in solution before processing
 270 them into a porous template.²⁵ The resulting nanoporous
 271 carbon showed an improved pore size distribution peaking at
 272 12 nm, which well matched the size of the employed silica
 273 particles. Apart from the surfactants used, later studies found
 274 that the silica sol content and the pH value had significant
 275 impacts on the porous structures and textural properties of the
 276 resulting mesoporous carbons.^{28,29}

277 It is important to note that ordered inorganic materials, such
 278 as mesoporous silica and zeolites, are also popularly used as
 279 hard templates to produce ordered porosity in carbon
 280 materials. In terms of silica templates, MCM-41, HMS,
 281 MSU-1, MSU-H, SBA-1, SBA-7, SBA-12, SBA-15, and SBA-
 282 16 are on the "hot list". For example, Wu et al.³⁰ reported the
 283 fabrication of N-doped ordered nanoporous carbons termed

"NONCs" by pyrolyzing a polydopamine (PDA)/SBA-15
 284 nanocomposite under N_2 at 800 °C for 3 h, followed by
 285 removal of the SBA-15 template to form NONCs with an S_{BET}
 286 value of 1013 $m^2 g^{-1}$ (Figure 3). At the same time, Zou et al.³¹
 287 synthesized nitrogenated graphitic ordered mesoporous
 288 carbons termed "G-OMCs" by using mesoporous nickel
 289 oxide as a catalytic template and dopamine as a precursor,
 290 which was carbonized at 900 °C for 4 h. The results revealed
 291 that G-OMC materials had a higher degree of graphitization
 292 than those prepared only from dopamine and the inert SBA-15
 293 template, which suggested a catalytic graphitization process
 294 involving nickel oxide. The I_D/I_G value was 0.69, which was
 295 lower than that of ordered mesoporous carbon CMK-3 (0.84).
 296

A major drawback associated with this approach lies in the
 297 multistep synthesis and the use of hydrofluoric acid (HF) or
 298 other toxic etching chemicals to remove the silica template. To
 299 mitigate this issue, inorganic nanostructures, such as porous
 300 anodic aluminum oxide (AAO), MgO, CoP, $CaCO_3$, and
 301 $Al(OH)_3$, that can be removed by relatively safe chemicals, e.g.,
 302 HCl and NaOH, have been utilized as templates.³² For
 303 example, Chen and co-workers prepared N-doped porous
 304 carbon nanocages (NCNCs) via an *in situ*-generated MgO
 305 template method using pyridine as a precursor.³³ The MgO
 306 template was etched away by a HCl solution at room
 307 temperature. The NCNCs exhibited an excellent oxygen
 308 reduction reaction (ORR) performance in alkaline solution
 309

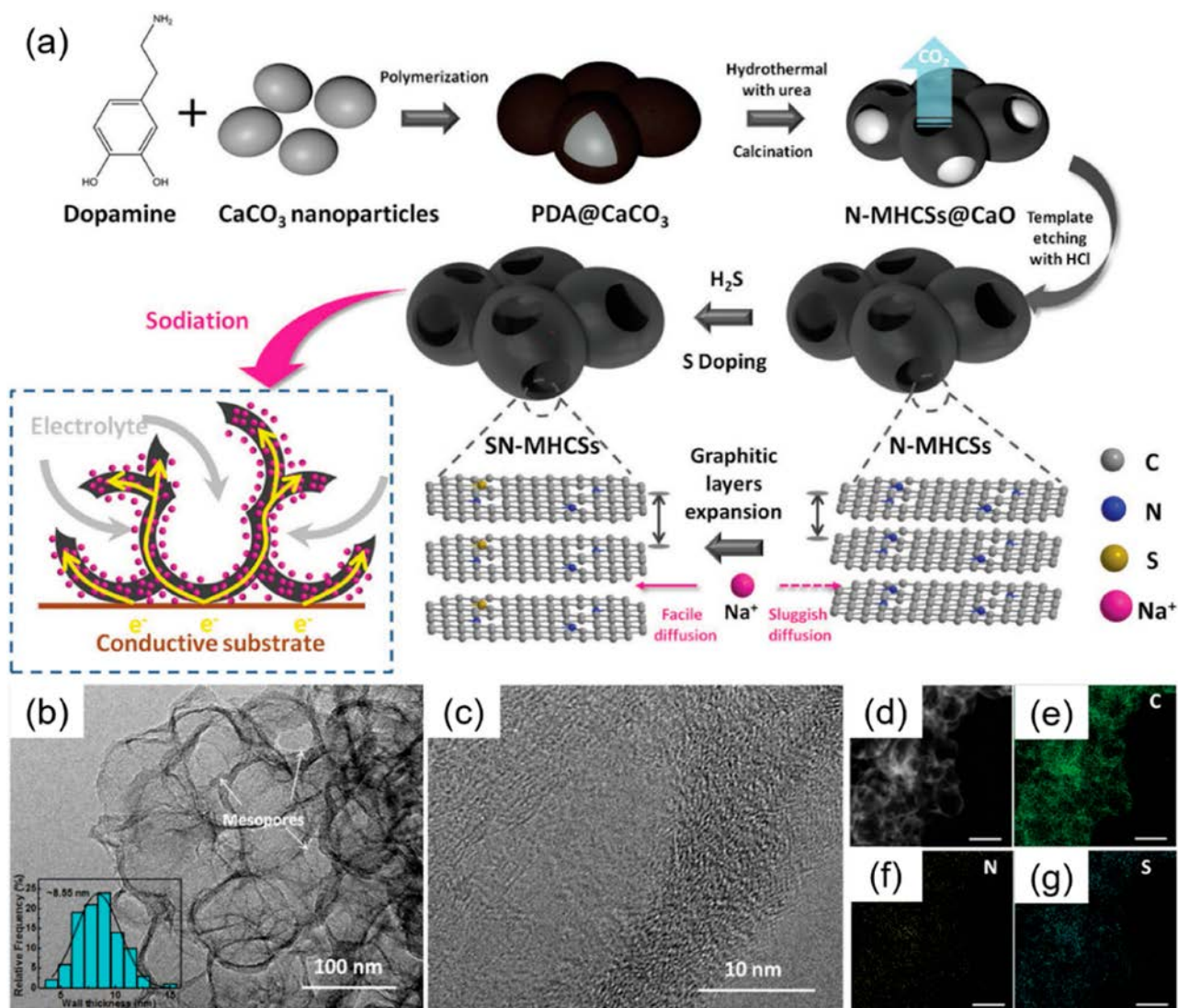


Figure 4. (a) Schematic illustration of the synthetic procedure for SNMHCSs using CaCO₃ as a template. (b, c) TEM image of SNMHCSs; the inset is a histogram of the carbon wall thickness distribution. (d) STEM image of SNMHCSs. (e–g) Corresponding distributions of the elemental C, N, and S. The scale bar is 100 nm. Reproduced with permission from ref 35. Copyright 2019 Wiley-VCH.

310 with superior stability toward methanol crossover and CO
 311 poisoning, at a level that could compete with the commercial
 312 Pt/C electrocatalyst. Similarly, Hu et al. reported a novel 3D
 313 hierarchical S- and N-codoped carbon nanocage termed
 314 “hSNCNC” as a bifunctional oxygen electrocatalyst, where
 315 MgO nanocubes were used as a template and a pyridine and
 316 thiophene mixture as a precursor.³⁴ The as-prepared hSNCNC
 317 exhibited a positive half-wave potential of 0.792 V (vs
 318 reversible hydrogen electrode, RHE) for the ORR and a low
 319 operating potential of 1.640 V at a 10 mA cm⁻² current density
 320 for the OER. The reversible oxygen electrode index was 0.847
 321 V, superior to those of commercial Pt/C and IrO₂. In another
 322 example, S- and N-codoped mesoporous hollow carbon
 323 spheres termed “SNMHCSs” were prepared by Sun’s group
 324 using low-cost CaCO₃ nanoparticles as self-sacrifice templates
 325 and PDA as a precursor (Figure 4).³⁵ During the calcination
 326 process, CaCO₃ decomposed to CaO and released CO₂ gas,
 327 which facilitated the formation of small pores in the carbon
 328 walls. Urea was used during the carbonization process as a N-
 329 content enhancer, followed by an additional thermal annealing
 330 under H₂S to induce S doping. When the porous carbon

product was applied as an anode for sodium-ion batteries, 331
 excellent rate and cycling performance was achieved due to the 332
 interconnected mesoporous hollow sphere structure that 333
 provided a large electrode/electrolyte interface for reactions; 334
 this in turn facilitated the diffusion of electrolyte, increased the 335
 transport rate of electrons and sodium ions, and buffered the 336
 volumetric expansion of the electrode during cycling. S doping 337
 could increase the interlayer space between adjacent graphitic 338
 layers, enable the carbon electrode to accommodate more 339
 sodium ions, and promote ion transport, while N doping could 340
 add functional groups and defects to increase the capacity. 341

2.1.2. Polymer Nanostructures as Sacrificial Templates. 342
 Polymer nanostructures are popular templates in the 343
 synthesis of porous materials due to the ease of morphological 344
 control by well-established, mature polymer processing 345
 techniques and simple removal through dissolution, calcina- 346
 tion, or other mild treatments.^{36–40} It should be stressed here 347
 that the removal of a polymeric template by calcination is 348
 usually performed in combination with the carbonization 349
 process, an obvious advantage of soft templates in comparison 350
 with the inorganic hard counterparts. It should also be 351

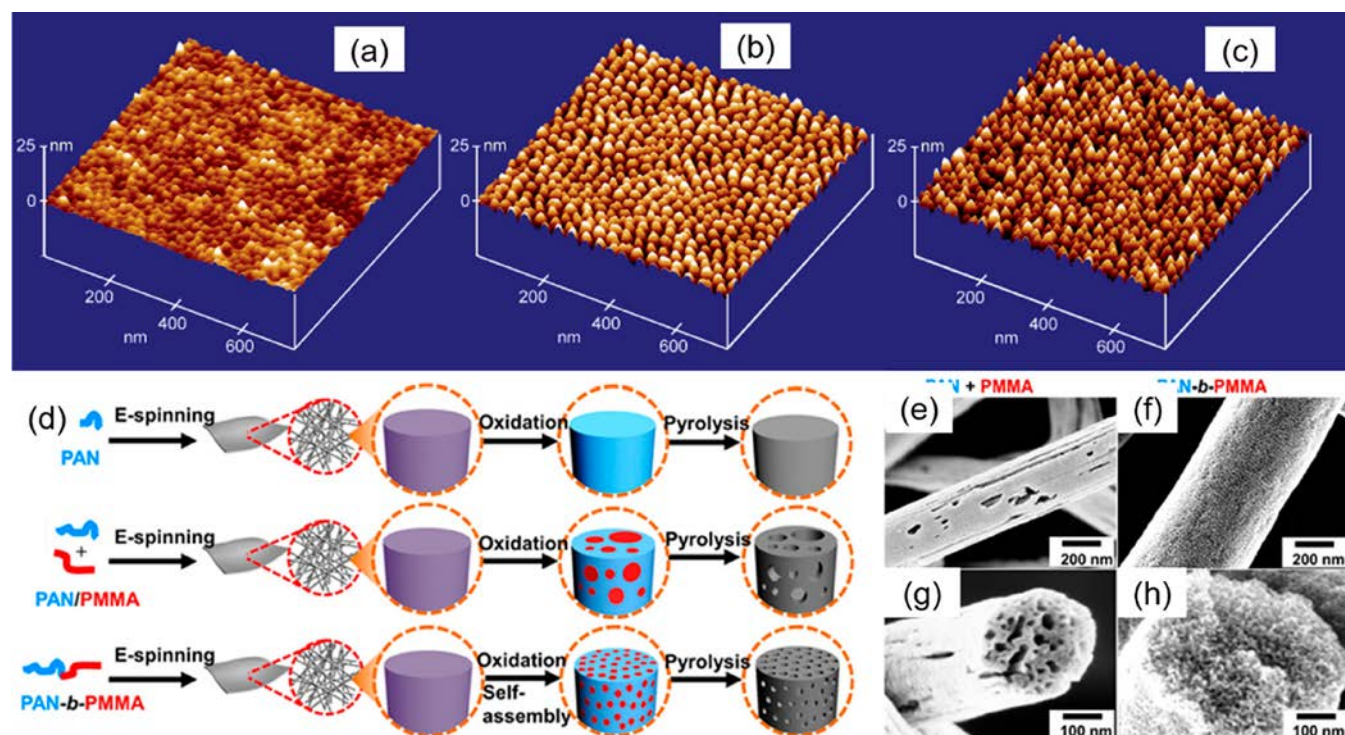


Figure 5. (a) $(AN)_{45}-(BA)_{530}-(AN)_{45}$ block copolymer film vacuum annealed for 2 h at 220 °C to equilibrate the morphology. Sample heated under N_2 to (b) 600 °C and (c) 1200 °C. Reproduced with permission from ref 42. Copyright 2002 American Chemical Society. (d) Fabrication scheme of N-doped porous carbon fibers from polymeric precursors: PAN (blue), PAN/PMMA (red) blend, and PAN-*b*-PMMA block copolymer. (e, f) SEM images of the carbon fibers derived from PAN/PMMA. (g, h) SEM images of the porous carbon fibers derived from PAN-*b*-PMMA. Reproduced with permission from ref 44, licensed under CC BY.

352 explained here that the polymer nanostructures included in this
 353 section (2.1.2) have at least one polymer component fully
 354 removed by thermal decomposition, dissolution, or etching to
 355 introduce pores. In the later section 2.2.1 “Direct Carbon-
 356 ization of Heteroatom-Rich Polymers”, the polymer serves as
 357 the carbon source, even though one part (but not all parts) of
 358 such a polymer may decompose into pores.

359 To date, polymeric nanostructures ranging from 0D
 360 nanoparticles to 1D fibers, 2D sheets, and 3D bulk species
 361 have been successfully used to template the pyrolytic growth of
 362 HPCMs. For example, polystyrene (PS) latexes or “nano-
 363 spheres” are one of the most commonly used templates due to
 364 their easy scale-up preparation at low cost. The interplay
 365 between the template and the carbon precursor is vital to
 366 generating the target products. To provide the required affinity
 367 of templates to polymeric precursors, PS nanospheres are
 368 usually surface functionalized with, e.g., polyvinylpyrrolidone
 369 (PVP) as a bridging layer to accommodate intermolecular
 370 interactions, such as hydrogen bonding. Hao and co-workers
 371 fabricated hollow N-doped carbon microspheres termed
 372 “HNCMs” using polyaniline (PANI) as a source of nitrogen
 373 and carbon for grafting onto PVP-functionalized PS spheres as
 374 a template.⁴¹ The organic PS core was burned off by
 375 carbonizing the core-shell microspheres under a N_2
 376 atmosphere at 500 °C for 2 h to produce HNCMs.

377 Utilizing microphase-separated structures of polymer blends
 378 or block copolymers as templates, well-organized nano-
 379 structured carbon materials can be fabricated by pyrolysis
 380 accompanied by volatilization of the sacrificial phase.
 381 Matyjaszewski et al.⁴² first demonstrated the success of such
 382 a strategy using the triblock copolymer of acrylonitrile (AN)
 383 and *n*-butyl acrylate (BA) with average composition $(AN)_{45}-$

$(BA)_{530}-(AN)_{45}$ as a precursor. For certain PAN/PBA ratios, 384
 the original morphology of the bulk precursor is well retained 385
 upon pyrolysis between 400 and 1200 °C (Figure 5a–c). 386
 Extension of this route to block copolymers with other 387
 morphologies (e.g., the gyroid phase) or polymer blends was 388
 also found to be successful and straightforward. The resulting 389
 carbon materials show a high surface area and accessibility of 390
 nitrogen functionalities, as inferred from their performance as 391
 electrodes for supercapacitors and sorbents for CO_2 capture as 392
 well as efficient electrocatalysts for the oxygen reduction 393
 reaction.⁴³ For example, in 2019, Liu’s group⁴⁴ reported the 394
 fabrication of porous carbon fibers (PCFs) with well- 395
 controlled mesopores of ~10 nm or micropores of ~0.5 nm 396
 in size by employing the microphase-separated PAN/PMMA 397
 blend or block copolymer PAN-*b*-PMMA, respectively, as a 398
 template (Figure 5d–h). PAN can be directly converted to N- 399
 doped PCFs, sometimes with oxygen (O) codoping due to a 400
 necessary aerobic thermal cross-linking/stabilization step at 401
 250–350 °C, while the porous structure is created by 402
 decomposition of the thermally labile PMMA domains. Such 403
 PCFs exhibited substantially reduced ion transport resistance 404
 and a high capacitance of 66 $\mu F cm^{-2}$ in an electrochemical 405
 supercapacitor test owing to the advantageous interconnected 406
 porous network and the highly optimal bimodal-size- 407
 distribution pores. 408

As mentioned above, block copolymers are powerful 409
 templates because of their rich phase diagrams accessible via 410
 self-assembly, and some are commercially available.^{45–48} 411
 Carbon materials with ordered mesopores and a narrow pore 412
 size distribution can be templated by micelles of amphiphilic 413
 block copolymers. The most common ones are poly(ethylene 414
 oxide)-*b*-poly(propylene oxide)-*b*-poly(ethylene oxide) tri- 415

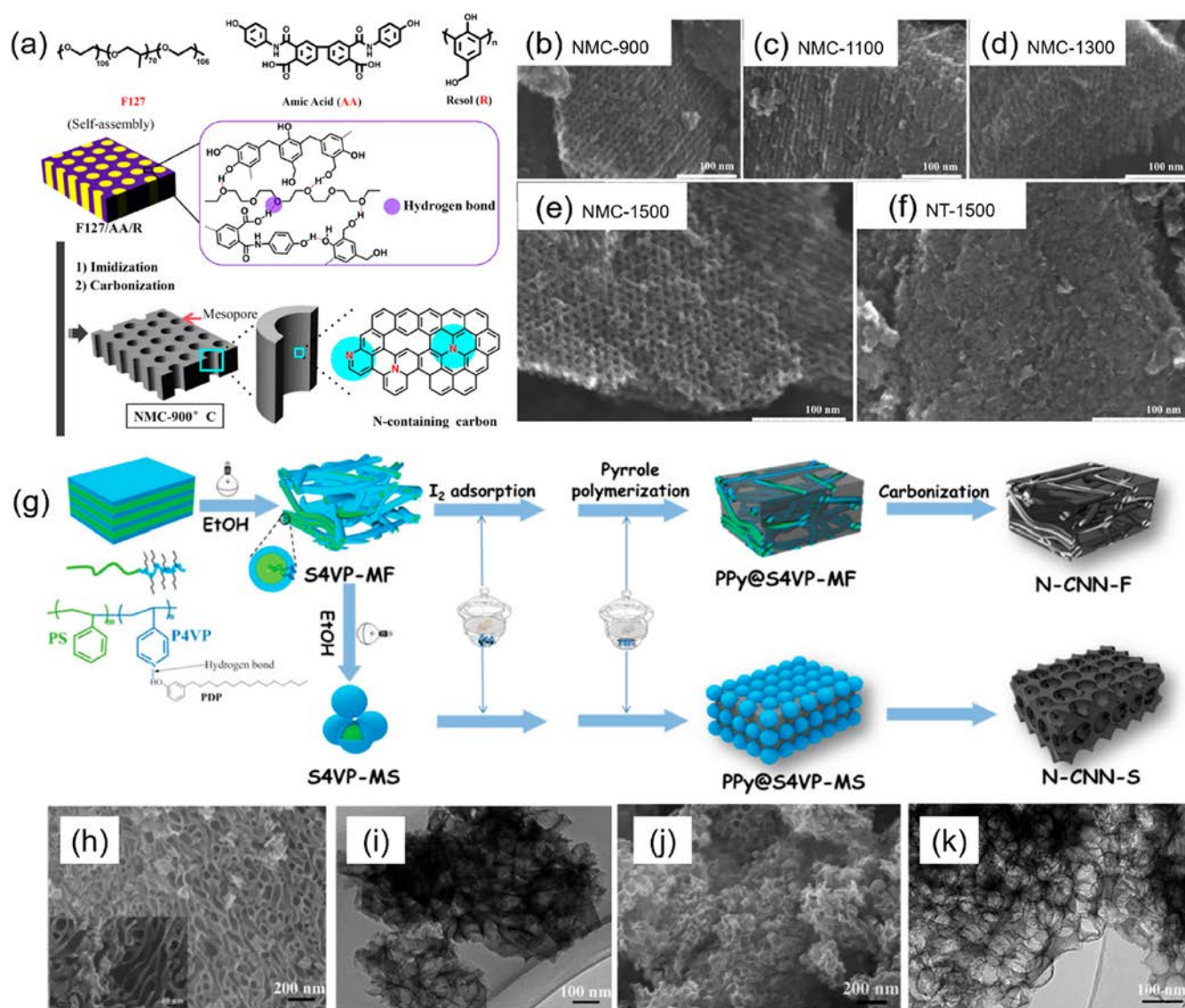


Figure 6. (a) Schematic illustration of the synthesis of NMCs (purple matrix, PEO block/AA/resol; yellow cylinders, PPO block) via the F127-block-copolymer-assisted self-assembly of an aromatic N-containing carbon precursor, amic acid (AA), and a cross-linker, a resol (R). (b–e) Porous structures of NMCs carbonized at different temperatures. The number represents the carbonization temperature (°C). (f) Morphology of disordered N-doped carbon (NF) as a comparison. Reproduced with permission from ref 50, licensed under CC BY. (g) Experimental procedure for the preparation of interconnected porous N-doped carbon networks (N-CNNs). (h, i) SEM and TEM images of N-CNNs templated from micellar fibers (N-CNN-F). (j, k) SEM and TEM images of N-CNNs templated from micellar spheres (N-CNN-S). Reproduced with permission from ref 37. Copyright 2018 Wiley-VCH.

416 block copolymers (PEO-*b*-PPO-*b*-PEO), i.e., the commercial
 417 Pluronic family,^{49–51} polystyrene-*b*-poly(4-vinylpyridine) (PS-
 418 *b*-P4VP),³⁷ or polystyrene-*b*-poly(ethylene oxide) (PS-*b*-
 419 PEO).⁵² The applied carbon precursors can be either
 420 heteroatom-containing or heteroatom-free polymers such as
 421 small clusters of phenol-formaldehyde, so-called “resol”,^{51–54}
 422 “RF resin” (resorcinol-formaldehyde),⁵⁵ or “PF resin” (phlor-
 423 oglucinol-formaldehyde).⁴⁹ Heteroatom-doped carbons can be
 424 synthesized by direct carbonization of heteroatom-containing
 425 polymers in the block copolymer template or post-treatment of
 426 carbons derived from heteroatom-free polymers. Fascinating
 427 porous carbon nanostructures have been produced from block
 428 copolymer nanostructures as sacrificial templates, including
 429 two-dimensional hexagonal (*p6mm*), three-dimensional bicon-
 430 tinuous (*Ia3d*), or body-centered cubic (*Im3m*) varieties.^{49–55}
 431 For example, Hayakawa’s group synthesized well-ordered N-

containing mesoporous carbons (termed NMCs) with
 432 hexagonally arranged, uniform 4 nm mesopores via a block
 433 copolymer template. The NMC films were obtained from a
 434 blend of Pluronic copolymer F127 ($M_w = 12600$ Da, PEO₁₀₆-
 435 PPO₇₀-PEO₁₀₆), amic acid (AA) as a N-containing precursor,
 436 and a resol as a stabilizer (Figure 6a–f).⁵⁰ Well-ordered NMCs
 437 bearing large mesopore volumes ($V_{\text{meso}} = \sim 0.8$ mL g⁻¹, $V_{\text{total}} =$
 438 ~ 0.9 mL g⁻¹) and a moderate S_{BET} of 532 m² g⁻¹ were
 439 achieved by pyrolysis of the self-assemblies of F127, AA, and
 440 the resol. Similarly, in 2018, Chen and co-workers reported 3D
 441 interconnected N-doped carbon networks (N-CNNs) with
 442 designable pore geometries (Figure 6g–k).³⁷ The authors
 443 applied a vapor-phase polymerization approach using self-
 444 assembled bicontinuous PS-*b*-P4VP membranes as templates.
 445 The template morphology was tuned by the addition of 3-*n*-
 446 pentadecylphenol (PDP) to PS-*b*-P4VP through ethanol
 447

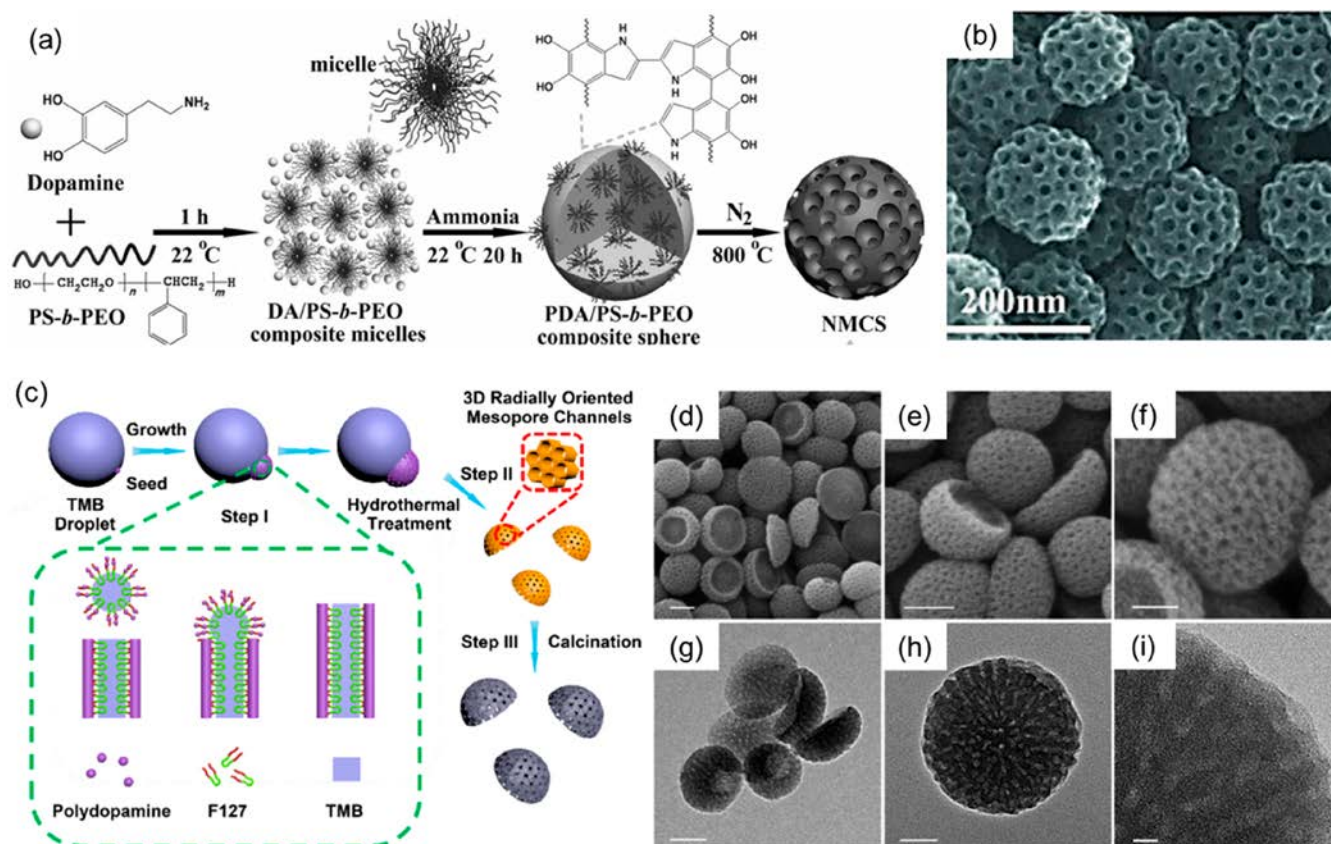


Figure 7. (a) Formation process and (b) SEM image of N-doped mesoporous carbon nanospheres (NMCSs) obtained via the self-assembly of block copolymer–PDA composite micelles followed by direct carbonization. Reproduced with permission from ref 56. Copyright 2015 Wiley-VCH. (c) Formation process of bowl-like mesoporous particles. Step I, formation of the block copolymer F127/TMB/PDA oligomer composite micelles and emulsion-induced interface anisotropic assembly of asymmetric bowl-like mesostructured PDA particles with radially oriented large mesochannels. Step II, hydrothermal treatment of the mesostructured PDA nanocomposites to stabilize the structure. Step III, carbonization at 800 °C for 2 h under N₂ to generate bowl-like mesoporous carbon particles with radially oriented mesochannels. (d–f) SEM images and (g–i) TEM images of the porous bowl-like carbon particles. Scale bars are 100 nm (d, e, g), 50 nm (f, h), and 10 nm (i). Reproduced with permission from ref 57. Copyright 2016 American Chemical Society.

448 swelling. This step formed hydrogen bonding of PDP with the
 449 P4VP block to increase the P4VP volume fraction in the block
 450 copolymer, which resulted in a microphase separation
 451 transformation from lamellar to interconnected micellar fibers
 452 or spheres with a PS@P4VP core–shell structure inside the
 453 PS-*b*-P4VP membranes. Different morphologies of block
 454 copolymer templates could be obtained by simple adjustment
 455 of the swelling time for the same PS-*b*-P4VP(PDP) system.
 456 Complexed iodine was used to initiate the polymerization of
 457 pyrrole to form polypyrrole on the outer surface of PS@P4VP
 458 core–shell micelles. Finally, the block copolymer template was
 459 removed after carbonization, and N-CNNs with different pore
 460 geometries were obtained. When applied as a metal-free
 461 oxygen reduction reaction (ORR) catalyst, the N-CNNs with
 462 interconnected network structures displayed a performance
 463 comparable to that of commercial Pt/C in alkaline media. The
 464 so-called vapor-phase polymerization approach using block
 465 copolymer assemblies as templates provides a synthetic
 466 alternative and important insights into the design of porous
 467 3D networks.

468 In addition to the most commonly reported ordered porous
 469 carbon films, individual carbon spheres with internal ordered
 470 porous channels are also accessible by using a block copolymer
 471 as a template. As an example, N-doped mesoporous carbon
 472 spheres (NMCSs) were synthesized by Yamauchi et al. in

2015.⁵⁶ A pore size of up to 16 nm was engineered inside
 473 NMCSs through self-polymerization of dopamine (DA) and
 474 spontaneous coassembly of diblock copolymer micelles (Figure
 475 7a). The resultant NMCSs featured characteristic mesopores
 476 of up to 16 nm and a uniform particle size of ~200 nm (Figure
 477 7b). Their high electrocatalytic activity in the ORR was related
 478 to the large mesopores and the small dimensions of the
 479 NMCSs, which promoted mass transport by reducing and
 480 smoothing the diffusion pathway. Similarly, an emulsion-
 481 induced interfacial anisotropic assembly approach was
 482 employed by Lou et al.⁵⁷ to produce N-doped porous bowl-
 483 shaped particles from a 1,3,5-trimethylbenzene (TMB)-in-
 484 water emulsion. Mesostructured PDA seeds were first
 485 produced through self-assembly of block copolymer F127/
 486 TMB/PDA composite micelles formed at the TMB/water
 487 interface. These micelles further anisotropically grew into
 488 bowl-like particles. The nucleation and anisotropic growth of
 489 PDA particles was then controlled by the TMB droplets as a
 490 soft template, which governed the mesoporous structure and
 491 particle morphology (Figure 7c–i). These bowl-shaped porous
 492 PDA particles were readily carbonized into mesoporous carbon
 493 particles with preserved morphology and mesostructure. This
 494 approach exemplifies a unique paradigm for the synthesis of
 495 dimensionally asymmetric porous carbon particles. At the same
 496 time, Feng and his group reported a coassembly method to
 497

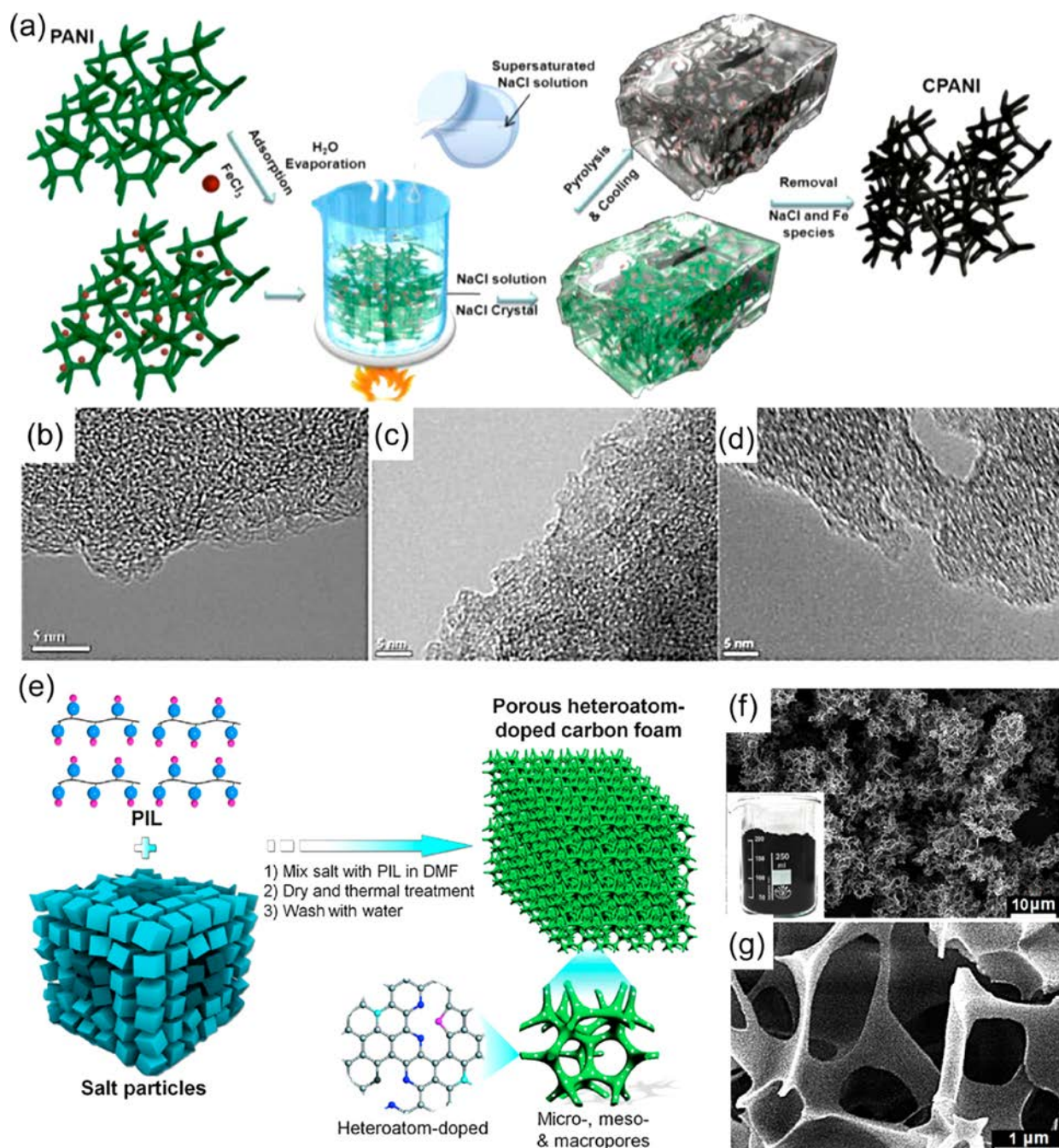


Figure 8. (a) Synthetic scheme for porous carbons via a salt recrystallization method. High magnification TEM images showing the porous structures and edges of CPANI (b), CPANI-NaCl (c), and CPANI-Fe-NaCl (d). Reproduced with permission from ref 61. Copyright 2015 American Chemical Society. (e) General fabrication procedure of hierarchically porous heteroatom-doped carbon foams using PILs as a N/C precursor and chemically inert solid salt as a template. (f, g) SEM images of PNCF with different magnifications. Reproduced with permission from ref 62. Copyright 2018 Elsevier.

498 synthesize N-doped mesoporous carbon nanospheres
 499 (MCNSs) with well-controlled pore sizes ranging from 8 to
 500 38 nm by employing PS-*b*-PEO with varied PS block length as
 501 soft templates and dopamine as a N-rich precursor.⁵² They
 502 introduced a linear equation to guide the quantitative control
 503 of the average pore size of MCNSs by adjusting the block
 504 length in the block copolymers, which precisely dictated the
 505 porosity of the PDA-derived carbon nanospheres. When these
 506 MCNSs were used as electrodes in supercapacitors, this group
 507 found that the capacitance normalized by S_{BET} remained

invariable, whereas the specific capacitance of the MCNSs
 508 decreased linearly with increasing pore size. 509

2.1.3. Polymer/Inorganic Hybrids as Templates. If the
 510 inorganic template and the polymeric carbon precursor are
 511 incompatible, then a nonuniform interface will form during the
 512 molding/casting procedure. This inevitably produces a non-
 513 porous and/or ill-defined porous structure due to the weak
 514 template–precursor interaction, which leads to incomplete
 515 filling of the pores in the template and unfavorable deposition
 516 of carbon on the external template surface. As the formation of
 517 a highly uniform interface between the template and carbon 518

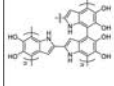
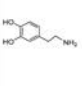
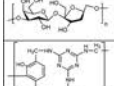
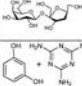
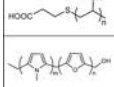
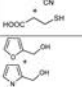
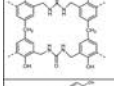
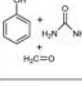
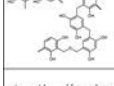
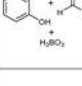
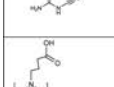
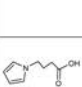

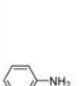
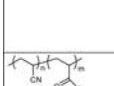
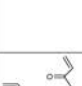
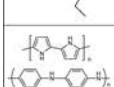
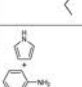
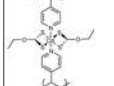
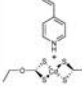
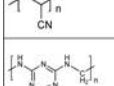
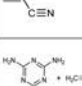
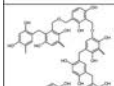
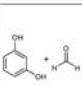
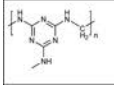
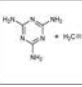
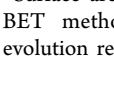
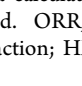




519 precursor is beneficial, the interfacial energies should be
 520 chemically controlled. Copolymerization of monomers with an
 521 alkoxide inorganic precursor, e.g., tetraethylorthosilicate
 522 (TEOS), is a practical approach to reach this goal.^{58,59} For
 523 example, Zhang and co-workers synthesized Br-containing
 524 organosilica NPs <5 nm in size using a brominated organosilica
 525 precursor; the NPs were then grafted with PAN chains to
 526 prepare silica-g-PAN composites by surface-initiated atom
 527 transfer radical polymerization (SI-ATRP).⁶⁰ Porous carbons
 528 were obtained with an S_{BET} value of 1244 $\text{m}^2 \text{g}^{-1}$ and a
 529 nitrogen content as high as 11.9 wt %.

530 As discussed above, the interaction of the carbon precursor
 531 with the template plays a vital role in governing the
 532 morphology of carbons. To optimize the precursor–inorganic
 533 interface in the templating method, other strategies employing
 534 inorganic salts or crystals as a template matrix and space
 535 confinement have been conducted. For example, Wei et al.
 536 demonstrated how to fix the precursor shape via a salt
 537 recrystallization method to synthesize N-doped carbon nano-
 538 materials with a high density of active sites as an ORR catalyst
 539 (Figure 8a–c).⁶¹ In their method, a NaCl crystal acted as a
 540 fully sealed nanoreactor, facilitating N incorporation and
 541 graphitization. As displayed in Figure 8a, they first fabricated a
 542 three-dimensional (3D) PANI network via a self-assembly
 543 process. After adsorption of FeCl_3 , a supersaturated NaCl
 544 solution was poured into a beaker containing PANI networks.
 545 The water was then evaporated so that NaCl recrystallized
 546 onto PANI at the bottom of the beaker. To fully cover the 3D
 547 PANI network with NaCl, cycles of NaCl solution addition,
 548 water evaporation, and NaCl recrystallization were repeated
 549 until the whole PANI was buried by and tightly sealed inside
 550 NaCl crystals. The NaCl-crystal-sealed PANI was first
 551 dehydrated at 120 °C before annealing at 900 °C under N_2 .
 552 A hot aqueous H_2SO_4 solution was applied to wash off the
 553 NaCl crystals and iron species. This method for synthesizing
 554 an Fe-doped catalyst benefited the formation of more FeN_x
 555 sites in the inner pores and graphitic structure. Later, in 2018,
 556 Yuan et al. prepared hierarchically porous N-doped carbon
 557 foams (PNCFs) via a facile bottom-up strategy by using PILs
 558 as the N/C precursor and common inorganic salts as the
 559 structural template, a method termed “cooking carbon in a
 560 solid salt” (Figure 8e–g).⁶² In their work, a salt/PIL physical
 561 mixture was first prepared by dropwise addition of an aqueous
 562 salt solution into a PIL solution in DMF, followed by thermal
 563 evaporation of the solvent. The mixture was calcined close to
 564 but below the melting point of the salt to convert the PILs into
 565 carbon inside the solid salt matrix. The salt was washed away
 566 by water, leaving carbon foams with rich heteroatoms and
 567 hierarchical micro/meso/macropores. This approach is uni-
 568 versal and can be applied to different common salts, such as
 569 NaCl, KCl, and Na_2SO_4 .

2.2. Direct Synthesis

570 Although hard templates may enable synthesis of heteroatom-
 571 doped carbons with better pore control, most hard templates
 572 have to be synthesized and then removed, which is a time/
 573 labor-consuming procedure.^{79–81} Beyond the costs of materi-
 574 als, labor, and time and toxic etching agents, the effect of these
 575 treatments on the carbon structure and catalytically active sites
 576 in particular remains a concern. For example, HF can remove
 577 oxygen functionalities from carbon nanotubes.⁸⁰ Similarly, to
 578 increase the surface area, “activating” steps with CO_2 or KOH
 579 can remove much of the nitrogen content.⁷³ By contrast, at the

Table 1. Polymer-Derived HPCMs Obtained by Template Methods Reported in the Literature

Precursor Polymer	Monomer	Template / T (°C)	Surface area ($\text{m}^2 \text{g}^{-1}$)	Pore volume ($\text{cm}^3 \text{g}^{-1}$)	Pore size (nm)	Content of heteroatom	Applications	Ref.
		SiO ₂ spheres 800 °C	1056	2.56	1–30	N (8.2 wt%)	Supercapacitor	64
		SBA-15	1013	1.14	~3.8	N (4.5 wt%)	Supercapacitor	50
		CdS nanowires 1000 °C	1054.8	—	5.93	N (5.09 at%) S (2.99 at%)	Catalyst	63
		PS- <i>b</i> -PEO 800 °C	~350	~0.5	5.4–16	N (7.5 wt%)	Electrocatalyst for the ORR	56
		APTS@SBA-15 450–900 °C	790	0.86	5.12	N (0.6 at%) O (2.9 at%)	Supercapacitor	65
		Silica particles 900 °C	836	2.96	1.74 12.3	N (13.2 at%) O (3.9 at%)	Li-S batteries	66
		SBA-15 1000 °C	1012	0.91	2–7	N (4.0 at%) O (0.6 at%)	Catalyst supports	67
		Mesoporous silica (KIT-6) 850 °C	1152	1.7	3.9	N (~10 at%)	Electrocatalyst for the ORR	68
		Pluronic F127 600 °C	557	0.29	2.8	N (0.38 at%)	CO_2/SO_2 capture	69
		Pluronic F127 800 °C	638	0.66	1 7	B (0.42 wt%) O (3.83 wt%)	Supercapacitor	39
		TiO ₂ 800 °C	2144	2.27	0.6 1.2 2.7 7–25	N (8.25 wt%) O (6.6 wt%)	Supercapacitor	23
		Pluronic P-123 800 °C	2369	0.88	<2	N (8.0 wt%)	CO_2 capture	70
		Phytic acid 1000 °C	1663	1.42	<10	N (1.8 wt%) O (3.3 wt%) P (0.1 wt%)	Electrocatalyst for the ORR and OER	71
		PS spheres 500 °C	323	0.78	2–5	N (19.22 wt%)	Electrocatalyst for the ORR, Supercapacitor	41
		$\text{Co}(\text{OH})_2$ 800 °C	236.8	—	1–30	N (3.4 at%)	Electrocatalyst for the ORR	72
		Poly(<i>n</i> -butyl acrylate) 700 °C	500	0.67	~13	N (18 at%) O (3.6 at%)	Electrocatalyst for the ORR, Supercapacitor	73
		Triton X-100 900 °C	3022	—	2.5	N (2.55 wt%)	Supercapacitor, Li-S batteries, Adsorbent	74
		CdS nanoparticles 1000 °C	2446	3.1	1.4, 4.8	N (2.79 at%) S (1.41 at%)	Electrocatalyst for the ORR	75
		Organosilica NPs 800 °C	1244	—	~2.5	N (11.9 wt%)	Supercapacitor	60
		Colloidal silica 700 °C	777	2.3	10–20	N (4.3 at%)	CO_2 adsorption	76
		Polyhedral oligosilsesquioxanes (POSS) and Pluronic F108 900 °C	2000	1.19	~1 ~4	N (~4 wt%)	Supercapacitor	77
		Pluronic P-123 and sodium silicate 900 °C	794	1.05	—	N (7.4 wt%)	Electrocatalyst for the ORR	78

^aSurface area calculated from the N_2 adsorption isotherm using the BET method. ORR, oxygen reduction reaction; OER, oxygen evolution reaction; HER, hydrogen evolution reaction

580 expense of less precise control of the porous structure, direct
 581 carbonization of polymers without an external template can
 582 reduce template-related etching procedures. By adjusting the
 583 pyrolysis program, the heteroatoms introduced into the carbon
 584 framework can be preserved at a relatively high content and are
 585 then also stable under harsh service conditions.^{82,83} In general,
 586 direct carbonization of heteroatom-rich polymers or a mixture
 587 of heteroatom-free polymers and heteroatom-containing
 588 compounds allows the production of HPCMs. The former
 589 involves homogeneous doping of heteroatoms in the bulk, the
 590 contents and types of which are dominated by the polymers
 591 themselves. In the latter, heteroatom-free or -poor polymers
 592 can be mixed with heteroatom-rich compounds, e.g., NH₃,
 593 urea, melamine, cyanamide, and dicyandiamide, before carbon-
 594 ization.^{82,84–87} However, compared with template methods,
 595 the control over the pore size distribution is usually weak due
 596 to potential phase changes of the mixture of the polymer and
 597 the heteroatom-containing compound. Recent progress in the
 598 synthesis of HPCMs directly from polymers without templates
 599 is summarized in Table 2. These studies include different types
 600 of polymeric precursors and heteroatom sources, S_{BET} , pore
 601 sizes, heteroatom contents, and carbonization conditions.

602 **2.2.1. Direct Carbonization of Heteroatom-Rich**
 603 **Polymers.** Heteroatom-rich polymers, such as the N-
 604 containing polymers of PAN, PI, PAM, PVP, PoPDA, PPy,
 605 PANI, PDA, and imidazolium-containing PILs and S-
 606 containing polymers such as polythiophene (PTh),^{8,88–96} can
 607 be directly carbonized. Owing to their rich abundance of
 608 heteroatoms, the easy access to most of them, and the simple
 609 control of the morphology by classical polymer processing
 610 techniques, the direct carbonization route is popular for the
 611 preparation of HPCMs by direct carbonization in an inert
 612 atmosphere (e.g., N₂, Ar, or Ar/H₂). In a typical procedure,
 613 heteroatom-containing polymers with defined structures (e.g.,
 614 nanospheres/nanotubes/nanofibers) are first prepared by
 615 organic reactions or polymerization of monomers under
 616 specific experimental conditions. Then, the as-prepared
 617 polymers are calcined in an inert atmosphere to generate
 618 porous carbons with partially, if not entirely, maintained
 619 micro/mesoporous structures from the polymers.

620 **2.2.1.1. Conjugated Polymers (CPs) as Heteroatom-**
 621 **Doped Carbon Precursors.** Conjugated polymers (CPs)
 622 usually possess highly conjugated polymeric main chains as
 623 well as a sufficient content of heteroatoms such as N and S.^{97,98}
 624 Heteroatom-doped carbon materials derived from CPs have
 625 been considered for applications in energy devices owing to
 626 their high carbonization yield, high heteroatom content, and
 627 maintained or even increased conductivity.⁹⁹ Advantageously,
 628 the heteroatoms homogeneously introduced into the polymer
 629 in an sp² or sp hybridization state are better preserved than
 630 nonconjugated species under the same carbonization condi-
 631 tions and are more stable under the harsh working
 632 conditions usually applied to carbons. Direct carbonization of
 633 CPs also avoids extra steps of conventional carbonization
 634 methods, such as thermal annealing in the presence of NH₃,
 635 chemical vapor deposition, the arc-discharge method, and
 636 nitrogen plasma treatment.

637 PANI with its structure of phenyl rings connected *via*
 638 nitrogen-atom bridges can be considered the archetype of a
 639 conjugated-polymer-based precursor for N-doped carbons.
 640 Direct carbonization of PANI, which serves as both the carbon
 641 and nitrogen sources, could preserve the homogeneous
 642 distribution of N sites on the resultant graphitic carbon

Table 2. Summary of the Polymeric Precursor, S_{BET} , Pore Size, N Content, and Carbonization Conditions for Diverse Porous Carbons Obtained by Direct Synthesis Strategies

Precursor Polymer	Monomer	Temperature (°C)	Surface area (m ² g ⁻¹)	Pore volume (cm ³ g ⁻¹)	Pore size (nm)	Content of heteroatom	Applications	Ref.
		800 °C	1513	1.13	2.98	N (8.4 wt%)	Supercapacitors	101
		900 °C	465	0.39	1.64	N (1.21 at%) O (4.61 at%)	Supercapacitors	108
		800 °C	20.35	0.03317	6.52	N (11.9 wt%)	Li-ion batteries	100
		1000 °C	1327	—	1–2	N (1.9 at%)	Supercapacitors	103
		800 °C	753	—	2	N (6.0 wt%)	Supercapacitors	98
		600 °C	1203	0.641	0.5–1.2–7	N (2.7 at%) O (5.4 at%)	Supercapacitors	94
		600 °C	159.6	—	3.8, 14, 70	N (20.6 at%) O (6.4 at%)	Li-ion batteries	102
		800 °C	2279	0.177	2.23	—	Supercapacitors	91
		700 °C	1852	0.964	0.5–1.0	N (1.72 wt%)	CO ₂ capture	105
		800 °C	815	0.733	10	P (1.62 at%)	Electrocatalyst for the ORR	104
		800 °C	38	0.022	—	N (1.3 at%) O (8.6 at%) S (1.7 at%)	Supercapacitors	92
		800 °C	290	0.157	<1	N (2.4 at%) O (9.3 at%) S (2.4 at%)	Supercapacitors	92
		600 °C	754	—	1–5	N (23.9 wt%)	Electrocatalyst for the ORR	103
		1000 °C	907	0.79	15	N (5.7 wt%)	Electrocatalyst for the HER and OER	106
		Direct synthesis (L-lysine)	537	0.258	—	N (1.28 wt%) O (3.44 wt%)	CO ₂ capture	108
		800 °C	215	0.26	1.81	N (5.63 wt%) B (3.34 wt%)	CO ₂ /CH ₄ capture	107
		800 °C	291	0.33	1.84	N (5.72 wt%) B (3.21 wt%)	Supercapacitors	107
		800 °C	268	0.23	1.72	N (4.89 wt%) B (2.91 wt%)	Supercapacitors	107
		800 °C	1051	1.93	7.4	O (7.90 at%)	Supercapacitors	108
		900 °C	1535	2.21	0.5–2–30	N (3.21 wt%) P (2.12 wt%)	Electrocatalyst for the ORR	107
		700 °C	496	0.25	10	N (12 at%) B (5.6 at%)	Electrocatalyst for the ORR	104
		900 °C	683.7	—	3–9	B (8.07 wt%)	Li-O ₂ batteries	100

^a S_{BET} calculated from the N₂ adsorption isotherm. ORR, oxygen reduction reaction; OER, oxygen evolution reaction; HER, hydrogen evolution reaction.

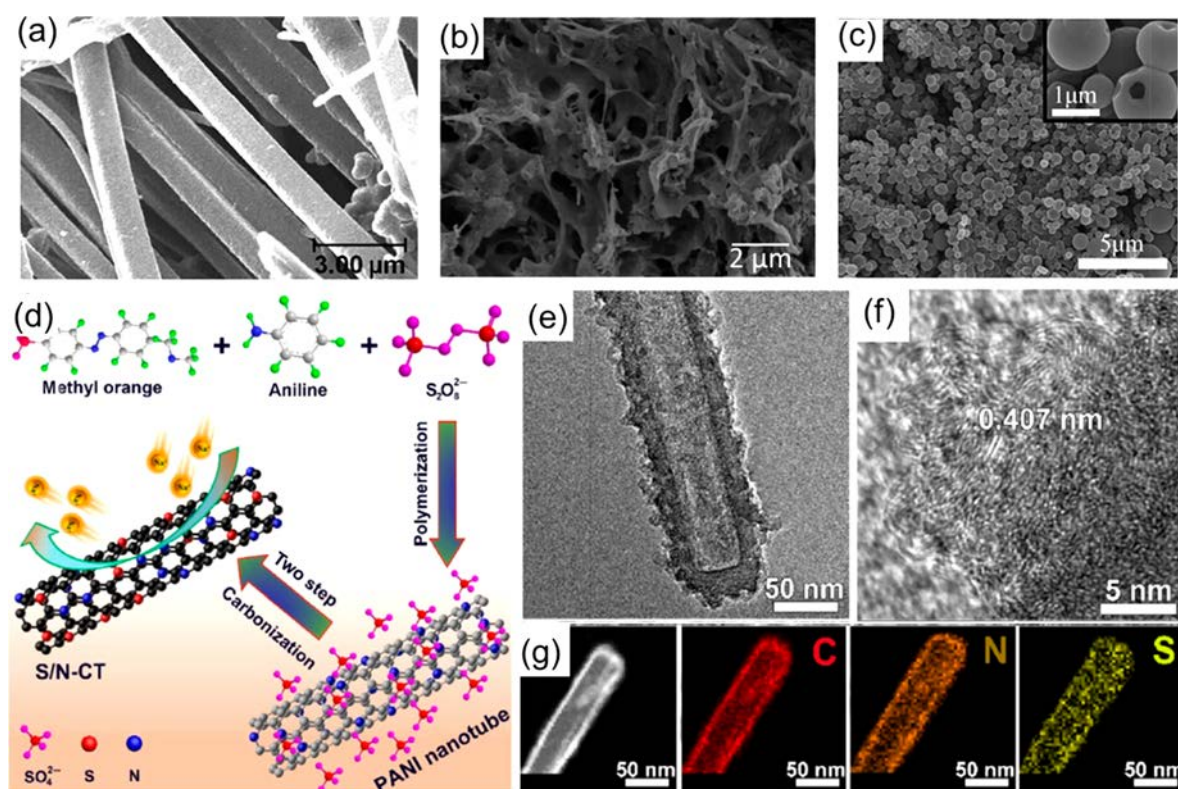


Figure 9. (a) SEM image of N-doped carbon fibers from PPy annealed at 800 °C. (b) SEM image of N-CNWs prepared from PpPD annealed at 700 °C. (c) SEM image of hollow carbon spheres obtained by annealing PoPD at 700 °C. (d) Synthetic schematic for PANI nanotubes via a soft template method and subsequent high-temperature conversion into S/N-CT samples. (e, f) TEM images of S/N-CT. (g) STEM image and energy-dispersive elemental maps of C, N, and S in S/N-CT. Reproduced with permission from ref 101, copyright 2012 Royal Society of Chemistry; ref 93, copyright 2014 American Chemical Society; ref 102, copyright 2015 Elsevier; and ref 105, copyright 2018 Springer.

643 surface.¹⁰⁰ In addition to PANI, PPy and polythiophene are
 644 other typical choices of conjugated polymers as carbon
 645 precursors. It is important to know that, beyond heteroatom
 646 doping, controlling the morphology and nanostructure is
 647 crucial to improving the functionality of CP-derived
 648 carbocatalysts.⁹⁷ For example, Joussleme and co-workers
 649 synthesized PPy with granular- and tubule-like morphologies
 650 and studied the relationship between the morphologies and the
 651 ORR performances of the resultant carbon materials (Figure
 652 9a).¹⁰¹ They found that the annealed PPy tubes showed better
 653 ORR performance, current density, and electron transfer
 654 number. Lei et al. prepared 3D porous N-doped carbon
 655 networks (3D N-CNWs) containing a high N content by
 656 carbonizing poly(*p*-phenylenediamine) (PpPD) through the
 657 integration of oxidative polymerization and catalytic carbon-
 658 ization procedures (Figure 9b).⁹³ The 3D N-CNWs obtained
 659 at 700 °C possessed a high S_{BET} value of up to 1513 m² g⁻¹.
 660 Similarly, to obtain N- and O-codoped hollow carbon spheres
 661 (HCSs), Yao's group directly carbonized PoPD submicron
 662 spheres with the assistance of a glycine dopant (Figure 9c).¹⁰²
 663 The as-synthesized mesoporous HCSs displayed an S_{BET} value
 664 of 355 m² g⁻¹, a high specific capacitance of 210 F g⁻¹, and
 665 good cycling stability in supercapacitor tests.

666 Thiophene and thiophene-based compounds, especially the
 667 commercially available 2-thiophenemethanols, are the most
 668 common choices for the synthesis of S-doped carbons.^{103,104}
 669 They are sufficiently thermostable to give a high yield under
 670 carbonization conditions. FeCl₃ is usually used to polymerize
 671 2-thiophenemethanol into a thermostable, S-rich linear
 672 polymer. In polythiophene-derived carbons, the incorporated

S atoms predominantly form aromatic five-ring sulfides and are
 673 not eliminated due to their high thermal stability. High-
 674 temperature treatment of carbon precursors with S-containing
 675 gases, such as CS₂ and H₂S, is also efficient for increasing the S
 676 doping in carbon materials; such a method is commonly used
 677 for doping graphene with S.
 678

Apart from a single type of heteroatom doping, Xu's group
 679 demonstrated conjugated-polymer-mediated synthesis of S-
 680 and N-codoped carbon nanotubes (S/N-CT) via carbonization
 681 of S-containing PANI nanotubes (Figure 9d–g).¹⁰⁵ In their
 682 work, ammonium persulfate (NH₄)₂S₂O₈ was applied as both
 683 an oxidant and a dopant. Their results indicated that the
 684 selected carbonization technique as well as the (NH₄)₂S₂O₈
 685 content had a great impact on the construction of the carbon
 686 framework, S_{BET} , pore volume, and relative contents of the S
 687 and N species, which can in turn alter the Na⁺ storage
 688 performance of the S/N-CT materials.
 689

2.2.1.2. Polydopamine (PDA) as a Heteroatom-Doped
Carbon Precursor. PDA is an alternative conjugated polymer
 691 for preparing N-doped porous carbons because it has not only
 692 rich N-containing groups but also a nearly 60% carbonization
 693 yield under N₂ at 800 °C.^{106–109} The first evidence of the high
 694 potential of PDA as a N-doped carbon precursor was
 695 demonstrated by Dai et al. in 2011, where PDA was used as
 696 a nitrogen and carbon precursor and silica nanospheres as a
 697 hard template to produce uniform hollow carbon spheres.¹⁰⁸
 698 Shortly after this work, in 2013, Lu and colleagues produced
 699 size-controlled monodispersed porous carbon submicron
 700 spheres (SMSs).¹⁰⁹ These authors identified that dopamine
 701 could directly polymerize into PDA in a submicron sphere 702

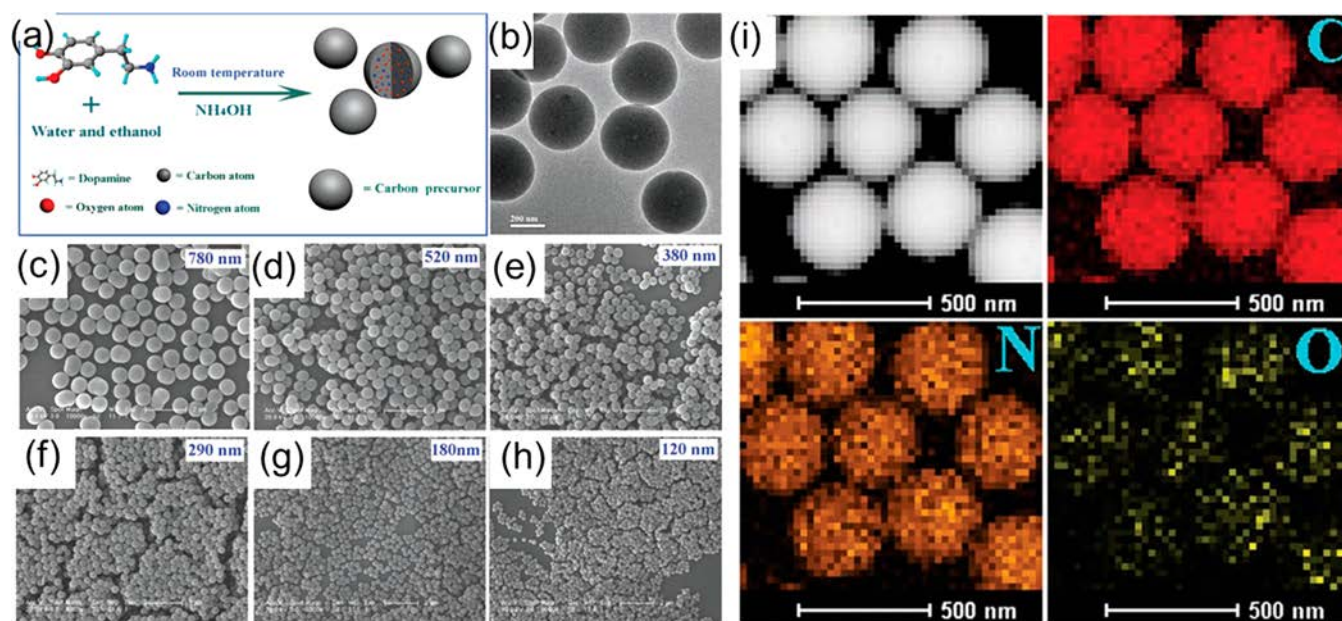


Figure 10. (a) Schematic illustration of the synthesis of PDA submicron spheres (SMSs). (b) Typical TEM image of PDA SMSs with an average diameter of 380 nm. (c–h) SEM images of PDA SMSs with different diameters prepared at different ratios of ammonia to dopamine. (i) EELS mapping analysis of PDA-based carbon spheres. Reproduced with permission from ref 109. Copyright 2013 Wiley-VCH.

703 state without any template in a mixture of ethanol, water, and
 704 ammonia at room temperature (Figure 10). After carbon-
 705 ization at 800 °C, the PDA spheres were converted into carbon
 706 spheres. Furthermore, the sizes of the carbon spheres could be
 707 precisely adjusted over a wide range, even down to below 200
 708 nm, by varying the ratio of ammonia to dopamine. In
 709 comparison to the phenol/formaldehyde resin-derived carbon
 710 spheres, the PDA-derived ones contain a higher degree of sp²
 711 carbon (graphitic carbon) as well as a high content of N active
 712 sites, thus exhibiting enhanced electron conductivity and
 713 catalytic activity. It should be noted that the functional groups
 714 of PDA, such as catechol and N–H, make it convenient to coat
 715 PDA on various solid surfaces to form hybrid materials with
 716 specific properties.

717 Apart from the structural regulation of PDA, different
 718 heteroatoms, such as S and B, can be easily introduced into the
 719 PDA matrix to obtain dual-doped carbons in combination with
 720 the intrinsic nitrogen in PDA. PDA can react with thiol groups
 721 under ambient conditions *via* Schiff base or Michael addition
 722 reactions, with the rate constant ranging from 4×10^5 to $3 \times$
 723 $10^7 \text{ M}^{-1}\cdot\text{s}^{-1}$ in the case of cysteine at pH 7.^{110,111} For example,
 724 Qiao et al. reported that, by reacting 2-mercaptoethanol with
 725 PDA, a 2.5 nm-thick PDA–GO hybrid could graft approx-
 726 imately 16.7 at. % S, which, after pyrolysis, yielded mesoporous
 727 N, S-codoped carbon nanosheets (N, S-CNs).¹¹² This S
 728 doping strategy could realize *in situ* and uniform N, S codoping
 729 and simultaneously achieve much higher doping efficiencies
 730 (4.1 at. % N and 6.1 at. % S) than those achieved by the post-
 731 treatment methods. The resultant N, S-CNs exhibited excellent
 732 performance as bifunctional electrocatalysts for the ORR/
 733 OER, which was attributed to the high level of dual doping,
 734 abundant pores, and favorable electron transfer ability. In
 735 addition, boronic acid can bind the catechol groups of PDA by
 736 boronic acid–diol complexation.¹¹¹ This strategy was utilized
 737 by Ahmed and co-workers to construct a N, B-codoped
 738 carbon, which showed enhanced ORR activity due to the
 739 synergy of B and N codoping in the carbon framework.¹¹³

To date, the shapes of PDA-derived HPCMs have been
 limited mainly to nano- or macroparticles due to the difficulty
 in morphology control without templates. When templates are
 applied, PDA can be easily manufactured into desired
 nanostructures depending on the utilized substrates. The
 unmatched adhesive properties, flexible component tunability,
 and structural regulation are the best features exclusive to
 PDA. In general, heteroatom-doped carbons with richly
 tailored structures can be synthesized from 0D nanodots, 1D
 fibers, 2D films, and 3D membranes by using different types of
 templates.

2.2.1.3. *Poly(ionic liquid) (PIL) as Heteroatom-Doped Carbon Precursors.* In recent years, the synthesis of HPCMs from PILs has become an increasingly growing topic.¹¹⁴ PILs are the polymer products of ionic liquid monomers. The interest in applying PILs as carbon precursors lies in the unique structural properties and functions of PILs, such as negligible vapor pressure and high thermostability and heteroatom content, in addition to the ease of shaping and processing.^{115–117} Thus, porous carbon materials with different morphologies can be obtained from PILs. The approach of doping carbons with heteroatoms using PILs is very efficient for adjusting the electrical conductivity, basicity, oxidation stability, and catalytic activity of PIL-derived carbons. The requirements on the chemical structure and the formation mechanism of porous structures from PILs are similar to those of ILs, which were reviewed previously.^{118,119} PILs bearing nitrile or cyano groups generally produce N-doped carbons with a higher yield than PILs without them because these nitrile/cyano groups undergo cyclization into triazine networks that stabilize the carbon intermediate to limit fragmentation, thus boosting the carbonization yield. Cyano groups can be easily incorporated into PILs either by attaching a nitrile group onto the polymer chain or *via* anion exchange to load nitrile/cyano-containing anions, such as dicyanamide (dca), tricyano-methanide (tcm), and tetracyanoborate (tcb). These condensable anions can couple different cations, such as

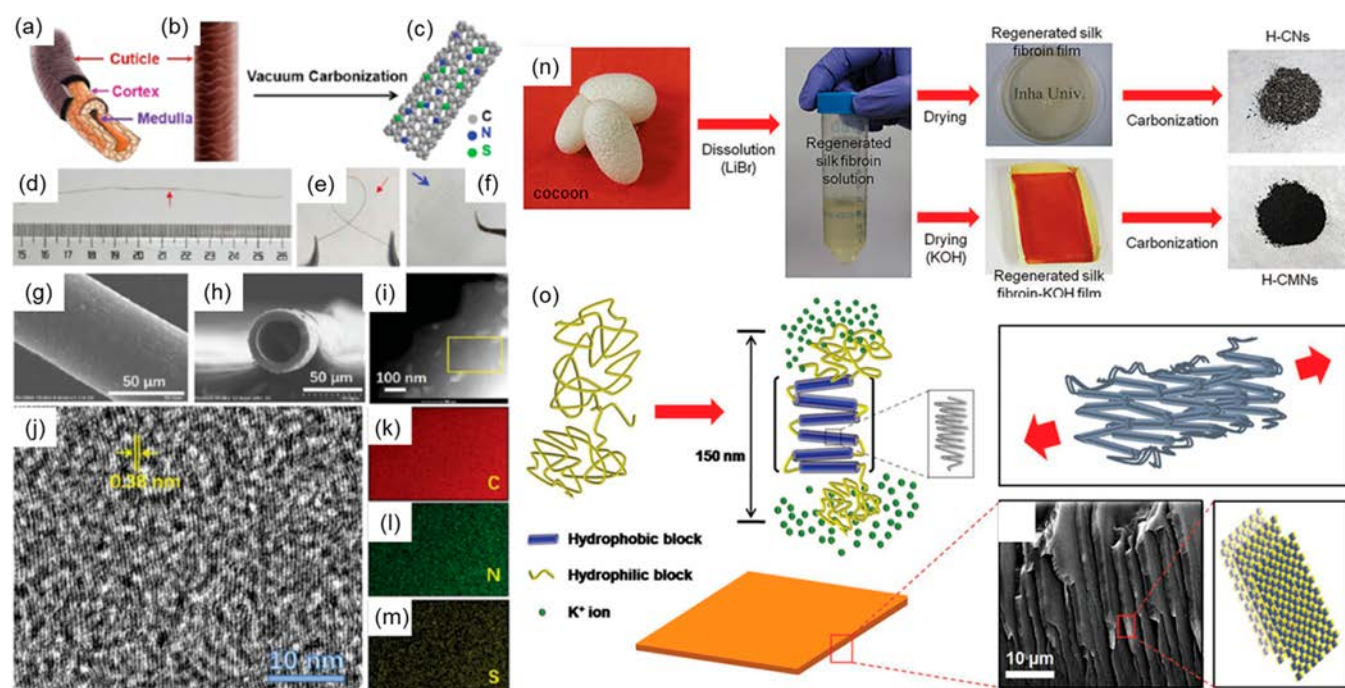


Figure 11. (a–c) Cartoon illustration of a heteroatom-doped graphitic carbon fiber derived from “human hair”. (d–f) Digital photographs of linear and bent carbon fibers and textile. (g, h) Surface and cross-sectional SEM images of carbon fibers. (i) HRTEM image of carbon fibers. (j–m) STEM image and corresponding elemental mappings. Reproduced with permission from ref 133. Copyright 2019 Royal Society of Chemistry. (n) Fabrication process of HCMNs from silk fibroin fibers. (o) Schematic model of *Bombyx mori* silk fibroin lamellar-like layer formation in water by self-assembly. The inset is an SEM image of regenerated silk fibroin film after thermal treatment at 200 °C. Reproduced with permission from ref 134. Copyright 2013 Wiley-VCH.

777 pyridinium, pyrrolidinium, or imidazolium derivatives, to
778 generate N-doped carbons in high yield.

779 In 2010, Yuan et al. demonstrated the first example of using
780 PILs as carbon precursors to produce highly graphitic,
781 mesoporous, and conductive carbon nanostructures by the
782 pyrolysis of IL monomers or PILs at 900 °C without a
783 template under nitrogen in the presence of iron(II)
784 chloride.¹²⁰ This synthetic route involved metal salts that
785 catalyzed the growth of folded-up or stiff graphite plates with
786 thicknesses in the range of 5–20 nm and therefore enabled
787 template-free synthesis of porous carbons. The employment of
788 metal chloride in this carbonization process improves the
789 graphitization degree of carbons at the expense of a low
790 nitrogen content due to the dissolution–precipitation
791 mechanism during carbonization, which is not active for
792 nitrogen. As a significant N content is essential for enhanced
793 electronic conductivity and (electro)catalytic activity, in most
794 of the following research activities, efforts were directed to
795 carbonization processes without Fe/Co/Ni metals or metal
796 salts to maintain the high nitrogen content in the final
797 products. In addition, to use the advantages of the polymeric
798 nature and rich processing approaches, various morphologies
799 of PILs were pursued and converted into the corresponding
800 carbons with well-designed shapes and structures. For example,
801 Wang et al. reported the synthesis of porous carbon
802 nanoparticles through a hydrothermal carbonization (HTC)
803 method (160–200 °C), using sugars as a carbon source and
804 PILs as an additive.¹¹⁷ In this template-free process, the PILs
805 acted as a stabilizer for the primary nanoparticles formed in the
806 initial stage and allowed for only growth through the further
807 addition of monomers. This occurred due to the electrostatic
808 repulsion exerted by the PIL attached to the nanoparticle

809 surface, which minimized agglomeration, lowering the particle
810 size to <50 nm. In addition, the PILs further improved the
811 porous structure of the final materials in the post-HTC
812 carbonization step. The porous carbon nanoparticles obtained
813 via this template-free approach showed a high surface area of
814 up to 572 m²·g⁻¹. Porous functional carbon monoliths can be
815 generated from sugar-based molecules and polysaccharide
816 biomass at comparably low temperatures of 400 °C under a N₂
817 atmosphere. PILs act as “soft activation agents” with their own
818 structural contribution and effectively promote the conversion
819 and pore generation even at a low addition amount of 7 wt %.
820 The obtained monolith can still preserve its natural shape, high
821 porosity, and good mechanical performance. In addition, all
822 aforementioned template methods can be applied to PILs
823 owing to their extremely good affinity and compatibility with
824 most template surfaces.

2.2.1.4. *Porous Polymers.* Porous organic polymers (POPs)
825 are a family of multidimensional porous network materials with
826 covalently bonded stable backbones that exhibit high specific
827 surface areas and nanometer-scale pores.^{5,121} According to
828 their degree of long-range order, POPs can be generally
829 divided into two categories: amorphous polymers (such as
830 most covalent organic frameworks, hyper-cross-linked poly-
831 mers, and polymers of intrinsic microporosity) and crystalline
832 polymers such as conjugated microporous polymers. They can
833 be easily designed at the molecular level and synthesized from
834 abundant monomers with desired active sites and porous
835 properties. POPs have been emerging as alternative precursors
836 for the preparation of HPCMs because of their intrinsic porous
837 structure, ease of preparation, and diverse heteroatom-
838 containing monomer units.^{122,123} POP-based self-templating
839 has many merits, such as potential preservation of high surface
840

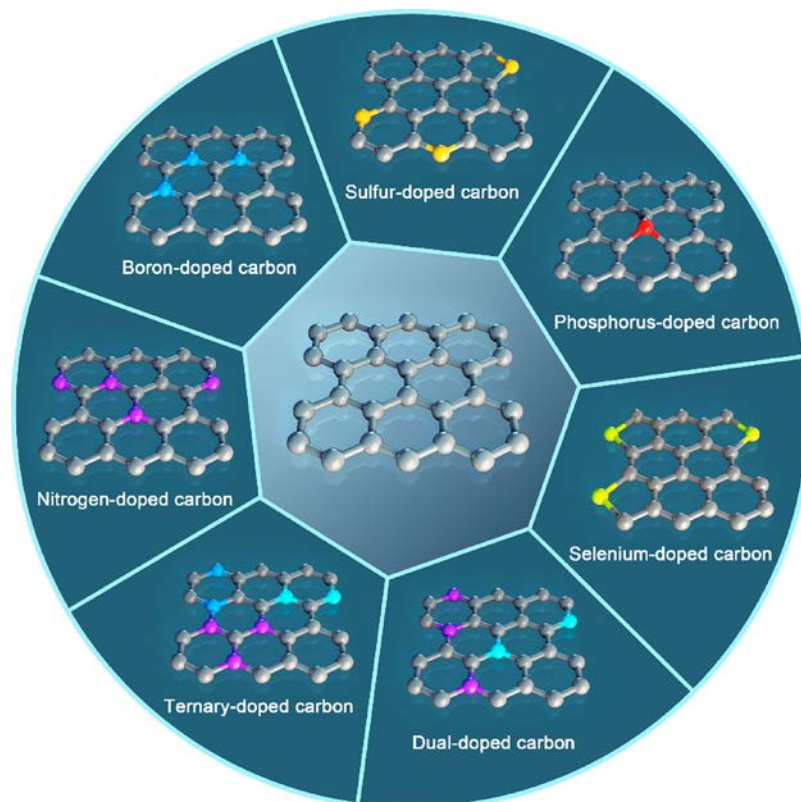


Figure 12. Schematic diagram of the structures of various heteroatom-doped carbons.

841 area and porosity and uniform heteroatom doping. Various
 842 POPs have been used to fabricate HPCMs for high-
 843 performance electrochemical devices, such as imine and
 844 benzimidazole-linked polymeric frameworks.^{5,124–126} As an
 845 example, Tan and co-workers prepared N, P-codoped carbon
 846 materials from an imine-linked POP.¹²⁷ Imine-linked POPs
 847 were first synthesized in one step with a high yield *via* Schiff
 848 base condensation in DMSO under catalyst-free conditions. N,
 849 P-codoped carbons with a hierarchical porosity traversing the
 850 micro-, meso-, and macropore ranges with a high S_{BET} value of
 851 $1535 \text{ m}^2 \text{ g}^{-1}$ were obtained by straightforward pyrolysis of
 852 imine-linked POPs. These N, P-codoped porous carbons
 853 displayed superior electrocatalytic activity in the ORR, along
 854 with excellent stability and high tolerance to methanol.
 855 Although numerous heteroatom-doped POPs have been
 856 reported as carbon precursors, large-scale preparation at low
 857 cost remains one of the greatest obstacles for practical
 858 applications. Another challenge could be the synthesis of
 859 “strictly” metal-free HPCMs because metallic catalysts or
 860 metal-containing starting materials are usually needed to
 861 prepare POPs and trapped in part if not entirely in POPs.

862 **2.2.1.5. Biomass Polymers as Heteroatom-Doped Carbon**
 863 **Precursors.** From an economic and environmental viewpoint,
 864 the use of renewable precursors to synthesize HPCMs is a
 865 rational choice. Pyrolysis of biomass or biomass waste into
 866 biochars has attracted increasing interest due to their
 867 availability and recyclable nature.^{128,129} Biomass in different
 868 forms, such as bean shells, pomelo peel, chicken feathers, waste
 869 coffee grounds, silk, amino acids, and willow catkins, has
 870 already been carbonized.^{128,130,131} The porosity and capaci-
 871 tance of the resulting carbons can be balanced by optimizing
 872 the carbonization conditions. The type and content of
 873 heteroatoms, morphology, and structure of carbons can be

874 tuned by the choice of biomass with or without chemical
 875 activation. For example, Qu et al. demonstrated green and
 876 scalable synthesis of N-doped porous carbon spheres by using
 877 fermented rice as the starting material, leading to a high S_{BET}
 878 value of $2105.9 \text{ m}^2 \text{ g}^{-1}$ and a high porosity of $1.14 \text{ cm}^3 \text{ g}^{-1}$.¹³²
 879 When used as an active electrode in supercapacitors, the
 880 carbon spheres presented a capacitance as large as $219 \text{ F} \cdot \text{g}^{-1}$ at
 881 a high discharge current density of $15 \text{ A} \cdot \text{g}^{-1}$ and a good cycling
 882 ability of over 4400 cycles at $1 \text{ A} \cdot \text{g}^{-1}$ in a three-electrode
 883 system, using 6 M KOH as the electrolyte. More recently,
 884 Wang et al. successfully fabricated macroscopic heteroatom-
 885 doped graphitic hollow carbon fibers at scale by vacuum
 886 carbonization of “human hair” (Figure 11a–m).¹³³ These
 887 fibers are highly flexible and display a remarkable conductivity
 888 of 257 S cm^{-1} , suggesting great promise for a large variety of
 889 applications from wearable to electrochemical devices. Jin et al.
 890 fabricated microporous carbon nanoplates with a high surface
 891 area and numerous heteroatoms (HCMNs) by using
 892 regenerated silk fibroin as a precursor, followed by KOH
 893 activation (Figure 11n).¹³⁴ The carbon nanoplates could form
 894 lamellar-like layers in water by self-assembly (Figure 11o)
 895 due to their uniform 2D structure. The obtained HCMNs showed
 896 potential applications in supercapacitors with high energy and
 897 power density. It should be mentioned that a low
 898 concentration of metal species, e.g., Fe and Cu, originally
 899 exists in the enzymes or cofactors of biomass, which can be
 900 unaffectedly incorporated into carbons. Although these metal
 901 species are typically at the ppm level in the biomass, their
 902 potential catalytic effect in the carbon product should not be
 903 overlooked.

2.2.2. Carbonization of Heteroatom-Free Polymers
 904 **with Heteroatom-Rich Coreactants.** Although the direct
 905 carbonization of heteroatom-containing polymers is more
 906

907 straightforward for producing HPCMs due to its simple
908 operation, the types and contents of heteroatom elements
909 within porous carbons rely largely, if not exclusively, on the
910 polymers. By contrast, mixing heteroatom-containing com-
911 pounds with heteroatom-free polymers provides more
912 flexibility in manipulating the type and content of heteroatoms.
913 In this regard, the raw material can be carbonized either by
914 mixing heteroatom-free polymers with heteroatom-rich small
915 organic precursors, such as N-containing arginine, dicyandia-
916 mide, melamine, adenine and urea,⁸⁵ P-containing phosphoric
917 acid and phytic acid,¹³⁵ B-containing boric acid and boron
918 trioxide, and S-containing thiophene and ammonium persul-
919 fate, or by carbonization in an active gas such as NH₃ and
920 H₂S.⁸⁴ The former is usually done in a “one-pot” approach. For
921 example, Hao et al. fabricated N-containing carbon monoliths
922 through direct pyrolysis of a mixture of resorcinol, form-
923 aldehyde, and lysine.¹³⁶ These carbon products possess a
924 higher nitrogen content in the bulk than on the surface. The
925 authors found that the carbon monolith obtained at 500 °C
926 exhibited a CO₂ adsorption capacity of 3.13 mmol g⁻¹ at room
927 temperature by balancing the N content and porosity *via*
928 optimization of the carbonization conditions. In another
929 example, Guo et al. prepared a N, B-codoped hierarchical
930 carbon monolith using poly(benzoxazine-*co*-resol) and ionic
931 liquid [C₆mim][BF₄] assemblies, in which [C₆mim][BF₄]
932 acted as a structure-directing agent and a heteroatom source of
933 N and B.¹³⁷ The obtained porous carbon monolith had a high
934 skeleton density and fully interconnected macro/meso/micro-
935 pores that facilitated the diffusion of electrolyte ions by
936 minimizing the diffusion resistance. The nanostructure of the
937 N, B-codoped carbon (CNB) contained a random combina-
938 tion of graphitic and turbostratic stacking with a short-range
939 order and displayed a graphite-like microstructure with good
940 electrical conductivity due to the multilength-connected
941 carbon framework, showing promise as an electrode material
942 for supercapacitors with a high gravimetric capacitance of 247
943 F g⁻¹.

944 Apart from direct “one-pot” synthesis by mixing heteroatom-
945 rich precursors with heteroatom-free polymers, post-treatment
946 methods, such as thermal annealing in active gas, i.e., NH₃, are
947 powerful approaches for introducing heteroatoms. Most
948 commonly, N doping is conducted in a NH₃ atmosphere.¹ It
949 has been demonstrated that the N content and N doping
950 environments could be controlled by changing the temperature
951 or flow rate of NH₃.¹³⁸ Note that post-treatment methods
952 generally lead to surface doping rather than full interior (bulk)
953 doping. In addition, NH₃ thermal treatment results in relatively
954 low doping levels, i.e., below 3 wt % for annealing between 800
955 and 900 °C. To increase the doping level, researchers often
956 employed N precursors such as melamine for direct doping in
957 combination with a postcarbonization NH₃ thermal treatment.

3. HETEROATOM DOPING EFFECT ON POROUS CARBONS

959 Chemical doping is one of the most popular strategies to
960 modulate carbon materials (Figure 12).^{151,152} The integration
961 of heteroatoms into the carbon matrix inevitably causes
962 structural distortions and changes the electronic band
963 structure, which alters physicochemical characteristics, such
964 as the thermal stability, electronic and optical properties,
965 surface chemistry, and magnetic properties. This endows
966 carbon materials with adjustable functions for catalysis,
967 environmental, and energy technologies.^{153–155} In this section,

doping by heteroatoms to tailor the function of porous carbons 968
will be extensively discussed from the perspectives of synthesis, 969
theoretical simulation, and applications, providing a solid 970
understanding of how to dope carbon materials for target 971
functions. The doping effects discussed here will exclude those 972
of metal atoms, although they are important for applications in 973
the energy and catalysis fields. Oxygen doping is also excluded, 974
as many porous carbon materials when produced already 975
contain oxygen due to oxidation of carbons to a certain extent by 976
air at high temperatures. 977

3.1. Characterization of Heteroatom-Doped Porous Carbons

To discuss the specific doping effects for various heteroatom- 979
doped carbons and the related applications, it is important to 980
begin with the characterization techniques that have been 981
utilized for determining the dopant type, content, state, 982
location, distribution, and atomic configurations in the carbon 983
framework. It is meaningless to claim that the higher the 984
dopant content, the better the material performance. Even at 985
the same dopant content, the binding state and locations of the 986
dopant elements can be drastically different. Beneath, several 987
key instrumental methods currently employed to characterize 988
heteroatom-doped carbons are discussed. 989

Elemental analysis (EA) is one of the most basic techniques 990
to determine the dopant type and content in carbon materials. 991
The advantage of EA characterization is that this method is 992
widely available in many chemical laboratories because it serves 993
multiple subfields of chemistry. Combustion EA is among the 994
most popular methods. By careful combustion of carbon 995
materials under designed conditions, organic elements, such as 996
C, N, hydrogen (H), and S, that can be converted into 997
oxidized volatiles, such as CO₂, H₂O, NO₂, and SO₂, can be 998
detected, whereby the heteroatom concentrations in the 999
carbon materials can be readily acquired based on the 1000
corresponding volatiles. For elements such as B, P, selenium 1001
(Se), or other elements, their corresponding oxidized species 1002
are not volatile, and other procedures are required to quantify 1003
their presence with EA. 1004

Scanning electron microscopy (SEM) and transmission 1005
electron microscopy (TEM) equipped with energy-dispersive 1006
X-ray spectroscopy (EDX) are frequently employed to describe 1007
the elemental compositions as well as their distributions in 1008
carbons.¹⁵⁶ When bombarding a heteroatom-doped carbon 1009
sample with high-energy X-rays or γ -rays, the electrons in the 1010
inner shell of every atom will be “kicked out”, thus producing 1011
vacancies, and then, electrons from a higher energy level fill the 1012
empty lower energy levels. This process emits characteristic X- 1013
rays that can be detected by the EDX system. Different 1014
elements display different characteristic X-ray signals. In this 1015
way, the types, quantities, and distributions of the as-expected 1016
elements in the sample can be monitored by collecting the 1017
emitted X-ray signals. Moreover, the emitted characteristic X- 1018
rays of heavy atoms are simpler to detect than those of light 1019
atoms, and EDX is hence a very effective tool for determining 1020
the contents and distributions of heavy dopants, such as Se, Sb, 1021
and Te, in carbons. In comparison to combustion EA, EDX 1022
analysis works at the local nm or μ m scale. The electrons in 1023
SEM typically enter the sample to depths of tens of nm; thus, 1024
the technique is surface-sensitive. In this context, samples with 1025
a homogeneous distribution of heteroatoms will provide close 1026
results when comparing EA and EDX data. Care should be 1027
taken for samples with nonhomogeneous or site-specific 1028

1029 distributions of heteroatoms, as the EDX analysis results can
1030 then be significantly different from the combustion EA method
1031 results.

1032 Beyond the elemental composition and spatial distribution
1033 in the carbon scaffolds, the chemical nature and the binding
1034 environment of the heteroatoms are also relevant. Generally,
1035 nuclear magnetic resonance (NMR) spectroscopy is widely
1036 employed to probe the local chemical structure of dissolved
1037 molecules. Similarly, solid-state NMR (SSNMR) could provide
1038 us with useful structural information of carbons. It is indeed
1039 one of the most powerful techniques, but with condensed
1040 carbon samples, some typical mistakes arise that often are not
1041 considered by the layman. First, one has to be sure that the
1042 sample is neither metallic nor contains unpaired electrons,
1043 which would greatly distort the signals, in the worst case
1044 causing loss of the entire or parts of the spectrum. Second,
1045 solid-state ^{13}C NMR is mostly performed with cross-polar-
1046 ization; that is, the carbon atom to be detected should be
1047 bound to a hydrogen atom, which in fact is often not the case
1048 in carbonaceous materials. The aromaticity is thereby
1049 massively underrepresented, as are carboxylate groups. This
1050 NMR problem in quantifying solid-state spectra of highly
1051 condensed organic materials can be resolved by using direct
1052 ^{13}C NMR and/or special pulse sequences. For more
1053 information on this topic, we point to the inspiring work of
1054 Schmidt-Rohr and co-workers.¹⁵⁷

1055 As a practical example, by utilizing ^{13}C cross-polarization
1056 magic-angle-spinning SSNMR (^{13}C CPMAS SSNMR), Mao
1057 and co-workers differentiated various C species in carbonized
1058 polymers (Figure 13).¹⁵⁸ The carbon resonance at 37.4 ppm is

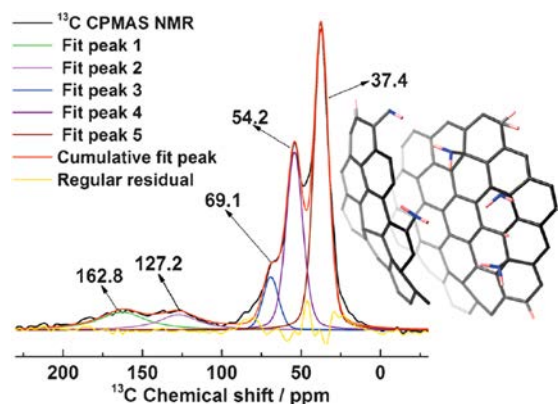


Figure 13. ^{13}C CPMAS SSNMR of a graphitic polymer condensate. Note that such SSNMR spectra are not quantitative, as they rely on cross-polarization. Reproduced with permission from ref 158. Copyright 2016 Wiley-VCH.

1059 attributed to aliphatic carbons, i.e., methylene or methine
1060 carbons. The signals at 54.2 and 69.1 ppm can be attributed to
1061 heteroatom-bound aliphatic carbons, such as the alpha-
1062 position of aliphatic amines or alcohols. The chemical shifts
1063 at 127.2 and 162.8 ppm correspond to benzene-like aromatic
1064 carbons and electron-poor aromatic carbons, respectively. It
1065 can be nicely seen here that, in these cross-polarization
1066 SSNMR spectra, the carbons not directly connected to
1067 hydrogen atoms are massively underrepresented. Notably,
1068 SSNMR spectroscopy can also be used to probe other NMR-
1069 active heteronuclei, such as ^{31}P , ^{11}B , ^{15}N , ^{19}F , ^{27}Al , and ^{77}Se .
1070 Undoubtedly, X-ray photoelectron spectroscopy (XPS) is
1071 the benchmark and most popular spectroscopic tool for

1072 qualitatively and quantitatively investigating the chemical
1073 compositions, chemical states, and electronic binding states
1074 of elements on carbon surfaces. XPS spectra are obtained by
1075 irradiating a sample with a beam of X-rays while simulta-
1076 neously recording the kinetic energy (KE) and number of
1077 electrons that escape from the top surface, i.e., from
1078 approximately 1 to 10 nm depths of the sample.¹⁵⁹ A typical
1079 XPS spectrum is a plot of the number of electrons vs the
1080 binding energy of the electrons detected. Each element
1081 produces a characteristic set of XPS peaks at specific binding
1082 energies that directly identify each element on the surface.
1083 These characteristic peaks correspond to the electron orbitals
1084 of the electrons within the atoms, i.e., 1s, 2s, 2p, 3s, etc. The
1085 number of detected electrons in each of the characteristic
1086 peaks is directly related to the amount of elements within the
1087 irradiated area, which corresponds to the atomic percentage
1088 values. For example, Joo et al. investigated the function of the
1089 N contents in carbons vs the carbonization temperature by
1090 XPS.¹⁶⁰ As illustrated in Figure 14a, the N 1s spectra clearly
1091 showed four fittable peaks at 398.0, 399.3, 400.7, and 402.1 eV,
1092 which were assigned to pyridinic N (N1), pyrrolic N (N2),
1093 graphitic N (N3), and oxidized N (N4), respectively. With
1094 increasing pyrolysis temperature, the peak area of N3
1095 increased, while the peak area of N1 decreased, which
1096 indicates that graphitic N is more stable than pyridinic N at
1097 high temperature. The relative ratios of the deconvoluted peak
1098 areas of the N 1s spectra were further analyzed to quantify the
1099 atomic percentage ratio for each N configuration, in which the
1100 percentage of N3 increased from 41.3 to 58% and that of N1
1101 decreased from 41.7 to 20.3% with increasing pyrolysis
1102 temperature from 800 to 1000 °C (Figure 14b). Care should
1103 be taken that the amount of quaternary N in the aromatic
1104 systems is approximately constant; i.e., aromatic carbons can
1105 take only a limited amount of N atoms within the planes
1106 without destroying or significantly weakening their aromaticity.
1107 Despite this fact, in many literature figures, researchers prefer
1108 to draw carbon frameworks with a relatively high content of N
1109 atoms, which is merely for educational purposes and does not
1110 represent the reality in carbon materials. Indeed, N is mostly
1111 an edge-termination element. In comparison with N atoms,
1112 other heteroatoms are even more edge-preferring in terms of
1113 their positions in the aromatic carbons.

1114 With the rapid development of advanced characterization
1115 techniques, the possibility of directly visualizing the atomic
1116 configuration in heteroatom-doped carbon has become reality.
1117 Atomic-resolution scanning transmission electron microscopy
1118 (STEM) uses a scanning beam mode that can be focused to a
1119 diameter as small as 0.1 nm by condenser lenses, which means
1120 that STEM can achieve the finest possible probe size of 0.5 Å
1121 with the maximum current available.¹⁶¹ This merit allows for
1122 atomic scale resolution in imaging and chemical analysis of
1123 heteroatom-doped carbons. The STEM images are formed by
1124 filtering the scattered electrons over a certain angular range of
1125 the diffracted beam, which usually allows differentiation
1126 between bright-field (BF) and dark-field (DF) imaging
1127 modes. If the analyzed region in the sample contains a higher
1128 atomic number element, then the STEM image will appear
1129 relatively dark in the low-angle annular BF (LAABF) or
1130 relatively bright in the high-angle annular DF (HAADF).

1131 For example, in a Se-doped carbon material, the heavy Se
1132 atoms have considerably higher Z than the light C atoms;
1133 therefore, in the HAADF images, these atomically dispersed Se
1134

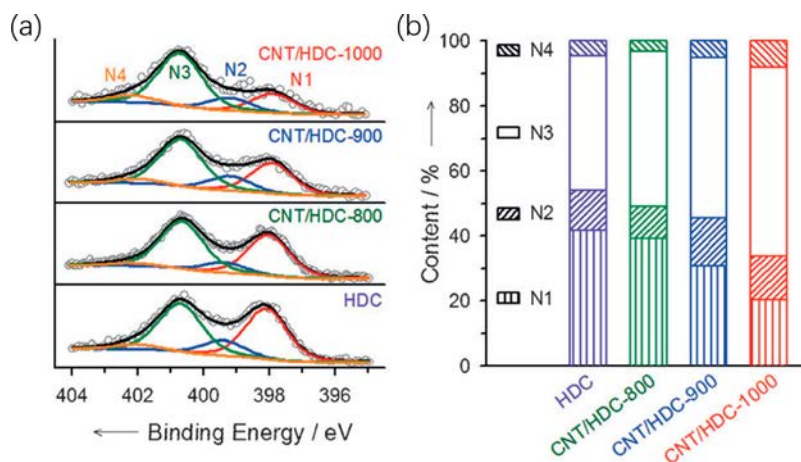


Figure 14. (a) High-resolution N 1s XPS spectra of heteroatom-doped carbon (CNT/HDC-*X*, where *X* represents the annealing temperature). (b) Relative ratios of the deconvoluted peak areas of the N 1s XPS spectra. Reproduced with permission from ref 160. Copyright 2014 Wiley-VCH.

atoms can be clearly visualized as individual bright dots (Figure 15a).¹⁶²

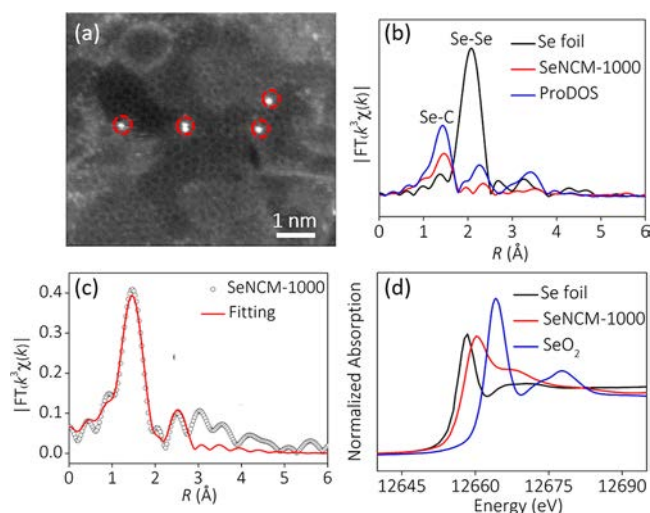


Figure 15. (a) Representative STEM-HAADF image of N, Se-codoped carbon. The Se atoms are highlighted by red circles. (b) Se K-edge Fourier transformed EXAFS spectra in the R space of the N, Se-codoped carbon compared with two other references. (c) Fourier transformed EXAFS spectrum of N, Se-codoped carbon and the corresponding simulation curve; the inset is a model structure of N, Se-codoped carbon. (d) Se K-edge XANES of the N, Se-codoped carbon as well as Se foil and SeO₂ as references. Reproduced with permission from ref 162. Copyright 2019 Wiley-VCH.

As a characterization technique complementary to STEM, X-ray absorption fine structure spectroscopy (XAFS) measurement could offer the coordination environment and chemical state of heteroatoms in carbons.¹⁵⁹ The fine structure is commonly divided into two regions: the near-edge region (XANES or NEXAFS, within ca. 50 eV) and extended fine structure (EXAFS), which may extend to more than 1000 eV above the edge. The XANES is very sensitive to the electronic binding structures, while the EXAFS region is focused on the distance and number of neighboring atoms. Taking Se-doped carbon as an example again, the EXAFS spectrum of Se-doped carbon membranes revealed that the Se atoms were indeed only bonded to C atoms, and no Se–Se bond was detected

(Figure 15b). Moreover, the atomic configuration of Se atoms was determined to be at the edge of graphitic planes (Figure 15c). The XANES also revealed the adsorption edge to be located between those of Se foil and SeO₂, indicating the positively charged character of the Se atoms (Figure 15d).

With the rapid development of various characterization methods, it is believed that the intrinsic relationship of the unique electronic structure of heteroatom-doped carbons with the material performance will be more clearly revealed and understood. This advance will help rationally design and prepare desirable functional heteroatom-doped carbons for specific applications.

3.2. Molecular Doping Effect of Heteroatoms on Porous Carbon

Heteroatom doping aims to tailor and adjust the bulk and/or surface properties of carbons to further optimize their performance toward a specific usage. In the case of molecular doping, the heteroatom is covalently and uniformly embedded in the carbon framework, which could readily disturb the sp² carbon network, inducing defects, bending individual graphitic planes, enlarging the interlayer spacing, and/or causing an uneven charge distribution in the carbon framework.¹⁶³ These structural parameters are usually considered to dictate active sites for various applications. In the following, the doping effects of N as the most widely used doping element in carbons and of non-N atoms, such as B, S, P, and Se, on tailoring the intrinsic structures/properties will be systematically discussed.

Charge redistribution induced by the electronegativity difference between a heteroatom and carbon is the most straightforward molecular doping effect.¹⁵¹ In a simplified model, a heteroatom with strong electronegativity, such as N, will drag electrons away from the adjacent carbons, making them partially positively charged. The density of the positive charge depends naturally on how strongly the heteroatom pulls the electron cloud away from the carbon atoms. This pulling effect is directly reflected in the classic characterization techniques, such as XPS, EELS, or SS NMR. For example, a difference of several eV is readily seen in the XPS spectrum. By contrast, a heteroatom of lower electronegativity, such as B, will endow adjacent carbons with electron density, resulting in partially negatively charged carbon.^{152,164} This uneven electron distribution creates active sites that are drastically different from the rest of the carbon framework, alters the collective

1191 electronic band structure, and subjects carbons to easier
1192 adsorption of or interaction with nucleophiles or electrophiles.
1193 The ORR of N- and B-doped carbon materials is a good
1194 illustrative example. Both theoretical calculations and exper-
1195 imental data have demonstrated that B- or N-doped carbons
1196 exhibit a higher oxygen (O_2) molecule adsorption energy,
1197 while a much lower adsorption energy is measured for pristine
1198 carbons.^{154,165} Density functional theory (DFT) calculations
1199 revealed that substitutional B in carbon nanotubes is present in
1200 a three-bonded form (BC_3), which exhibits sp^2 hybridization
1201 characteristics in the B–C bonds. The electronegativity
1202 difference between B and C induces a sufficient positive
1203 charge on B, which facilitates chemisorption of O_2 on B-doped
1204 carbon nanotubes.¹⁶⁶ For N-doped carbons, the larger
1205 electronegativity of N can induce a positive charge on the
1206 adjacent C atoms. These two different positively charged
1207 atoms in the different materials act as active sites to capture O_2
1208 molecules and play an important role in enhancing the ORR
1209 catalytic activity.¹⁵⁴ According to theoretical calculations,
1210 different heteroatoms (N, B, S, and P) in graphene display
1211 different binding energies for O_2 , in which B- and N-doped
1212 graphenes exhibit the lowest overall reaction free energy at U^0 ,
1213 suggesting a high ORR performance.¹⁶⁷ The exchange current
1214 density predicted for ideal heteroatom-doped graphene (α -
1215 graphene) is calculated to be 2.12×10^{-6} A/cm², which is 5
1216 times that of conventional Pt/C catalysts under the same test
1217 conditions, underlining the great potential of heteroatom-
1218 doped graphenes as metal-free electrocatalysts for the ORR.
1219 Unlike B and N, heteroatoms such as S and Se have a similar
1220 electronegativity as carbon, which means that the charge
1221 redistribution in carbon planes induced by these heteroatoms
1222 is negligible within this simplified local description. However,
1223 their considerably larger atomic size turns out to be the
1224 decisive factor in the doping effect. First, incorporating large-
1225 sized heteroatoms inevitably distorts the carbon framework
1226 and enlarges the graphitic spacing, which could create
1227 numerous defects and strain inside the carbon framework.
1228 These structural defects in carbon materials are responsible for
1229 breaking the symmetry of the charge density (or spin density)
1230 distribution, causing the electrons to be localized at specific
1231 locations and thus resulting in active sites. Meanwhile, the
1232 enlarged interlayer spacing can effectively enhance intercala-
1233 tion. These parameters are crucial for multiple application
1234 purposes.
1235 Apart from creating active sites and defects in the carbon
1236 matrix *via* heteroatoms, the introduction of strong coordina-
1237 tion heteroatoms, such as N and P, enables the anchoring of
1238 metal ions or nanoparticles (MNPs) as catalytic centers.¹⁶⁸
1239 These ligand-type interactions can maximize the dispersion of
1240 MNPs, avoid their agglomeration, and promote strong and
1241 direct carbon–metal interactions to establish an efficient
1242 metal–ligand electron transfer between MNPs and carbon.
1243 MNPs supported in heteroatom-doped carbons have a huge
1244 potential in electrocatalysis, organic transformation, photo-
1245 catalysis, etc. Though how the interaction of heteroatom-
1246 doped carbons and MNPs determines their performance in
1247 these applications is still under debate, the specific mechanism
1248 of a Mott–Schottky layer between MNPs and heteroatom-
1249 doped carbon appears to be the most widely accepted
1250 mechanism.¹⁶⁹

3.3. N-Doped Porous Carbons

3.3.1. Bulk Doping. To give a better view of the N doping
effect inside carbons, in this section, the concept of bulk and
surface doping will be discussed separately. Bulk doping mainly
focuses on the ability to modulate the electronic band structure
such as the Fermi level, bandgap, and charge distribution, while
surface doping modulates surface properties such as the
basicity, chelating power, and wettability of the carbon
materials. For heteroatom-doped graphene, bulk and surface
doping are identical, as the boundary between the bulk and
surface vanishes in 2D structures.

N, as one of the neighboring elements next to C in the
periodic table, can form stable covalent bonds with carbon. It
has been the most studied foreign element in carbon materials
over the past decade. The main reason is closely associated
with its abundance and the easy synthesis, unique properties,
and outstanding performance of N-doped carbons.¹⁷⁰

N has a similar atomic size to C, which makes the C–N
bond length (1.41 Å) very close to the actual C–C bond
length (1.42 Å). These similar atomic sizes between N and C
atoms can effectively minimize the structural distortion of the
carbon network and, thus, to a large extent, maintain the
geometry of the carbon network. As discussed above, N has a
much stronger electronegativity than carbon, in most scenarios
increasing the electron density around N. Depending on the
structural binding in the carbon framework, the configuration
of N can be divided into pyridinic, pyrrolic, and graphitic N.¹⁷¹
Other configurations, such as oxidized N, quaternary N, or N
atoms located near a vacancy, are also possible. In this section,
the specific effect of different N configurations inside the
carbon framework will be analyzed.

Pyridinic N is sp^2 hybridized and bonded to two C atoms at
the edge of the hexagonal carbon units; it contributes one p-
electron to the π system. Electronically, the lone electron pair
on pyridinic N is in an sp^2 orbital and is not a part of the
delocalized π system but creates an edge termination. Thus, it
is significantly basic and displays a strong electron donating
character. The pyridinic N configuration is on top negatively
polarized, while the surrounding C atoms are positively
charged. The valence band as such moves to more positive
values.¹⁷² N-Doped carbons tend to oxidize other compounds
instead of being oxidized and combusting.

As an illustrative example, Wang et al. recently demonstrated
the excellent high-temperature oxidative stability of a N-doped
porous carbon membrane. Its original state can be well
preserved even in a butane flame (~ 1300 °C) in air for at least
60 s (Figure 16).¹⁷³ In the recent review by Antonietti et al.,
the ability of N-doped carbons to protect against oxidation is
named “nobility”, and multiple doping effects are summar-
ized.¹⁷⁴

Similarly, quaternary N substitutes C atoms in hexagonal
rings and adopts an sp^2 hybridization bound to three carbon
neighbors. However, the electronic structure is completely
different compared to pyridinic N.¹⁷⁵ Experimentally, the
chemical shift of graphitic N is approximately 401.1 eV in
XPS.¹⁷⁶ This value is comparable to that of a pyridinium ion
 $C_5H_5NH^+$ (401.2 eV) and an ammonium ion NH_4^+ (401.5
eV), suggesting a positive charge character of such N. This can
be explained by the fact that the lone electron pair is now
contributing to the π system.¹⁷⁷ In addition, the positively
charged N atoms indicate that the surrounding C atoms should
be negatively polarized due to Coulomb screening. Then, the
energy levels of the carbon materials are shifted to more

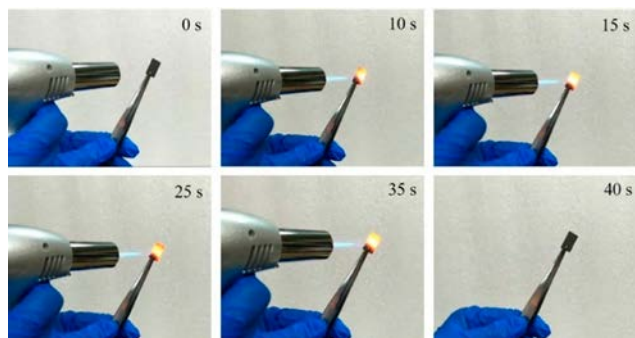


Figure 16. Fire retardancy of a N-doped porous carbon membrane. Reproduced with permission from ref 173. Copyright 2018 American Chemical Society.

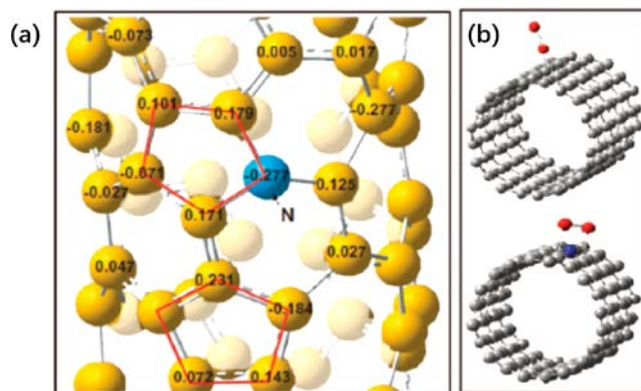


Figure 17. (a) Calculated charge density distribution of N-doped carbon nanotubes. (b) Schematic representations showing the O_2 adsorption mode change from end-on to side-on. Reprinted with permission from ref 185. Copyright 2009 AAAS.

negative values, which is consistent with the theoretical calculation.¹⁷⁸

The different N configurations are all possible and can be beneficial for different purposes. Therefore, selectively constructing carbons with solely one N configuration can be both interesting and important, as it will provide a solid understanding of the material performance attributed to N doping. As an example, Wang et al. constructed mesoporous carbons with exclusively the graphitic N configuration from chitin by utilizing TiO_2 as a catalyst.¹⁷⁹ At the same time, by changing the catalyst to $Fe(NO_3)_3$, carbons with solely pyridinic N were obtained. Lin et al. achieved pure pyridinic N doping by thermal CVD of hydrogen and ethylene on Cu foils in the presence of NH_3 .¹⁸⁰ Interestingly, by adjusting the flow rate of NH_3 , the atomic ratio of N and C could be rationally tailored. Other strategies, such as hydrofluoric acid etching^{181,182} and a solution-based method,¹⁸³ have also been reported to achieve pyridinic N-dominated carbons. For pyrrolic N-doped carbon, steam etching has shown some potential to increase the level of pyrrolic N content among all N species.¹⁸⁴ It is noted that, since N is mostly an edge-termination element, pyridinic N is usually more feasible than other configurations.

For the ORR, it is generally believed that positively polarized atoms facilitate the interaction with electron-rich reaction species and act as active centers in chemical reactions, e.g., in the electroreduction of O_2 , CO_2 , and N_2 . Theoretical studies suggest that the binding energy of O_2 is stronger in N-doped carbons due to the overall positive charge on carbon atoms adjacent to N, which changes the O_2 adsorption mode from end-on to side-on (Figure 17).¹⁸⁵ This is regarded as crucial to breaking the O–O bond to finally facilitate the ORR. However, the precise active site for the ORR in N-doped carbon materials is still under debate. Kang et al. suggested that charge back-donation from the electron-rich N atom to O_2 significantly increased the adsorption energy of O_2 on the pyridinic N-rich carbon surface in comparison to N-free pristine carbons.¹⁷⁵ The binding energy per O_2 is considerably larger for higher N content. In many of the studies, the specific active sites for the ORR were closely related to graphitic N. This may be a reasonable assumption because the lone pair of N in graphitic coordination is partly donated to the π^* antibonding orbitals of the carbon, making the nitrogen formally positive and the carbon negative. This provides efficient active sites for the ORR. Pyridinic N only has one electron for the p_z orbital and negligible occupation in the π^* antibonding orbitals.^{186,187} In a recent theoretical calculation

by Li et al., graphitic N induced n-type doping, while pyridinic N and pyrrolic N led to p-type doping in graphene nanosheets. The n-type doping favored the adsorption of O, and the p-type doping favored the adsorption of H.¹⁸⁸ Although the additional pyridinic N might not be the active sites for the ORR in this model, studies do suggest that the intrinsic locations of pyridinic sites nevertheless increase the kinetics of electrocatalytic reactions. Therefore, the widely accepted view is that graphitic N can improve the limiting current density, while pyridinic N can determine the onset potential for the ORR ($4e^-$ pathway). However, by precisely engineering the active sites of carbons, it is possible to selectively manipulate the ORR pathway. Recently, Harris et al. utilized the metal organic framework (MOF) amino-MIL-101(Al) as a carbonization precursor to construct N-doped carbons with a specific N configuration.¹⁹⁰ By changing the carbonization condition, carbons with and without quaternary N were obtained. According to their study, the presence of quaternary N sites can exclusively catalyze ORR *via* the $4e^-$ pathway, while pyridinic and pyrrolic N were ineffective. For the $2e^-$ pathway, Antonietti et al. obtained mesoporous N-doped carbons by direct carbonization of an ionic liquid.¹⁹¹ Interestingly, the obtained carbons displayed production of H_2O_2 with a remarkable faradaic efficiency of 65.15%. In this work, the production of H_2O_2 was attributed to the high level of pyrrolic N and the “radical” character induced by the low degree of delocalization. Fornasiero et al. developed N-doped graphitized carbon nanohorns for H_2O_2 production with a faradaic efficiency as high as 98%.¹⁹² In their study, the presence of microporosity was believed to favor the $2e^-$ pathway, as the residence time of H_2O_2 was short, preventing further reduction to water. At the same time, the ratio of pyridinic N and pyrrolic N also played a significant role in achieving high productivity of H_2O_2 .

Recently, N-doped carbons as metal-free, low-cost electrocatalysts for the CO_2 RR have received increasing attention in both academic and industrial fields. Harada et al. demonstrated that the localized electronic state of carbon materials induced by N atoms played a crucial role in achieving high CO_2 adsorption and facilitating the subsequent reduction reaction.¹⁹³ Particularly, the authors suggested that the edge pyridinic N and plane-located graphitic N sites could effectively stabilize the adsorbed CO_2 through an efficient charge transfer between N sites and CO_2 . This point was

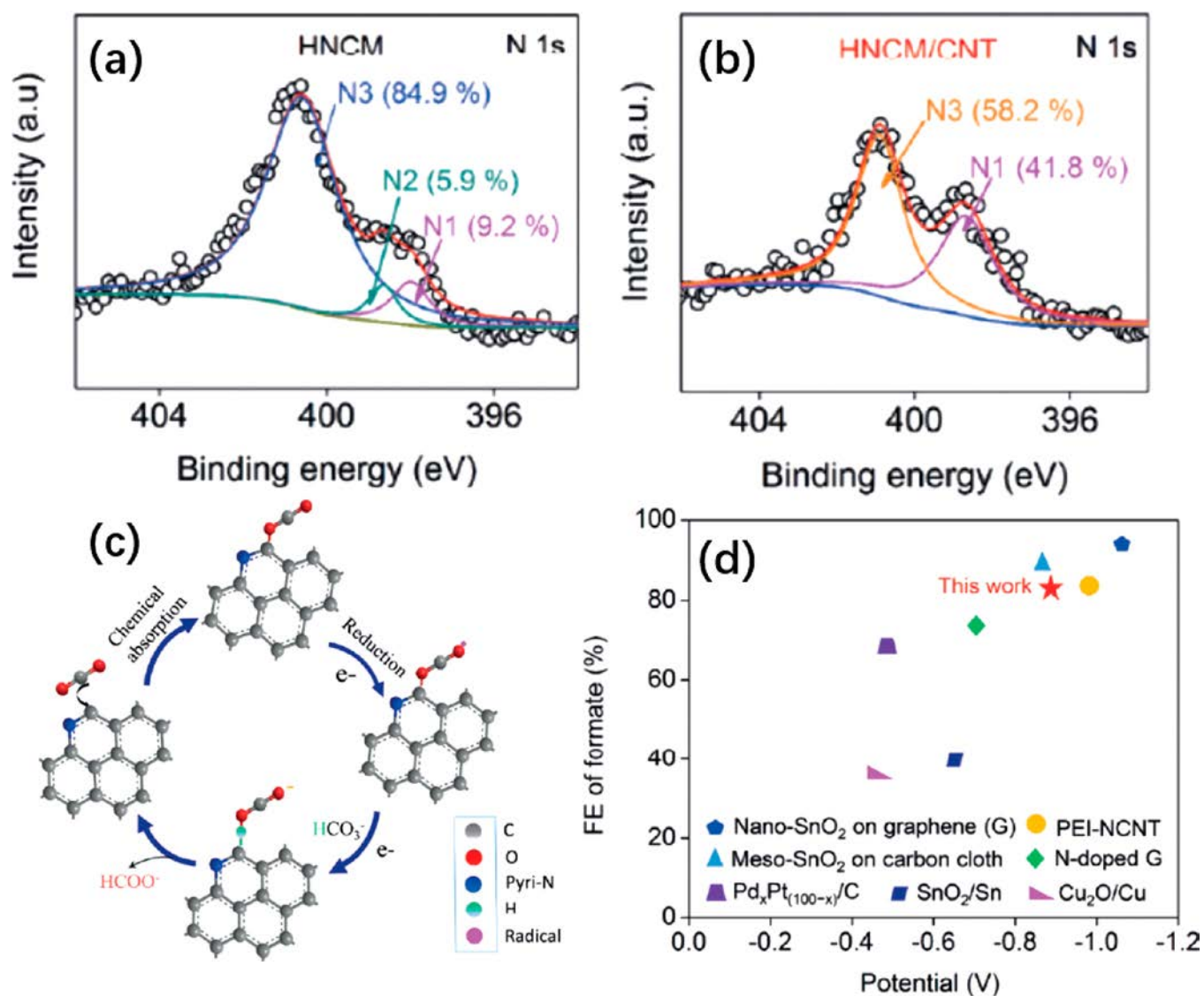


Figure 18. (a, b) High-resolution N1 XPS spectra of HNCMs and CNT-doped HNCMs/CNTs. (c) Proposed mechanism of the CO₂ RR. (d) Comparison of the potentials and faradaic efficiencies for the formation of formate on HNCMs/CNTs with those on other electrocatalysts. Reproduced with permission from ref 197. Copyright 2017 Wiley-VCH.

1404 further confirmed by Yuan and coauthors. They constructed
 1405 biphasic N-doped porous carbons by direct carbonization of
 1406 PIL-coated porous carbon fibers.¹⁹⁴ The unique biphasic
 1407 structure NPCFs could serve as a high-performance CO₂
 1408 adsorption material. The main reason why the NPCFs
 1409 exhibited a miraculously high CO₂ uptake value was mainly
 1410 attributed to the biphasic heterojunction that amplifies the
 1411 interaction between the carbon material and CO₂. Such a
 1412 heterojunction structure is similar to previously reported
 1413 heterojunction systems and may be beneficial for other
 1414 applications.^{195,196}

1415 In 2017, Wang et al. reported efficient electrocatalytic
 1416 reduction of CO₂ to formate in 0.1 M KHCO₃ by
 1417 hierarchically structured N-doped nanoporous carbon/CNT
 1418 hybrid membranes.¹⁹⁷ The formed carbon on the surface of
 1419 CNTs is rich in defects and short-range ordered micropores.
 1420 The introduction of CNTs into the N-doped carbon
 1421 membranes (HNCMs) could substantially increase the relative
 1422 content of pyridinic N from 9.2 to 41.9%, as shown in the XPS
 1423 spectrum analysis (Figure 18a,b); that is, the presence of

nanotubes promotes the formation of edge termination. It is
 1424 noteworthy that the reported selectivity and catalytic efficiency
 1425 are some of the highest for the metal-free CO₂RR and even
 1426 comparable to those of the state-of-the-art tin oxide nano-
 1427 crystals (Figure 18c,d). In another example, Zheng et al.
 1428 specifically constructed N-doped carbons with pyrrolic N as
 1429 the dominant N configuration by water steam treatment of N-
 1430 doped carbon nanotubes (NCNs). The authors found that
 1431 NCNs with a pyrrolic N domain show excellent electrocatalytic
 1432 CO₂ reduction performance but very low hydrogen evolution
 1433 reaction activity.¹⁹⁸

1435 The exact electronic effect of different N configurations in
 1436 the carbon matrix for the CO₂RR is still controversial. For
 1437 example, Ajayan et al. analyzed the Gibbs free energy for each
 1438 configuration of N in CNTs for the CO₂RR by employing
 1439 DFT simulations.¹⁹⁹ The results showed that pyridinic N
 1440 exhibited the lowest adsorption barrier for the *COOH
 1441 intermediate during the CO₂RR. The conclusion from Guo
 1442 and colleagues was that the carbon atoms adjacent to the
 1443 graphitic N in graphene were the most active sites for CO₂

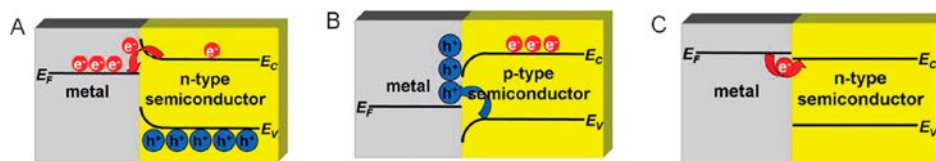


Figure 19. Schematic view of typical (a) rectifying metal–n-type semiconductor contact, (b) rectifying metal–p-type semiconductor contact, and (c) metal–semiconductor ohmic contact. Reproduced with permission from ref 169. Copyright 2013 Royal Society of Chemistry.

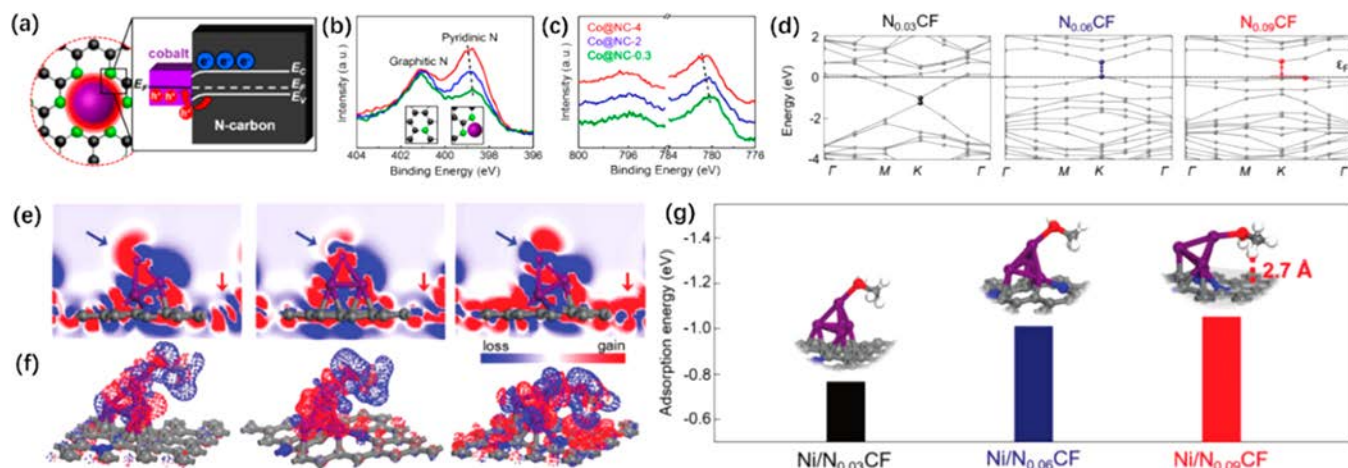


Figure 20. (a) Schematic illustration of the Mott–Schottky-type contact in a Co@NC-4 sample. (b) N 1s and (c) Co 2p XPS spectra of Co@NC-*x*. Reproduced with permission from ref 201. Copyright 2017 American Chemical Society. (d) DFT calculations of diverse N-doped carbons and opening of the bandgap. (e, f) Electron densities of an adsorbed model Ni₄ cluster and methanol adsorbed on the diode. (g) Methanol adsorption energies and molecular conformations of the bonding states with diverse N doping levels. Reproduced with permission from ref 202. Copyright 2018 Wiley-VCH.

1444 adsorption.²⁰⁰ In this regard, future works are required to
1445 alleviate the confusion and reveal the catalytic mechanism of
1446 different N configurations.

1447 Apart from utilization as metal-free electrocatalysts, N-doped
1448 porous carbons can act as catalyst supports. The incorporation
1449 of N can cause the work function of electrons to be more
1450 positive than those in undoped carbons. The positive work
1451 function implies that these then “noble” carbons are more
1452 likely to accept rather than donate electrons. Thus, when
1453 MNPs are loaded onto the N-doped carbon supports, the
1454 electron density inevitably moves from the electron-rich MNPs
1455 toward the N-doped carbons, making the MNPs more positive
1456 (or reactive). In solid-state physics, such electronic interaction
1457 between a metal and a semiconductor is described as the
1458 Mott–Schottky effect, and electrons in the system will flow
1459 until the Fermi levels on both sides of the interfaces are equal
1460 (Figure 19).¹⁶⁹

1461 The Mott–Schottky effect between MNPs and N-doped
1462 carbon supports is somehow analogous to the function of a
1463 ligand in homogeneous catalysts, and the electron density on
1464 the MNPs can be rationally tailored by using different carbon
1465 supports. For example, Chen et al. constructed a Mott–
1466 Schottky type of heterogeneous catalyst for oxidation of
1467 alcohols by covering cobalt nanoparticles with N-doped carbon
1468 shells.²⁰¹ It is important to note that incorporation of N atoms
1469 into the carbon matrix can effectively lower the valence band
1470 (p-type) and elevate the conduction band (n-type), enlarging
1471 the bandgap (work function) of the carbon materials.
1472 Therefore, with a higher flat band potential than the metallic
1473 cobalt nanoparticles, the N-doped carbon shell can readily
1474 withdraw electrons from the cobalt nanoparticles to balance
1475 the Fermi levels (Figure 20a). Such Mott–Schottky electron

1476 flow across metal–carbon interfaces can obviously redistribute
1477 the electron density at the interface between cobalt and N-
1478 doped carbon, causing the metallic cobalt to be more positively
1479 charged to attract and activate O₂. Such electron redistribution
1480 is supported by the XPS analysis, as the binding energies of N
1481 and Co increase gradually (Figure 20b,c). In this regard, the N
1482 atoms on the carbon surface can behave as a base to constitute
1483 an overall mild and additive-free catalytic system. Later, in
1484 2018, the same group constructed N-doped carbon-supported
1485 Ni nanoparticles for highly efficient dehydrogenation of gas-
1486 phase methanol.²⁰² The observed enormous catalytic rate and
1487 long-term stability were attributed to the Mott–Schottky effect
1488 and Mott–Schottky barrier across the N-carbon interfaces. In
1489 addition, DFT calculations demonstrated that electrons
1490 transferred from the nickel nanoparticles to the N-doped
1491 carbon supports due to the enlarged bandgap of N-doped
1492 carbon induced by the N atoms (Figure 20d). Therefore, the
1493 enhanced electron deficiency of the Ni nanoparticles led to a
1494 much stronger interaction with the O–H bond in methanol,
1495 thereby promoting the dehydrogenation reaction (Figure
1496 20e,f). Furthermore, the relatively “electron-rich” carbons
1497 also showed unusual binding to the electron-deficient methyl
1498 group, enhancing the binding energy (Figure 20g).

1499 The introduction of coordinative heteroatoms, such as N, P,
1500 or S, into carbons can coordinate metal ions or MNPs to
1501 effectively prevent their agglomeration and coarsening. This
1502 feature is highly important in the controllable synthesis of
1503 specific morphology size and lattice. For example, Li et al.
1504 constructed single-atom Co–N₃ porous carbon spheres with
1505 nearly 100% selectivity for the CO₂RR by immobilization of
1506 cobalt phthalocyanine (CoPc) in N-doped porous carbon
1507 spheres.²⁰³ The N atoms in the carbon network provide CoPc

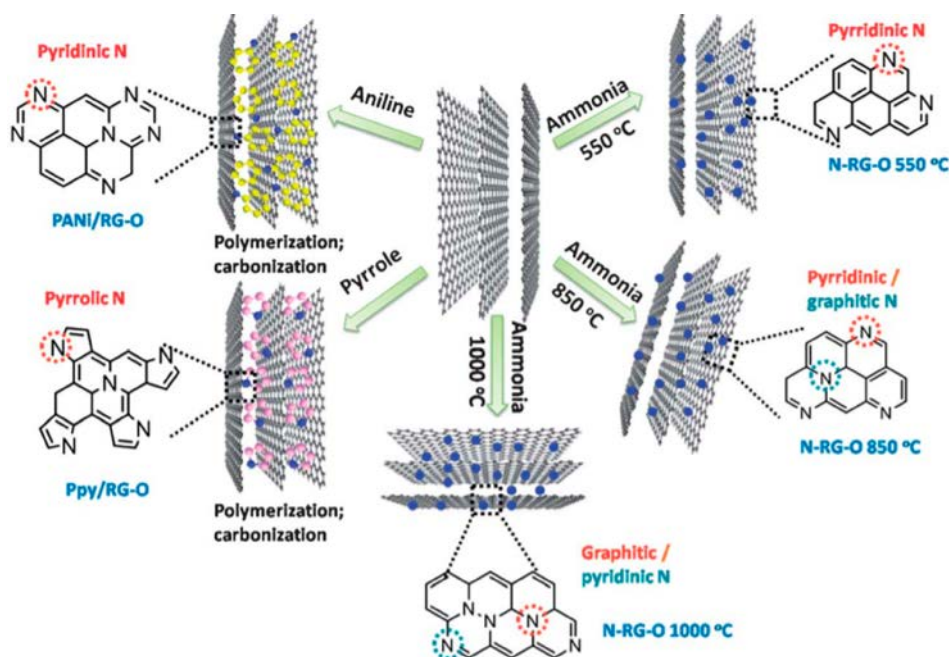


Figure 21. Surface doping of graphene using selective polymer precursors and temperatures. Reproduced with permission from ref 206. Copyright 2012 Royal Society of Chemistry.

chelating sites. It is noteworthy that utilizing N-doped carbon as a support for preparing single-atom catalysts is a simple yet versatile strategy, which is currently a topic under intensive research.

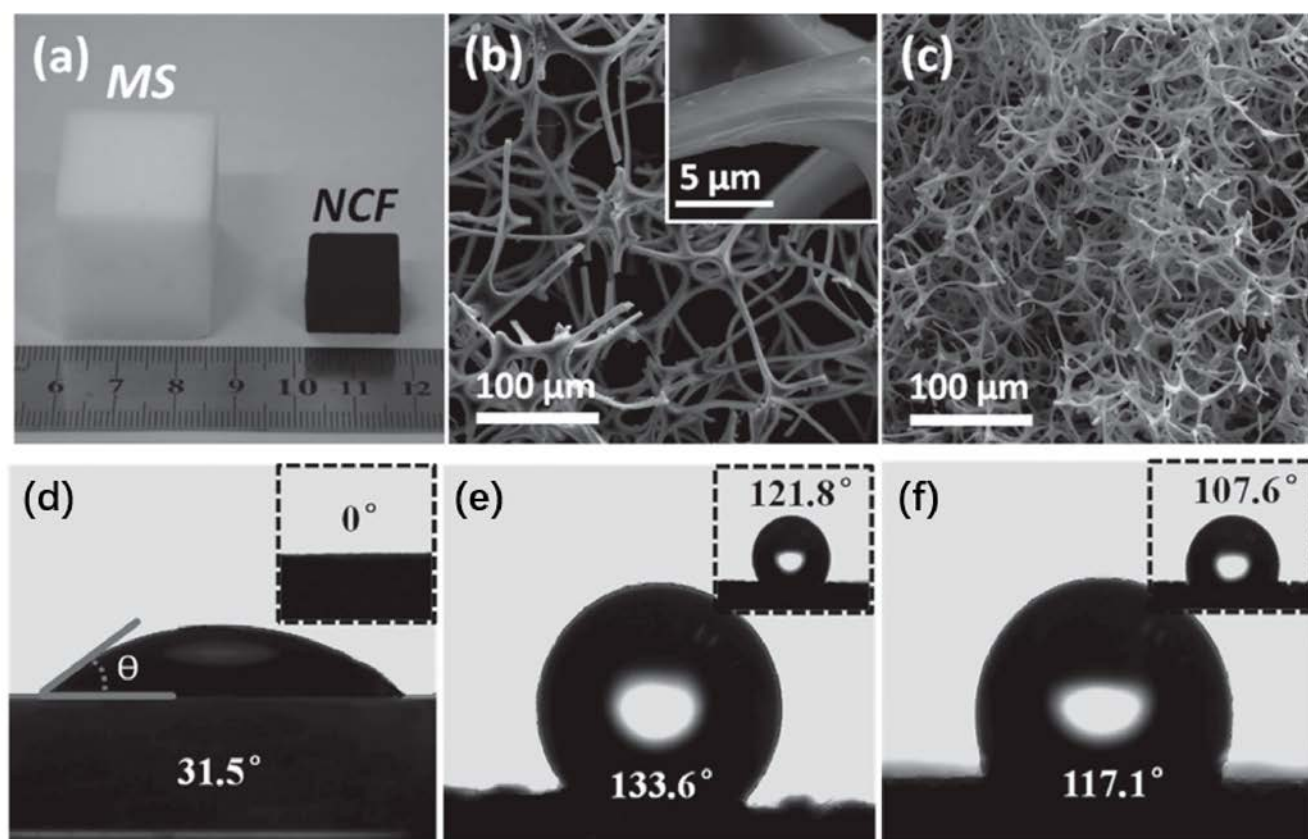
3.3.2. Surface Doping. Surface doping is the second heteroatom doping strategy to tailor the surface properties of carbon, i.e., the basicity, chelating capability, wettability, and roughness, as these properties are important for applications.^{6,204,205} For instance, in energy storage applications, N atoms on the carbon surface can considerably increase the surface hydrophilicity, which helps a polar electrolyte wet the electrode surface. In the adsorption and separation field, the strong basicity of surface N atoms could promote the adsorption efficiency for various acidic molecules.

Post-treatment of carbon materials in the presence of N-containing precursors is a simple yet effective route to engineer carbon surfaces with heteroatoms (Figure 21).²⁰⁶ As mentioned previously, NH₃ has been thus far the most popular source of N to dope carbons. At high temperature, NH₃ will decompose into reactive •NH₂ or •NH radicals to etch carbon fragments into a N-containing functional group such as –NH₂, –CN, or pyrrolic entities. This etching process could alter the surface properties, electronic structure, and porosity of the carbon materials.

Economy et al. found that NH₃-activated carbon fibers could act as efficient adsorbents of acidic gases, i.e., SO₂.²⁰⁷ The NH₃ treatment could not only basify the carbon surface but also substitute and remove oxygen-containing moieties. At elevated temperatures, the oxygen moieties on the carbon surface formed lactams, imides, and other active nitrogen groups, which improved the surface basicity of the carbon materials. This was shown to be favorable for the diffusion of a polar electrolyte into the carbon electrodes in supercapacitor devices.²⁰⁸ The quantum chemical calculation by Thrower et al. demonstrated that the introduction of pyrrolic N and –NH groups by ammoxidation also improved the charge mobility inside the carbon matrix by bringing electron-donor character-

istics to enhance the electron transfer behavior, thereby impacting the performance in energy devices.²⁰⁹ The N configurations in a carbon framework are a function of the post-treatment temperatures. Mangun et al. confirmed that NH₃ treatment below 600 °C generates amide, imide, imine, amine, and nitrile groups, while thermally stable aromatic rings, such as pyrrole and pyridinic N, form above 600 °C.²¹⁰ This is particularly important, since different N configurations play different roles for task-specific applications.

The surface wettability of carbons is an important factor that affects the performance of carbon materials in practical applications because it can effectively enhance the diffusion of electrolytes into carbon structures and promote ion transport. Previously, Yu et al. constructed N-doped carbon nanofibers by pyrolysis of polypyrrole-coated carbon nanofibers, in which the N content, surface area, surface wettability, and pore size could be well controlled by the pyrolysis temperature.²¹¹ They found that the performance of these N-doped carbon nanofibers in supercapacitor devices is closely dependent on their structural features because the surface wettability of these N-doped carbon nanofibers controls the ion transport. Wang and co-workers developed a type of freestanding and hydrophilic N-doped carbon foam by direct carbonization of melamine sponges (Figure 22a–c).²¹² The dynamic water contact angle measurements demonstrated a highly hydrophilic nature of the N-doped carbon foams with an initial contact angle of 31.5°, while a commercial carbon cloth was very hydrophobic with a higher water contact of 107.6° (Figure 22d–f). Similarly, Kaskel et al. constructed carbon materials with an amphiphilic surface as a supercapacitor electrode by post-treatment of carbon nanotubes and graphenes with bipyridine and boronate at elevated temperatures.²¹³ The synthesized carbons were composed of sp² carbon with a hydrophobic inner layer and a hydrophilic outer layer due to the N and B functionalities there. The unique bipolar surfaces and high heteroatom doping level rendered excellent wettability to promote the energy density



Nanocarbon Surface Engineering: From Monopolar to Bipolar Amphiphile

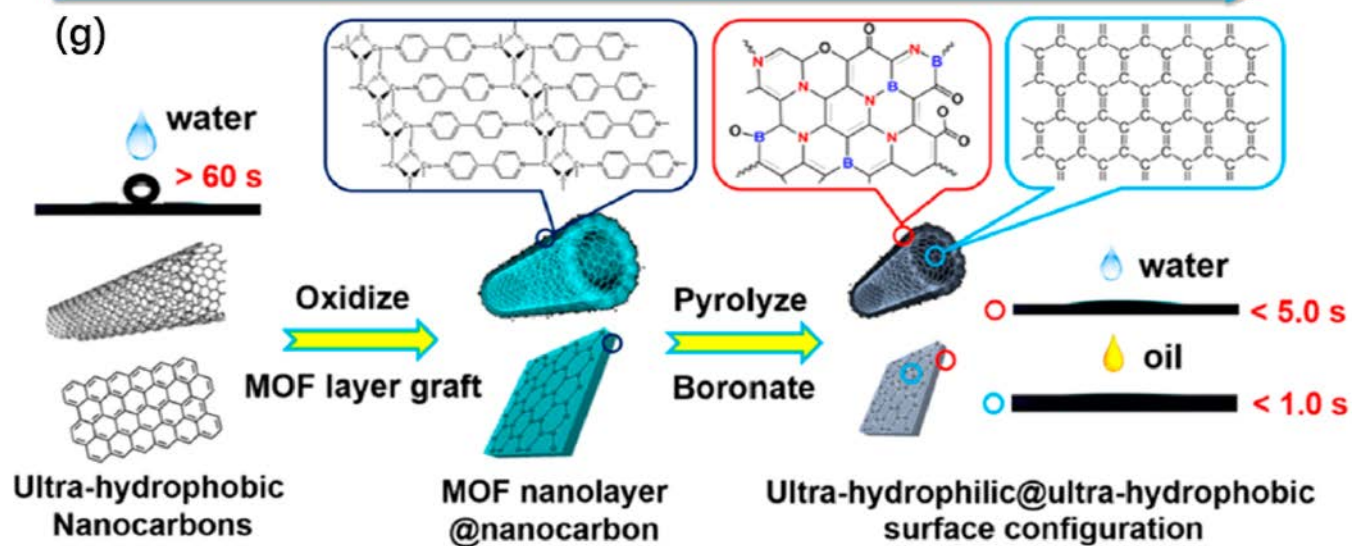


Figure 22. (a) Photographs of a melamine foam and a N-doped carbon foam. (b, c) SEM images of the melamine and carbon foams. Water contact angles of (d) N-doped carbon foam, (e) nickel foam, and (f) carbon cloth. Reproduced with permission from ref 212. Copyright 2016 Wiley-VCH. (g) Synthesis schematic of bipolar nanocarbon hybrids with a hydrophilic@hydrophobic surface configuration. Reproduced with permission from ref 213. Copyright 2016 American Chemical Society.

1582 by 2–3 times compared with typical benchmark materials
1583 (Figure 22g).

1584 We can state that N doping is clearly able to modulate the
1585 electronic structure, defects, and surface properties of carbon
1586 materials. N-Doped porous carbon materials as metal-free
1587 catalysts and electrodes are promising for modern energy
1588 conversion applications. Moreover, the unique electron

1589 donating nature of N could help anchor MNPs. This feature
1590 successfully widens N-doped porous carbon applications to
1591 catalyst supports and the construction of single-atom catalysts.

3.4. Non-Nitrogen-Atom (B, S, Se, and P)-Doped Porous Carbons

1592
1593 In addition to N, the introduction of other heteroatoms, such
1594 as B, S, Se, and P, into carbon materials has also been widely

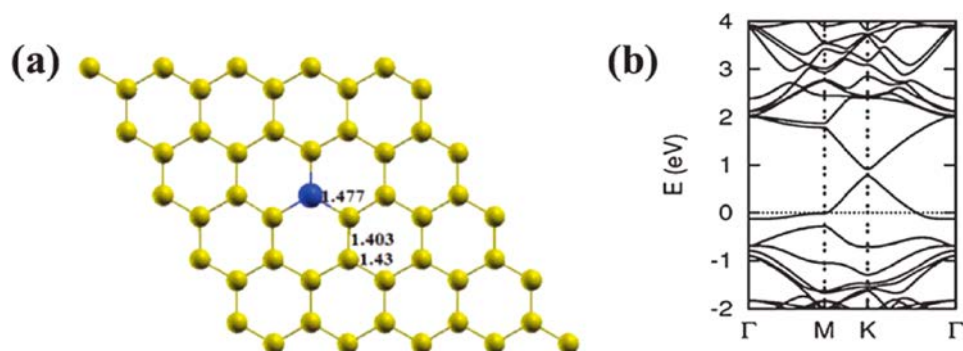


Figure 23. (a) Substitutional doping of B (blue ball). (b) Band structure of a single B-doped graphene sheet. Reproduced with permission from ref 214. Copyright 2013 Royal Society of Chemistry.

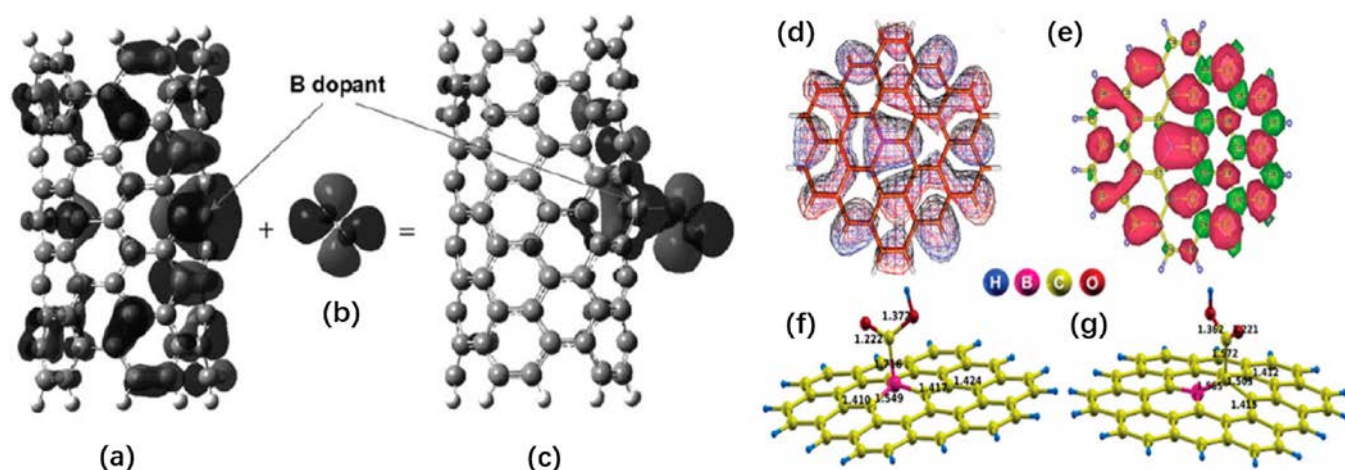


Figure 24. Molecular orbitals involved in O_2 adsorption on B-doped CNT (5,5). (a) Spin-down HOMO-1 of B-doped CNT (5,5). (b) LUMO of triplet O_2 . (c) Spin-down HOMO-2 of O_2 adsorbed on B-doped CNT (5,5). Reproduced with permission from ref 166. Copyright 2011 Wiley-VCH. (d) HOMO and (e) spin density mapping of constructed B-doped carbons. Chemisorption of $*COOH$ on B-doped carbons *via* B atoms (f) and C atoms (g). Reproduced with permission from ref 218. Copyright 2015 Royal Society of Chemistry.

1595 investigated. For example, B-doped carbons are particularly
1596 useful in heterogeneous organocatalysis due to their electron-
1597 deficient characteristic. S- and P-doped carbons can enlarge the
1598 graphitic spacing and are popular in battery and supercapacitor
1599 devices. Se, as one of the latest doping elements, has begun to
1600 stand out in carbon-based heterogeneous catalysis. In the
1601 following, the properties of these non-N element-doped porous
1602 carbons from polymers will be detailed.

1603 **3.4.1. B Doping.** The B atom with an outer electron shell
1604 of $2s^2 2p^1$ is, similar to nitrogen, a second row element in the
1605 periodic table. The electronic structure of B is opposite to that
1606 of N. B has only three valence electrons with three covalent
1607 bonds, which can only bring up to six electrons in total, being
1608 an electron-deficient element that always hungers for two more
1609 electrons to form a stable four-coordinate bond (or adduct), as
1610 occurs with most Lewis bases. When B is doped into carbons,
1611 the most stable form is planar, which is also referred to as in-
1612 plane doping. For the in-plane doping, B can maintain the sp^2
1613 hybridization of the carbon network in the form of BC_3 and
1614 join the π system (Figure 23a).²¹⁴ With stable substitution
1615 patterns, e.g., phenyl groups, it can also enter sp^3 hybridization,
1616 here negatively charged BC_4 . Note that BC_4 as an out-of-plane
1617 structure would eventually relax to the in-plane BC_3 structure
1618 due to thermally induced elimination.²¹⁵ Although the bond
1619 length of the C–B bond (~ 1.50 Å) is longer than that of an
1620 sp^2 C–C bond (1.42 Å), the strong polarization between

1621 neighboring C atoms and electron-deficient B can minimize
1622 the mechanical stress on the host carbon structure.²¹⁶ The
1623 empty orbital of B can readily withdraw electron density from
1624 the carbon network *via* pi-bonding, which inevitably increases
1625 the work function of the carbon materials to more negative
1626 values (Figure 23b).

1627 Previously, several groups found that moderate B doping
1628 could enhance the ORR performance.²¹⁷ The DFT calcu-
1629 lations by Hu et al. showed that the intrinsic electron-deficient
1630 nature of B can readily withdraw electrons from the pi-system
1631 and act as a bridge for a fast electron process toward O_2 in the
1632 ORR. Upon adsorption, the protruding lobe of the spin-down
1633 HOMO (highest occupied molecular orbital) of a B-doped
1634 CNT (BCNT(5,5)) maximized the overlap with the LUMO
1635 (lowest unoccupied molecular orbital) of triplet O_2 to create
1636 end-on adsorption, thereby facilitating the ORR process
1637 (Figure 24a–c).¹⁶⁶ Similarly, B-doped carbons also displayed
1638 exceptional catalytic performance for the CO_2RR . In the
1639 calculation from Phani's work, the electron delocalization
1640 symmetry is broken in B-doped carbons (Figure 24d,e).²¹⁸ The
1641 introduction of B also induces asymmetric charge and spin
1642 density distributions, making B-doped carbons function in the
1643 electrocatalytic CO_2RR (Figure 24f,g).

1644 In addition to catalysis, B-doped porous carbons have also
1645 been applied in energy storage systems. For instance, Zhang et
1646 al. prepared B-doped OMCs by direct carbonization of self-

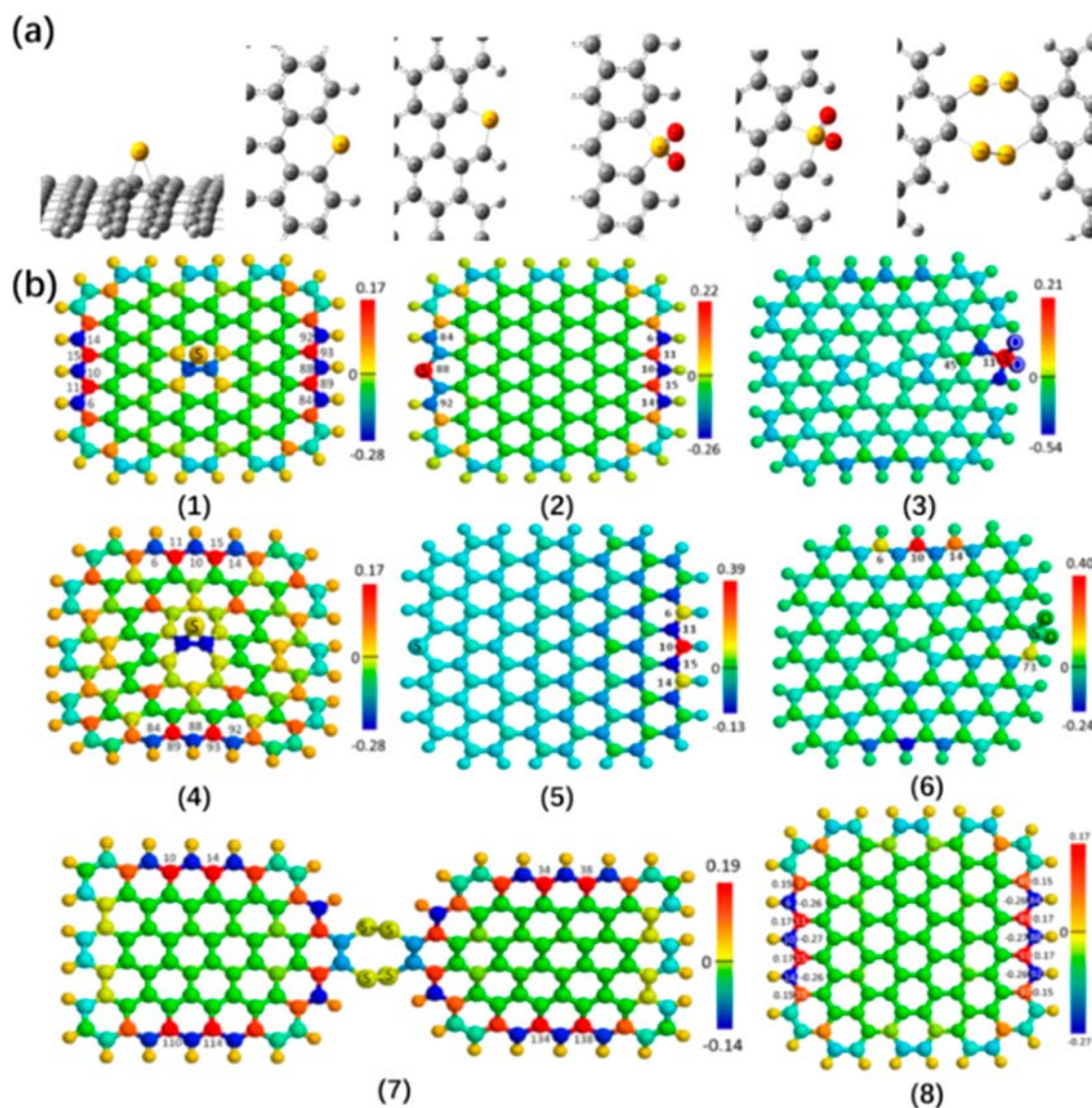


Figure 25. (a) Different mathematical models of S-doped graphene clusters. Small white, gray, yellow, and red spheres represent hydrogen, carbon, sulfur, and oxygen, respectively. (b) Atomic charge density distribution on S-adsorbed graphene clusters with (1) a perfect structure and (2) one Stone–Wales defect; (3) atomic charge density and (4) spin density distributions on a perfect graphene cluster with S substituting at the zigzag edge; (5) atomic charge density and (6) spin density on SO_2 -doped graphene with a Stone–Wales defect; atomic charge density on (7) a sulfur ring cluster connecting two pieces of graphene clusters and (8) a pure graphene cluster. The colors of the balls represent relative values of charge and spin density; the density decreases linearly from positive to negative values in the color order of red, orange, yellow, green, and blue. Sulfur and oxygen atoms are labeled with S and O, respectively. The unlabeled small and large balls represent H and C, respectively. Reproduced with permission from ref 225. Copyright 2014 American Chemical Society.

assembled resorcinol and formaldehyde (RF resin) with the triblock copolymer Pluronic F127 as a soft template in the presence of boric acid. The obtained carbon materials exhibited a moderate S_{BET} value of $700 \text{ m}^2 \text{ g}^{-1}$ with a uniform micropore size of 0.6 nm. The incorporation of B atoms into the carbon framework rendered a carbon surface with surface oxygen groups. These functional groups can conduct faradaic reactions with a wide range of onset potentials, thus enhancing the pseudocapacitance of supercapacitor devices.²¹⁹

Although B is one of the interesting doping elements in fundamental chemistry, effectively utilizing B in carbon materials is challenging, since it can be easily oxidized into boron oxide in air owing to its oxyphilic nature. Therefore, how to precisely synthesize B-doped carbon rather than oxidized B-doped carbon is being actively pursued.

3.4.2. S Doping. Unlike N and B, the S atom ($\chi = 2.58$) has a similar electronegativity to C ($\chi = 2.55$), which indicates that the covalent bond between S and C atoms is basically not polarized. However, the C–S bond length is 1.78 Å, which is approximately 25% longer than the C–C bond.²²⁰ This structural mismatch between S and C atoms makes five-ring species (i.e., thiophene and thiazole) the preferred species. In other cases, it can also bend the sp^2 flat configuration of graphenes and distort the aromatic system to a certain extent. In addition, carbons with higher S contents were found to become ribbon-like,²²¹ which means that sulfur preferentially contributes to extended edge termination. Such structural expansion and worsened packing are beneficial for mass transfer.¹⁵³ Theoretical calculations showed that introducing S atoms in a mathematical way into graphitic carbons opens a bandgap of the materials. S Doping (n-type dopant) could also

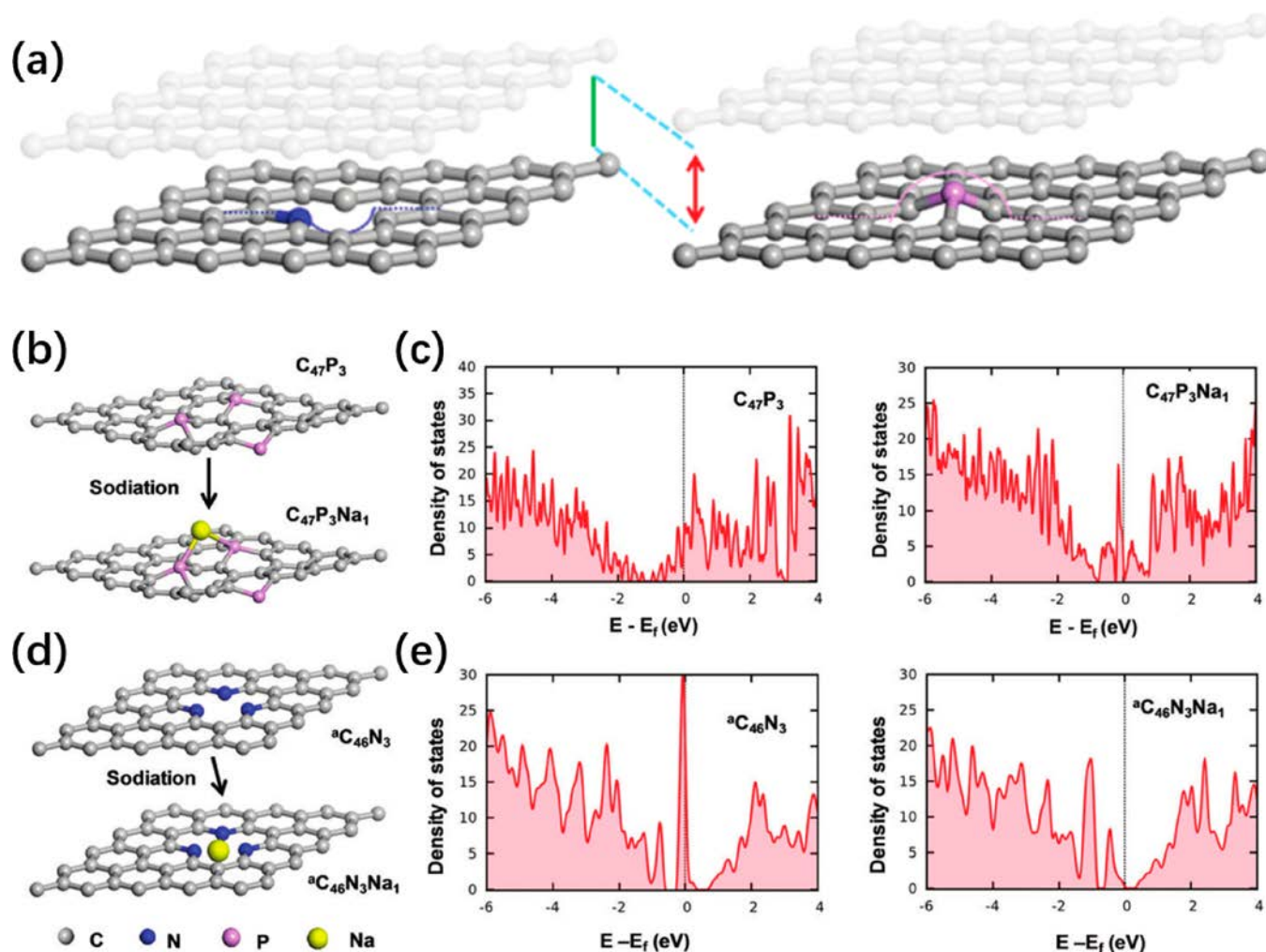


Figure 26. (a) A model in-plane “hole” defect induced by pyridinic N doping (blue) and an out-of-plane “protrusion” defect caused by P doping. (b) Schematic illustrations of P-doped states in graphene before and after sodiation. (c) Partial density of states (PDOS) of P-doped states in graphene before and after sodiation. (d) Schematic illustrations of N-doped states in graphene before and after sodiation. (e) PDOS diagrams of N-doped states in graphene before and after sodiation. Reproduced with permission from ref 229. Copyright 2017 Royal Society of Chemistry.

1678 increase the polarization and, when charged, enhance the
1679 electronic conductivity of carbons, making S-doped carbons
1680 suitable as anodes in batteries.²²² For example, Huang et al.
1681 demonstrated that S-doped carbons performed better than
1682 their N-doped counterparts in Na-ion batteries, which mainly
1683 stems from the large interlayer distance of S-doped carbon
1684 (0.39 nm) compared to the value of 0.36 nm in N-doped
1685 carbon, thereby facilitating the insertion and extraction of
1686 Na.²²³

1687 S-Doped carbon materials were also capable of promoting
1688 the ORR. In 2012, Huang et al. prepared S-doped carbons by
1689 thermal annealing of graphene oxide and benzyl disulfide in an
1690 argon atmosphere.²²⁴ They found that S-doped carbons are
1691 better catalysts in the ORR than commercial Pt/C in alkaline
1692 media. This finding was particularly interesting, as S has a
1693 similar electronegativity to C, which excludes the traditional
1694 explanation of a charge redistribution effect induced by the
1695 electronegativity difference causing an improved ORR. In light
1696 of DFT calculations from Xia and co-workers, S could
1697 substitute C atoms at the graphene edges in the form of
1698 sulfur, sulfur oxide, or sulfur cluster rings (Figure 25a).²²⁵
1699 Mathematical replacement of C by S atoms at the edges of
1700 graphitic layers enhanced the charge and spin density. The

most effective catalytic active sites were identified to be located
at the zigzag edge or the neighboring carbon atoms of the
doped sulfur oxide, which also possessed a large spin or charge
density (Figure 25b). Thus, the larger atomic radius of S atoms
was believed to result in a mismatch of the outermost orbitals
between S and C, leading to a nonuniform spin density
distribution and an increase in the catalytic activity. In
addition, the polarized environment of the S–C bonding will
improve the interaction with O₂, and the greater strain on the
polarized O₂ will promote the ORR.²²⁶

3.4.3. P Doping. P as a group V element has a similar
binding shell electron configuration as N. However, the
significantly larger atomic size of P and vacant 3d orbitals
endow P-doped carbons with different features. For example,
the P–C bond length is ~24% longer than the C–C bond
length, again resulting in a serious structural distortion of the
carbon frameworks.²²⁷ Moreover, the smaller electronegativity
is sufficient to induce charge redistribution between P and C
atoms, a property that is interesting for energy storage
applications. Yu et al. introduced P atoms into carbons and
found that more edges and topological defects were created in
P-doped carbons, which accelerated efficient lithium ion
diffusion and thus led to superior lithium ion storage

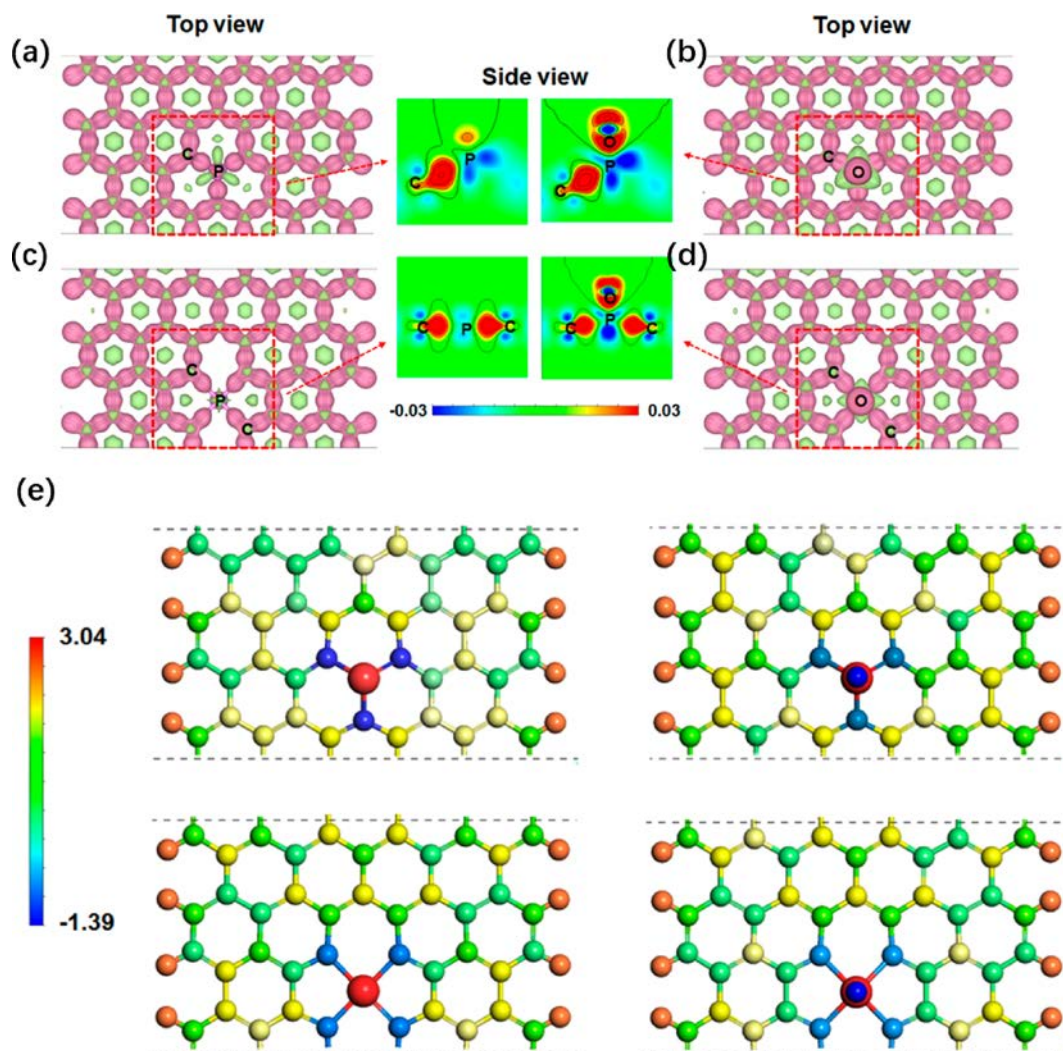


Figure 27. Deformation electronic density of hypothetical (a) PC3G, (b) OPC3G, (c) PC4G, and (d) OPC4G. The pink and yellow regions represent the areas of electron accumulation and loss, and the red and blue regions in the side view signify the areas of electron gain and loss. (e) Bader charges of the constructed models. Red and blue indicate positive and negative charges, respectively. The gray, white, red, and pink spheres represent the C, H, O, and P atoms, respectively. Reproduced with permission from ref 232. Copyright 2017 American Chemical Society.

1724 performance.²²⁸ These results are in agreement with the study
 1725 by Wang's group, in which the "protrusion" type P-doped
 1726 graphene exhibited better performance in Na batteries than N-
 1727 doped graphene (Figure 26a).²²⁹ From their DFT calculation,
 1728 the maximum theoretical capacity of Na for P-doped graphene
 1729 is calculated to be ~ 770 mAh/g, which is much larger than the
 1730 values for the N-doped versions (225.6 mAh/g for pyridinic N
 1731 and 406.1 mAh/g for pyrrolic N) in a hypothetical $C_{46}N_3$
 1732 structure. In addition, the metallic properties of P-doped
 1733 graphene remain mostly unchanged after sodium adsorption,
 1734 which results in fast electron transport during sodium-ion
 1735 insertion and extraction (Figure 26b–e).

1736 In 2011, Yang et al. reported the first metal-free P-doped
 1737 porous carbons as an efficient catalyst for the ORR.²³⁰ The as-
 1738 obtained porous carbons were flake-like graphitic layer
 1739 structures with convex cuplike structures on the surface of
 1740 each layer. The P-doped carbons exhibited high electrocatalytic
 1741 activity, long-term stability, and outstanding tolerance to the
 1742 crossover effects of methanol in the ORR compared to
 1743 conventional Pt/C in alkaline media. Similarly, Yu et al.
 1744 prepared P-doped carbons with an ordered mesoporous
 1745 architecture by employing triphenylphosphine and phenol as

P and carbon sources and SBA-15 as a hard template.²³¹ The
 1746 obtained porous carbons exhibited the morphology of
 1747 microspheres with an S_{BET} value of $1182 \text{ m}^2 \text{ g}^{-1}$. The XPS
 1748 spectrum confirmed the existence of P–C and P–O bonding
 1749 with a total P content of 1.36 at. %. Despite this low P content,
 1750 the P-doped porous carbons displayed outstanding perform-
 1751 ance toward the ORR and long-term stability.
 1752

From a theoretical calculation point of view, Wei et al.
 1753 explained the influence of different P configurations on the
 1754 electronic structures of graphene for the ORR.²³² The oxidized
 1755 P atom with three P–C bonds (OPC3G) was found to
 1756 possess the highest stability, followed by the oxidized P atom
 1757 with four P–C bonds (OPC4G), P atom with four P–C
 1758 bonds (PC4G), and P atom with three P–C bonds (PC3G).
 1759 The deformation electronic density showed substantial
 1760 electron accumulation around the O and C atoms because
 1761 the P atom had the lowest electronegativity ($\chi = 2.19$)
 1762 compared to O ($\chi = 3.44$) and C ($\chi = 2.55$) (Figure 27a–d).
 1763 The C atoms adjacent to P atoms have a partial negative
 1764 charge and can act as active sites for the ORR (Figure 27e).
 1765 Similar effects have also been proposed in the oxidation of
 1766 alcohol with P-doped porous carbons, where the enhanced
 1767

1768 catalytic activity is attributed to the existence of P—OH/P=O
1769 O moieties.²³³ Moreover, the PBE (Perdew–Burke–Ernzerhof)
1770 DFT calculations showed that the binding energy of O₂ for P-doped
1771 graphene is much larger than that for N-doped graphene. The magnetic
1772 moment was found to vanish upon O₂ adsorption, thus drastically
1773 enhancing the electrical conductivity. Furthermore, P has vacant 3d
1774 orbitals. Studies are still ongoing to understand the role of the vacant
1775 3d orbital in altering the properties of P-doped porous carbons.

3.5. Codoping Effect of Heteroatoms on Porous Carbons

1779 Each heteroatom can contribute its distinct characteristics to optimize
1780 the carbon materials for specific tasks. Codoping involves doping of two
1781 different heteroatoms into the carbon network, which could bring structural
1782 synergy. However, codoping is less studied than single-heteroatom doping
1783 in the porous carbon field due to its complexity, and future work is
1784 needed.

1786 **3.5.1. N, B Codoping.** N and B-codoped carbons have been applied
1787 in fields such as catalysis and energy storage. In the previous sections,
1788 studies showed that single doping of N or B can readily adjust the
1789 electronic structure of carbons. The similar atomic sizes of B, C, and N
1790 can effectively minimize the structural distortion, but the contrary
1791 electronic properties between B and N could induce a distinct electronic
1792 effect. For example, the intrinsic electron-deficient nature of B atoms
1793 could lead to p-type doping, while the electron-rich N atoms could lead
1794 to n-type doping. Taken together, these unique features have numerous
1795 unexpected synergistic merits for multiple applications.

1798 As an example, Antonietti et al. prepared B/N-codoped carbons with a
1799 high S_{BET} value of 978 m² g⁻¹ by direct carbonization of a
1800 constructed B/N-codoped monolithic precursor under N₂ for selective
1801 oxidation of amine.²³⁵ The synergistic effect of B and N could uniquely
1802 modulate the carbon electronic structure, in which B atoms (electron
1803 acceptors) could lower the valence band (or HOMO) and N atoms (electron
1804 donors) could elevate the conduction band (LUMO), thus relocalizing
1805 electrons to activate the substrate and oxygen molecules for oxidation
1806 reactions.

1808 Previously, Oya et al. found that a N, B-codoped carbon material
1809 exhibited higher ORR catalytic activity than individual N- or B-doped
1810 carbons. The authors attributed this ORR phenomenon to a synergistic
1811 effect of B–C–N-type moieties in the carbon network.^{236,237} This
1812 suggestion was confirmed by Qiao et al. through DFT calculations.
1813 In the constructed models, the 2p orbital of C in the B–C–N heteroring
1814 is polarized by adjacent N atoms, which inevitably donate extra
1815 electrons to the adjacent B atoms.²³⁸ The activated B atoms could
1816 facilitate the adsorption and bonding of HO₂. This charge transfer
1817 induced by the B and N doping synergy was believed to account for
1818 the enhanced catalytic activity in the ORR. In 2011, Dai et al.
1819 demonstrated that the catalytic performance of B/N-codoped carbon
1820 in the ORR was largely related to the concentration of the dopants.
1821 First-principles DFT calculations with four different models, pure
1822 graphene, B₇C₈₇N₆H₂₆, B₁₂C₇₇N₁₁H₂₆, and B₃₈C₂₈N₃₄H₂₆, were
1823 performed to understand the relationship between the dopant
1824 concentration and the catalytic capability of B/N-codoped carbons.
1825 As shown in Figure 28, the B₃₈C₂₈N₃₄H₂₆ model exhibited overloaded
1826 B and N atoms in the carbon network,

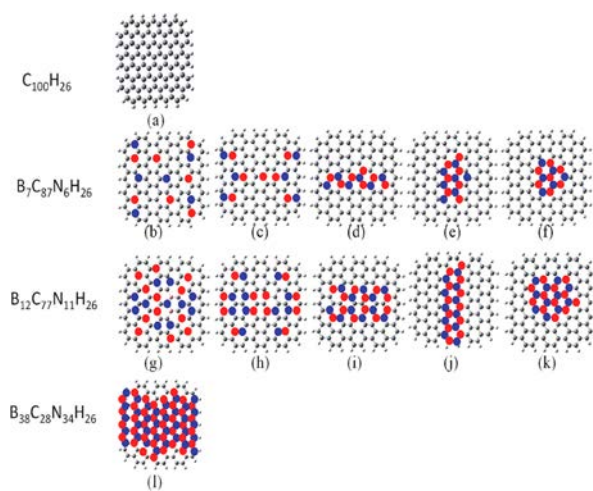


Figure 28. Different constructed B/N-codoped models. Reproduced with permission from ref 239. Copyright 2012 Wiley-VCH.

1829 resulting in a low electrical conductivity due to the largely
1830 formed BN clusters. The B₃₈C₂₈N₃₄H₂₆ model displayed the
1831 highest energy gap for the ORR owing to the low conductivity,
1832 which inevitably hindered efficient electron transfer. In the
1833 B₇C₈₇N₆H₂₆ and B₁₂C₇₇N₁₁H₂₆ models, randomly distributed
1834 B/N atoms or a smaller amount of BN clusters exist, and their
1835 energy gap was found to be significantly smaller than that of
1836 the B₃₈C₂₈N₃₄H₂₆ carbon. Therefore, the electrocatalytic
1837 activity of moderately doped B/N-codoped carbons was expected to
1838 be higher than that of pristine or overdoped B₃₈C₂₈N₃₄H₂₆
1839 carbons. In addition, B₁₂C₇₇N₁₁H₂₆ has higher B and N
1840 contents than B₇C₈₇N₆H₂₆; thus, more carbon atoms with
1841 relatively high spin density and charge density are created,
1842 which could act as active sites toward the ORR. Taken
1843 together, the electrocatalytic activity of the moderately doped
1844 B₁₂C₇₇N₁₁H₂₆ was calculated to be the highest in the ORR,
1845 which was later proven experimentally. Feng et al. found that
1846 the introduction of B and N atoms into the carbon network
1847 could induce the formation of dipole moments in the scaffold
1848 of the materials due to the uneven electronegativities among B,
1849 N, and C moieties.¹⁴⁷ Such an uneven charge distribution is
1850 beneficial for absorbing quadrupolar CO₂ through dipole–
1851 dipole interactions. Therefore, the B/N-codoped carbon
1852 exhibited high selectivity for CO₂/CH₄ adsorption with a
1853 ratio of more than 5:1 at 298 K, showing great promise in gas
1854 separation and purification.

1855 In 2006, Stephan and colleagues reported the first example
1856 of main group elements other than metals that could reversibly
1857 activate H₂.²⁴⁰ The chemistry of such unique activation of
1858 small molecules is referred to as a “frustrated Lewis pair
1859 (FLP)”, where the Lewis acid and Lewis base are separated
1860 from each other by steric hindrance. In solid-state chemistry,
1861 an FLP-like configuration anchored on catalyst supports is also
1862 found to be successful in catalyzing various reactions.^{241,242}
1863 Recently, several carbon-based FLP catalysts, such as Au@N-
1864 doped carbon²⁴³ and particularly graphene,²⁴⁴ have been
1865 reported in the literature. In a theoretical calculation, Su et al.
1866 predicted that, with a suitable space between N and B atoms,
1867 codoped carbons can overcome the energy barrier and
1868 heterolytically dissociate H₂.²⁴⁵ However, challenges remain,
1869 as the synthesis of FLP-like codoped carbons has to be
1870 precisely controlled.

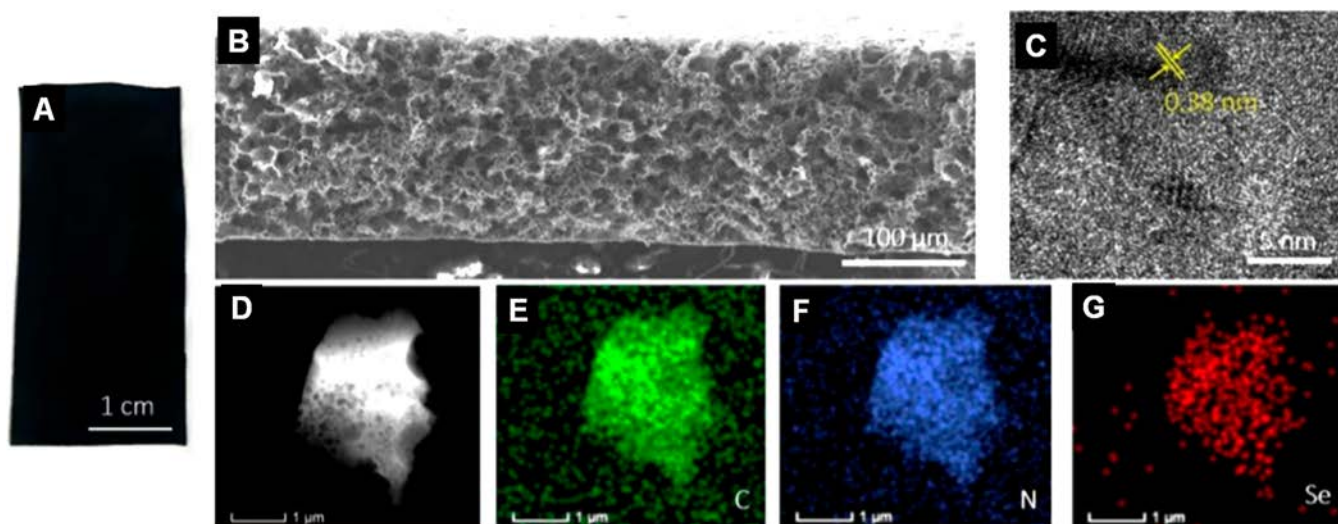


Figure 29. (a–c) Digital photograph, cross-sectional SEM image, and HRTEM image of carbon membranes. (d–g) STEM image and corresponding elemental mapping. Reproduced with permission from ref 162. Copyright 2019 Wiley-VCH.

1871 **3.5.2. N, S Codoping.** N/S-codoped porous carbons are
1872 exotic materials for electrochemical applications. Not only can
1873 the N atoms effectively increase the carbon electrode
1874 conductivity, but also, the S atoms can enlarge the carbon
1875 interlayer spacing, thus boosting the charge mobility and
1876 accessibility to reactive species.

1877 As an example, Yan et al. constructed N/S-codoped porous
1878 carbons from direct thermal annealing of human hair with
1879 KOH activation for electrochemical supercapacitors.²⁴⁶ The
1880 KOH-activated N/S-codoped carbons possessed micro/meso-
1881 pores with an S_{BET} value of $1306 \text{ m}^2 \text{ g}^{-1}$ and a high N/S
1882 content, delivering outstanding specific capacitances of 340 F
1883 g^{-1} in 6 M KOH and 126 F g^{-1} in 1 M LiPF_6 organic
1884 electrolyte at a current density of 1 A g^{-1} . Incorporation of N
1885 and S atoms can significantly improve the electrical
1886 conductivity and surface wettability and provide multiple
1887 redox active sites, thus enlarging the pseudocapacitance and
1888 specific capacitance.

1889 In addition, N/S-codoped porous carbons are potential
1890 anode materials for batteries, i.e., Na-ion batteries, because the
1891 enlarged interlayer spacing is beneficial for ion transport, while
1892 the introduction of N atoms can increase the first cycle
1893 Coulombic efficiency through improved electronic conductiv-
1894 ity. This point was further confirmed by dispersion-corrected
1895 DFT calculations. Yang et al. indicated that N/S codoping
1896 could effectively enlarge the adsorption capacity and mobility
1897 of Na ions.²⁴⁷ According to their calculations, the N/S-
1898 codoped carbons carried the highest spin density to promote
1899 the adsorption capacity of Na ions compared to other
1900 constructed models. They found that the adsorption capacity
1901 of Na^+ will be weakened with excess O atoms in N/S-codoped
1902 carbons. The increased interlayer spacing induced by the S
1903 atoms could significantly lower the energy barrier for the
1904 diffusion of Na ions from 126.83 to 97.87 meV.

1905 In addition to applications in energy storage, N/S-codoped
1906 porous carbons are known catalysts. Feng and co-workers
1907 prepared N/S-codoped porous carbons directly from the
1908 carbonization of conjugated polymer nanosheets.²⁴⁸ These
1909 porous carbons are catalytically active and stable in zinc-air
1910 batteries compared to conventional Pt/C. According to the
1911 DFT calculations from Qiao and colleagues, the codoping of N

and S could induce asymmetrical spin and charge density,
which are responsible for catalytic reactions.²⁴⁹ In addition,
due to the large size of the S atom in the carbon matrix, the
orbital mismatch between S and C will create active sites that
catalyze the ORR. Similarly, N/S-codoped porous carbons are
also active catalysts for the HER. For example, Chen et al.
found that the introduction of S atoms led to more defects
within carbons.²⁵⁰ These defect sites could create a negative
charge character on the S atoms, while the N atoms generated
a positive charge inside the carbon matrix. Both positively and
negatively charged species in the carbon framework could
provide a fast electron transfer pathway for the HER. In a
theoretical study from Qiao et al., N/S-codoped carbons
displayed the highest HER performance compared to N-, N/
B-, and N/P-(co)doped carbons.²⁵¹ These results implied that
the hydrogen adsorption energy was crucial to determining the
HER process.

Even though S atoms have the same electronegativity as C
atoms, their large atomic size and unique electron config-
uration could lead to numerous unexpected properties, i.e.,
redistribution of the spin density and creation of defects inside
the carbon framework. At the same time, incorporation of N
atoms could further bring about favorable electronic proper-
ties, making N/S-codoped porous carbons promising in the
field of electrochemical applications.

3.5.3. N, Se Codoping. Selenium, as one of the chalcogen
elements, has similar chemical properties but a larger atomic
size and a higher polarizability compared to sulfur.²⁵² Very
recently, Wang's group successfully achieved molecular doping
of Se atoms into carbon membranes by direct carbonization of
a PIL porous membrane bearing a $\text{Se}(\text{CN})_2^-$ anion (Figure
29).¹⁶² As a semimetal, the Se atoms were found to bond to
adjacent carbons with a uniform atomic dispersion throughout
the carbon framework (Figure 15). Analogous to bulk doping,
it is crucial to tune the electronic structure of carbons because
covalent incorporation of Se atoms can readily induce strain,
defects, and charged species into the carbon matrix. The XRD
spectra confirmed that molecular doping of Se could enlarge
the interlayer spacing (d_{002}) of graphitic domains, which is
favorable for ion transfer. EXAFS spectra and STEM images
confirmed that each Se atom existed individually in the carbon

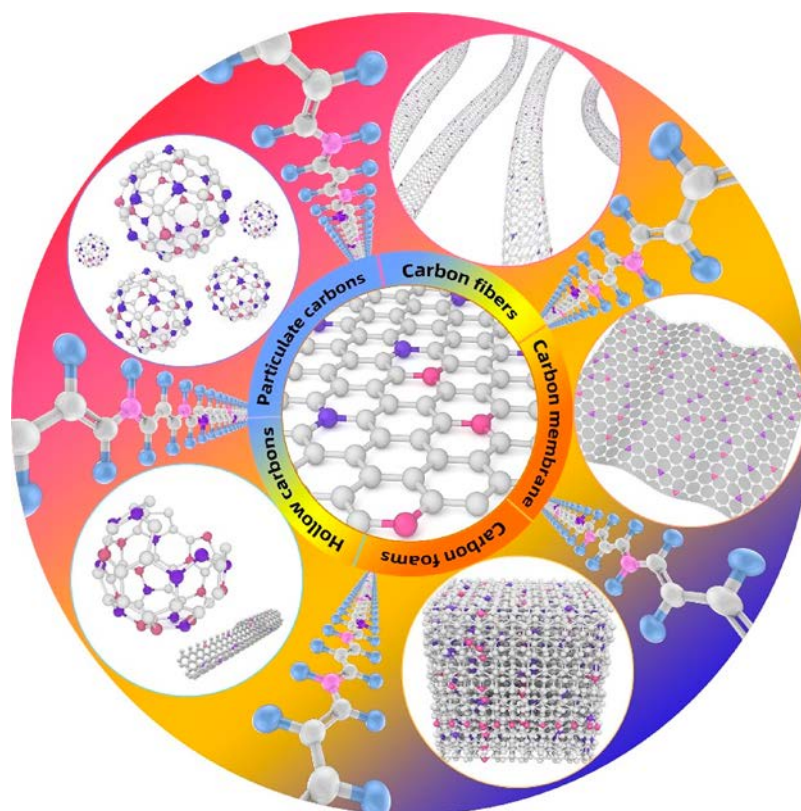


Figure 30. Schematic illustration of carbon materials with different morphologies.

1953 framework, located at the edge of graphitic domains in the
1954 membrane. The valence state of Se was between 0 and +4
1955 according to XANES, indicative of a positive charge character-
1956 istic. The enlarged graphitic layer, positively charged Se atoms,
1957 and hierarchically porous membrane structure endowed the
1958 membrane with striking hydrazine oxidation performance in
1959 practical hydrazine fuel cells.

1960 As an emerging doping element, Se is starting to become
1961 relevant in various applications. It is important to note that
1962 how the large atomic size and “semimetal-like” properties of Se
1963 could impact intrinsic carbon properties remains largely
1964 unknown. Therefore, it is possible that synergistic interplay
1965 between Se doping and other heteroatoms might lead to
1966 unexpected results.

1967 **3.5.4. N, P Codoping.** Yuan et al. constructed N/P-
1968 codoped microporous carbon spheres by direct carbonization
1969 of self-assembled PDA with diphosphonic acid.²⁵³ The
1970 utilization of diphosphonic acid was particularly interesting
1971 because it not only initiated the self-polymerization of
1972 dopamine but also induced the acid–base interaction with
1973 amine to incorporate P moieties into the polymer backbones.
1974 During the carbonization process with F127 as the porogen,
1975 the P/N moieties inevitably fused into the carbon matrix.
1976 These P/N-codoped porous carbons demonstrated a high
1977 performance in the ORR and HER. In 2015, Dai and
1978 colleagues reported the first N/P-codoped porous nanocarbon
1979 foams as efficient bifunctional electrocatalysts for the ORR and
1980 OER in Zn-air batteries.⁷¹ The porosity and N/P doping level
1981 of porous nanocarbon foams could be well tailored by the
1982 carbonization temperature to optimize the electrocatalytic
1983 performance (e.g., NPMC-1000 or NPMC-1100). The first-
1984 principles DFT calculations revealed that the N/P-codoped
1985 carbons exhibited the lowest ORR and OER overpotentials

1986 compared to those of individual N- or P-doped carbons and
1987 even the state-of-the-art Pt and RuO₂ electrocatalysts in
1988 alkaline media. Later, in 2018, the same group constructed
1989 microporous N/P-codoped graphitic nanosheets by thermal
1990 annealing of conjugated microporous polymers in the presence
1991 of phytic acid.²⁵⁴ Interestingly, incorporation of P was found to
1992 enhance S_{BET} due to a carbon-etching process. The XRD
1993 profiles indicated an increased interlayer spacing, suggesting
1994 that P atoms were doped into the carbon matrix. The
1995 enhanced $I_{\text{D}}/I_{\text{G}}$ ratio in the Raman spectra was also attributed
1996 to the P doping and edge defects associated with the porous
1997 structures of the carbon network. As a consequence, through
1998 the synergistic effects between N and P, the enhanced
1999 microstructures of N/P-codoped porous carbons presented
2000 superior electrocatalytic activity for the ORR with a low
2001 overpotential, a high current density, and good stability over
2002 the entire pH range.

2003 **3.5.5. Ternary Doping by Three Types of Hetero-**
2004 **atoms.** Ternary-doped porous carbons are rarely reported.
2005 In early 2012, Woo et al. reported post-treatment of
2006 synthesized N-doped carbons with boric acid and phosphoric
2007 acid to construct N/B/P ternary-doped carbons.²⁵⁵ This work
2008 showed that B effectively reinforced the sp^2 structure of
2009 carbon, N increased the portion of pyridinic N, and the larger
2010 atomic size P could severely distort the carbon framework to
2011 add edges. Therefore, the N/B- and N/P-codoped carbons
2012 showed 1.2 and 2.1 times higher ORR activity than that of N-
2013 doped carbons, while N/B/P ternary doping further improved
2014 the ORR activity, as the additional doping of B and P was
2015 expected to promote an asymmetric atomic spin density as well
2016 as charge localization of the carbon atoms.

2017 Recently, Song et al. developed N/S/P ternary-doped
2018 carbocatalysts by carbonization of poly(cyclotriphosphazene-

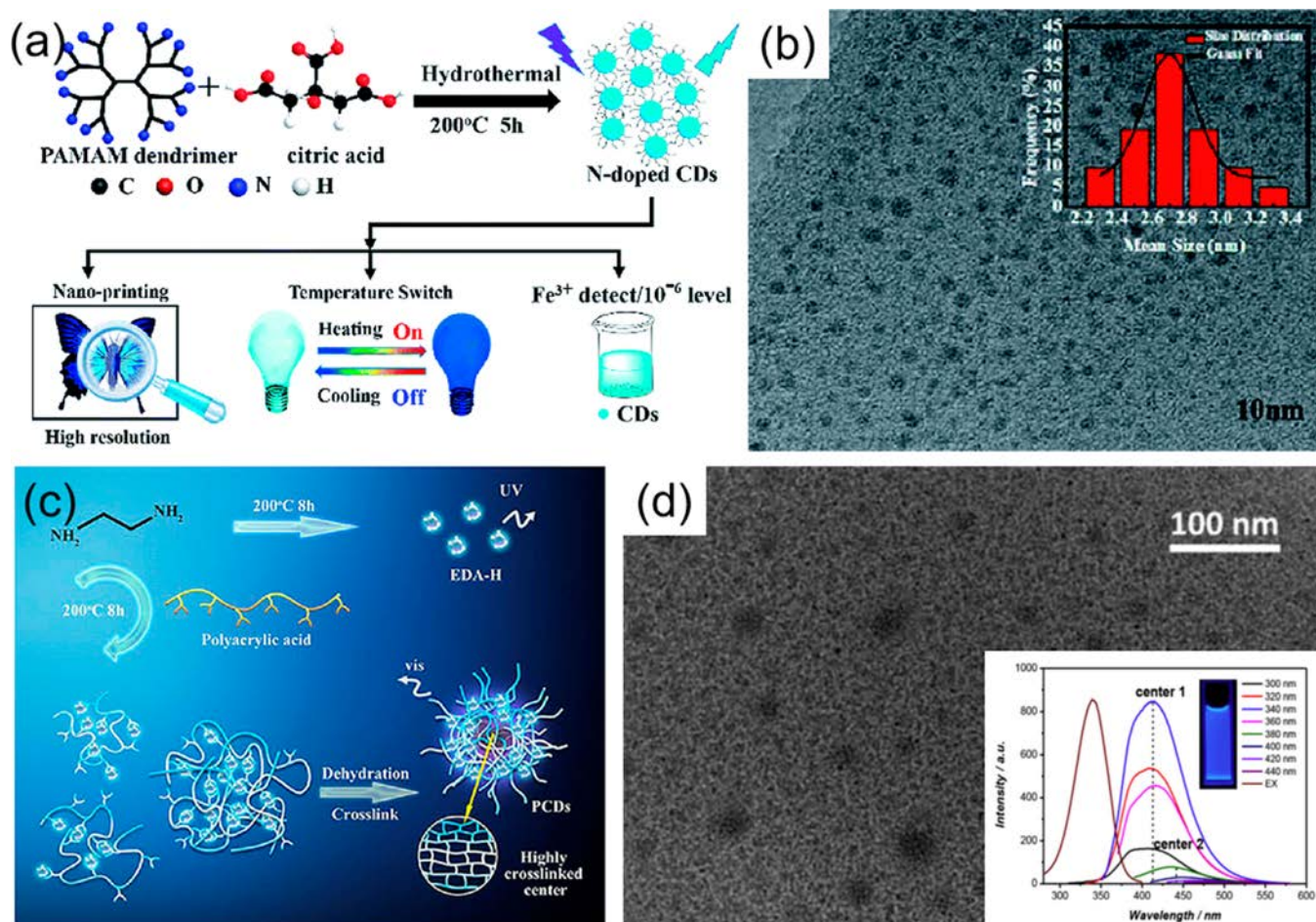


Figure 31. (a) Schematic diagram of the synthetic procedure for CQDs from PAA and EDA. (b) HRTEM image of the CQDs. The inset shows the photoluminescence excitation and emission (300–440 nm) spectra. Reproduced with permission from ref 268. Copyright 2016 Royal Society of Chemistry. (c) Schematic illustration of the synthesis of CQDs from a PAMAM dendrimer and their exemplary applications. (d) HRTEM image of CQDs along with a particle size distribution plot (inset). Reproduced with permission from ref 269. Copyright 2017 Elsevier.

2019 *co*-4,4'-sulfonyldiphenol) (PZS)-coated ZIF-67 followed by
 2020 acid etching to remove metals.²⁵⁶ The TEM images of ZIF-67
 2021 displayed a typical polyhedral structure, which was well
 2022 maintained after coating with PZS and carbonization. After
 2023 acid etching, hollow carbon shells of ca. 20 nm in thickness
 2024 were obtained. Remarkably, the hollow carbon shells exhibited
 2025 a high S_{BET} value of 1020 m² g⁻¹ with a pore size of 4.3 nm.
 2026 Moreover, the introduction of heteroatoms readily changed the
 2027 surface wettability of the carbon materials, which made them
 2028 well dispersed in aqueous solution. In addition, the
 2029 incorporation of N into the carbon materials was considered
 2030 important to activate the C–H bond, while the N/S codoping
 2031 could modulate the carbon electronic structure. Therefore, the
 2032 N/S/P-codoped carbon exhibited high selectivity in the
 2033 oxidation of aromatic alkanes in an aqueous solution.
 2034 Multiheteroatom doping of porous carbons is apparently
 2035 also beneficial for a variety of applications. N Doping can
 2036 change the electronic structure and promote the conductivity;
 2037 B doping can increase the in-plane defects and even act as
 2038 electron-deficient sites for various reactions; and P, S, and Se
 2039 doping can enlarge the interlayer spacing and cause significant
 2040 lattice distortion and defects, thus making carbons chemically
 2041 more active. Furthermore, the asymmetrical spin and charge
 2042 density induced by these large heteroatoms could functionalize
 2043 the carbon materials. Therefore, carefully designed multi-

heteroatom doping can work synergistically, and the detailed
 interplay mechanism has yet to be fully understood.

4. MORPHOLOGICAL CONTROL OF POROUS CARBONS

In addition to the intrinsic chemical composition, the morphology of heteroatom-doped carbons is related to their electronic properties and corresponding electrochemical performances. The surface areas and mass transport capabilities vary greatly among 0D nanoparticles, 1D fibers and tubes, 2D sheets, and 3D bulk. Therefore, the choice of the carbon morphology has been widely studied in the literature. In this section, we highlight some particularly interesting morphologies involved in porous carbons derived from polymers ranging from porous particles to fibers, nanotubes, films, and freestanding membranes along with their corresponding processing techniques and their specific applications (Figure 30).

4.1. Heteroatom-Doped Porous Carbon Particles

Porous carbon particles, such as nano/microspheres, bubble-like hollow particles, and particles with anisotropic/asymmetric morphologies, are unique in terms of a low apparent density, a low percolation threshold, a high surface-to-volume ratio, and high thermal and chemical stability.²⁵⁷ Comparably, porous carbon particles have obvious merits such as being easier to

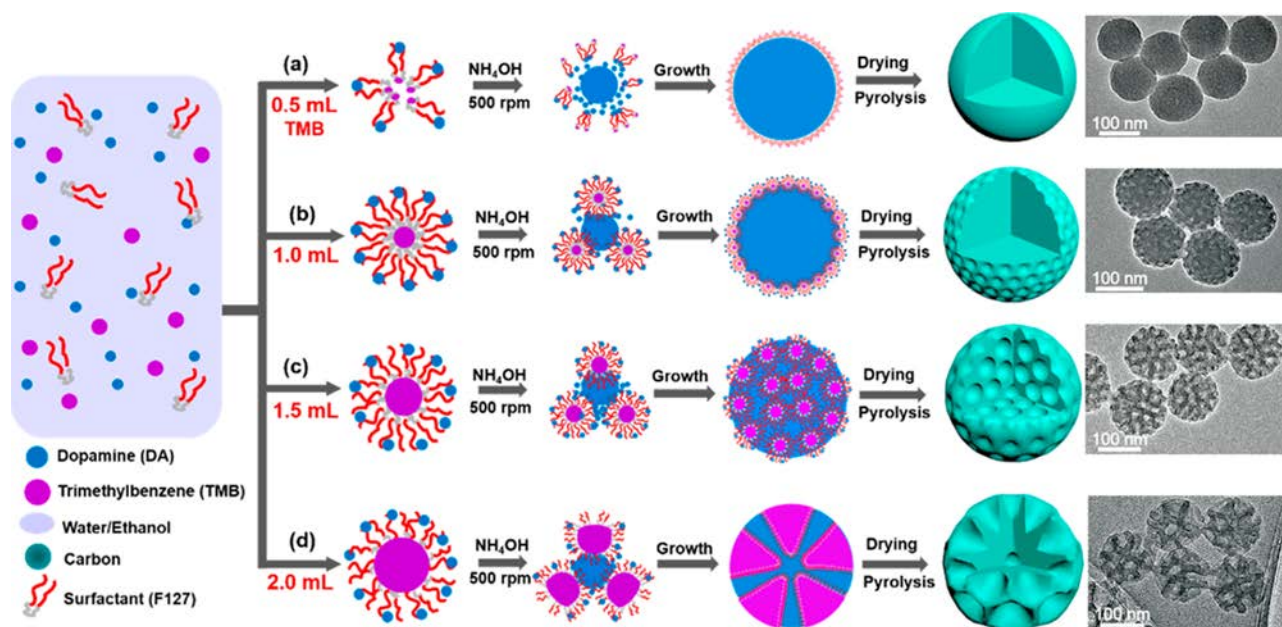


Figure 32. Formation process for the N-doped mesoporous carbon nanospheres with various morphologies prepared by the versatile nanoemulsion assembly approach and corresponding TEM images of the carbon nanospheres. Reproduced with permission from ref 274. Copyright 2019 American Chemical Society.

2066 disperse, having shorter pathways from the bulk to the particle
2067 surface for electron transfer, and having more accessible active
2068 sites.²⁵⁸ To date, polymer-derived porous carbon particles have
2069 been prepared *via* different approaches, including hard and soft
2070 template methods, controlled polymerization methods, and
2071 Stöber-based methods.^{257–260} In this section, porous carbon
2072 particles with different structural features, including nano/
2073 microspheres, hollow porous particles, and anisotropic/
2074 asymmetric porous carbon particles, will be discussed.

2075 **4.1.1. Carbon Quantum Dots (CQDs).** Though the
2076 chemical nature and origin of the optical properties of carbon
2077 quantum dots (CQDs) are still under debate, they have
2078 emerged as innovative carbon-based sub-10-nm nanoparticles
2079 with interesting properties due to the quantum confinement
2080 effect, i.e., a carbonaceous version of classic quantum dots in
2081 nanoscience. CQDs feature unique properties, including a
2082 small size that is rather unusual for carbons, fluorescence
2083 emission, chemical stability, water solubility, easy synthesis,
2084 and the possibility of surface functionalization, plus geo-
2085 graphically unlimited access to carbon precursors globally.
2086 Because of the combined property profile, CQDs are a rising
2087 star in the field of nanostructured carbon materials widely
2088 studied for imaging, sensing, drug delivery, optics, and
2089 catalysis.²⁶¹ Multiple techniques have been developed to
2090 prepare CQDs simply and inexpensively, such as the
2091 hydrothermal method, electrochemical synthesis, the arc-
2092 discharge method, and microwave pyrolysis.^{261–263} These
2093 top-down or bottom-up methods involve several categories of
2094 precursors covering bulk carbon, small organic molecules,
2095 natural polymers, and synthetic polymers. Among them,
2096 natural and synthetic polymer precursors provide more
2097 synthetic flexibilities on the basis of their tunable structures
2098 to define their positive, negative, zwitterionic or nonionic, and
2099 hydrophilic or hydrophobic features.

2100 Many natural polymers have been reported for the synthesis
2101 of CQDs, including chitosan, xylan, citrus pectin, silk fibroin,
2102 gelatin, and polysaccharide.²⁶⁴ As an example, CQDs of 4–7

2103 nm in size with a remarkably high quantum yield (QY) of 43%,
2104 excellent photostability, and low cytotoxicity were hydro-
2105 thermally synthesized from chitosan at 180 °C for 12 h and
2106 used as a cell imaging agent.²⁶⁵ The high QY was possibly
2107 attributed to the inherent nitrogen doping effect endowed by
2108 the chitosan precursor. In addition to chemically pure natural
2109 polymers, direct use of crude natural materials (including
2110 biomass) as CQD precursors has appeared as a hot topic due
2111 to their renewable feature with little to no involvement of toxic
2112 chemicals. For instance, amphibious CQDs of 2–5 nm could
2113 be prepared by hydrothermal treatment of peach gum
2114 polysaccharide at 180 °C for 12 h.²⁶⁶ The obtained CQDs
2115 exhibited strong photoluminescence and excellent dispersibility
2116 both in water and in organic solvents. More natural polymeric
2117 precursors, e.g., cashew gum, peanut shell, sweet potato,
2118 pomelo peel, grass, egg white or egg yolk, bagasse, paper ash,
2119 plant leaf, and plant peel, used to generate CQDs were
2120 summarized in earlier reviews.^{264,267}

2121 Compared to abundant, diverse natural polymer precursors,
2122 by taking advantage of the controllable chemical structures of
2123 synthetic polymers, CQDs for target applications can be
2124 designed and synthesized from different types of synthetic
2125 polymers, including negative/zwitterionic/neutral and hydro-
2126 philic/hydrophobic ones.²⁶⁴ Typically, N-doped CQDs can be
2127 generated from N-containing polymers, such as polyethylene-
2128 imine, polyacrylamide, polydopamine, and polyamidoamine
2129 dendrimers. Using a polyamidoamine (PAMAM) dendrimer as a
2130 precursor, CQDs with a QY of 40% were synthesized
2131 through a hydrothermal process. They were further hybridized
2132 with poly(*N*-isopropylacrylamide) and used for sensitive
2133 detection of Fe³⁺, as printing ink, and in thermosensitive
2134 devices (Figure 31a,b).²⁶⁸ Tao et al. reported the synthesis of
2135 fluorescent CQDs (20–30 nm) with an absolute QY of 44%
2136 by hydrothermally cross-linking poly(acrylic acid) (PAA, MW
2137 = 3500 g/mol) and ethylenediamine (EDA).²⁶⁹ The
2138 fluorescence mechanism was studied by investigating the
2139 optical properties of individually or co-treated PAA and EDA

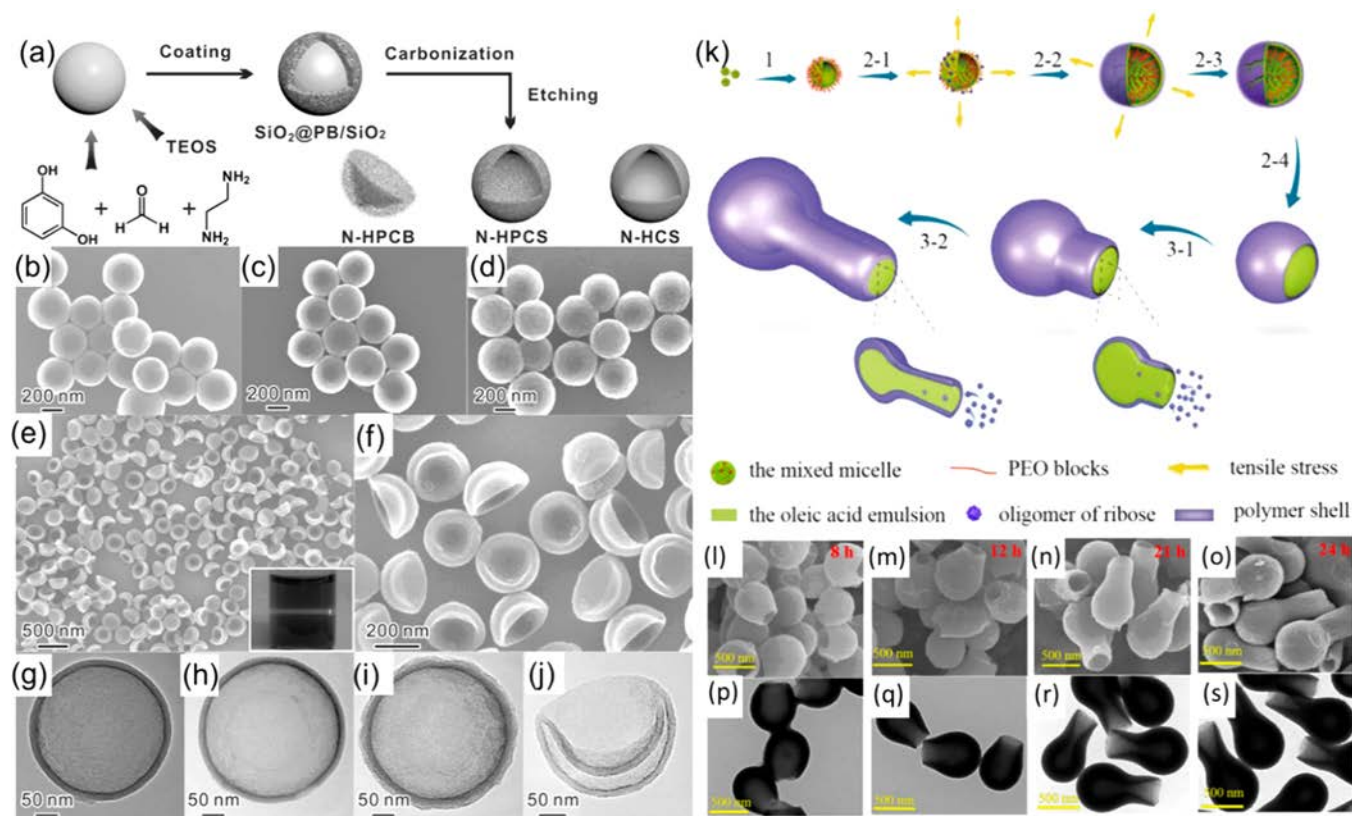


Figure 33. (a) Schematic illustration of the silica-assisted PB coating strategy for the synthesis of N-HCSs, N-HPCSs, and N-HPCBs. SEM images of (b) HCSs, (c) N-HCSs, (d) N-HPCSs, and (e, f) N-HPCBs. TEM images of (g) HCSs, (h) N-HCSs, (i) N-HPCSs, and (j) N-HPCBs (inset: optical image of the dispersed solution of N-HPCBs and the corresponding Tyndall effect). Reproduced with permission from ref 282. Copyright 2016 Wiley-VCH. (k) Schematic mechanism of the growth of HOCFs. (1) Formation of nanoemulsions. (2) Formation of openings: (2-1, 2-2) PEO blocks caused the nanoemulsions to swell. (2-3, 2-4) The shells were cracked by the tensile stress. (3) Formation of necks: the derivatives filled in, and the nanoemulsion flowed out gradually. (l-o) SEM and (p-s) TEM images of the HOCFs prepared with different hydrothermal times: (l and p) for 8 h, (m and q) for 12 h, (n and r) for 21 h, and (o and s) for 24 h. Reproduced with permission from ref 283. Copyright 2017 American Chemical Society.

2140 products. It was revealed that the synergistic effect of PAA
2141 chains and fluorescence centers in EDA might contribute to
2142 the fluorescence. Specifically, the PAA chains were considered
2143 to decrease the motion freedom and provide a solvation effect
2144 by cross-linking and wrapping the fluorescence centers of EDA,
2145 leading to improved QY and red-shifted emission (Figure
2146 31c,d).

2147 In other studies, efforts have been made to address the
2148 aggregation problem of CQDs,²⁷⁰ which hinders their
2149 applications in imaging and drug delivery. To this end,
2150 “zwitterionic polymers” containing equimolar anionic and
2151 cationic groups in their structures have been recently explored
2152 through a simple microwave heating method.²⁷⁰ In addition to
2153 their well-known superhydrophilic and antifouling properties
2154 in resisting nonspecific binding of proteins, cells, and
2155 microorganisms, zwitterionic polymers have also been
2156 demonstrated to efficiently protect nanoparticles from
2157 aggregation.^{271,272}

2158 **4.1.2. Porous Carbon Spheres.** Carbon nanospheres are
2159 widely used in drug delivery, heterogeneous catalysis, and
2160 encapsulation of support and electrode materials. Precise
2161 control of the particle size, chemical composition, pore size,
2162 and dispersity of carbon nanospheres has been enabled by the
2163 rapid progress in synthesis. A number of strategies, such as
2164 extended Stöber synthesis, templating routes, and organic–
2165 organic self-assembly *via* different binding methods, have been

widely reported. Stöber synthesis is a typical sol–gel approach 2166
for preparing monodisperse silica spheres, which has been 2167
extended to prepare porous carbon spheres by ammonia- 2168
catalyzed polymerization of resorcinol and formaldehyde in the 2169
ethanol–water phase, followed by carbonization in an inert 2170
atmosphere.²⁶⁰ By using suitable precursors, heteroatom-rich 2171
carbon spheres with unique porous structures can be fabricated 2172
via the extended Stöber-based method.²⁷³ As discussed in 2173
section 2.1.1, by using the micelles of block polymers as a soft 2174
template, a coassembly strategy was developed by Yamauchi et 2175
al. to prepare N-doped carbon spheres with large mesopore 2176
sizes.⁵⁶ This unconventional templating and coassembly 2177
method sheds light on the role of the interfacial interactions 2178
between soft templates and carbon precursors, which allows 2179
the synthesis of various carbon nanospheres with tunable pore 2180
sizes and chemical components. Very recently, Zhao et al. 2181
extended this method to prepare N-doped carbon nanospheres 2182
with high uniformity and large tunable pore sizes ranging from 2183
5 to 37 nm (Figure 32).²⁷⁴ In this work, dopamine was used as 2184 f32
the carbon precursor and F127 as the soft template. TMB was 2185
used to control the formation of a uniform Pluronic F127/ 2186
TMB/dopamine microemulsion in the ethanol/water system. 2187
They showed that TMB not only plays an important role in the 2188
evolution of pore sizes but also significantly affects the 2189
interfacial interaction between the soft template and carbon 2190
precursor. After the polymerization of dopamine and 2191

subsequent carbonization, N-doped carbon nanospheres with diverse novel structures, such as smooth, golf ball, multi-chambered, and dendritic architectures, could be obtained. The uniform dendritic mesoporous carbon nanospheres showed a large pore size (~37 nm), a small particle size (~128 nm), a high surface area (~635 m² g⁻¹), and abundant N content (~6.8 wt %) and delivered a high current density and an excellent durability for the ORR in alkaline solution. This microemulsion strategy provides new insights into the interfacial assembly and synthesis of mesoporous carbons beyond conventional block copolymer templating.

Other methods, such as spray carbonization, autogenic pressure carbonization, or hydrothermal carbonization of biomass-based resources, are available to construct carbon spheres.^{275–277} Utilizing polymers as carbonization precursors is particularly intriguing, as it demonstrates a facile, versatile strategy for manufacturing carbon materials with tailored morphologies (in this case, carbon spheres) along with heteroatom doping without complicated post-treatment.

4.1.3. Hollow Porous Particles and Anisotropic/Asymmetric Porous Carbon Particles. The template approach also provides opportunities for developing various anisotropic or asymmetric porous carbon particles, such as bowl-like, concave, Janus, rattle-type, and patchy particles.^{57,277–280} Strategies involving hard, soft, and self-templating methods have been successfully explored for the fabrication of heteroatom-doped carbon particles with anisotropic or asymmetric shapes.^{277–281} The hard template method has been used frequently owing to the well-established preparation of solid anisotropic polymer nanostructures through approaches ranging from stretching to controlled deformation methods, microfluidic and photolithographic approaches, single-phase swelling reformation, and seeded polymerization.²⁸¹ Compared with polymer templates, the creation of anisotropic/asymmetric inorganic templates, such as silica, remains a challenge, especially by wet chemical approaches owing to the natural primary principle of symmetry that leads to isotropic morphologies. Very few works have been reported on the fabrication of asymmetric carbon particles by employing isotropic silica nanospheres as templates. One example was given by Zheng et al. in 2016. They synthesized N-doped hollow carbon spheres (N-HCSs) and their bowl-like (N-HCB) counterparts by applying polybenzoxazine (PB) in the Stöber coating method for template synthesis.²⁸² In their work, SiO₂ spheres were used as a template, and resorcinol/formaldehyde/ethylenediamine (EDA) was used as the PB precursor. PB-coated SiO₂ spheres (SiO₂@PB) were first obtained *via* a modified Stöber coating process, i.e., a one-pot polymerization of the PB precursors in a mixture containing TEOS, ethanol, and H₂O. N-Doped hollow porous carbon spheres (N-HPCSs) and bowls (N-HPCBs) could be obtained after calcination and removal of the hard template (Figure 33a–j). The ratio of TEOS to EDA was crucial to determining the morphology of the carbon particles. In comparison with N-HPCSs, a higher concentration of TEOS was required to synthesize N-HPCBs. The formation mechanism of N-HPCBs was proposed to be that, after the removal of SiO₂, the porous carbon framework in N-HPCBs was not rigid enough to support the hollow structure due to its high porosity, and the carbon shell thus collapsed into its internal cavity and finally formed a bowl-like structure.

Most recently, new insights have been provided into the synthetic methodology beyond conventional hard and soft

template methods. A mechanism of synergetic interactions between the template and biomass was applied by Wang's group to synthesize hollow open carbonaceous nanoflasks (Figure 33k–s).²⁸³ In this work, P123 copolymer and sodium oleate (SO) were chosen as double surfactants, while ribose acted as a carbon source. The asymmetric carbon nanoflasks were obtained via hydrothermal carbonization (HTC) treatment of ribose in aqueous P123 and sodium oleate (SO). During the HTC process, mixed micelles were first formed due to the strong interaction between the two surfactants, which were then transferred into nanoemulsions at high temperature. These nanoemulsions were not stable at 160 °C due to the vulnerable P123, which could be easily swollen by the hydrophilic PEO blocks of P123, leading to cracking of carbonaceous polymer shells at the interface, facilitating the anisotropic deposition of biomass polymers. The necks of the nanoflasks could be derived from the anisotropic growth of carbonaceous shells at the newly formed interface of the broken nanoemulsions driven by the gradual filling by oligomers from the biomass. The resulting carbonaceous nanoflasks showed a narrow size distribution and excellent performance in supercapacitor devices. Their proposed dynamic process induced by the synergetic interactions between the template and biomass would enable access to novel inspirational methodologies for fabrication of carbonaceous materials of high structural complexity.

4.2. Heteroatom-Doped Porous Carbon Fibers and Tubes

4.2.1. Porous Carbon Fibers. With the rapid development of portable and wearable electronics, carbon fibers are receiving increasing attention due to their light weight, high conductivity, large surface area, high chemical stability, and outstanding mechanical strength.²⁸⁴ In fact, fibrous carbon materials have already been applied in the field of flexible devices as sensors,^{285–290} actuators,^{291–296} energy storage materials,^{297–301} and many more. Although conventional carbon fibers can be made from CNTs or graphene, these processes usually require transition metals as catalysts, which causes concerns in applications where even trace fractions of metals are a problem. Furthermore, the high price of CNT-based fibers hinders their daily usage. In this regard, direct carbonization of polymers to fabricate carbon fibers aims to provide a low-cost yet versatile approach to produce carbon fibers for diverse applications. In this section, we will highlight some of the representative heteroatom-doped porous carbon fibers derived from polymers.

CNFs can be prepared mainly by two methods. One is catalytic thermal chemical vapor deposition growth, and the other is electrospinning followed by thermal annealing. As a versatile, cost-effective and simple technology for preparing polymer-derived CNFs as well as their composites with controllable architectural parameters, electrospinning is already widely applied in both industrial production and research laboratories. The principle of electrospinning has been well introduced in several previous reviews on electrospun materials for energy-related applications.²⁹⁷ To date, the polymer fibers that serve as carbon fiber precursors can be polyacrylonitrile (PAN), polyimide, poly(vinyl alcohol), poly(vinylidene fluoride), and pitch. Among them, PAN is one of the most common because it can rearrange into thermally stable pyrazine ladder polymers prior to carbonization at elevated temperature. Recently, Wu et al. fabricated carbon fibers by carbonization of electrospun polymer fibers using PAN and

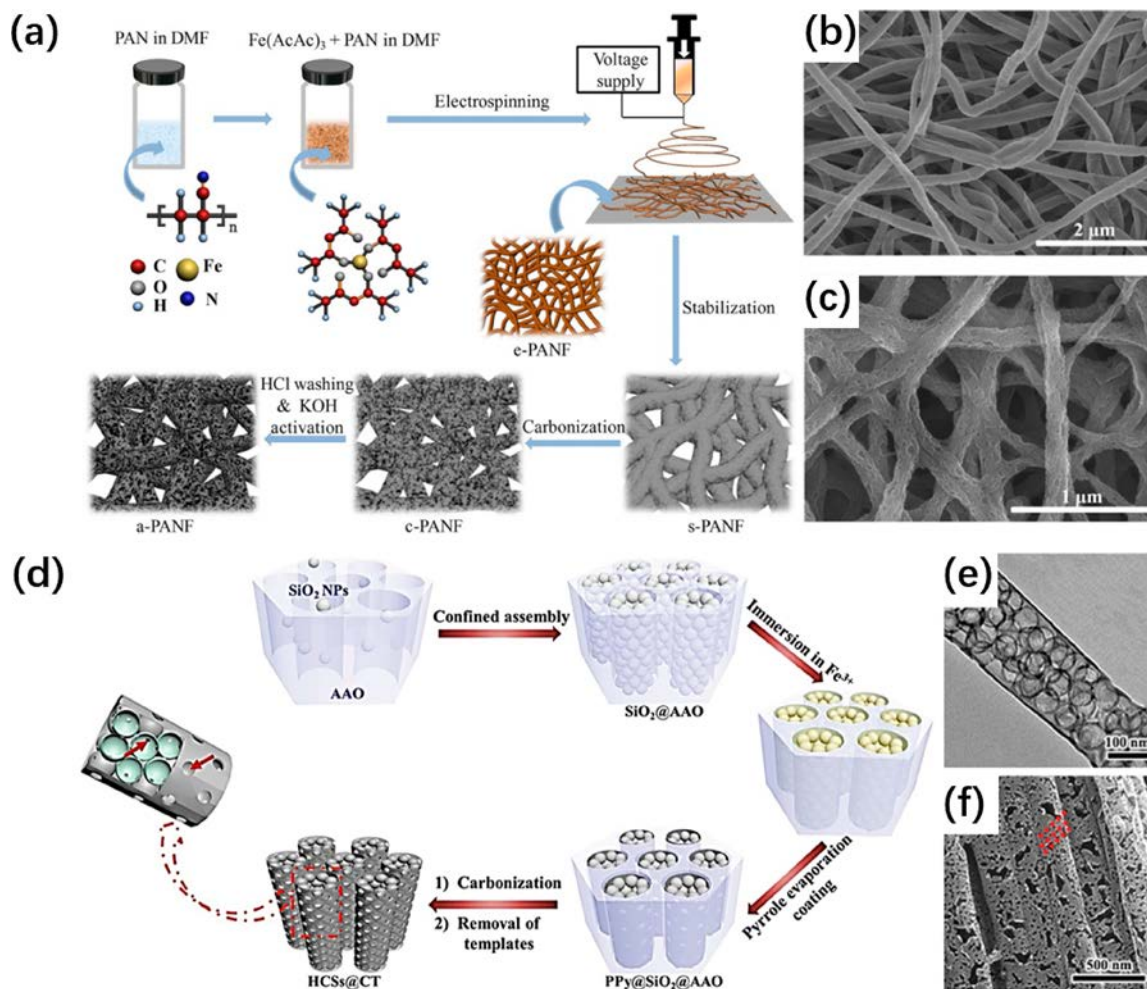


Figure 34. (a) Synthesis scheme of N-doped carbon fibers and membranes by electrospinning. (b, c) SEM images of N-doped carbon fibers prepared from electrospun fibers. Reproduced with permission from ref 303. Copyright 2018 Wiley-VCH. (d) Schematic illustration of the production of HCSs@CT with the assistance of the dual template formed by confined assembly. In the enlarged view of HCSs@CT, meso/macropores are visualized between the interconnection of HCSs and the connection of the CT and HCSs (green spheres show the internal circumstances of HCSs). (e) TEM and (f) SEM images of the obtained HCSs@CT. Reproduced with permission from ref 307. Copyright 2018 Wiley-VCH.

H_3PO_4 as precursors.³⁰² The as-obtained carbon fibers possessed more defects and less long-range order in the carbon network, and the interlayer spacing was significantly expanded by the incorporation of P. This enlarged d -spacing and defect-laden N, P-codoped carbon fiber exhibited excellent performance in sodium batteries as a fiber electrode. It was demonstrated that adding inorganic salts into the spinning solution is an effective route toward the preparation of advanced carbon fiber composites. For example, PAN and $\text{Fe}(\text{acetate})_3$ can be directly codissolved in N,N -dimethylformamide (DMF) and electrospun into $\text{Fe}(\text{acetate})_3$ -PAN composite fibers (Figure 34a–c).³⁰³ Fe NP-functionalized carbon fibers could be readily prepared by carbonization of $\text{Fe}(\text{acetate})_3$ -PAN fibers.

PILs have recently emerged as a new type of carbon precursor. Their tunable chemical compositions and structures endow them with a myriad of opportunities to fabricate advanced carbon fibers. For instance, Yuan et al. first synthesized a PIL with dicyanamide counteranions, which are known for undergoing condensation reactions at 280–300 °C to stabilize the carbon network. N-Doped carbon fibers with a high conductivity of $200 \pm 60 \text{ S cm}^{-1}$ could be easily

obtained by direct carbonization of PIL-based fibers under rather moderate conditions.³⁰⁴

Owing to their light weight, high conductivity, and chemical stability, macroscopic flexible carbon fibers are extremely appealing for flexible devices. It is believed that the development of thermally stable polymer fibers that can be converted into carbon fibers could provide a versatile platform to fabricate fiber electrodes for conduction, electron storage, and energy conversion.

4.2.2. Porous Carbon Tubes. Heteroatom-doped carbon micro/nanotubes used as electrode materials for batteries have shown significant advantages compared to fiber materials due to their enhanced surface-to-volume ratio for the electrode–electrolyte interface.^{305,306} Moreover, these 1D hollow carbon tubes can be easily functionalized with various secondary structural components to meet the requirements of energy conversion and storage devices for real-life applications. For instance, Lee et al. successfully fabricated N-doped hollow CNFs by carbonization of polymer fibers. They first prepared core–shell structured polymer fibers utilizing the coaxial electrospinning technique, in which PS-co-PAN (SAN) was the core and PAN was the shell material.¹⁴⁰ Before

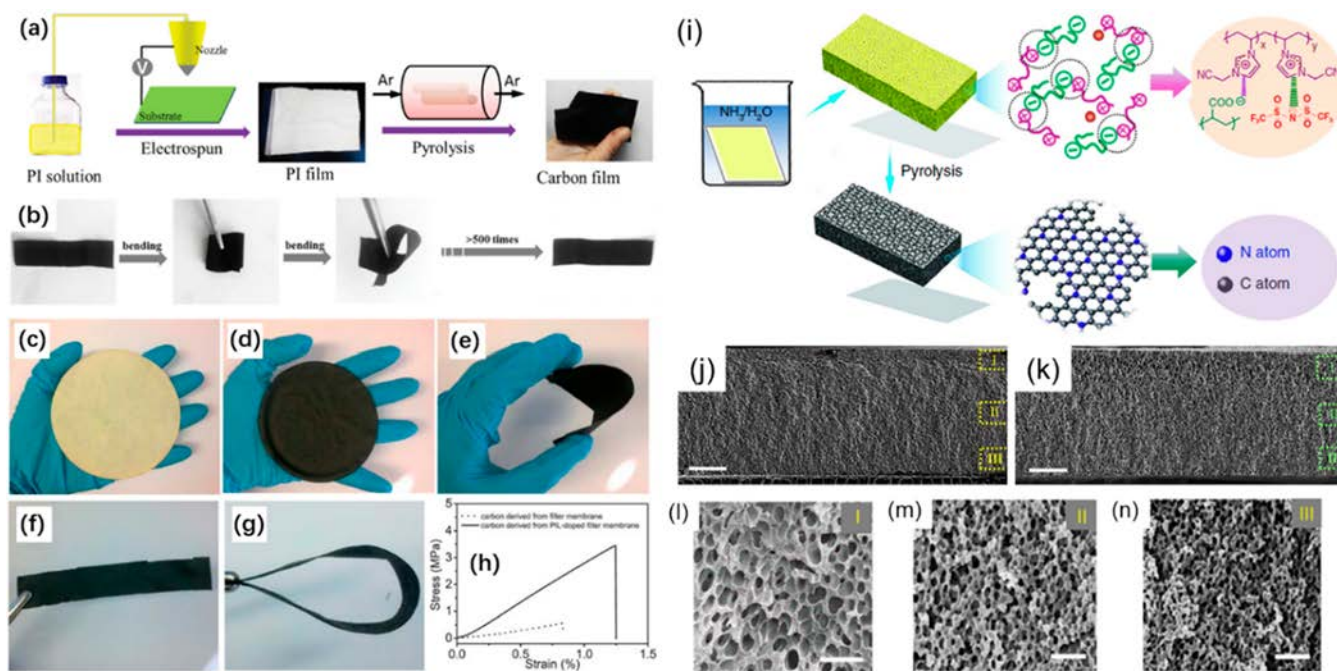


Figure 35. (a) Schematic illustration of the fabrication of nanoporous carbon fiber films. (b) Photographs of the resultant flexible nanoporous carbon fiber films. Reproduced with permission from ref 324. Copyright 2016 Wiley-VCH. Photographs of (c) PIL wetted filter paper, (d) the paper after carbonization at 400 °C, (e) bending test of the carbonaceous membrane paper, and (f) a carbonaceous strip cut from a carbonaceous membrane. (g) Bending test of the strip. (h) Plots of the tensile testing experiments of carbon membranes derived from a pure cellulose filter membrane (dotted line) and from a PIL-doped filter membrane (solid line). Reproduced with permission from ref 325. Copyright 2013 Royal Society of Chemistry. (i) Preparation procedure of HNDCMs. (j) Cross-section scanning electron microscopy (SEM) image of HNDCM-100000 calcined at 1000 °C. (k) SEM image of the cross section of HNDCM-250000 calcined at 1000 °C; the scale bars in parts j and k are 20 μm . (l–n) High-magnification images of part k. The scale bars represent 500 nm. Reproduced with permission from ref 146, licensed under CC BY.

2360 carbonization, these as-spun nanofibers were first stabilized at
 2361 270–300 °C for 1 h in air and then pyrolyzed at 800, 1000,
 2362 1200, and 1600 °C for 1 h under nitrogen. During thermal
 2363 treatment, the core component burned out, and linear PAN
 2364 molecules could be transformed into ladder structures and
 2365 then further carbonized into N-doped hollow carbon fibers.
 2366 The large continuous central porous structure in the N-doped
 2367 hollow carbon fibers facilitates the penetration of Li^+ -carrying
 2368 electrolyte into the inner part of the carbon fibers, thus
 2369 promoting the full use of the active lithium-storage part and
 2370 improving the performance of the lithium battery.

2371 Apart from the electrospinning technique, porous carbon
 2372 tubes were also achieved in the laboratory by template
 2373 methods. For example, heteroatom-doped carbon nanotubes
 2374 can be produced using anodic aluminum oxide (AAO)
 2375 membranes (200 nm in channel size) as hard templates. The
 2376 inner channel of AAO was filled with a heteroatom-rich
 2377 polymeric solution driven by capillary force, where a thin
 2378 polymeric coating layer formed upon evaporation of the
 2379 solvent. The thickness of the coating layer could be fine-tuned
 2380 by the polymer concentration. The polymer tubes on the walls
 2381 of AAO were then carbonized into heteroatom-doped carbon
 2382 nanotubes. Furthermore, by introducing a second inorganic
 2383 template into the AAO channels, hierarchical porous carbon
 2384 tubes could be obtained after removal of the template. For
 2385 instance, Yang's group constructed a sphere-in-tube structure
 2386 by using AAO and SiO_2 nanoparticles as co-templates, where
 2387 hollow carbon spheres were encapsulated in a carbon nanotube
 2388 (HCSs@CT) after removal of the AAO and SiO_2 nano-
 2389 particles.³⁰⁷ In their approach, confined assembly of SiO_2
 2390 nanoparticles in the channels of AAO generated a SiO_2 @

AAO co-template for subsequent filling with polypyrrole,
 followed by carbonization and template removal to form N-
 doped HCSs@CT (Figure 34d–f). At the same time, Zhang's
 group similarly prepared porous carbon tubes as cathode
 materials for Li–S batteries.³⁰⁸ This novel architecture
 combines several merits for electrode application: (1)
 optimized utilization of the carbon nanotube intracavity to
 improve S_{BET} ; (2) a hierarchical porous structure (micro/
 meso/macropores) for rapid electrolyte access; (3) a high
 charge transport capability; and (4) a N doping effect result-
 ing from the N-rich carbon precursor. In this context, heteroatom-
 doped carbon materials with such architectures function not
 only in lithium batteries but also in supercapacitors due to
 their high surface area, well-defined porous structures, good
 electrical conductivity, and long-term stability.

4.3. Heteroatom-Doped Porous Carbon Thin Films and Membranes

Porous carbon films and membranes with large sizes are highly
 valued, especially for electronics and electrochemical applica-
 tions, catalysis, separation, and purification, due to their
 structural integrity, continuity, and purity.³⁰⁹ Such applica-
 tions require carbon materials with a large and easily accessible
 surface. Additional requirements could be good conductivity,
 efficient mass transport of chemical species to and from the
 surface, or the capability to deform through bending, buckling,
 twisting, rotation, and so on. In this regard, a well-defined
 porous structure should be taken into account. To date, porous
 carbon membranes have been synthesized *via* different
 methods, including pyrolysis of block copolymer–colloidal
 silica hybrids and direct carbonization of self-assembled

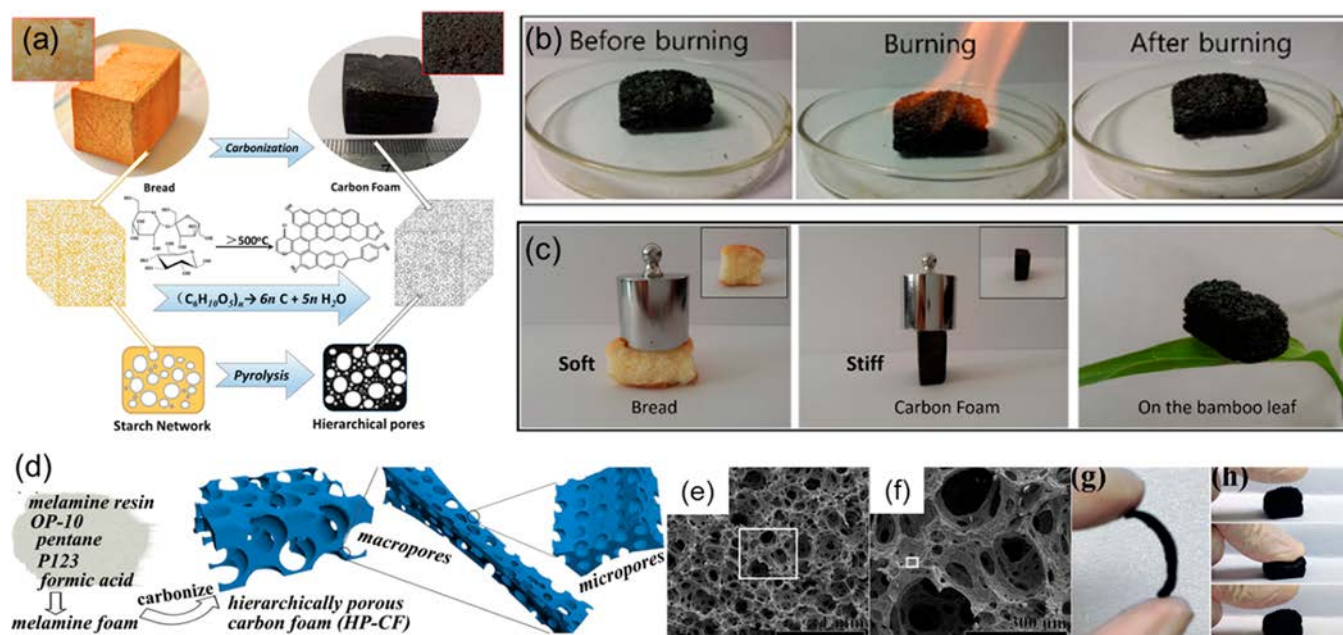


Figure 36. (a) Schematic illustration of porous carbon foams derived from bread. (b) Photographs illustrating the mechanical properties and light weight of the carbon foams. (c) Photographs illustrating the thermal stability of the carbon foams. Reproduced with permission from ref 338. Copyright 2016 American Chemical Society. (d) Synthetic route toward porous carbon foams using P123 as a soft template. (e, f) SEM images of the porous carbon foams. (g, h) Photograph illustrating the mechanical strength of the porous carbon foams. Reproduced with permission from ref 340. Copyright 2016 Elsevier.

2420 heteroatom-rich polymer films and electrospun fiber-based
2421 polymer films.^{310,311}

2422 Porous carbon films derived from carbon fibers are indeed
2423 widely applied in catalysis,^{312–316} energy storage,^{301,317–319}
2424 separation,^{320–323} and so forth. Owing to the interconnected
2425 fiber network, these carbon films are composed of numerous
2426 macropores, which facilitate mass diffusion but also enable a
2427 sponge-like elasticity. For example, Yao et al. prepared
2428 nanoporous carbon fiber films by direct carbonization of an
2429 electrospun polyimide (PI) film under Ar (Figure 35a).³²⁴ Due
2430 to the highly aromatic nature of PI, the structural integrity of
2431 the polymer films was largely maintained during carbonization.
2432 In addition, the as-obtained carbon films were flexible with an
2433 electrical conductivity of 147 S cm^{-1} and as such are useful in
2434 wearable devices (Figure 35b).

2435 As mentioned in the previous section, precursors to be
2436 carbonized in high mass yields and under structural
2437 preservation are rather limited to only a few polymers, which
2438 significantly hinders broader applications. To this end, Yuan et
2439 al. utilized ILs/PILs as efficient carbonization/activation
2440 coating agents to promote the co-conversion of diverse
2441 biopolymers.³²⁵ For example, commercially available cellulose
2442 filter membranes can be coated with ILs/PILs and are then
2443 sufficiently stable to undergo carbonization to form carbon
2444 membranes. Remarkably, such hybrid polymer carbon
2445 membranes display outstanding flexibility and high thermal
2446 stability (Figure 35c–h). Moreover, the introduction of N
2447 atoms by the IL/PIL coating significantly improves the
2448 oxidation stability of the final carbon membranes.

2449 In addition to fiber-based carbon films, a series of
2450 hierarchically structured porous carbon films/membranes
2451 have been synthesized *via* different techniques. For instance,
2452 Muench and co-workers synthesized hierarchically porous N-
2453 doped carbon membranes featuring continuously organized
2454 macro- and mesopore channels.³²⁶ This was achieved by

2455 pyrolysis of ion-track-etched polyimide. In another example,
2456 Wang and co-workers developed a bottom-up approach for the
2457 fabrication of N-doped, hierarchically structured, graphitic
2458 nanoporous carbon membranes (termed HNDICMs) through
2459 morphology retaining carbonization of a porous PIL
2460 membrane as a sacrificial template and a N/C precursor
2461 (Figure 35i–n).¹⁴⁶ Assembly of the polymeric precursor
2462 occurred directly by interpolyelectrolyte complexation between
2463 the cationic PIL and anionic neutralized poly(acrylic acid)
2464 (PAA), thus resulting in parental porous polymer membranes.
2465 In particular, the obtained carbon membrane exhibited an
2466 unusual single-crystal-like carbon orientation in the wall and a
2467 gradient size distribution of the pores along the membrane
2468 cross-section. Moreover, the N-doped nanoporous carbon
2469 membranes could be loaded with cobalt nanoparticles and
2470 function as an active carbon-based bifunctional electrocatalyst
2471 for overall water splitting. This promising strategy was then
2472 extended as a scalable synthetic approach for multiheteroatom-
2473 doped porous carbon membranes and applied for photo-
2474 thermal conversion in seawater desalination.¹⁷³

2475 Considering the diverse structures of PILs, it has been
2476 demonstrated that taking PIL-based assemblies as precursors
2477 to manufacture heteroatom-doped porous carbon membranes
2478 is promising. These membranes have already exhibited
2479 advantages over their powdery counterparts in electrocatalytic
2480 fields because they can be directly employed in devices,
2481 avoiding the use of binders and powder grain surface
2482 polarization.

4.4. Heteroatom-Doped Porous Carbon Foams and Monoliths

2483 “Bulk” carbons, such as porous carbon foams and monoliths,
2484 have macroscopic 3D porous structures while being mechan-
2485 ically robust and can operate even under extreme conditions
2486 (high pressure or stress). Moreover, these 3D structured
2487

2488 carbons have a higher volume to take up guest molecules for
2489 capacity-limited real-life applications, such as energy stor-
2490 age,^{327–330} gas separation or storage,^{331,332} environmental
2491 remediation,^{333–337} and so forth.

2492 One of the most straightforward strategies for fabricating
2493 “bulk” porous carbon materials is direct carbonization of bulk
2494 biomass pieces. Li et al. prepared hierarchically nanoporous
2495 carbon foams by carbonization of (porous) bread (Figure
2496 36a).³³⁸ The porous architectures of carbon foam could be
2497 controlled by the amount of yeast and the strength of gluten.
2498 The carbon foam produced under optimized conditions
2499 exhibited an outstanding compressive strength of 3.6 MPa
2500 with a density of 0.29 g/cm⁻³, excellent thermal stability
2501 (Figure 36b,c), and a high S_{BET} value of 988 m²/g.
2502 Carbonization of biomass with PILs could also lead to 3D
2503 porous carbon foam. Yuan et al. prepared porous carbon foams
2504 by carbonization of natural cotton in the presence of PILs.³²⁵
2505 In this process, the PILs effectively preserved the overall
2506 morphology and microtexture of the cotton. These sponge-like
2507 carbon foams removed methylene blue and crystal violet
2508 quickly from their aqueous solutions.

2509 In addition to the construction of porous bulk carbons from
2510 biomass polymers, synthetic polymers are an alternative. For
2511 example, Lu et al. prepared porous carbon monoliths through
2512 the self-assembly of poly(benzoxazine-co-resol) with the soft
2513 template Pluronic F127 followed by thermal annealing.³³⁹ The
2514 as-obtained porous N-doped carbon monoliths displayed a
2515 hierarchical nanoporous architecture with an S_{BET} value of 670
2516 m² g⁻¹. Similarly, Wong et al. constructed N-doped hierarchi-
2517 cally porous carbon foams by direct carbonization of soft
2518 template (P123)-cast melamine foams (Figure 36d–f).³⁴⁰ In
2519 this process, the pyrolysis of P123 created micropores, while
2520 the macropores resulted from the release of volatiles at
2521 elevated temperatures. With an S_{BET} value of 1231 m² g⁻¹,
2522 these hierarchically porous carbon foams were flexible and
2523 compressible (Figure 36g,h).

2524 One of the most unique features of carbon foams and
2525 monoliths is their 3D morphology and mechanical robustness,
2526 which facilitates reusability for practical handling. This unusual
2527 behavior can be mainly attributed to the hierarchically porous
2528 structure; as polymer-derived carbon materials are usually
2529 brittle and can sustain little compressive deformation. To date,
2530 both experimental and theoretical analyses have indicated that
2531 hierarchically porous structures are critical for the mechanical
2532 properties.

5. PORE ENGINEERING IN HETEROATOM-DOPED CARBONS DERIVED FROM POLYMERS

2534 A key feature of activated carbons is their high surface area and
2535 pore structure, which increases the absorption capacity for
2536 guest molecules. In this regard, porosity plays a pivotal role in
2537 determining their material performance. The pore size
2538 distribution (micro-, meso-, and macropores and hierarchical
2539 pores) is an intrinsic characteristic that determines the surface
2540 area and mass transport capability beyond the outer
2541 morphology. In this section, we summarize strategies to
2542 engineer pores in heteroatom-doped carbons derived from
2543 polymers.

5.1. Control of Microporosity

2544 **5.1.1. Activation Approach to Construct Microporous**
2545 **Structures.** We discussed above that the usage of template
2546 methods and the intrinsic nature of precursors generally create

meso- and macropores in carbons.^{11,341} The micropores in
2547 carbons are usually formed by *in situ* activation during
2548 carbonization or postsynthetic activation by gases (mainly
2549 H₂O steam or CO₂) and alkalis, i.e., KOH.^{342–344} The first
2550 technique is activation by gases at elevated temperature, which
2551 is referred to as “physical activation”. The second technique is
2552 activation by heating the solid mixture of carbon and KOH or
2553 other chemicals in an inert atmosphere, which is known as
2554 “chemical activation”. It is industrially well established that the
2555 activation of carbon materials enhances their porosity and
2556 pore-related performance.
2557

Physical activation of nonporous or less porous carbon
2558 materials by CO₂ is well-known. Boudouard equilibrium
2559 between CO₂ and carbon produces CO gas at moderate
2560 (600 °C) to high (approximately 1000 °C) temperatures,
2561 which can be expressed as C + CO₂ = 2CO ($\Delta H = +159$ kJ/
2562 mol). Significant amounts of carbon are thereby lost. Note that
2563 the porosity is closely dependent on the activation temper-
2564 ature, degree of burnoff, and CO₂ flow rate. Apart from CO₂,
2565 activation gases such as water vapor³⁴⁵ and ammonia (NH₃)³⁴⁶
2566 are also popular in industry. Water vapor activation could lead
2567 to a large amount of micropores, accounting for 45–62% of
2568 the total surface area of carbons. This value is higher than that
2569 of CO₂-activated carbon but still lower than that of KOH-
2570 activated carbon. NH₃ activation is another efficient way to
2571 increase the S_{BET} value and pore volume, as well as the N
2572 content, of carbons. Note that NH₃ activation can generate
2573 extremely toxic HCN during the activation reaction and thus
2574 should be avoided in the laboratory.
2575

KOH is widely utilized to activate carbon material to create
2576 micropores. The activation can be performed by heating a
2577 physical mixture of carbon materials with solid KOH under N₂
2578 at a desired temperature (400–1000 °C). During this process,
2579 KOH first melts and dehydrates into potassium oxide (K₂O) at
2580 approximately 400 °C. K₂O is further reduced into intercalated
2581 K by carbon at higher temperatures. Therefore, the
2582 consumption of carbon during the reaction with K₂O and
2583 the intercalation of K into the graphitic stacks are considered
2584 the two major factors for developing microporosity and a
2585 higher S_{BET} . This simple yet powerful chemical is broadly
2586 employed in industry to construct well-defined micropores.
2587 The textural properties of the carbons can be greatly varied by
2588 tuning the quantity of KOH and the activation temperature.
2589 Generally, the micropore volume, S_{BET} , and total pore volume
2590 increase with increasing mass ratio of KOH/carbon or
2591 activation temperature. More KOH and a higher activation
2592 temperature can cause high carbon burnoff, which is
2593 undesirable from both economic and environmental perspec-
2594 tives. Therefore, the trade-off between S_{BET} and the carbon
2595 yield is usually considered.
2596

Similar to KOH activation, post-treatment or carbonization
2597 in the presence of NH₃ could also lead to microporosity and
2598 favorable *in situ* N doping. As mentioned in the previous
2599 section, NH₃ will decompose into various radical species at
2600 high temperature, which effectively etch the carbon framework
2601 and create defects and a microporous structure. At the same
2602 time, this process can also lead to *in situ* N doping. In an early
2603 study, Jaouen et al. activated pristine carbons in the presence of
2604 NH₃.³⁴⁷ This process can simultaneously create micropores
2605 and N functionalities inside carbons. In another study, NH₃-
2606 pyrolyzed carbons displayed remarkable ORR activity
2607 compared to Ar-pyrolyzed carbons, which was attributed to
2608 their highly basic N functionalities and the existence of
2609

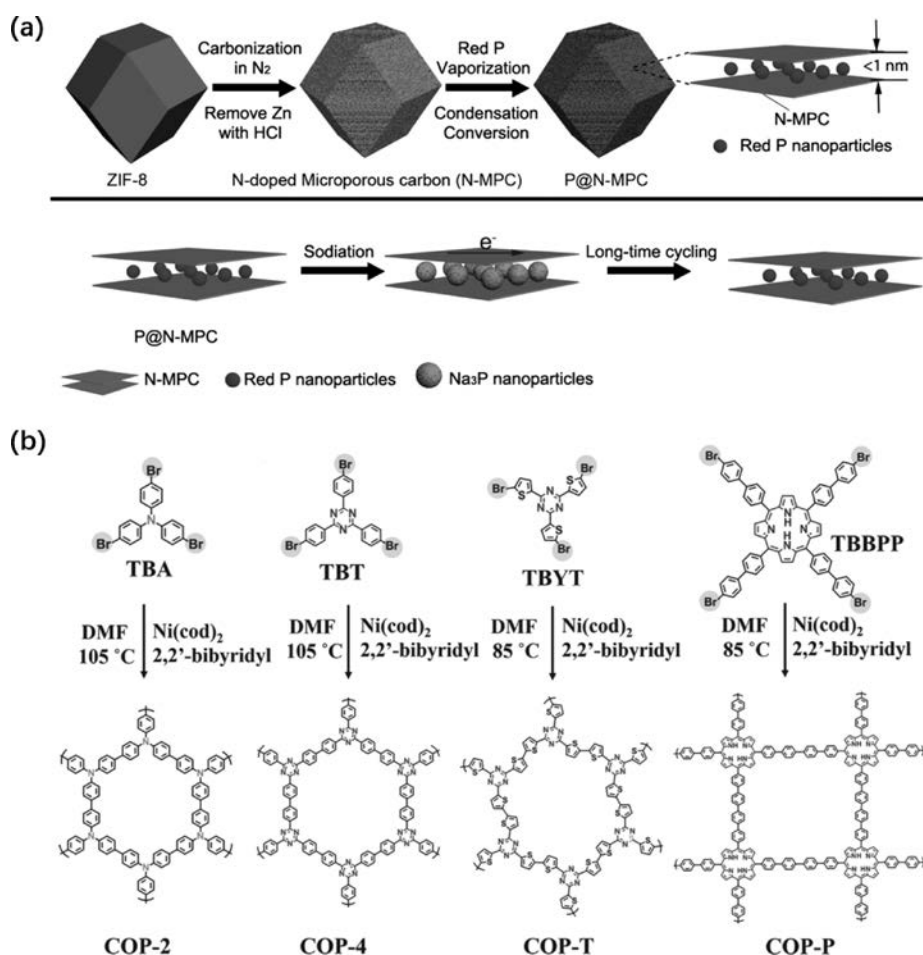


Figure 37. (a) Synthetic route toward microporous carbon materials derived from ZIF-8. Reproduced with permission from ref 356. Copyright 2017 Wiley-VCH. (b) Schematic diagram of the synthesis of COPs as carbonaceous precursors. Reproduced with permission from ref 358. Copyright 2014 Wiley-VCH.

porphyrin-like FeN₄C₁₂ moieties.³⁴⁸ Mukerjee et al. utilized a similar approach to activate carbon materials.³⁴⁹ During heat treatment with NH₃, the remaining amorphous carbons were etched, and N functionalities were doped into the carbon scaffold. Other examples have also been reported, and improvements in various catalytic performances were observed.^{350,351} This strategy, compared to KOH activation, is less corrosive.

To bypass the dilemma of using corrosive agents, the “salt templating” strategy was recently developed as an alternative solution to produce porous carbon materials with more micropores and small mesopores. As an example, Antonietti et al. employed different eutectic mixtures as a porogen in combination with an ionic liquid as a carbon source to construct porous materials with high surface areas ranging from 1000 to 2000 m² g⁻¹.¹¹⁸ The porogen salts included eutectic LiCl/ZnCl₂ (*S_m* 294 °C), NaCl/ZnCl₂ (*S_m* 270 °C), and KCl/ZnCl₂ (*S_m* 230 °C), which can be recovered for further use, rendering sustainable salt recycling. Similarly, Matyjaszewski and colleagues utilized an aqueous solution of low molecular weight PAN and ZnCl₂ as a template and effectively functionalized various carbonaceous materials. By templating in the presence of SiO₂, nanoporous carbons with a high *S_{BET}* up to 1776 m² g⁻¹ were reported.³⁵² Other examples, such as utilizing potassium oxalate,³⁵³ molten KCl,³⁵⁴ and molten ZnCl₂³⁵⁵ to endow carbon materials with micro-

porosity have also been presented. These methods are highly effective yet less corrosive, meaning that the overall morphology and functionality of the materials could be well retained after carbonization, especially compared to the rather destructive KOH activation.

5.1.2. Utilization of the Polymeric Structure and Composition to Construct Microporous Structures. A straightforward strategy to effectively construct a microporous architecture in carbon without losing too much material is desirable. The utilization of microporous polymeric structures to construct microporous carbons is one of the most commonly used methods. In particular, direct pyrolysis of organic frameworks (MOFs, COFs, or COPs) to produce porous carbons has recently stimulated much interest because their intrinsic micropores could be partially retained during carbonization. In addition, these organic polymeric frameworks usually contain a high content of heteroatoms, which simultaneously functionalize the product upon carbonization. For example, Yu et al. prepared P-doped microporous carbon by direct pyrolysis of ZIF-8 followed by encapsulation of red P into the microporous carbon (Figure 37a). The textural morphology of the MOF was well preserved after the carbonization process, and a polyhedron-like carbon material was isolated.³⁵⁶ After the removal of metallic Zn with HCl washing, the *S_{BET}* value of the polyhedron-like carbon reached 1135.1 m² g⁻¹ with a uniform narrow pore size distribution of

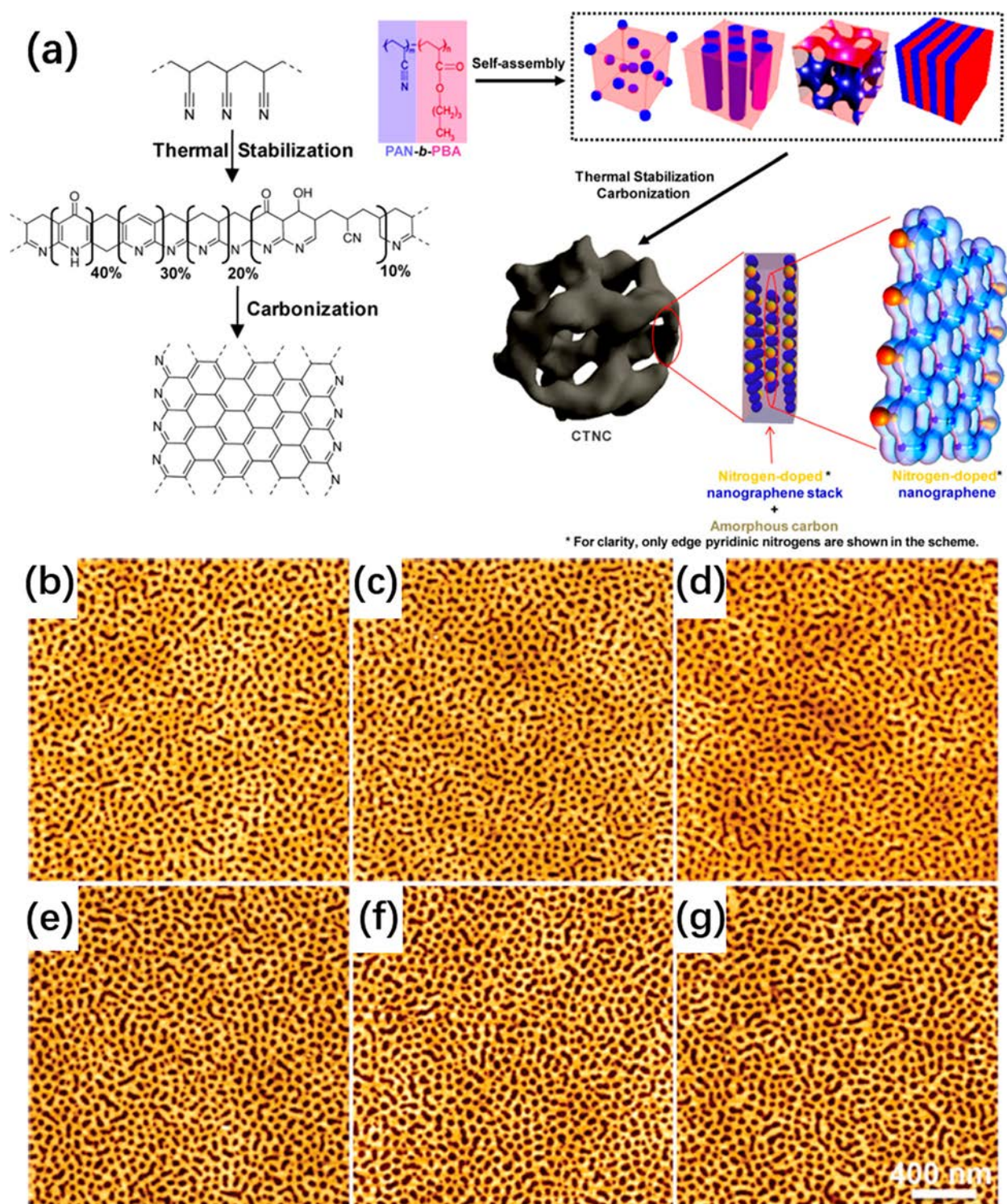


Figure 38. (a) Synthetic route toward N-doped nanoporous carbons from phase-separated block copolymers. Reproduced with permission from ref 73. Copyright 2012 American Chemical Society. AFM height images of PAN-*b*-PMMA-derived mesoporous carbon thin film after thermal annealing at (b) 100 °C, (c) 140 °C, (d) 180 °C, (e) 220 °C, (f) 260 °C, and (g) 300 °C for 1 h before carbonization. Reproduced with permission from ref 369. Copyright 2017 Wiley-VCH.

approximately 0.5 nm. Such microporous architectures are favorable for the diffusion of guest molecules. Similarly, Park and colleagues presented the synthesis of highly porous carbons derived from a MOF with a narrow pore size centered at 1.3 nm.³⁵⁷ These microporous carbons exhibited BET specific surface areas as high as 3447 m² g⁻¹ and showed great promise in H₂ storage. Despite the great potential of MOFs in

the synthesis of N-doped porous carbons, we will not expand upon this area in this Review, as, strictly speaking, MOFs as a rising group of carbon precursors are not directly related to polymers.

In addition to MOFs, Dai et al. specifically designed and synthesized a series of COPs with different N distributions and hole sizes (Figure 37b).³⁵⁸ The subsequent carbonization of

these COPs created well-controlled N-doped holey graphitic carbon materials with average pore sizes below 1 nm. Similarly, Shiraki et al. constructed microporous N-doped carbons by direct carbonization of COFs with an azine-linked 2D molecular network.³⁵⁹ Interestingly, the carbonized COFs displayed a higher S_{BET} value ($1596 \text{ m}^2 \text{ g}^{-1}$) than pristine COFs ($1168 \text{ m}^2 \text{ g}^{-1}$). The pore size was found to be reduced from 0.97 to 0.68 nm after carbonization, indicating partial shrinkage of the porous structure during the carbonization process. Recently, Bai and colleagues utilized a thermally stable covalent triazine framework and constructed a microporous carbon nitride-like material through direct carbonization.³⁶⁰ Remarkably, the as-obtained carbon nitride displayed a uniform pore size distribution of approximately 0.5 nm and a maximum surface area of $401 \text{ m}^2 \text{ g}^{-1}$. These examples prove that carbonization of predesigned microporous precursors is a valid method to directly prepare microporous carbons.

Composition engineering is another effective strategy to construct microporosity inside carbons. Previously, Dai et al. demonstrated that, by engineering the counteranion of an ionic liquid, well-developed microporous structures can be achieved without using either templates or activating agents.³⁶¹ In this regard, by carefully tailoring the composition of PILs with certain anions, e.g., bis(trifluoromethane sulfonyl)imide (TFSI), Yuan et al. demonstrated that direct pyrolysis of poly(3-cyanomethyl-1-vinylimidazolium TFSI) can effectively afford microporous N-doped carbons.¹⁴⁵ Remarkably, micropores of the size of the counterion were dominant, coexisting with only a small amount of mesopores less than 5 nm, while mesopores larger than 5 nm and macropores were essentially absent. It is believed that the bulky counteranion TFSI was aggregated and evaporated in protonated form during carbonization, thereby creating micropores in the carbons. This feature was particularly important because the polymeric cation could be utilized as both carbon and heteroatom sources, while the counteranion could simultaneously act as a molecular template of sufficient size. Taking advantage of the ionic nature of PILs, Wang et al. utilized electrostatic cross-linking of the cation of PILs with poly(acrylic acid) and constructed porous PIL membranes.¹⁴⁶ The subsequent carbonization ultimately led to hierarchical N-doped porous carbon membranes. Notably, the large macroporous structure was constructed by electrostatic cross-linking, while the micropores were simultaneously derived from the counteranion TFSI upon carbonization. Moreover, these PILs could be used as activating agents to create micropores in various carbonaceous species upon carbonization. Wang et al. utilized PILs as surface active agents and effectively constructed nanoporous N-doped carbon materials with S_{BET} up to $496 \text{ m}^2 \text{ g}^{-1}$ by hydrothermal carbonization.³⁶² Without PIL additives, the as-obtained carbons showed small S_{BET} and were basically nonporous. Similarly, PILs could also be utilized to activate already condensed carbon materials. Yuan et al. prepared N-doped nanoporous carbon composites by incorporating PILs and carbon nitride as precursors.³⁶³ Remarkably, the carbon nitride became highly porous, and the S_{BET} was boosted up to $1120 \text{ m}^2 \text{ g}^{-1}$ with the addition of PILs.

Utilizing the polymeric structure and composition to directly obtain carbon materials with microporous structures is efficient and avoids the drawbacks of the other techniques discussed above. With their highly tunable chemical composition and surface activating nature, PILs have proven to be an especially promising carbonaceous precursor to build microporous

carbon materials with various morphologies. More importantly, these PILs are by their construction rich in heteroatoms such as N, S, or P, which can in turn be incorporated into carbon materials without any postsynthetic treatment, providing a versatile platform to design microporous carbon materials with desirable heteroatom doping.

5.2. Control of Mesoporosity

One of the most fundamental characteristics of block copolymers is their ability to form versatile morphologies *via* phase separation in selective solvents. Especially, with different chemical compositions, a variety of beautiful mesostructures, such as cubes, cylinders, or lamellae, can be well constructed. In this regard, porous carbon materials derived from block copolymers are particularly interesting, as no activation steps or post-treatments are required, and a variety of carbon morphologies can be readily copied from the original block-copolymer-derived structures.

As previously demonstrated, Yamauchi and colleagues directly constructed N-doped mesoporous carbon spheres through self-polymerization of DA and spontaneous coassembly of diblock copolymer PS-*b*-PEO micelles.⁵⁶ The as-obtained carbon spheres displayed a remarkably uniform mesopore size of 16 nm. Similarly, Zhao et al. utilized the micelle fusion-aggregation assembly method and successfully constructed mesoporous carbon materials.³⁶⁴ Notably, by utilizing the phase separation of PS-*b*-PEO as a template, ordered mesoporous carbon materials with pore sizes ranging from 26.2 to 36.3 nm were rationally fabricated. This method is facile yet powerful for constructing mesoporous carbons with different morphologies with a narrow pore size. At the same time, other block copolymer templates, such as PS-*b*-PAA³⁶⁵ or poly(ethylene oxide-*b*-caprolactone) (PEO-*b*-PCL),³⁶⁶ are also possible.

In addition to thermally labile diblock copolymers, PAN-containing block copolymers are one of the most commonly used carbonaceous precursors for constructing organized N-doped mesoporous carbons. In 2012, Kowalewski et al. successfully fabricated N-doped mesoporous carbons by direct carbonization of the self-assembled block copolymer poly(*n*-butyl acrylate)-*b*-PAN (PBA-*b*-PAN).⁷³ In the carbonization process, the PAN chains underwent a cyclization reaction to form stable pyrazine ladder networks, while the thermally unstable PBA chains underwent thermolysis, leaving mesopores inside the carbon matrix (Figure 38a). Recently, the same groups also extended this method and fabricated mesoporous N/S-codoped carbons for supercapacitor applications.³⁶⁷ By carefully adjusting the length of PBA blocks, the mesoporous structures were found to be highly tunable with a narrow pore size distribution ranging from 5.6 to 21.7 nm in a surprisingly linear fashion. To construct more ordered mesoporous structures, Kim et al. utilized a prestabilization method and obtained N-doped mesoporous carbon materials with an S_{BET} value of $860 \text{ m}^2 \text{ g}^{-1}$ and an average mesopore size of 8.1 nm by carbonization of a PAN-*b*-PMMA block polymer.³⁶⁸ Interestingly, thermal stabilization at 250 °C prior to carbonization to stabilize the self-assembled structure was a prerequisite for successful preparation of the ordered mesopores; i.e., the polymer must be cross-linked before the template vanishes. Liu et al. further investigated the assembly behavior of PAN-*b*-PMMA during thermal and solvent annealing.³⁶⁹ Interestingly, as the thermal annealing temperature increased from 100 to 300 °C, the pore size increased by

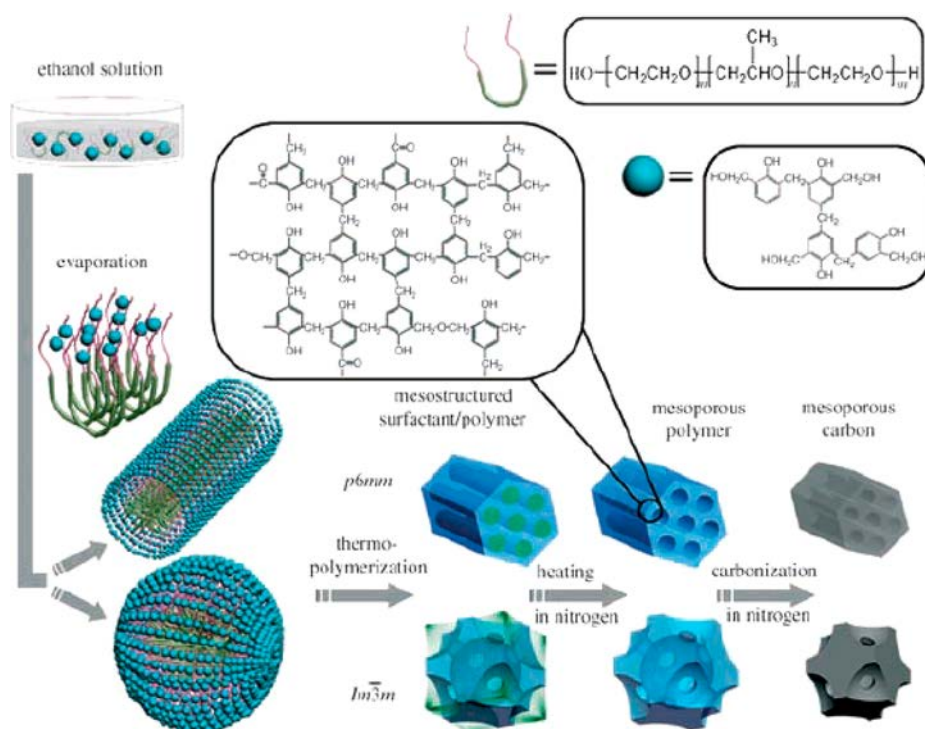


Figure 39. Schematic illustration of utilizing surfactants to construct different mesoporous polymers and corresponding carbon materials. Reproduced with permission from ref 53. Copyright 2005 Wiley-VCH.

approximately 25% (Figure 38b–g). At the same time, the pore size also varied as the solvent was changed from dimethyl sulfoxide to chloroform. Other examples of utilizing a thermal stabilization strategy prior to carbonization, such as PBA-*b*-PAN, were also recently presented by Matyjaszewski.^{370,371} These N-doped porous carbons displayed uniformly distributed mesopores and could be applied in various energy storage applications.

In another example, Zhao et al. prepared ordered mesoporous polymers by solvent-induced self-assembly of amphiphilic triblock copolymers with phenol and formaldehyde resin as building blocks (Figure 39).⁵³ The resin contained a large number of hydroxyl groups, which could interact strongly with the triblock copolymers through the formation of hydrogen bonds. These features made the polymers particularly stable and permitted direct transformation into homologous carbon frameworks upon carbonization. Interestingly, by simply changing the concentration of surfactants, 2D hexagonal (FDU-15) and 3D cubic (FDU-16) structures were obtained, while a lamellar mesostructure was prepared by P123. Further carbonization of precalcined polymers led to mesoporous carbons with a slight shrinkage of the carbon network. The S_{BET} value of the carbon materials derived from FDU-15 and FDU-16 at 900 °C was found to be 968 and 778 $\text{m}^2 \text{g}^{-1}$ with narrow pore size distributions around 2.9 and 3.7 nm, respectively.

5.3. Control of Macroporosity

Compared to the active pursuit of micro/mesopores in carbon materials, macropores are generally less studied because they generally contribute less to the surface area. However, creating macropores in carbon materials is sometimes needed for enhancing mass transport in specific applications. This point was detailed in Sung et al.'s work, as they systematically investigated the specific relationship between macroporous and

micro/mesoporous carbon materials in the ORR by electrochemical analysis.³⁷² According to their electrochemical measurements, the macroporosity greatly enhanced the mass transport efficiency, and the interplay between micro/mesoporosity and macroporosity should be considered in the design of active-site-laden carbon materials.

One effective strategy to construct macropores is to use large-sized (>50 nm) templates, which could either be hard or soft. Inspiring works were reported by Stein's group using colloidal silica particles and silica gels as templates for the synthesis of ordered macroporous carbon.²⁷ A series of related approaches were developed in the following years. Yu et al. utilized polystyrene (PS) spheres and silica as nanocomposite templates to direct the polymerization of divinylbenzene.¹² The PS spheres in this case acted as a soft template, which could be readily removed by postsynthesis calcination to leave macroporous architectures. Satcher Jr. and Baumann prepared carbon aerogels with periodic macroporous architectures by utilizing a RF sol-gel solution as a carbon source along with PS spheres as a template.¹³ The sol-gel solution was infused into the interstitial voids of the PS sphere template with the assistance of a filtration technique. After the formation of the gel, the RF/PS composites were soaked in toluene to dissolve the PS template and further dried by supercritical CO_2 into an aerogel. This RF aerogel displayed hexagonally ordered domains of spherical cavities close to the size of the PS template. The RF aerogel was finally carbonized into a periodic macroporous monolith. In a recent study, PS spheres were directly mixed with precursors of N-doped carbon and carbonized into P-doped well-ordered 3D porous networks (Figure 40a).³⁷³ Tang et al. constructed hollow carbon spheres by utilizing colloidal PS spheres as sacrificial templates (Figure 40b,c). Upon carbonization at high temperature, the inner templates were thermally fragmented, leaving a N, P-codoped

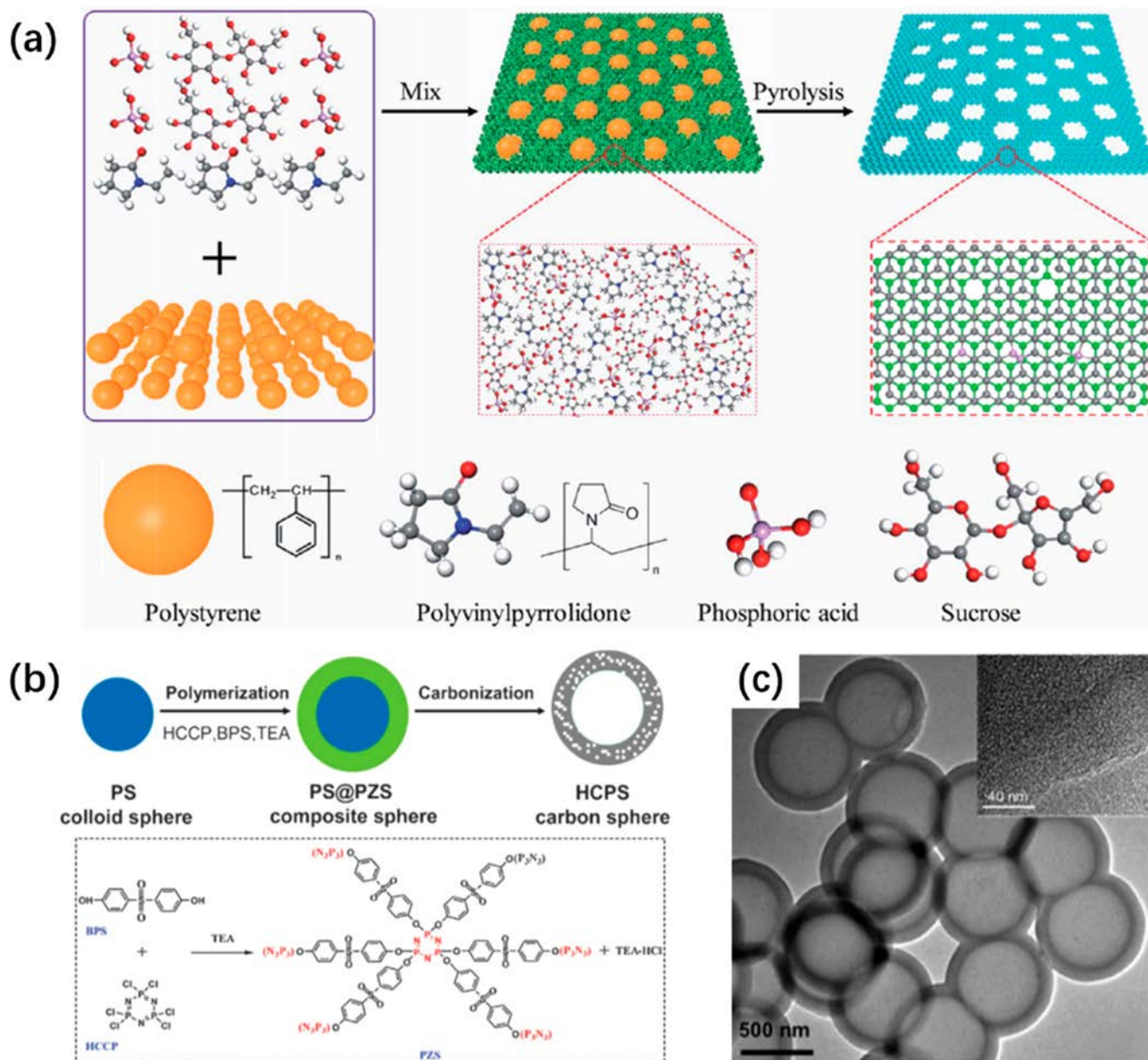


Figure 40. (a) Schematic illustration of the preparation of macroporous carbon aerogels utilizing PS spheres as a template. SEM images of the replicated RF aerogel before (b) and after (c) carbonization. Reproduced with permission from ref 373. Copyright 2019 Royal Society of Chemistry. (d) Schematic illustration of the preparation of hollow carbon spheres utilizing PS as a template. (e) Representative TEM images of hollow carbon spheres. The inset shows an HRTEM image of the carbon shell. Reproduced with permission from ref 374. Copyright 2010 Royal Society of Chemistry.

2867 carbon shell. More importantly, by adjusting the mass ratio of
2868 PS by a comonomer, the thickness of the shell could be
2869 rationally tailored.³⁷⁴

2870 PMMA nanospheres are excellent alternatives for construct-
2871 ing macroporous carbon materials because of their ease of
2872 preparation and low cost, as well as their ability to
2873 depolymerize completely at slightly elevated temperatures.
2874 Zhu et al. reported highly ordered macroporous N-doped
2875 carbon materials obtained by assembly and sequential
2876 carbonization of PMMA/PAN core-shell nanoparticles.³⁷⁵
2877 Prestabilization before the carbonization of the PMMA/PAN
2878 nanoparticles was important for the formation of the ordered
2879 macropore architectures, since the PAN molecule chains
2880 needed to be cross-linked and cyclized to form the carbon

2881 framework upon heating prior to the thermal decomposition of
2882 PMMA.

2883 In addition to templating methods, electrostatic cross-linking
2884 of polymers can establish macroporous structures. As
2885 previously demonstrated, the electrostatically cross-linked
2886 PIL membranes displayed porous architectures, in which the
2887 size of the macropores was closely related to the cross-link
2888 density. Recently, Wang et al. demonstrated that the
2889 macropore size could also be regulated by the diffusion rate
2890 of NH_3 solution.¹⁷³ Generally, as the hydrophilicity of the PIL
2891 increased, the diffusion rate of NH_3 solution into the PIL-
2892 containing polymeric blend was enhanced. As a result, the
2893 accelerated infiltration of NH_3 solution induced fast, poorly
2894 regulated phase separation, forming irregular large macropores.

2895 On the other hand, increasing the hydrophobicity of PILs
2896 effectively lowered the diffusion rate of NH_3 solution, and
2897 much smaller pores were formed. Upon vacuum carbonization,
2898 these macroporous structures were well retained and trans-
2899 formed into hierarchically porous carbon membranes.

2900 Dai and Liang demonstrated a spinodal polymer decom-
2901 position strategy to manufacture bicontinuous macroporous
2902 carbon.³⁷⁶ They synthesized polymer rods by assembly of
2903 phloroglucinol/formaldehyde copolymer and triblock copoly-
2904 mer F127 under various reaction conditions. The as-obtained
2905 polymer rods further underwent carbonization to form a
2906 bimodal meso/macroporous carbon monolith. With carefully
2907 designed preparation conditions (concentration, temperature,
2908 etc.), the pore architectures of the final carbon can be
2909 rationally tailored.

6. CONCLUSION

2910 Porous carbons are one of the major research areas of materials
2911 science. This comprehensive Review discusses porous carbons
2912 that are derived either partially or exclusively from polymers
2913 and are simultaneously doped with heteroatom(s). One of the
2914 most important properties of such porous carbon materials is
2915 their large porosity and high specific surface area, which has led
2916 to many applications ranging from adsorption/separation to
2917 fire protection, energy management, and catalysis. Both
2918 template-based and template-free strategies are utilized for
2919 controlling the porosity and pore shape of carbons. Because of
2920 the multifarious hard templates and their easily tunable surface
2921 functionality, size, and porosity, the hard template method is
2922 popular for replicating HPCMs with a range of desirable
2923 ordered porous structures. However, a major drawback
2924 associated with this approach lies in the multistep synthesis
2925 and the involvement of etching chemicals to remove the
2926 template, which is generally considered a time/labor-intensive
2927 process inhibiting technical scale-up. The soft template method
2928 is straightforward and less time/work-demanding in terms of
2929 the template removal process at the expense of less precise
2930 control of the porous structure and morphology at the nano/
2931 microscale. The direct carbonization of pristine polymers
2932 without an external template is preferred for large-scale
2933 production of HPCMs, where, typically, the required control
2934 of the porous structure is less important for their applications.
2935 Note that polymers in the direct carbonization method may
2936 have a part of their molecular structure used as an internal
2937 template. For example, ion clusters formed by ionic polymers
2938 can serve as progens to produce micropores or small
2939 mesopores in HPCMs.

2940 It has been well-established in the carbon materials
2941 community that heteroatom doping is a promising strategy
2942 to selectively modulate the physicochemical properties of
2943 HPCMs and endow them with targeted catalytic activities. At
2944 the beginning of section 3, we interpreted in detail the
2945 techniques utilized to characterize HPCMs to help illustrate
2946 how to determine their structures down to an atomic level.
2947 Nitrogen-doped porous carbon materials first came into the
2948 view of researchers in the 1980s and sparked wider interest in
2949 2009 with the discovery of the unusual activity of N-doped
2950 carbon nanotubes for the ORR. Meanwhile, recent studies
2951 demonstrated that codoping of two or more heteroatoms in
2952 carbon frameworks could endow HPCMs with structural
2953 synergy, showing great promise for the field of electrocatalysis
2954 in general. Codoping is much less studied and understood than
2955 single-heteroatom doping in the porous carbon field due to its

complexity. It is believed that, by pairing judicious polymeric
precursor choices with appropriate polymer processing
techniques, desirable HPCMs can be readily fabricated to
contribute to efforts to mitigate the current energy and
environmental issues.

Because the morphology of HPCMs plays an essential role
in determining their application spectrum, studies have been
devoted to controlling the local architectures. By employing
template methods and rich polymer processing tools, HPCMs
in the form of spheres, fibers, sheets, and membranes were
created as functional materials for the adsorption/separation
and energy conversion fields. In this regard, considering that
many applications of HPCMs are currently centered around
the energy-related electrocatalysis field, fibers or membranes of
HPCMs might be prioritized, since they can be directly utilized
as electrodes without the traditionally complicated processing
of powdery carbocatalysts for gluing by electronically insulating
polymeric binders. The challenges lie in their scalable
fabrication with robust electrochemical and mechanical
stability and flexibility.

It is necessary to state that the selection of polymers is
crucial in determining the local binding properties of the final
carbons. For example, the pyrolysis of PAN and cellulose at
1000 °C only leads to amorphous or poorly crystalline carbons,
while carbonization of PILs at 1000 °C readily produces
heteroatom-doped carbons with medium-to-high yields, and
their atomic structure has a particularly high short-range order,
which is needed for improving their conductive properties,
bringing about fire-retardant properties as well as catalytic
activity.

Currently, the state-of-the-art research on HPCMs is
application-oriented and covers the adsorption/separation,
catalysis, and energy conversion fields. We believe that the
use of HPCMs could be easily expanded into other fields, e.g.,
water purification and electrosynthesis of valuable organics, as
well as to “smart” actuators and flexible electronics, by careful
design of their structures at all scales. Furthermore, utilizing
polymers as carbonization precursors enables more compli-
cated carbon morphologies to be achieved, such as anisotropic,
hierarchical, and chiral carbons, to name a few. These
morphologies are usually hard to obtain by other polymer-
free methods. By carefully engineering the composition of
polymers, it is also possible to systematically manipulate the
electronic structures of the resulting carbons. Recent advance-
ments in controlling electronic structures, including *via* SACs,
Mott–Schottky effects, or even FLP chemistry, are all possible
by utilizing predesigned polymers as carbon precursors.
Therefore, we encourage researchers to further explore this
exciting field, discover more interesting carbon materials, and
hunt for their novel applications.

AUTHOR INFORMATION

Corresponding Authors

Hong Wang – Key Laboratory of Functional Polymer Materials
(Ministry of Education), Institute of Polymer Chemistry, College
of Chemistry, Nankai University, Tianjin 300071, P. R. China;
orcid.org/0000-0003-4260-3734; Email: 017155@nankai.edu.cn

Jiayin Yuan – Department of Materials and Environmental
Chemistry, Stockholm University, 10691 Stockholm, Sweden;
orcid.org/0000-0003-1016-5135; Email: jiayin.yuan@mink.su.se

3017 **Authors**

3018 **Yue Shao** – *Key Laboratory of Functional Polymer Materials*
3019 *(Ministry of Education), Institute of Polymer Chemistry, College*
3020 *of Chemistry, Nankai University, Tianjin 300071, P. R. China*

3021 **Shilin Mei** – *Department for Electrochemical Energy Storage,*
3022 *Helmholtz-Zentrum Berlin für Materialien und Energie, 14109*
3023 *Berlin, Germany*

3024 **Yan Lu** – *Department for Electrochemical Energy Storage,*
3025 *Helmholtz-Zentrum Berlin für Materialien und Energie, 14109*
3026 *Berlin, Germany; Institute of Chemistry, University of Potsdam,*
3027 *14476 Potsdam, Germany*

3028 **Miao Zhang** – *Department of Materials and Environmental*
3029 *Chemistry, Stockholm University, 10691 Stockholm, Sweden;*
3030 orcid.org/0000-0003-3582-6075

3031 **Jian-ke Sun** – *Department of Materials and Environmental*
3032 *Chemistry, Stockholm University, 10691 Stockholm, Sweden;*
3033 *School of Chemistry and Chemical Engineering, Beijing Institute*
3034 *of Technology, Beijing, P. R. China*

3035 **Krzysztof Matyjaszewski** – *Department of Chemistry, Carnegie*
3036 *Mellon University, Pittsburgh, Pennsylvania 15213, United*
3037 *States; orcid.org/0000-0003-1960-3402*

3038 **Markus Antonietti** – *Department of Colloid Chemistry, Max*
3039 *Planck Institute of Colloids and Interfaces, 14469 Potsdam,*
3040 *Germany; orcid.org/0000-0002-8395-7558*

3041 Complete contact information is available at:

3042 <https://pubs.acs.org/10.1021/acs.chemrev.0c00080>

3043 **Notes**

3044 The authors declare no competing financial interest.

3045 **Biographies**

3046 Hong Wang received his Ph.D. degree from the Lab of Advanced
3047 Materials, Fudan University, in 2013. After multiple research stays in
3048 Hong Kong University of Science and Technology (Hong Kong),
3049 King Abdullah University of Science and Technology (Kingdom of
3050 Saudi Arabia), Max Planck Institute of Colloids and Interfaces
3051 (Germany), and University of Toronto (Canada), he joined College
3052 of Chemistry, Nankai University, as a professor in China (2017). His
3053 current research is exclusively in the area of poly(ionic liquid)-based
3054 functional materials science.

3055 Yue Shao received his B.S. (Honours) in the Department of
3056 Chemistry at University of Prince Edward Island. After graduated,
3057 he worked under the supervision of Prof. Douglas Stephan at
3058 University of Toronto in frustrated Lewis pairs chemistry. Then, he
3059 continued his research under the supervision of Prof. Hong Wang at
3060 Nankai University on poly(ionic liquid)-derived functional materials.
3061 He is currently a master student under the supervision of Prof. Yang
3062 Zhenzhong at Tsinghua University, and his research interests focus on
3063 the design of soft Janus nanoparticles and their self-organized
3064 nanostructures.

3065 Shilin Mei received his B.S. and M.S. degrees in Chemistry from
3066 Renmin University, China, in 2009 and 2012, respectively, and
3067 completed his Ph.D. with Prof. Matthias Ballauff at Humboldt
3068 University of Berlin, Germany, in 2017. He joined the Department of
3069 Electrochemical Energy Storage, Helmholtz-Zentrum Berlin für
3070 Materialien und Energie GmbH, from 2017 to 2020 for his
3071 postdoctoral research on energy storage materials. His research
3072 interests focus on functional hybrid nanomaterials and energy storage.

3073 Yan Lu studied chemistry at Donghua University (China) in 1994.
3074 She received her M.Sc. from Donghua University in 2001. In 2005,
3075 she received her Ph.D. with summa cum laude under the supervision

of Prof. H.-J. P. Adler in macromolecular chemistry at the Dresden
University of Technology, Germany. After that, she worked first as
postdoctor then research scientist in Prof. Matthias Ballauff's group at
the University of Bayreuth. Since 2009, she joined the Helmholtz-
Zentrum Berlin für Materialien und Energie (HZB) as a group leader
in Colloid Chemistry. She received "Dr. Hermann-Schnell-Stipen-
dium" by the German Chemical Society (GDCh) in 2011. She was
selected as a top female researcher (W2/W3-Programme) in
Helmholtz Association in 2015. Since 2017, she has been a professor
in the Institute of Chemistry at the University of Potsdam. Since
2019, she is the head of the Department for Electrochemical Energy
Storage at HZB.

Miao Zhang received his B.S. degree from Jilin University, China, in
2012 and finished his Ph.D. at Tsinghua University, China, in 2016.
After 2 years of postdoctoral research on energy storage at Tsinghua
University, he joined the Department of Materials and Environmental
Chemistry, Stockholm University, for further postdoctoral research.
His current research interest is focused on polymer-based functional
materials for energy and environmental application.

Jian-ke Sun received his Ph.D. degree from the Fujian Institute of
Research on the Structure of Matter (FJIRSM), Chinese Academy of
Sciences, in 2012. Then, he worked as an assistant professor in
FJIRSM for one year. After research experience in National Institute
of Advanced Industrial Science and Technology (Japan), Max Planck
Institute of Colloids and Interfaces (Germany), IBS Center for Soft
and Living Matter (South Korea), and Stockholm University
(Sweden), he joined Beijing Institute of Technology (BIT) as a full
professor in China (2019). He is currently interested in development
of ionic porous materials and nanostructured composites.

Krzysztof (Kris) Matyjaszewski received his Ph.D. at Polish Academy
of Sciences in 1976. Since 1985, he has been J.C. Warner University
Professor of Natural Sciences at Carnegie Mellon University. In 1994,
he discovered Cu-mediated atom transfer radical polymerization,
commercialized in 2004 in US, Japan, and Europe to prepare various
advanced materials. His research is focused on synthesis of well-
defined macromolecules and hybrid materials via living and controlled
polymerizations using radical and ionic mechanisms to prepare
advanced materials for optoelectronic, biomedical, environmental, and
energy-related applications. He has coauthored >1100 publications,
coedited >24 books, and holds 62 US patents. He is the editor of
Progress in Polymer Science. He is a member of National Academy of
Engineering, National Academy of Sciences, National Academy of
Inventors, as well as Australian, Polish, and Russian Academies of
Sciences. He received 2017 Franklin Medal in Chemistry, 2015
Dreyfus Prize in Chemical Sciences, 2011 Wolf Prize in Chemistry,
2009 Presidential Green Chemistry Challenge Award, ACS Awards in
Chemistry of Materials (2019), Applied Polymer Science (2011) and
Polymer Chemistry (2002,) as well as 11 honorary degrees.

Markus Antonietti studied chemistry in Mainz, where he also received
his Ph.D. in 1985 and his Habilitation in 1990. Since 1993, he has
been the director of the Max Planck Institute of Colloids and
Interfaces and has worked in the field of functional materials for 30
years. He now works on modern materials chemistry, with sustainable
processes and materials being a central theme. Carbon and carbon-
nitrogen materials exert a special fascination to him. Besides being a
devoted chemist and a teacher of many senior academics, he is also a
passionate chef specialized in fusion cuisine and performs in a rock 'n'
roll band.

Jiayin Yuan received his Ph.D. from Universitaet Bayreuth Germany
in 2009 with Axel H. E. Müller. He joined the Max Planck Institute of
Colloids and Interfaces in Potsdam and served as a research group

3137 leader. He completed his Habilitation in 2015, and after a one year
3138 Associate Professor appointment at Clarkson University, USA, he has
3139 since December 2018 been a Full Professor at Stockholm University
3140 (Sweden). He received the European Research Council (ERC)
3141 Starting Grant in 2014, Dr. Hermann-Schnell Award in 2015, the
3142 Dozentenpreis from the Fund of Chemical Industry in 2016, and a
3143 Wallenberg Academy Fellowship from the Knut and Alice Wallenberg
3144 Foundation in 2017. He is a member of the Young Academy of
3145 Europe (YAE) and editorial advisor board member of Wiley
3146 Macromolecular journals and Applied Materials Today. He is the
3147 associate Editor of Nano Select. He has published 160+ papers and
3148 9000+ citations, with an H-index of 53.

3149 ACKNOWLEDGMENTS

3150 H.W. acknowledges the financial support from Nankai
3151 University, the National Science Foundation of China (No.
3152 21875119), the Natural Science Foundation of Tianjin
3153 (19JCYBJC17500), and the Fundamental Research Funds for
3154 the Central Universities, Nankai University (63201043). J.Y. is
3155 grateful for financial support from European Research Council
3156 (ERC) Starting Grant NAPOLI-639720, Swedish Research
3157 Council Grant 2018-05351, Dozentenpreis 15126 from
3158 Verband der Chemischen Industrie e.V. (VCI) in Germany,
3159 the Wallenberg Academy Fellow program (Grant KAW
3160 2017.0166) in Sweden, and the Stockholm University Strategic
3161 Fund SU FV-2.1.1-005. K.M. acknowledges the financial
3162 support from NSF grant DMR 1501324.

3163 REFERENCES

3164 (1) Paraknowitsch, J. P.; Thomas, A. Doping Carbons Beyond
3165 Nitrogen: An Overview of Advanced Heteroatom Doped Carbons
3166 With Boron, Sulphur and Phosphorus for Energy Applications. *Energy*
3167 *Environ. Sci.* **2013**, *6*, 2839–2855.
3168 (2) Gawande, M. B.; Fornasiero, P.; Zbořil, R. Carbon-Based Single-
3169 Atom Catalysts for Advanced Applications. *ACS Catal.* **2020**, *10*,
3170 2231–2259.
3171 (3) Zhao, D.; Zhuang, Z.; Cao, X.; Zhang, C.; Peng, Q.; Chen, C.;
3172 Li, Y. Atomic Site Electrocatalysts for Water Splitting, Oxygen
3173 Reduction and Selective Oxidation. *Chem. Soc. Rev.* **2020**, *49*, 2215–
3174 2264.
3175 (4) Zheng, B.; Lin, X.; Zhang, X.; Wu, D.; Matyjaszewski, K.
3176 Emerging Functional Porous Polymeric and Carbonaceous Materials
3177 for Environmental Treatment and Energy Storage. *Adv. Funct. Mater.*
3178 **2019**, *1907006*.
3179 (5) Zhou, Y. Q.; Sharma, S. K.; Peng, Z. L.; Leblanc, R. M. Polymers
3180 in Carbon Dots: A review. *Polymers* **2017**, *9*, 67–86.
3181 (6) Wood, K. N.; O'Hayre, R.; Pylpenko, S. Recent Progress on
3182 Nitrogen/Carbon Structures Designed for Use in Energy and
3183 Sustainability Applications. *Energy Environ. Sci.* **2014**, *7*, 1212–1249.
3184 (7) Gottlieb, E.; Matyjaszewski, K.; Kowalewski, T. Polymer-Based
3185 Synthetic Routes to Carbon-Based Metal-Free Catalysts. *Adv. Mater.*
3186 **2019**, *31*, 1804626.
3187 (8) Gottlieb, E.; Matyjaszewski, K.; Kowalewski, T. In *Carbon-Based*
3188 *Metal-Free Catalysts: Design and Applications*; Dai, L., Ed.; Wiley-VCH
3189 Verlag GmbH & Co. KGaA: 2018.
3190 (9) Ma, T. Y.; Liu, L.; Yuan, Z. Y. Direct Synthesis of Ordered
3191 Mesoporous Carbons. *Chem. Soc. Rev.* **2013**, *42*, 3977–4003.
3192 (10) Yang, W. P.; Li, X. X.; Li, Y.; Zhu, R. M.; Pang, H. Applications
3193 of Metal-Organic-Framework-Derived Carbon Materials. *Adv. Mater.*
3194 **2018**, *31*, 1804740.
3195 (11) Liang, C. D.; Li, Z. J.; Dai, S. Mesoporous Carbon Materials:
3196 Synthesis and Modification. *Angew. Chem., Int. Ed.* **2008**, *47*, 3696–
3197 3717.
3198 (12) Chai, G. S.; Shin, I. S.; Yu, J. S. Synthesis of Ordered, Uniform,
3199 Macroporous Carbons With Mesoporous Walls Templated by
3200 Aggregates of Polystyrene Spheres and Silica Particles for Use as

Catalyst Supports in Direct Methanol Fuel Cells. *Adv. Mater.* **2004**, *16*, 2057–2061. 3201
3202
(13) Baumann, T. F.; Satcher, J. H. Template-Directed Synthesis of
3203 Periodic Macroporous Organic and Carbon Aerogels. *J. Non-Cryst.* 3204
Solids **2004**, *350*, 120–125. 3205
(14) Wan, Y.; Shi, Y. F.; Zhao, D. Y. Supramolecular Aggregates as
3206 Templates: Ordered Mesoporous Polymers and Carbons. *Chem.* 3207
Mater. **2008**, *20*, 932–945. 3208
(15) Wan, Y.; Yang, H. F.; Zhao, D. Y. Host-Guest Chemistry in the
3209 Synthesis of Ordered Nonsiliceous Mesoporous Materials. *Acc. Chem.* 3210
Res. **2006**, *39*, 423–432. 3211
(16) Li, Z. J.; Jaroniec, M. Colloidal Imprinting: A Novel Approach
3212 to the Synthesis of Mesoporous Carbons. *J. Am. Chem. Soc.* **2001**, *123*, 3213
9208–9209. 3214
(17) Yoon, S. B.; Chai, G. S.; Kang, S. K.; Yu, J. S.; Gierszal, K. P.;
3215 Jaroniec, M. Graphitized Pitch-Based Carbons With Ordered
3216 Nanopores Synthesized by Using Colloidal Crystals as Templates. *J.* 3217
Am. Chem. Soc. **2005**, *127*, 4188–4189. 3218
(18) Jang, J.; Lim, B. Selective Fabrication of Carbon Nanocapsules
3219 and Mesocellular Foams by Surface-Modified Colloidal Silica
3220 Templating. *Adv. Mater.* **2002**, *14*, 1390–1393. 3221
(19) Kyotani, T.; Tsai, L. F.; Tomita, A. Preparation of Ultrafine
3222 Carbon Tubes in Nanochannels of an Anodic Aluminum Oxide Film.
3223 *Chem. Mater.* **1996**, *8*, 2109–2113. 3224
(20) Li, J.; Papadopoulos, C.; Xu, J. M.; Moskovits, M. Highly-
3225 Ordered Carbon Nanotube Arrays for Electronics Applications. *Appl.* 3226
Phys. Lett. **1999**, *75*, 367–369. 3227
(21) Lee, J.; Sohn, K.; Hyeon, T. Fabrication of Novel Mesocellular
3228 Carbon Foams With Uniform Ultralarge Mesopores. *J. Am. Chem. Soc.* 3229
2001, *123*, 5146–5147. 3230
(22) Oda, Y.; Fukuyama, K.; Nishikawa, K.; Namba, S.; Yoshitake,
3231 H.; Tatsumi, T. Mesocellular Foam Carbons: Aggregates of Hollow
3232 Carbon Spheres With Open and Closed Wall Structures. *Chem. Mater.* 3233
2004, *16*, 3860–3866. 3234
(23) Han, L.-N.; Wei, X.; Zhu, Q.-C.; Xu, S.-M.; Wang, K.-X.; Chen,
3235 J.-S. Nitrogen-Doped Carbon Nets With Micro/Mesoporous
3236 Structures as Electrodes for High-Performance Supercapacitors. *J.* 3237
Mater. Chem. A **2016**, *4*, 16698–16705. 3238
(24) Kyotani, T. Control of Pore Structure in Carbon. *Carbon* **2000**, 3239
38, 269–286. 3240
(25) Han, S. J.; Hyeon, T. Simple Silica-Particle Template Synthesis
3241 of Mesoporous Carbons. *Chem. Commun.* **1999**, 1955–1956. 3242
(26) Han, S. J.; Sohn, K.; Hyeon, T. Fabrication of New
3243 Nanoporous Carbons Through Silica Templates and Their
3244 Application to the Adsorption of Bulky Dyes. *Chem. Mater.* **2000**, 3245
12, 3337–3341. 3246
(27) Wang, Z. Y.; Li, F.; Ergang, N. S.; Stein, A. Effects of
3247 Hierarchical Architecture on Electronic and Mechanical Properties of
3248 Nanocast Monolithic Porous Carbons and Carbon-Carbon Nano-
3249 composites. *Chem. Mater.* **2006**, *18*, 5543–5553. 3250
(28) Han, S.; Lee, K. T.; Oh, S. M.; Hyeon, T. The Effect of Silica
3251 Template Structure on the Pore Structure of Mesoporous Carbons. 3252
Carbon **2003**, *41*, 1049–1056. 3253
(29) Lu, Y. F. Surfactant-Templated Mesoporous Materials: From
3254 Inorganic to Hybrid to Organic. *Angew. Chem., Int. Ed.* **2006**, *45*, 3255
7664–7667. 3256
(30) Liang, Y. R.; Liu, H.; Li, Z. H.; Fu, R. W.; Wu, D. C. In Situ
3257 Polydopamine Coating-Directed Synthesis of Nitrogen-Doped
3258 Ordered Nanoporous Carbons With Superior Performance in
3259 Supercapacitors. *J. Mater. Chem. A* **2013**, *1*, 15207–15211. 3260
(31) Yuan, D. S.; Zeng, F. L.; Yan, J.; Yuan, X. L.; Huang, X. J.; Zou,
3261 W. J. A Novel Route for Preparing Graphitic Ordered Mesoporous
3262 Carbon As Electrochemical Energy Storage Material. *RSC Adv.* **2013**, 3263
3, 5570–5576. 3264
(32) Gu, H.; Cao, D.; Wang, J.; Lu, X.; Li, Z.; Niu, C.; Wang, H. 3265
Micro-CaCO₃ Conformal Template Synthesis of Hierarchical Porous
3266 Carbon Bricks: As A Host For SnO₂ Nanoparticles With Superior
3267 Lithium Storage Performance. *Mater. Today Energy.* **2017**, *4*, 75–80. 3268

- 3269 (33) Chen, S.; Bi, J. Y.; Zhao, Y.; Yang, L. J.; Zhang, C.; Ma, Y. W.;
3270 Wu, Q.; Wang, X. Z.; Hu, Z. Nitrogen-Doped Carbon Nanocages as
3271 Efficient Metal-Free Electrocatlysts for Oxygen Reduction Reaction.
3272 *Adv. Mater.* **2012**, *24*, 5593–5597.
- 3273 (34) Fan, H.; Wang, Y.; Gao, F. J.; Yang, L. Q.; Liu, M.; Du, X.;
3274 Wang, P.; Yang, L. J.; Wu, Q.; Wang, X. Z.; Hu, Z. Hierarchical Sulfur
3275 and Nitrogen Co-Doped Carbon Nanocages as Efficient Bifunctional
3276 Oxygen Electrocatalysts for Rechargeable Zn-Air Battery. *J. Energy*
3277 *Chem.* **2019**, *34*, 64–71.
- 3278 (35) Ni, D.; Sun, W.; Wang, Z. H.; Bai, Y.; Lei, H. S.; Lai, X. H.;
3279 Sun, K. N. Heteroatom-Doped Mesoporous Hollow Carbon Spheres
3280 for Fast Sodium Storage With an Ultralong Cycle Life. *Adv. Energy*
3281 *Mater.* **2019**, *9*, 1900036.
- 3282 (36) Meng, X. J.; Xiao, F. S. Green Routes for Synthesis of Zeolites.
3283 *Chem. Rev.* **2014**, *114*, 1521–1543.
- 3284 (37) Zhang, A.; Qu, T.; Cao, S. B.; Li, Y. Y.; Zhao, Y. B.; Chen, A. H.
3285 Vapor-Phase Polymerization and Carbonization to Nitrogen-Doped
3286 Carbon Nanoscale Networks With Designable Pore Geometries
3287 Templated From Block Copolymers. *Adv. Mater. Interfaces* **2018**, *5*,
3288 1701390.
- 3289 (38) Li, W.; Zhao, D. Y. An Overview of the Synthesis of Ordered
3290 Mesoporous Materials. *Chem. Commun.* **2013**, *49*, 943–946.
- 3291 (39) Enterría, M.; Pereira, M. F. R.; Martins, J. I.; Figueiredo, J. L.
3292 Hydrothermal Functionalization of Ordered Mesoporous Carbons:
3293 The Effect of Boron on Supercapacitor Performance. *Carbon* **2015**,
3294 *95*, 72–83.
- 3295 (40) Wan, Y.; Zhao, D. Y. On the Controllable Soft-Templating
3296 Approach to Mesoporous Silicates. *Chem. Rev.* **2007**, *107*, 2821–
3297 2860.
- 3298 (41) Hassan, M.; Wu, D. D.; Song, X. D.; Qiu, W. W.; Mao, Q.; Ren,
3299 S. Z.; Hao, C. Polyaniline-Derived Metal-free Hollow Nitrogen-
3300 Doped Carbon Microspheres as an Efficient Electrocatalyst for
3301 Supercapacitors and Oxygen Reduction. *J. Electroanal. Chem.* **2018**,
3302 *829*, 157–167.
- 3303 (42) Kowalewski, T.; Tsarevsky, N. V.; Matyjaszewski, K. Nano-
3304 structured Carbon Arrays from Block Copolymers of Polyacrylonitrile.
3305 *J. Am. Chem. Soc.* **2002**, *124*, 10632–10633.
- 3306 (43) Zhong, M. J.; Kowalewski, T.; Matyjaszewski, K. Block
3307 Copolymer Templated Nitrogen-Enriched Porous Nanocarbons:
3308 From Synthesis, Characterization, to Applications. *Chem. Abstr.*
3309 **2013**, 245.
- 3310 (44) Zhou, Z. P.; Liu, T. Y.; Khan, A. U.; Liu, G. L. Block
3311 Copolymer-Based Porous Carbon Fibers. *Sci. Adv.* **2019**, *5*, eaau6852.
- 3312 (45) Bates, F. S.; Fredrickson, G. H. Block Copolymers-Designer
3313 Soft Materials. *Phys. Today* **1999**, *52*, 32–38.
- 3314 (46) Bockstaller, M. R.; Thomas, E. L. Proximity Effects in Self-
3315 Organized Binary Particle-Block Copolymer Blends. *Phys. Rev. Lett.*
3316 **2004**, *93*, 166106.
- 3317 (47) Templin, M.; Franck, A.; DuChesne, A.; Leist, H.; Zhang, Y.
3318 M.; Ulrich, R.; Schadler, V.; Wiesner, U. Organically Modified
3319 Aluminosilicate Mesostructures from Block Copolymer Phases.
3320 *Science* **1997**, *278*, 1795–1798.
- 3321 (48) Morkved, T. L.; Lu, M.; Urbas, A. M.; Ehrichs, E. E.; Jaeger, H.
3322 M.; Mansky, P.; Russell, T. P. Local Control of Microdomain
3323 Orientation in Diblock Copolymer Thin Films with Electric Fields.
3324 *Science* **1996**, *273*, 931–933.
- 3325 (49) Liang, C. D.; Dai, S. Synthesis of Mesoporous Carbon Materials
3326 via Enhanced Hydrogen-Bonding Interaction. *J. Am. Chem. Soc.* **2006**,
3327 *128*, 5316–5317.
- 3328 (50) Gao, L.; Chandra, A.; Nabaee, Y.; Hayakawa, T. Inducing
3329 Defects in Ordered Mesoporous Carbons via the Block Copolymer-
3330 Templated High-Temperature Carbonization of Nitrogen-Containing
3331 Polymeric Precursors. *Polym. J.* **2018**, *50*, 389–396.
- 3332 (51) Liu, C. Y.; Li, L. X.; Song, H. H.; Chen, X. H. Facile Synthesis
3333 of Ordered Mesoporous Carbons From F108/Resorcinol-Form-
3334 aldehyde Composites Obtained in Basic Media. *Chem. Commun.*
3335 **2007**, 757–759.
- 3336 (52) Tian, H.; Lin, Z. X.; Xu, F. G.; Zheng, J. X.; Zhuang, X. D.; Mai,
3337 Y. Y.; Feng, X. L. Quantitative Control of Pore Size of Mesoporous
Carbon Nanospheres Through the Self-Assembly of Diblock
Copolymer Micelles in Solution. *Small* **2016**, *12*, 3155–3163.
- (53) Meng, Y.; Gu, D.; Zhang, F.; Shi, Y.; Yang, H.; Li, Z.; Yu, C.;
Tu, B.; Zhao, D. Ordered Mesoporous Polymers and Homologous
Carbon Frameworks: Amphiphilic Surfactant Templating and Direct
Transformation. *Angew. Chem.* **2005**, *117*, 7215–7221.
- (54) Meng, Y.; Gu, D.; Zhang, F. Q.; Shi, Y. F.; Cheng, L.; Feng, D.;
Wu, Z. X.; Chen, Z. X.; Wan, Y.; Stein, A.; Zhao, D. Y. A Family of
Highly Ordered Mesoporous Polymer Resin and Carbon Structures
From Organic-Organic Self-Assembly. *Chem. Mater.* **2006**, *18*, 4447–
4464.
- (55) Liang, C. D.; Hong, K. L.; Guiochon, G. A.; Mays, J. W.; Dai, S.
Synthesis of a Large-Scale Highly Ordered Porous Carbon Film by
Self-Assembly of Block Copolymers. *Angew. Chem., Int. Ed.* **2004**, *43*,
5785–5789.
- (56) Tang, J.; Liu, J.; Li, C.; Li, Y.; Tade, M. O.; Dai, S.; Yamauchi,
Y. Synthesis of Nitrogen-Doped Mesoporous Carbon Spheres With
Extra-Large Pores Through Assembly of Diblock Copolymer Micelles.
Angew. Chem., Int. Ed. **2015**, *54*, 588–593.
- (57) Guan, B. Y.; Yu, L.; Lou, X. W. Formation of Asymmetric Bowl-
Like Mesoporous Particles via Emulsion-Induced Interface Aniso-
tropic Assembly. *J. Am. Chem. Soc.* **2016**, *138*, 11306–11311.
- (58) Kawashima, D.; Aihara, T.; Kobayashi, Y.; Kyotani, T.; Tomita,
A. Preparation of Mesoporous Carbon From Organic Polymer/Silica
Nanocomposite. *Chem. Mater.* **2000**, *12*, 3397–3401.
- (59) Pang, J. B.; Li, X.; Wang, D. H.; Wu, Z. W.; John, V. T.; Yang,
Z. Z.; Lu, Y. F. Silica-Templated Continuous Mesoporous Carbon
Films by a Spin-Coating Technique. *Adv. Mater.* **2004**, *16*, 884–886.
- (60) Zhang, J. A.; Song, Y.; Zhao, Y. P.; Zhao, S.; Yan, J. J.; Lee, J.;
Wang, Z. Y.; Liu, S. Y.; Yuan, R.; Luo, D. L.; Kopec, M.; Gottlieb, E.;
Kowalewski, T.; Matyjaszewski, K.; Bockstaller, M. R. Organosilica
With Grafted Polyacrylonitrile Brushes for High Surface Area
Nitrogen-Enriched Nanoporous Carbons. *Chem. Mater.* **2018**, *30*,
2208–2212.
- (61) Ding, W.; Li, L.; Xiong, K.; Wang, Y.; Li, W.; Nie, Y.; Chen, S.
G.; Qi, X. Q.; Wei, Z. D. Shape Fixing via Salt Recrystallization: A
Morphology-Controlled Approach to Convert Nanostructured
Polymer to Carbon Nanomaterial as a Highly Active Catalyst for
Oxygen Reduction Reaction. *J. Am. Chem. Soc.* **2015**, *137*, 5414–
5420.
- (62) Gong, J.; Zhang, J. S.; Lin, H. J.; Yuan, J. Y. Cooking Carbon in
a Solid Salt[†]: Synthesis of Porous Heteroatom-Doped Carbon Foams
for Enhanced Organic Pollutant Degradation Under Visible Light.
Appl. Mater. Today **2018**, *12*, 168–176.
- (63) Wang, F.; Song, S. Y.; Li, K.; Li, J. Q.; Pan, J.; Yao, S.; Ge, X.;
Feng, J.; Wang, X.; Zhang, H. J. A “Solid Dual-Ions-Transformation”
Route to S, N Co-Doped Carbon Nanotubes As Highly Efficient
“Metal-Free” Catalysts for Organic Reactions. *Adv. Mater.* **2016**, *28*,
10679–10683.
- (64) Tang, J.; Wang, T.; Salunkhe, R. R.; Alshehri, S. M.; Malgras,
V.; Yamauchi, Y. Three-Dimensional Nitrogen-Doped Hierarchical
Porous Carbon as an Electrode for High-Performance Super-
capacitors. *Chem. - Eur. J.* **2015**, *21*, 17293–17298.
- (65) Almeida, V. C.; Silva, R.; Acerce, M.; Pezoti, O.; Cazetta, A. L.;
Martins, A. C.; Huang, X. X.; Chhowalla, M.; Asefa, T. N-Doped
Ordered Mesoporous Carbons With Improved Charge Storage
Capacity by Tailoring N-Dopant Density With Solvent-Assisted
Synthesis. *J. Mater. Chem. A* **2014**, *2*, 15181–15190.
- (66) Balach, J.; Jaumann, T.; Klose, M.; Oswald, S.; Eckert, J.;
Giebeler, L. Improved Cycling Stability of Lithium-Sulfur Batteries
Using a Polypropylene-Supported Nitrogen-Doped Mesoporous
Carbon Hybrid Separator as Polysulfide Adsorbent. *J. Power Sources*
2016, *303*, 317–324.
- (67) Chang, Y. Q.; Hong, F.; Liu, J. X.; Xie, M. S.; Zhang, Q. L.; He,
C. X.; Niu, H. B.; Liu, J. H. Nitrogen/Sulfur Dual-Doped Mesoporous
Carbon With Controllable Morphology as a Catalyst Support for the
Methanol Oxidation Reaction. *Carbon* **2015**, *87*, 424–433.

- (68) Park, J.; Nabaee, Y.; Hayakawa, T.; Kakimoto, M. A. Highly Selective Two-Electron Oxygen Reduction Catalyzed by Mesoporous Nitrogen-Doped Carbon. *ACS Catal.* **2014**, *4*, 3749–3754. 3405
- (69) Chen, A. B.; Yu, Y. F.; Zhang, Y.; Zang, W. W.; Yu, Y. H.; Zhang, Y. X.; Shen, S. F.; Zhang, J. Aqueous-Phase Synthesis of Nitrogen-Doped Ordered Mesoporous Carbon Nanospheres as an Efficient Adsorbent for Acidic Gases. *Carbon* **2014**, *80*, 19–27. 3406
- (70) To, J. W. F.; He, J.; Mei, J.; Haghpanah, R.; Chen, Z.; Kurosawa, T.; Chen, S.; Bae, W.-G.; Pan, L.; Tok, J. B. H.; Wilcox, J.; Bao, Z. Hierarchical N-Doped Carbon as CO₂ Adsorbent With High CO₂ Selectivity From Rationally Designed Polypyrrole Precursor. *J. Am. Chem. Soc.* **2016**, *138*, 1001–1009. 3407
- (71) Zhang, J.; Zhao, Z.; Xia, Z.; Dai, L. A Metal-Free Bifunctional Electrocatalyst for Oxygen Reduction and Oxygen Evolution Reactions. *Nat. Nanotechnol.* **2015**, *10*, 444–452. 3408
- (72) Jing, F.; Chen, M.; Tang, Y. P.; Xu, Z. X.; Huang, T.; Su, Y. Z.; Wu, D. Q. Bottom-Up Fabrication of Nitrogen-Doped Mesoporous Carbon Nanosheets as High Performance Oxygen Reduction Catalysts. *J. Colloid Interface Sci.* **2017**, *492*, 8–14. 3409
- (73) Zhong, M.; Kim, E. K.; McGann, J. P.; Chun, S. E.; Whitacre, J. F.; Jaroniec, M.; Matyjaszewski, K.; Kowalewski, T. Electrochemically Active Nitrogen-Enriched Nanocarbons With Well-Defined Morphology Synthesized by Pyrolysis of Self-Assembled Block Copolymer. *J. Am. Chem. Soc.* **2012**, *134*, 14846–14857. 3410
- (74) Xu, F.; Tang, Z. W.; Huang, S. Q.; Chen, L. Y.; Liang, Y. R.; Mai, W. C.; Zhong, H.; Fu, R. W.; Wu, D. C. Facile Synthesis of Ultrahigh-Surface-Area Hollow Carbon Nanospheres for Enhanced Adsorption and Energy Storage. *Nat. Commun.* **2015**, *6*, 7221. 3411
- (75) Yuan, K.; Lu, C. B.; Sfaelou, S.; Liao, X. X.; Zhuang, X. D.; Chen, Y. W.; Scherf, U.; Feng, X. L. In Situ Nanoarchitecturing and Active-Site Engineering Toward Highly Efficient Carbonaceous Electrocatalysts. *Nano Energy* **2019**, *59*, 207–215. 3412
- (76) Chen, H. C.; Sun, F. G.; Wang, J. T.; Li, W. C.; Qiao, W. M.; Ling, L. C.; Long, D. H. Nitrogen Doping Effects on the Physical and Chemical Properties of Mesoporous Carbons. *J. Phys. Chem. C* **2013**, *117*, 8318–8328. 3413
- (77) Liu, D.; Cheng, G.; Zhao, H.; Zeng, C.; Qu, D. Y.; Xiao, L.; Tang, H. L.; Deng, Z.; Li, Y.; Su, B. L. Self-Assembly of Polyhedral Oligosilsesquioxane (POSS) Into Hierarchically Ordered Mesoporous Carbons With Uniform Microporosity and Nitrogen-Doping for High Performance Supercapacitors. *Nano Energy* **2016**, *22*, 255–268. 3414
- (78) Hung, C. T.; Yu, N. Y.; Chen, C. T.; Wu, P. H.; Han, X. X.; Kao, Y. S.; Liu, T. C.; Chu, Y. Y.; Deng, F.; Zheng, A. M.; Liu, S. B. Highly Nitrogen-Doped Mesoscopic Carbons as Efficient Metal-Free Electrocatalysts for Oxygen Reduction Reactions. *J. Mater. Chem. A* **2014**, *2*, 20030–20037. 3415
- (79) Huang, X. X.; Zhou, L. J.; Voiry, D.; Chhowalla, M.; Zou, X. X.; Asefa, T. Monodisperse Mesoporous Carbon Nanoparticles From Polymer/Silica Self-Aggregates and Their Electrocatalytic Activities. *ACS Appl. Mater. Interfaces* **2016**, *8*, 18891–18903. 3416
- (80) Yang, T. Y.; Liu, J.; Zhou, R. F.; Chen, Z. G.; Xu, H. Y.; Qiao, S. Z.; Monteiro, M. J. N-Doped Mesoporous Carbon Spheres as the Oxygen Reduction Reaction Catalysts. *J. Mater. Chem. A* **2014**, *2*, 18139–18146. 3417
- (81) Liu, H. J.; Wang, J.; Wang, C. X.; Xia, Y. Y. Ordered Hierarchical Mesoporous/Microporous Carbon Derived From Mesoporous Titanium-Carbide/Carbon Composites and Its Electrochemical Performance in Supercapacitor. *Adv. Energy Mater.* **2011**, *1*, 1101–1108. 3418
- (82) Sheng, Z. H.; Shao, L.; Chen, J. J.; Bao, W. J.; Wang, F. B.; Xia, X. H. Catalyst-Free Synthesis of Nitrogen-Doped Graphene via Thermal Annealing Graphite Oxide With Melamine and Its Excellent Electrocatalysis. *ACS Nano* **2011**, *5*, 4350–4358. 3419
- (83) Shrestha, S.; Mustain, W. E. Properties of Nitrogen-Functionalized Ordered Mesoporous Carbon Prepared Using Polypyrrole Precursor. *J. Electrochem. Soc.* **2010**, *157*, B1665–B1672. 3420
- (84) Li, X. L.; Wang, H. L.; Robinson, J. T.; Sanchez, H.; Diankov, G.; Dai, H. J. Simultaneous Nitrogen Doping and Reduction of Graphene Oxide. *J. Am. Chem. Soc.* **2009**, *131*, 15939–15944. 3421
- (85) Lin, Z. Y.; Waller, G.; Liu, Y.; Liu, M. L.; Wong, C. P. Facile Synthesis of Nitrogen-Doped Graphene via Pyrolysis of Graphene Oxide and Urea, and Its Electrochemical Activity Toward the Oxygen-Reduction Reaction. *Adv. Energy Mater.* **2012**, *2*, 884–888. 3422
- (86) Hou, S. C.; Cai, X.; Wu, H. W.; Yu, X.; Peng, M.; Yan, K.; Zou, D. C. Nitrogen-Doped Graphene for Dye-Sensitized Solar Cells and the Role of Nitrogen States in Triiodide Reduction. *Energy Environ. Sci.* **2013**, *6*, 3356–3362. 3423
- (87) Choi, C. H.; Chung, M. W.; Park, S. H.; Woo, S. I. Enhanced Electrochemical Oxygen Reduction Reaction by Restacking of N-Doped Single Graphene Layers. *RSC Adv.* **2013**, *3*, 4246–4253. 3424
- (88) Ma, F. W.; Zhao, H.; Sun, L. P.; Li, Q.; Huo, L. H.; Xia, T.; Gao, S.; Pang, G. S.; Shi, Z.; Feng, S. H. A Facile Route for Nitrogen-Doped Hollow Graphitic Carbon Spheres With Superior Performance in Supercapacitors. *J. Mater. Chem.* **2012**, *22*, 13464–13468. 3425
- (89) Fan, Z.; Ding, B.; Guo, H.; Shi, M.; Zhang, Y.; Dong, S.; Zhang, T.; Dou, H.; Zhang, X. Dual Dopamine Derived Polydopamine Coated N-Doped Porous Carbon Spheres as a Sulfur Host for High-Performance Lithium–Sulfur Batteries. *Chem. - Eur. J.* **2019**, *25*, 10710–10717. 3426
- (90) Liu, X. H.; Zhou, L.; Zhao, Y. Q.; Bian, L.; Feng, X. T.; Pu, Q. S. Hollow, Spherical Nitrogen-Rich Porous Carbon Shells Obtained From a Porous Organic Framework for the Supercapacitor. *ACS Appl. Mater. Interfaces* **2013**, *5*, 10280–10287. 3427
- (91) Wang, S. P.; Zhang, J. N.; Shang, P.; Li, Y. Y.; Chen, Z. M.; Xu, Q. N-Doped Carbon Spheres With Hierarchical Micropore-Nanosheet Networks for High Performance Supercapacitors. *Chem. Commun.* **2014**, *50*, 12091–12094. 3428
- (92) Seredych, M.; Rodriguez-Castellon, E.; Biggs, M. J.; Skinner, W.; Bandosz, T. J. Effect of Visible Light and Electrode Wetting on the Capacitive Performance of S- and N-Doped Nanoporous Carbons: Importance of Surface Chemistry. *Carbon* **2014**, *78*, 540–558. 3429
- (93) Peng, H.; Ma, G. F.; Sun, K. J.; Mu, J. J.; Zhang, Z.; Lei, Z. Q. Facile Synthesis of Poly(p-Phenylenediamine)-Derived Three-Dimensional Porous Nitrogen-Doped Carbon Networks for High Performance Supercapacitors. *J. Phys. Chem. C* **2014**, *118*, 29507–29516. 3430
- (94) Wei, J. S.; Ding, H.; Wang, Y. G.; Xiong, H. M. Hierarchical Porous Carbon Materials With High Capacitance Derived From Schiff-Base Networks. *ACS Appl. Mater. Interfaces* **2015**, *7*, 5811–5819. 3431
- (95) Jiang, J. G.; Chen, H.; Wang, Z.; Bao, L. K.; Qiang, Y. W.; Guan, S. Y.; Chen, J. D. Nitrogen-Doped Hierarchical Porous Carbon Microsphere Through KOH Activation for Supercapacitors. *J. Colloid Interface Sci.* **2015**, *452*, 54–61. 3432
- (96) Guo, Y.; Zeng, Z.; Li, Y.; Huang, Z.; Cui, Y. In-Situ Sulfur-Doped Carbon as a Metal-Free Catalyst for Persulfate Activated Oxidation of Aqueous Organics. *Catal. Today* **2018**, *307*, 12–19. 3433
- (97) Wei, H.; Xu, M. W.; Bao, S. J.; Yang, F.; Chai, H. Design and Synthesis of Carbonized Polypyrrole-Coated Graphene Aerogel Acting as an Efficient Metal-Free Catalyst for Oxygen Reduction. *RSC Adv.* **2014**, *4*, 16979–16984. 3434
- (98) Park, S. H.; Kang, Y. J.; Majid, S. A Review of Patterned Organic Bioelectronic Materials and Their Biomedical Applications. *Adv. Mater.* **2015**, *27*, 7583–7619. 3435
- (99) Jin, C.; Nagaiah, T. C.; Xia, W.; Spliethoff, B.; Wang, S. S.; Bron, M.; Schuhmann, W.; Muhler, M. Metal-Free and Electrocatalytically Active Nitrogen-Doped Carbon Nanotubes Synthesized by Coating With Polyaniline. *Nanoscale* **2010**, *2*, 981–987. 3436
- (100) Wu, G.; More, K. L.; Johnston, C. M.; Zelenay, P. High-Performance Electrocatalysts for Oxygen Reduction Derived From Polyaniline, Iron, and Cobalt. *Science* **2011**, *332*, 443–447. 3437
- (101) Morozan, A.; Jegou, P.; Campidelli, S.; Palacin, S.; Josselme, B. Relationship Between Polypyrrole Morphology and Electrochemical Activity Towards Oxygen Reduction Reaction. *Chem. Commun.* **2012**, *48*, 4627–4629. 3438
- (102) Yuan, C. Q.; Liu, X. H.; Jia, M. Y.; Luo, Z. X.; Yao, J. N. Facile Preparation of N- and O-Doped Hollow Carbon Spheres Derived 3439

- 3542 From Poly(o-Phenylenediamine) for Supercapacitors. *J. Mater. Chem.* **2015**, *3*, 3409–3415.
- 3544 (103) Shin, Y. S.; Fryxell, G.; Um, W. Y.; Parker, K.; Mattigod, S. V.; Skaggs, R. Sulfur-Functionalized Mesoporous Carbon. *Adv. Funct. Mater.* **2007**, *17*, 2897–2901.
- 3547 (104) Sevilla, M.; Fuertes, A. B. Highly Porous S-doped Carbons. *Microporous Mesoporous Mater.* **2012**, *158*, 318–323.
- 3549 (105) He, Y. Z.; Han, X. J.; Du, Y. C.; Song, B.; Zhang, B.; Zhang, W.; Xu, P. Conjugated Polymer-Mediated Synthesis of Sulfur- and Nitrogen-Doped Carbon Nanotubes As Efficient Anode Materials for Sodium Ion Batteries. *Nano Res.* **2018**, *11*, 2573–2585.
- 3553 (106) Liu, Y. L.; Ai, K. L.; Lu, L. H. Polydopamine and Its Derivative Materials: Synthesis and Promising Applications in Energy, Environmental, and Biomedical Fields. *Chem. Rev.* **2014**, *114*, 5057–5115.
- 3556 (107) Ryu, J. H.; Messersmith, P. B.; Lee, H. Polydopamine Surface Chemistry: A Decade of Discovery. *ACS Appl. Mater. Interfaces* **2018**, *10*, 7523–7540.
- 3559 (108) Liu, R.; Mahurin, S. M.; Li, C.; Unocic, R. R.; Idrobo, J. C.; Gao, H. J.; Pennycook, S. J.; Dai, S. Dopamine as a Carbon Source: The Controlled Synthesis of Hollow Carbon Spheres and Yolk-Structured Carbon Nanocomposites. *Angew. Chem., Int. Ed.* **2011**, *50*, 6799–6802.
- 3564 (109) Ai, K. L.; Liu, Y. L.; Ruan, C. P.; Lu, L. H.; Lu, G. Q. Sp² C-Dominant N-Doped Carbon Sub-Micrometer Spheres With a Tunable Size: A Versatile Platform for Highly Efficient Oxygen-Reduction Catalysts. *Adv. Mater.* **2013**, *25*, 998–1003.
- 3568 (110) Lee, H.; Dellatore, S. M.; Miller, W. M.; Messersmith, P. B. Mussel-Inspired Surface Chemistry for Multifunctional Coatings. *Science* **2007**, *318*, 426–430.
- 3571 (111) LaVoie, M. J.; Ostaszewski, B. L.; Weihofen, A.; Schlossmacher, M. G.; Selkoe, D. J. Dopamine Covalently Modifies and Functionally Inactivates Parkin. *Nat. Med.* **2005**, *11*, 1214–1221.
- 3574 (112) Qu, K. G.; Zheng, Y.; Dai, S.; Qiao, S. Z. Graphene Oxide-Polydopamine Derived N, S-Codoped Carbon Nanosheets As Superior Bifunctional Electrocatalysts for Oxygen Reduction and Evolution. *Nano Energy* **2016**, *19*, 373–381.
- 3578 (113) Zhong, S. K.; Zhou, L. H.; Wu, L.; Tang, L. F.; He, Q. Y.; Ahmed, J. Nitrogen- and Boron-Co-Doped Core Shell Carbon Nanoparticles as Efficient Metal-Free Catalysts for Oxygen Reduction Reactions in Microbial Fuel Cells. *J. Power Sources* **2014**, *272*, 344–358.
- 3582 (114) Yuan, J. Y.; Mecerreyes, D.; Antonietti, M. Poly(Ionic Liquid)s: An Update. *Prog. Polym. Sci.* **2013**, *38*, 1009–1036.
- 3585 (115) Green, O.; Grubjesic, S.; Lee, S. W.; Firestone, M. A. The Design of Polymeric Ionic Liquids for the Preparation of Functional Materials. *Polym. Rev.* **2009**, *49*, 339–360.
- 3588 (116) Mecerreyes, D. Polymeric Ionic Liquids: Broadening the Properties and Applications of Polyelectrolytes. *Prog. Polym. Sci.* **2011**, *36*, 1629–1648.
- 3591 (117) Zhang, P.; Yuan, J.; Feller, T.-P.; Antonietti, M.; Li, H.; Wang, Y. Improving Hydrothermal Carbonization by Using Poly(Ionic Liquid)s. *Angew. Chem., Int. Ed.* **2013**, *52*, 6028–6032.
- 3594 (118) Fechler, N.; Feller, T. P.; Antonietti, M. Salt Templating: A Simple and Sustainable Pathway Toward Highly Porous Functional Carbons From Ionic Liquids. *Adv. Mater.* **2013**, *25*, 75–79.
- 3597 (119) Paraknowitsch, J. P.; Thomas, A.; Antonietti, M. A Detailed View on the Polycondensation of Ionic Liquid Monomers Towards Nitrogen Doped Carbon Materials. *J. Mater. Chem.* **2010**, *20*, 6746–6758.
- 3601 (120) Yuan, J. Y.; Giordano, C.; Antonietti, M. Ionic Liquid Monomers and Polymers as Precursors of Highly Conductive, Mesoporous, Graphitic Carbon Nanostructures. *Chem. Mater.* **2010**, *22*, 5003–5012.
- 3605 (121) Dawson, R.; Cooper, A. I.; Adams, D. J. Nanoporous Organic Polymer Networks. *Prog. Polym. Sci.* **2012**, *37*, 530–563.
- 3607 (122) Sun, Y. H.; Zhao, J. H.; Wang, J. L.; Tang, N.; Zhao, R. J.; Zhang, D. D.; Guan, T. T.; Li, K. X. Sulfur-Doped Millimeter-Sized Microporous Activated Carbon Spheres Derived From Sulfonated Poly(Styrene-Divinylbenzene) for CO₂ Capture. *J. Phys. Chem. C* **2017**, *121*, 10000–10009.
- (123) Gu, S.; He, J. Q.; Zhu, Y. L.; Wang, Z. Q.; Chen, D. Y.; Yu, G. P.; Pan, C. Y.; Guan, J. G.; Tao, K. Facile Carbonization of Microporous Organic Polymers Into Hierarchically Porous Carbons Targeted for Effective CO₂ Uptake at Low Pressures. *ACS Appl. Mater. Interfaces* **2016**, *8*, 18383–18392.
- (124) Yang, M.; Long, X.; Li, H. M.; Chen, H. B.; Liu, P. L. Porous Organic-Polymer-Derived Nitrogen-Doped Porous Carbon Nanoparticles for Efficient Oxygen Reduction Electrocatalysis and Supercapacitors. *ACS Sustainable Chem. Eng.* **2019**, *7*, 2236–2244.
- (125) Rehman, A.; Park, S. J. Facile Synthesis of Nitrogen-Enriched Microporous Carbons Derived From Imine and Benzimidazole-Linked Polymeric Framework for Efficient CO₂ Adsorption. *J. Co2 Util.* **2017**, *21*, 503–512.
- (126) Alabadi, A.; Abbood, H. A.; Li, Q. Y.; Jing, N.; Tan, B. Imine-Linked Polymer Based Nitrogen-Doped Porous Activated Carbon for Efficient and Selective CO₂ Capture. *Sci. Rep.* **2016**, *6*, 38614.
- (127) Yang, J.; Xu, M.; Wang, J. Y.; Jin, S. B.; Tan, B. E. A Facile Approach to Prepare Multiple Heteroatom-Doped Carbon Materials From Imine-Linked Porous Organic Polymers. *Sci. Rep.* **2018**, *8*, 4200.
- (128) Deng, J.; Li, M.; Wang, Y. Biomass-Derived Carbon: Synthesis and Applications in Energy Storage and Conversion. *Green Chem.* **2016**, *18*, 4824–4854.
- (129) Xu, B.; Hou, S. S.; Cao, G. P.; Wu, F.; Yang, Y. S. Sustainable Nitrogen-Doped Porous Carbon With High Surface Areas Prepared From Gelatin for Supercapacitors. *J. Mater. Chem.* **2012**, *22*, 19088–19093.
- (130) Hou, J. H.; Cao, C. B.; Idrees, F.; Ma, X. L. Hierarchical Porous Nitrogen-Doped Carbon Nanosheets Derived From Silk for Ultrahigh-Capacity Battery Anodes and Supercapacitors. *ACS Nano* **2015**, *9*, 2556–2564.
- (131) Yang, D. P.; Li, Z. B.; Liu, M. H.; Zhang, X. Y.; Chen, Y. S.; Xue, H.; Ye, E. Y.; Luque, R. Biomass-Derived Carbonaceous Materials: Recent Progress in Synthetic Approaches, Advantages, and Applications. *ACS Sustainable Chem. Eng.* **2019**, *7*, 4564–4585.
- (132) Gao, S. Y.; Chen, Y. L.; Fan, H.; Wei, X. J.; Hu, C. G.; Luo, H. X.; Qu, L. T. Large Scale Production of Biomass-Derived N-Doped Porous Carbon Spheres for Oxygen Reduction and Supercapacitors. *J. Mater. Chem. A* **2014**, *2*, 3317–3324.
- (133) Jiang, Z.; Shao, Y.; Zhao, P.; Wang, H. Flexible Heteroatom-Doped Graphitic Hollow Carbon Fibers for Ultrasensitive and Reusable Electric Current Sensing. *Chem. Commun.* **2019**, *55*, 12853–12856.
- (134) Yun, Y. S.; Cho, S. Y.; Shim, J.; Kim, B. H.; Chang, S. J.; Baek, S. J.; Huh, Y. S.; Tak, Y.; Park, Y. W.; Park, S.; Jin, H. J. Microporous Carbon Nanoplates from Regenerated Silk Proteins for Supercapacitors. *Adv. Mater.* **2013**, *25*, 1993–1998.
- (135) Wang, C. L.; Zhou, Y.; Sun, L.; Wan, P.; Zhang, X.; Qiu, J. S. Sustainable Synthesis of Phosphorus- and Nitrogen-Co-Doped Porous Carbons With Tunable Surface Properties for Supercapacitors. *J. Power Sources* **2013**, *239*, 81–88.
- (136) Hao, G. P.; Li, W. C.; Qian, D.; Lu, A. H. Rapid Synthesis of Nitrogen-Doped Porous Carbon Monolith for CO₂ Capture. *Adv. Mater.* **2010**, *22*, 853–857.
- (137) Guo, D.-C.; Mi, J.; Hao, G.-P.; Dong, W.; Xiong, G.; Li, W.-C.; Lu, A.-H. Ionic Liquid c16mimbf₄ Assisted Synthesis of Poly(benzoxazine-Co-Resol)-Based Hierarchically Porous Carbons With Superior Performance in Supercapacitors. *Energy Environ. Sci.* **2013**, *6*, 652–659.
- (138) Liu, J. W.; Webster, S.; Carroll, D. L. Temperature and Flow Rate of NH₃ Effects on Nitrogen Content and Doping Environments of Carbon Nanotubes Grown by Injection CVD Method. *J. Phys. Chem. B* **2005**, *109*, 15769–15774.
- (139) Zhu, D. Z.; Wang, Y. W.; Gan, L. H.; Liu, M. X.; Cheng, K.; Zhao, Y. H.; Deng, X. X.; Sun, D. M. Nitrogen-Containing Carbon Microspheres for Supercapacitor Electrodes. *Electrochim. Acta* **2015**, *158*, 166–174.

- 3678 (140) Lee, B. S.; Son, S. B.; Park, K. M.; Yu, W. R.; Oh, K. H.; Lee, S. H. Anodic Properties of Hollow Carbon Nanofibers for Li-Ion Battery. *J. Power Sources* **2012**, *199*, 53–60.
- 3681 (141) Puthusseri, D.; Aravindan, V.; Madhavi, S.; Ogale, S. 3D Micro-Porous Conducting Carbon Beehive by Single Step Polymer Carbonization for High Performance Supercapacitors: The Magic of *in situ* Porogen Formation. *Energy Environ. Sci.* **2014**, *7*, 728–735.
- 3685 (142) Gu, J. N.; Du, Z. G.; Zhang, C.; Yang, S. B. Pyridinic Nitrogen-Enriched Carbon Nanogears With Thin Teeth for Superior Lithium Storage. *Adv. Energy Mater.* **2016**, *6*, 1600917.
- 3688 (143) Peng, A. Z.; Qi, S. C.; Liu, X.; Xue, D. M.; Peng, S. S.; Yu, G. X.; Liu, X. Q.; Sun, L. B. Fabrication of N-Doped Porous Carbons for Enhanced CO₂ Capture: Rational Design of an Ammoniated Polymer Precursor. *Chem. Eng. J.* **2019**, *369*, 170–179.
- 3692 (144) Zhu, Y. P.; Liu, Y. L.; Liu, Y. P.; Ren, T. Z.; Chen, T. H.; Yuan, Z. Y. Direct Synthesis of Phosphorus-Doped Mesoporous Carbon Materials for Efficient Electrocatalytic Oxygen Reduction. *ChemCatChem* **2015**, *7*, 2903–2909.
- 3696 (145) Zhao, Q.; Fellinger, T.-P.; Antonietti, M.; Yuan, J. A Novel Polymeric Precursor for Micro/mesoporous Nitrogen-Doped Carbons. *J. Mater. Chem. A* **2013**, *1*, 5113.
- 3699 (146) Wang, H.; Min, S.; Ma, C.; Liu, Z.; Zhang, W.; Wang, Q.; Li, 3700 D.; Li, Y.; Turner, S.; Han, Y.; Zhu, H.; Abou-Hamad, E.; Hedhili, M. 3701 N.; Pan, J.; Yu, W.; Huang, K. W.; Li, L. J.; Yuan, J.; Antonietti, M.; 3702 Wu, T. Synthesis of Single-Crystal-Like Nanoporous Carbon 3703 Membranes and Their Application in Overall Water Splitting. *Nat. 3704 Commun.* **2017**, *8*, 13592.
- 3705 (147) Zhao, W.; Han, S.; Zhuang, X.; Zhang, F.; Mai, Y.; Feng, X. 3706 Cross-Linked Polymer-Derived B/N Co-Doped Carbon Materials 3707 With Selective Capture of CO₂. *J. Mater. Chem. A* **2015**, *3*, 23352– 3708 23359.
- 3709 (148) Chen, X. Y.; Chen, C.; Zhang, Z. J.; Xie, D. H.; Liu, J. W. A 3710 General Conversion of Polyacrylate-Metal Complexes Into Porous 3711 Carbons Especially Evinced in the Case of Magnesium Polyacrylate. *J. 3712 Mater. Chem. A* **2013**, *1*, 4017–4025.
- 3713 (149) You, B.; Kang, F.; Yin, P. Q.; Zhang, Q. Hydrogel-Derived 3714 Heteroatom-Doped Porous Carbon Networks for Supercapacitor and 3715 Electrocatalytic Oxygen Reduction. *Carbon* **2016**, *103*, 9–15.
- 3716 (150) Meng, W.; Wen, L. N.; Song, Z. H.; Cao, N.; Qin, X. Metal- 3717 Free Boron-Doped Carbon Microspheres as Excellent Cathode 3718 Catalyst for Rechargeable Li-O₂ Battery. *J. Solid State Electrochem.* 3719 **2017**, *21*, 665–671.
- 3720 (151) Liu, X.; Dai, L. Carbon-Based Metal-Free Catalysts. *Nat. Rev.* 3721 *Mater.* **2016**, *1*, 16064.
- 3722 (152) Wang, X.; Sun, G.; Routh, P.; Kim, D. H.; Huang, W.; Chen, 3723 P. Heteroatom-Doped Graphene Materials: Syntheses, Properties and 3724 Applications. *Chem. Soc. Rev.* **2014**, *43*, 7067–7098.
- 3725 (153) Chen, W.; Wan, M.; Liu, Q.; Xiong, X.; Yu, F.; Huang, Y. 3726 Heteroatom-Doped Carbon Materials: Synthesis, Mechanism, and 3727 Application for Sodium-Ion Batteries. *Small Methods* **2019**, *3*, 3728 1800323.
- 3729 (154) Dai, L.; Xue, Y.; Qu, L.; Choi, H. J.; Baek, J. B. Metal-Free 3730 Catalysts for Oxygen Reduction Reaction. *Chem. Rev.* **2015**, *115*, 3731 4823–4892.
- 3732 (155) Deng, Y.; Xie, Y.; Zou, K.; Ji, X. Review on Recent Advances 3733 in Nitrogen-Doped Carbons: Preparations and Applications in 3734 Supercapacitors. *J. Mater. Chem. A* **2016**, *4*, 1144–1173.
- 3735 (156) Nasrazadani, S.; Hassani, S. Modern Analytical Techniques in 3736 Failure Analysis of Aerospace, Chemical, and Oil and Gas Industries. 3737 *Handbook of Materials Failure Analysis with Case Studies from the Oil 3738 and Gas Industry*; Elsevier: 2016; pp 39–54.
- 3739 (157) Johnson, R. L.; Schmidt-Rohr, K. Quantitative Solid-State ¹³C 3740 NMR With Signal Enhancement by Multiple Cross Polarization. *J. 3741 Magn. Reson.* **2014**, *239*, 44–49.
- 3742 (158) Zheng, H.; Li, K.; Cody, G. D.; Tulk, C. A.; Dong, X.; Gao, 3743 G.; Molaison, J. J.; Liu, Z.; Feyngenson, M.; Yang, W.; Ivanov, I. N.; 3744 Basile, L.; Idrobo, J. C.; Guthrie, M.; Mao, H. K. Polymerization of 3745 Acetonitrile via a Hydrogen Transfer Reaction From CH₃ to CN Under Extreme Conditions. *Angew. Chem., Int. Ed.* **2016**, *55*, 12040– 3746 12044. 3747
- (159) Koide, A.; Fujikawa, T.; Ichikuni, N. Recent Progress in Exafs/ 3748 Nexafs Spectroscopy. *J. Electron Spectrosc. Relat. Phenom.* **2014**, *195*, 3749 375–381. 3750
- (160) Sa, Y. J.; Park, C.; Jeong, H. Y.; Park, S. H.; Lee, Z.; Kim, K. 3751 T.; Park, G. G.; Joo, S. H. Carbon Nanotubes/Heteroatom-Doped 3752 Carbon Core-Sheath Nanostructures As Highly Active, Metal-Free 3753 Oxygen Reduction Electrocatalysts for Alkaline Fuel Cells. *Angew. 3754 Chem.* **2014**, *126*, 4186–4190. 3755
- (161) Kim, B.; Hochella, M. F. Analytical Transmission Electron 3756 Microscopy and Scanning Transmission Electron Microscopy 3757 Techniques for the Characterization of Nanomaterial Composition, 3758 Phase and Crystallinity. *Front. Nanosci.* **2015**, *8*, 123–152. 3759
- (162) Wang, T.; Wang, Q.; Wang, Y.; Da, Y.; Zhou, W.; Shao, Y.; Li, 3760 D.; Zhan, S.; Yuan, J.; Wang, H. Atomically Dispersed Semimetallic 3761 Selenium on Porous Carbon Membrane as an Electrode for 3762 Hydrazine Fuel Cells. *Angew. Chem., Int. Ed.* **2019**, *58*, 13466–13471. 3763
- (163) Duan, J.; Chen, S.; Jaroniec, M.; Qiao, S. Z. Heteroatom- 3764 Doped Graphene-Based Materials for Energy-Relevant Electro- 3765 catalytic Processes. *ACS Catal.* **2015**, *5*, 5207–5234. 3766
- (164) Zhang, T.; Asefa, T. Heteroatom-Doped Carbon Materials for 3767 Hydrazine Oxidation. *Adv. Mater.* **2019**, *31*, 1804394. 3768
- (165) Fan, X.; Zheng, W. T.; Kuo, J.-L. Oxygen Reduction Reaction 3769 on Active Sites of Heteroatom-Doped Graphene. *RSC Adv.* **2013**, *3*, 3770 5498. 3771
- (166) Yang, L.; Jiang, S.; Zhao, Y.; Zhu, L.; Chen, S.; Wang, X.; Wu, 3772 Q.; Ma, J.; Ma, Y.; Hu, Z. Boron-Doped Carbon Nanotubes as Metal- 3773 Free Electrocatalysts for the Oxygen Reduction Reaction. *Angew. 3774 Chem., Int. Ed.* **2011**, *50*, 7132–7135. 3775
- (167) Jiao, Y.; Zheng, Y.; Jaroniec, M.; Qiao, S. Z. Origin of the 3776 Electrocatalytic Oxygen Reduction Activity of Graphene-Based 3777 Catalysts: A Roadmap to Achieve the Best Performance. *J. Am. 3778 Chem. Soc.* **2014**, *136*, 4394–4403. 3779
- (168) Zhou, Y.; Neyerlin, K.; Olson, T. S.; Pylpyenko, S.; Bult, J.; 3780 Dinh, H. N.; Gennett, T.; Shao, Z.; O’Hayre, R. Enhancement of Pt 3781 and Pt-Alloy Fuel Cell Catalyst Activity and Durability via Nitrogen- 3782 Modified Carbon Supports. *Energy Environ. Sci.* **2010**, *3*, 1437. 3783
- (169) Li, X. H.; Antonietti, M. Metal Nanoparticles at Mesoporous 3784 N-Doped Carbons and Carbon Nitrides: Functional Mott-Schottky 3785 Heterojunctions for Catalysis. *Chem. Soc. Rev.* **2013**, *42*, 6593–6604. 3786
- (170) Liu, W. J.; Li, W. W.; Jiang, H.; Yu, H. Q. Fates of Chemical 3787 Elements in Biomass During Its Pyrolysis. *Chem. Rev.* **2017**, *117*, 3788 6367–6398. 3789
- (171) Einert, M.; Wessel, C.; Badaczewski, F.; Leichtweiß, T.; 3790 Eufinger, C.; Janek, J.; Yuan, J.; Antonietti, M.; Smarsly, B. M. 3791 Nitrogen-Doped Carbon Electrodes: Influence of Microstructure and 3792 Nitrogen Configuration on the Electrical Conductivity of Carbonized 3793 Polyacrylonitrile and Poly(ionic Liquid) Blends. *Macromol. Chem. 3794 Phys.* **2015**, *216*, 1930–1944. 3795
- (172) Ewels, C. P.; Glerup, M. Nitrogen Doping in Carbon 3796 Nanotubes. *J. Nanosci. Nanotechnol.* **2005**, *5*, 1345–1363. 3797
- (173) Shao, Y.; Jiang, Z.; Zhang, Y.; Wang, T.; Zhao, P.; Zhang, Z.; 3798 Yuan, J.; Wang, H. All-Poly(ionic Liquid) Membrane-Derived Porous 3799 Carbon Membranes: Scalable Synthesis and Application for Photo- 3800 thermal Conversion in Seawater Desalination. *ACS Nano* **2018**, *12*, 3801 11704–11710. 3802
- (174) Antonietti, M.; Oschatz, M. The Concept of “Noble, 3803 Heteroatom-Doped Carbons,” Their Directed Synthesis by Electronic 3804 Band Control of Carbonization, and Applications in Catalysis and 3805 Energy Materials. *Adv. Mater.* **2018**, *30*, 1706836. 3806
- (175) Pramanik, A.; Kang, H. S. Density Functional Theory Study of 3807 O₂ and NO Adsorption on Heteroatom-Doped Graphenes Including 3808 the Van der Waals Interaction. *J. Phys. Chem. C* **2011**, *115*, 10971– 3809 10978. 3810
- (176) Arrigo, R.; Hävecker, M.; Wrabetz, S.; Blume, R.; Lerch, M.; 3811 McGregor, J.; Parrott, E. P. J.; Zeitler, J. A.; Gladden, L. F.; Knop- 3812 Gericke, A.; Schlögl, R.; Su, D. S. Tuning the Acid/Base Properties of 3813

- 3814 Nanocarbons by Functionalization via Amination. *J. Am. Chem. Soc.* 3815 **2010**, *132*, 9616–9630.
- 3816 (177) Nicol, E. J.; Carbotte, J. P. Properties of the Superconducting 3817 State in a Two-Band Model. *Phys. Rev. B: Condens. Matter Mater. Phys.* 3818 **2005**, *71*, 054501.
- 3819 (178) Schiros, T.; Nordlund, D.; Pálková, L.; Prezzi, D.; Zhao, L.; 3820 Kim, K. S.; Wurstbauer, U.; Gutiérrez, C.; Delongchamp, D.; Jaye, C.; 3821 Fischer, D.; Ogasawara, H.; Pettersson, L. G. M.; Reichman, D. R.; 3822 Kim, P.; Hybertsen, M. S.; Pasupathy, A. N. Connecting Dopant Bond 3823 Type With Electronic Structure in N-Doped Graphene. *Nano Lett.* 3824 **2012**, *12*, 4025–4031.
- 3825 (179) Zhang, B.; Wang, C.; Liu, D.; Liu, Y.; Yu, X.; Wang, L. 3826 Boosting Orr Electrocatalytic Performance of Metal-Free Mesoporous 3827 Biomass Carbon by Synergism of Huge Specific Surface Area and 3828 Ultrahigh Pyridinic Nitrogen Doping. *ACS Sustainable Chem. Eng.* 3829 **2018**, *6*, 13807–13812.
- 3830 (180) Luo, Z.; Lim, S.; Tian, Z.; Shang, J.; Lai, L.; MacDonald, B.; 3831 Fu, C.; Shen, Z.; Yu, T.; Lin, J. Pyridinic N Doped Graphene: 3832 Synthesis, Electronic Structure, and Electrocatalytic Property. *J. Mater.* 3833 *Chem.* **2011**, *21*, 8038–8044.
- 3834 (181) Sun, M.; Wu, X.; Deng, X.; Zhang, W.; Xie, Z.; Huang, Q.; 3835 Huang, B. Synthesis of Pyridinic-N Doped Carbon Nanofibers and Its 3836 Electro-Catalytic Activity for Oxygen Reduction Reaction. *Mater. Lett.* 3837 **2018**, *220*, 313–316.
- 3838 (182) Sun, M.; Wu, X.; Xie, Z.; Deng, X.; Wen, J.; Huang, Q.; 3839 Huang, B. Tailoring Platelet Carbon Nanofibers for High-Purity 3840 Pyridinic-N Doping: A Novel Method for Synthesizing Oxygen 3841 Reduction Reaction Catalysts. *Carbon* **2017**, *125*, 401–408.
- 3842 (183) Liu, T.; Zhang, X.; Huang, T.; Yu, A. Pyridinic-N-Dominated 3843 Carbon Frameworks With Porous Tungsten Trioxide Nano-Lamellae 3844 as a Promising Bi-Functional Catalyst for Li–Oxygen Batteries. 3845 *Nanoscale* **2018**, *10*, 15763–15770.
- 3846 (184) Cui, X.; Pan, Z.; Zhang, L.; Peng, H.; Zheng, G. Selective 3847 Etching of Nitrogen-Doped Carbon by Steam for Enhanced 3848 Electrochemical CO₂ Reduction. *Adv. Energy Mater.* **2017**, *7*, 3849 1701456.
- 3850 (185) Gong, K.; Du, F.; Xia, Z.; Durstock, M.; Dai, L. Nitrogen- 3851 Doped Carbon Nanotube Arrays With High Electrocatalytic Activity 3852 for Oxygen Reduction. *Science* **2009**, *323*, 760–764.
- 3853 (186) Geng, D.; Chen, Y.; Chen, Y.; Li, Y.; Li, R.; Sun, X.; Ye, S.; 3854 Knights, S. High Oxygen-Reduction Activity and Durability of 3855 Nitrogen-Doped Graphene. *Energy Environ. Sci.* **2011**, *4*, 760.
- 3856 (187) Niwa, H.; Horiba, K.; Harada, Y.; Oshima, M.; Ikeda, T.; 3857 Terakura, K.; Ozaki, J.-i.; Miyata, S. X-Ray Absorption Analysis of 3858 Nitrogen Contribution to Oxygen Reduction Reaction in Carbon 3859 Alloy Cathode Catalysts for Polymer Electrolyte Fuel Cells. *J. Power* 3860 *Sources* **2009**, *187*, 93–97.
- 3861 (188) Jiang, H.; Gu, J.; Zheng, X.; Liu, M.; Qiu, X.; Wang, L.; Li, W.; 3862 Chen, Z.; Ji, X.; Li, J. Defect-Rich and Ultrathin N Doped Carbon 3863 Nanosheets as Advanced Trifunctional Metal-Free Electrocatalysts for 3864 the ORR, OER and HER. *Energy Environ. Sci.* **2019**, *12*, 322–333.
- 3865 (189) Hu, C. G.; Dai, L. M. Doping of Carbon Materials for Metal- 3866 Free Electrocatalysis. *Adv. Mater.* **2019**, *31*, 1804672.
- 3867 (190) Haque, E.; Zavabeti, A.; Uddin, N.; Wang, Y. C.; Rahim, M. 3868 A.; Syed, N.; Xu, K.; Jannat, A.; Haque, F.; Zhang, B. Y.; Shoaib, M. 3869 A.; Shamsuddin, S.; Nurunnabi, M.; Minett, A. I.; Ou, J. Z.; Harris, A. 3870 T. Deciphering the Role of Quaternary N in O₂ Reduction Over 3871 Controlled N-Doped Carbon Catalysts. *Chem. Mater.* **2020**, *32*, 3872 1384–1392.
- 3873 (191) Fellingner, T. P.; Hasche, F.; Strasser, P.; Antonietti, M. 3874 Mesoporous Nitrogen-Doped Carbon for the Electrocatalytic Syn- 3875 thesis of Hydrogen Peroxide. *J. Am. Chem. Soc.* **2012**, *134*, 4072– 3876 4075.
- 3877 (192) Iglesias, D.; Giuliani, A.; Melchionna, M.; Marchesan, S.; 3878 Criado, A.; Nasi, L.; Bevilacqua, M.; Tavagnacco, C.; Vizza, F.; Prato, 3879 M.; Fornasiero, P. N-Doped Graphitized Carbon Nanohorns as a 3880 Forefront Electrocatalyst in Highly Selective O₂ Reduction to H₂O₂. 3881 *Chem.* **2018**, *4*, 106–123.
- (193) Kiuchi, H.; Shibuya, R.; Kondo, T.; Nakamura, J.; Niwa, H.; 3882 Miyawaki, J.; Kawai, M.; Oshima, M.; Harada, Y. Lewis Basicity of 3883 Nitrogen-Doped Graphite Observed by CO₂ Chemisorption. *Nano-* 3884 *scale Res. Lett.* **2016**, *11*, 127.
- (194) Gong, J.; Antonietti, M.; Yuan, J. Poly(ionic Liquid)-Derived 3886 Carbon With Site-Specific N-Doping and Biphasic Heterojunction for 3887 Enhanced CO₂ Capture and Sensing. *Angew. Chem., Int. Ed.* **2017**, *56*, 3888 7557–7563. 3889
- (195) Du, A.; Sanvito, S.; Li, Z.; Wang, D.; Jiao, Y.; Liao, T.; Sun, 3890 Q.; Ng, Y. H.; Zhu, Z.; Amal, R.; Smith, S. C. Hybrid Graphene and 3891 Graphitic Carbon Nitride Nanocomposite: Gap Opening, Electron– 3892 Hole Puddle, Interfacial Charge Transfer, and Enhanced Visible Light 3893 Response. *J. Am. Chem. Soc.* **2012**, *134*, 4393–4397. 3894
- (196) Kuzmicz, D.; Prescher, S.; Polzer, F.; Soll, S.; Seitz, C.; 3895 Antonietti, M.; Yuan, J. The Colloidal Stabilization of Carbon With 3896 Carbon: Carbon Nanobubbles As Both Dispersant and Glue for 3897 Carbon Nanotubes. *Angew. Chem., Int. Ed.* **2014**, *53*, 1062–1066. 3898
- (197) Wang, H.; Jia, J.; Song, P.; Wang, Q.; Li, D.; Min, S.; Qian, C.; 3899 Wang, L.; Li, Y. F.; Ma, C.; Wu, T.; Yuan, J.; Antonietti, M.; Ozin, G. 3900 A. Efficient Electrocatalytic Reduction of CO₂ by Nitrogen-Doped 3901 Nanoporous Carbon/Carbon Nanotube Membranes: A Step Towards 3902 the Electrochemical CO₂ Refinery. *Angew. Chem., Int. Ed.* **2017**, *56*, 3903 7847. 3904
- (198) Cui, X.; Pan, Z.; Zhang, L.; Peng, H.; Zheng, G. Selective 3905 Etching of Nitrogen-Doped Carbon by Steam for Enhanced 3906 Electrochemical CO₂ Reduction. *Adv. Energy Mater.* **2017**, *7*, 3907 1701456. 3908
- (199) Wu, J.; Liu, M.; Sharma, P. P.; Yadav, R. M.; Ma, L.; Yang, Y.; 3909 Zou, X.; Zhou, X. D.; Vajtai, R.; Jakobson, B. I.; Lou, J.; Ajayan, P. M. 3910 Incorporation of Nitrogen Defects for Efficient Reduction of CO₂ via 3911 Two-Electron Pathway on Three-Dimensional Graphene Foam. *Nano* 3912 *Let.* **2016**, *16*, 466–470. 3913
- (200) Chai, G. L.; Guo, Z. X. Highly Effective Sites and Selectivity of 3914 Nitrogen-Doped Graphene/CNT Catalysts for CO₂ Electrochemical 3915 Reduction. *Chem. Sci.* **2016**, *7*, 1268–1275. 3916
- (201) Su, H.; Zhang, K. X.; Zhang, B.; Wang, H. H.; Yu, Q. Y.; Li, X. 3917 H.; Antonietti, M.; Chen, J. S. Activating Cobalt Nanoparticles via the 3918 Mott-Schottky Effect in Nitrogen-Rich Carbon Shells for Base-Free 3919 Aerobic Oxidation of Alcohols to Esters. *J. Am. Chem. Soc.* **2017**, *139*, 3920 811–818. 3921
- (202) Xue, Z.-H.; Han, J.-T.; Feng, W.-J.; Yu, Q.-Y.; Li, X.-H.; 3922 Antonietti, M.; Chen, J.-S. Tuning the Adsorption Energy of 3923 Methanol Molecules Along Ni-N-Doped Carbon Phase Boundaries 3924 by the Mott–Schottky Effect for Gas-Phase Methanol Dehydrogen- 3925 ation. *Angew. Chem., Int. Ed.* **2018**, *57*, 2697–2701. 3926
- (203) Pan, Y.; Lin, R.; Chen, Y.; Liu, S.; Zhu, W.; Cao, X.; Chen, W.; 3927 Wu, K.; Cheong, W. C.; Wang, Y.; Zheng, L.; Luo, J.; Lin, Y.; Liu, Y.; 3928 Liu, C.; Li, J.; Lu, Q.; Chen, X.; Wang, D.; Peng, Q.; Chen, C.; Li, Y. 3929 Design of Single-Atom Co-N₅ Catalytic Site: A Robust Electrocatalyst 3930 for CO₂ Reduction With Nearly 100% CO Selectivity and Remarkable 3931 Stability. *J. Am. Chem. Soc.* **2018**, *140*, 4218–4221. 3932
- (204) Shen, W.; Fan, W. Nitrogen-Containing Porous Carbons: 3933 Synthesis and Application. *J. Mater. Chem. A* **2013**, *1*, 999–1013. 3934
- (205) Shafeeyan, M. S.; Daud, W. M. A. W.; Houshmand, A.; 3935 Shamiri, A. A Review on Surface Modification of Activated Carbon for 3936 Carbon Dioxide Adsorption. *J. Anal. Appl. Pyrolysis* **2010**, *89*, 143– 3937 151. 3938
- (206) Lai, L.; Potts, J. R.; Zhan, D.; Wang, L.; Poh, C. K.; Tang, C.; 3939 Gong, H.; Shen, Z.; Lin, J.; Ruoff, R. S. Exploration of the Active 3940 Center Structure of Nitrogen-Doped Graphene-Based Catalysts for 3941 Oxygen Reduction Reaction. *Energy Environ. Sci.* **2012**, *5*, 7936–7942. 3942
- (207) Economy, J.; Foster, K.; Andreopoulos, A.; Jung, H. Tailoring 3943 Carbon Fibers for Adsorbing Volatiles: Various Chemical Treatments 3944 Are Used to Change Surface Area, Pore Geometry, and Adsorption 3945 Characteristics. *CHEMTECH* **1992**, *22*, 597–603. 3946
- (208) Hulicova-Jurcakova, D.; Kodama, M.; Shiraishi, S.; Hatori, H.; 3947 Zhu, Z. H.; Lu, G. Q. Nitrogen-Enriched Nonporous Carbon 3948 Electrodes With Extraordinary Supercapacitance. *Adv. Funct. Mater.* 3949 **2009**, *19*, 1800–1809. 3950

- 3951 (209) Strelko, V. V.; Kuts, V. S.; Thrower, P. A. On the Mechanism
3952 of Possible Influence of Heteroatoms of Nitrogen, Boron and
3953 Phosphorus in a Carbon Matrix on the Catalytic Activity of Carbons
3954 in Electron Transfer Reactions. *Carbon* **2000**, *38*, 1499–1503.
- 3955 (210) Mangun, C. L.; Benak, K. R.; Economy, J.; Foster, K. L.
3956 Surface Chemistry, Pore Sizes and Adsorption Properties of Activated
3957 Carbon Fibers and Precursors Treated With Ammonia. *Carbon* **2001**,
3958 *39*, 1809–1820.
- 3959 (211) Chen, L.-F.; Zhang, X.-D.; Liang, H.-W.; Kong, M.; Guan, Q.-
3960 F.; Chen, P.; Wu, Z.-Y.; Yu, S.-H. Synthesis of Nitrogen-Doped
3961 Porous Carbon Nanofibers as an Efficient Electrode Material for
3962 Supercapacitors. *ACS Nano* **2012**, *6*, 7092–7102.
- 3963 (212) Xiao, K.; Ding, L. X.; Liu, G.; Chen, H.; Wang, S.; Wang, H.
3964 Freestanding, Hydrophilic Nitrogen-Doped Carbon Foams for Highly
3965 Compressible All Solid-State Supercapacitors. *Adv. Mater.* **2016**, *28*,
3966 5997–6002.
- 3967 (213) Hao, G.-P.; Zhang, Q.; Sin, M.; Hippauf, F.; Borchardt, L.;
3968 Brunner, E.; Kaskel, S. Design of Hierarchically Porous Carbons With
3969 Interlinked Hydrophilic and Hydrophobic Surface and Their
3970 Capacitive Behavior. *Chem. Mater.* **2016**, *28*, 8715–8725.
- 3971 (214) Rani, P.; Jindal, V. K. Designing Band Gap of Graphene by B
3972 and N Dopant Atoms. *RSC Adv.* **2013**, *3*, 802–812.
- 3973 (215) Faccio, R.; Fernández-Werner, L.; Pardo, H.; Goyenola, C.;
3974 Ventura, O. N.; Mombrú, A. W. Electronic and Structural Distortions
3975 in Graphene Induced by Carbon Vacancies and Boron Doping. *J.*
3976 *Phys. Chem. C* **2010**, *114*, 18961–18971.
- 3977 (216) Mortazavi, B.; Ahzi, S. Molecular Dynamics Study on the
3978 Thermal Conductivity and Mechanical Properties of Boron Doped
3979 Graphene. *Solid State Commun.* **2012**, *152*, 1503–1507.
- 3980 (217) Bo, X.; Guo, L. Ordered Mesoporous Boron-Doped Carbons
3981 as Metal-Free Electrocatalysts for the Oxygen Reduction Reaction in
3982 Alkaline Solution. *Phys. Chem. Chem. Phys.* **2013**, *15*, 2459–2465.
- 3983 (218) Sreekanth, N.; Nazrulla, M. A.; Vineesh, T. V.; Sailaja, K.;
3984 Phani, K. L. Metal-Free Boron-Doped Graphene for Selective
3985 Electroreduction of Carbon Dioxide to Formic Acid/Formate.
3986 *Chem. Commun.* **2015**, *51*, 16061–16064.
- 3987 (219) Zhao, X.; Wang, A.; Yan, J.; Sun, G.; Sun, L.; Zhang, T.
3988 Synthesis and Electrochemical Performance of Heteroatom-Incorpo-
3989 rated Ordered Mesoporous Carbons. *Chem. Mater.* **2010**, *22*, 5463–
3990 5473.
- 3991 (220) Denis, P. A. Band Gap Opening of Monolayer and Bilayer
3992 Graphene Doped With Aluminium, Silicon, Phosphorus, and Sulfur.
3993 *Chem. Phys. Lett.* **2010**, *492*, 251–257.
- 3994 (221) Liu, X. F.; Antonietti, M. Moderating Black Powder Chemistry
3995 for the Synthesis of Doped and Highly Porous Graphene Nano-
3996 platelets and Their Use in Electrocatalysis. *Adv. Mater.* **2013**, *25*,
3997 6284–6290.
- 3998 (222) Zhou, Y. G.; Zu, X. T.; Gao, F.; Xiao, H. Y.; Lv, H. F.
3999 Electronic and Magnetic Properties of Graphene Absorbed With S
4000 Atom: A First-Principles Study. *J. Appl. Phys.* **2009**, *105*, 104311.
- 4001 (223) Qje, L.; Chen, W.; Xiong, X.; Hu, C.; Zou, F.; Hu, P.; Huang,
4002 Y. Sulfur-Doped Carbon With Enlarged Interlayer Distance as a High-
4003 Performance Anode Material for Sodium-Ion Batteries. *Adv. Sci.* **2015**,
4004 *2*, 1500195.
- 4005 (224) Yang, Z.; Yao, Z.; Li, G.; Fang, G.; Nie, H.; Liu, Z.; Zhou, X.;
4006 Chen, X. a.; Huang, S. Sulfur-Doped Graphene as an Efficient Metal-
4007 free Cathode Catalyst for Oxygen Reduction. *ACS Nano* **2012**, *6*,
4008 205–211.
- 4009 (225) Zhang, L.; Niu, J.; Li, M.; Xia, Z. Catalytic Mechanisms of
4010 Sulfur-Doped Graphene as Efficient Oxygen Reduction Reaction
4011 Catalysts for Fuel Cells. *J. Phys. Chem. C* **2014**, *118*, 3545–3553.
- 4012 (226) Inamdar, S.; Choi, H.-S.; Wang, P.; Song, M. Y.; Yu, J.-S.
4013 Sulfur-Containing Carbon by Flame Synthesis as Efficient Metal-Free
4014 Electrocatalyst for Oxygen Reduction Reaction. *Electrochem. Commun.*
4015 **2013**, *30*, 9–12.
- 4016 (227) Wang, H.-m.; Wang, H.-x.; Chen, Y.; Liu, Y.-j.; Zhao, J.-x.; Cai,
4017 Q.-h.; Wang, X.-z. Phosphorus-Doped Graphene and (8, 0) Carbon
4018 Nanotube: Structural, Electronic, Magnetic Properties, and Chemical
4019 Reactivity. *Appl. Surf. Sci.* **2013**, *273*, 302–309.
- (228) Wang, J.; Yang, Z.; Pan, F.; Zhong, X.; Liu, X.; Gu, L.; Yu, Y.
Phosphorus-Doped Porous Carbon Derived From Rice Husk as
Anode for Lithium Ion Batteries. *RSC Adv.* **2015**, *5*, 55136–55142.
- (229) Yang, Y.; Tang, D.-M.; Zhang, C.; Zhang, Y.; Liang, Q.; Chen,
S.; Weng, Q.; Zhou, M.; Xue, Y.; Liu, J.; Wu, J.; Cui, Q. H.; Lian, C.;
Hou, G.; Yuan, F.; Bando, Y.; Golberg, D.; Wang, X. “Protrusions” or
“Holes” in Graphene: Which Is the Better Choice for Sodium Ion
Storage? *Energy Environ. Sci.* **2017**, *10*, 979–986.
- (230) Liu, Z. W.; Peng, F.; Wang, H. J.; Yu, H.; Zheng, W. X.; Yang,
J. Phosphorus-Doped Graphite Layers With High Electrocatalytic
Activity for the O₂ Reduction in an Alkaline Medium. *Angew. Chem.,*
Int. Ed. **2011**, *50*, 3257–3261.
- (231) Yang, D. S.; Bhattacharjya, D.; Inamdar, S.; Park, J.; Yu, J. S.
Phosphorus-Doped Ordered Mesoporous Carbons With Different
Lengths As Efficient Metal-Free Electrocatalysts for Oxygen
Reduction Reaction in Alkaline Media. *J. Am. Chem. Soc.* **2012**, *134*,
16127–16130.
- (232) Yang, N.; Zheng, X.; Li, L.; Li, J.; Wei, Z. Influence of
Phosphorus Configuration on Electronic Structure and Oxygen
Reduction Reactions of Phosphorus-Doped Graphene. *J. Phys.*
Chem. C **2017**, *121*, 19321–19328.
- (233) Patel, M. A.; Luo, F.; Khoshi, M. R.; Rabie, E.; Zhang, Q.;
Flach, C. R.; Mendelsohn, R.; Garfunkel, E.; Szostak, M.; He, H. P.
Doped Porous Carbon as Metal Free Catalysts for Selective Aerobic
Oxidation With an Unexpected Mechanism. *ACS Nano* **2016**, *10*,
2305–2315.
- (234) Gao, R.; Pan, L.; Wang, H.; Zhang, X.; Wang, L.; Zou, J.-J.
Ultradispersed Nickel Phosphide on Phosphorus-Doped Carbon With
Tailored D-Band Center for Efficient and Chemoselective Hydro-
genation of Nitroarenes. *ACS Catal.* **2018**, *8*, 8420–8429.
- (235) Li, X. H.; Antonietti, M. Polycondensation of Boron- and
Nitrogen-Codoped Holey Graphene Monoliths From Molecules:
Carbocatalysts for Selective Oxidation. *Angew. Chem., Int. Ed.* **2013**,
52, 4572–4576.
- (236) Ozaki, J.-i.; Anahara, T.; Kimura, N.; Oya, A. Simultaneous
Doping of Boron and Nitrogen Into a Carbon to Enhance Its Oxygen
Reduction Activity in Proton Exchange Membrane Fuel Cells. *Carbon*
2006, *44*, 3358–3361.
- (237) Ozaki, J.-i.; Kimura, N.; Anahara, T.; Oya, A. Preparation and
Oxygen Reduction Activity of BN-Doped Carbons. *Carbon* **2007**, *45*,
1847–1853.
- (238) Zheng, Y.; Jiao, Y.; Ge, L.; Jaroniec, M.; Qiao, S. Z. Two-Step
Boron and Nitrogen Doping in Graphene for Enhanced Synergistic
Catalysis. *Angew. Chem., Int. Ed.* **2013**, *52*, 3110–3116.
- (239) Wang, S.; Zhang, L.; Xia, Z.; Roy, A.; Chang, D. W.; Baek, J.
B.; Dai, L. BCN Graphene As Efficient Metal-Free Electrocatalyst for
the Oxygen Reduction Reaction. *Angew. Chem., Int. Ed.* **2012**, *51*,
4209–4212.
- (240) Welch, G. C.; Juan, R. R. S.; Masuda, J. D.; Stephan, D. W.
Reversible, Metal-Free Hydrogen Activation. *Science* **2006**, *314*,
1124–1126.
- (241) Zhang, S.; Huang, Z. Q.; Ma, Y.; Gao, W.; Li, J.; Cao, F.; Li,
L.; Chang, C. R.; Qu, Y. Solid Frustrated-Lewis-Pair Catalysts
Constructed by Regulations on Surface Defects of Porous Nanorods
of CeO₂. *Nat. Commun.* **2017**, *8*, 15266.
- (242) Ma, Y.; Zhang, S.; Chang, C.-R.; Huang, Z.-Q.; Ho, J. C.; Qu,
Y. Semi-Solid and Solid Frustrated Lewis Pair Catalysts. *Chem. Soc.*
Rev. **2018**, *47*, 5541–5553.
- (243) Fiorio, J. L.; Gonçalves, R. V.; Teixeira-Neto, E.; Ortuño, M.
A.; López, N.; Rossi, L. M. Accessing Frustrated Lewis Pair Chemistry
Through Robust Gold@N-Doped Carbon for Selective Hydro-
genation of Alkynes. *ACS Catal.* **2018**, *8*, 3516–3524.
- (244) Primo, A.; Neatu, F.; Florea, M.; Parvulescu, V.; Garcia, H.
Graphenes in the Absence of Metals as Carbocatalysts for Selective
Acetylene Hydrogenation and Alkene Hydrogenation. *Nat. Commun.*
2014, *5*, 5291.
- (245) Sun, X.; Li, B.; Liu, T.; Song, J.; Su, D. S. Designing Graphene
as a New Frustrated Lewis Pair Catalyst for Hydrogen Activation by
Co-Doping. *Phys. Chem. Chem. Phys.* **2016**, *18*, 11120–11124.

- 4089 (246) Qian, W.; Sun, F.; Xu, Y.; Qiu, L.; Liu, C.; Wang, S.; Yan, F. Human Hair-Derived Carbon Flakes for Electrochemical Super-4100 capacitors. *Energy Environ. Sci.* **2014**, *7*, 379–386.
- 4092 (247) Qiao, Y.; Ma, M.; Liu, Y.; Li, S.; Lu, Z.; Yue, H.; Dong, H.; 4093 Cao, Z.; Yin, Y.; Yang, S. First-Principles and Experimental Study of 4094 Nitrogen/Sulfur Co-Doped Carbon Nanosheets As Anodes for 4095 Rechargeable Sodium Ion Batteries. *J. Mater. Chem. A* **2016**, *4*, 4096 15565–15574.
- 4097 (248) Su, Y.; Yao, Z.; Zhang, F.; Wang, H.; Mics, Z.; Cánovas, E.; 4098 Bonn, M.; Zhuang, X.; Feng, X. Sulfur-Enriched Conjugated Polymer 4099 Nanosheet Derived Sulfur and Nitrogen Co-Doped Porous Carbon 4100 Nanosheets as Electrocatalysts for Oxygen Reduction Reaction and 4101 Zinc–Air Battery. *Adv. Funct. Mater.* **2016**, *26*, 5893–5902.
- 4102 (249) Liang, J.; Jiao, Y.; Jaroniec, M.; Qiao, S. Z. Sulfur and Nitrogen 4103 Dual-Doped Mesoporous Graphene Electrocatalyst for Oxygen 4104 Reduction With Synergistically Enhanced Performance. *Angew. 4105 Chem., Int. Ed.* **2012**, *51*, 11496–11500.
- 4106 (250) Ito, Y.; Cong, W.; Fujita, T.; Tang, Z.; Chen, M. High 4107 Catalytic Activity of Nitrogen and Sulfur Co-Doped Nanoporous 4108 Graphene in the Hydrogen Evolution Reaction. *Angew. Chem., Int. Ed.* 4109 **2015**, *54*, 2131–2136.
- 4110 (251) Qu, K.; Zheng, Y.; Zhang, X.; Davey, K.; Dai, S.; Qiao, S. Z. 4111 Promotion of Electrocatalytic Hydrogen Evolution Reaction on 4112 Nitrogen-Doped Carbon Nanosheets With Secondary Heteroatoms. 4113 *ACS Nano* **2017**, *11*, 7293–7300.
- 4114 (252) Jin, Z. P.; Nie, H. G.; Yang, Z.; Zhang, J.; Liu, Z.; Xu, X. J.; 4115 Huang, S. M. Metal-Free Selenium Doped Carbon Nanotube/ 4116 Graphene Networks as a Synergistically Improved Cathode Catalyst 4117 for Oxygen Reduction Reaction. *Nanoscale* **2012**, *4*, 6455–6460.
- 4118 (253) Zhu, Y. P.; Liu, Y. P.; Yuan, Z. Y. Biochemistry-Inspired Direct 4119 Synthesis of Nitrogen and Phosphorus Dual-Doped Microporous 4120 Carbon Spheres for Enhanced Electrocatalysis. *Chem. Commun.* **2016**, 4121 52, 2118–2121.
- 4122 (254) Lin, D.; Hu, C.; Chen, H.; Qu, L.; Dai, L. Microporous N,P- 4123 Codoped Graphitic Nanosheets as an Efficient Electrocatalyst for 4124 Oxygen Reduction in Whole pH Range for Energy Conversion and 4125 Biosensing Dissolved Oxygen. *Chem. - Eur. J.* **2018**, *24*, 18487.
- 4126 (255) Choi, C. H.; Park, S. H.; Woo, S. I. Binary and Ternary 4127 Doping of Nitrogen, Boron, and Phosphorus Into Carbon for 4128 Enhancing Electrochemical Oxygen Reduction Activity. *ACS Nano* 4129 **2012**, *6*, 7084–7091.
- 4130 (256) Yang, S.; Peng, L.; Huang, P.; Wang, X.; Sun, Y.; Cao, C.; 4131 Song, W. Nitrogen, Phosphorus, and Sulfur Co-Doped Hollow 4132 Carbon Shell as Superior Metal-Free Catalyst for Selective Oxidation 4133 of Aromatic Alkanes. *Angew. Chem., Int. Ed.* **2016**, *55*, 4016–4020.
- 4134 (257) Soll, S.; Fellinger, T. P.; Wang, X. C.; Zhao, Q.; Antonietti, 4135 M.; Yuan, J. Y. Water Dispersible, Highly Graphitic and Nitrogen- 4136 Doped Carbon Nanobubbles. *Small* **2013**, *9*, 4135–4141.
- 4137 (258) Wang, T.; Sun, Y.; Zhang, L. L.; Li, K. Q.; Yi, Y. K.; Song, S. 4138 Y.; Li, M. T.; Qiao, Z. A.; Dai, S. Space-Confined Polymerization: 4139 Controlled Fabrication of Nitrogen-Doped Polymer and Carbon 4140 Microspheres With Refined Hierarchical Architectures. *Adv. Mater.* 4141 **2019**, *31*, 1807876.
- 4142 (259) Liu, J.; Qiao, S. Z.; Liu, H.; Chen, J.; Orpe, A.; Zhao, D. Y.; 4143 Lu, G. Q. Extension of the Stöber Method to the Preparation of 4144 Monodisperse Resorcinol-Formaldehyde Resin Polymer and Carbon 4145 Spheres. *Angew. Chem., Int. Ed.* **2011**, *50*, 5947–5951.
- 4146 (260) Choma, J.; Jamiola, D.; Augustynek, K.; Marszewski, M.; Gao, 4147 M.; Jaroniec, M. New Opportunities in Stober Synthesis: Preparation 4148 of Microporous and Mesoporous Carbon Spheres. *J. Mater. Chem.* 4149 **2012**, *22*, 12636–12642.
- 4150 (261) Molaei, M. J. Carbon Quantum Dots and Their Biomedical 4151 and Therapeutic Applications: A Review. *RSC Adv.* **2019**, *9*, 6460– 4152 6481.
- 4153 (262) Zhou, Y. Q.; Mintz, K. J.; Sharma, S. K.; Leblanc, R. M. 4154 Carbon Dots: Diverse Preparation, Application, and Perspective in 4155 Surface Chemistry. *Langmuir* **2019**, *35*, 9115–9132.
- (263) Wang, X.; Feng, Y. Q.; Dong, P. P.; Huang, J. F. A Mini 4156 Review on Carbon Quantum Dots: Preparation, Properties, and 4157 Electrochemical Application. *Front. Chem.* **2019**, *7*, 671.
- (264) Chu, K. W.; Lee, S. L.; Chang, C. J.; Liu, L. Y. Recent Progress 4159 of Carbon Dot Precursors and Photocatalysis Applications. *Polymers* 4160 **2019**, *11*, 689.
- (265) Yang, Y.; Cui, J.; Zheng, M.; Hu, C.; Tan, S.; Xiao, Y.; Yang, 4162 Q.; Liu, Y. One-Step Synthesis of Amino-Functionalized Fluorescent 4163 Carbon Nanoparticles by Hydrothermal Carbonization of Chitosan. 4164 *Chem. Commun.* **2012**, *48*, 380–382.
- (266) Zhou, L.; He, B.; Huang, J. Amphibious Fluorescent Carbon 4166 Dots: One-Step Green Synthesis and Application for Light-Emitting 4167 Polymer Nanocomposites. *Chem. Commun.* **2013**, *49*, 8078–8080.
- (267) Pires, N. R.; Santos, C. M. W.; Sousa, R. R.; Paula, R. C. M. d.; 4169 Cunha, P. L. R.; Feitosa, J. P. A. Novel and Fast Microwave-Assisted 4170 Synthesis of Carbon Quantum Dots From Raw Cashew Gum. *J. 4171 Brazil. Chem. Soc.* **2015**, *26*, 1274–1282.
- (268) Shen, J.; Li, Q.; Zhang, Y.; She, X.-j.; Wang, C.-F.; Chen, S. 4173 Nitrogen-Doped Carbon Dots Derived From Polyamidoamine 4174 Dendrimer. *RSC Adv.* **2016**, *6*, 59702–59707.
- (269) Tao, S.; Song, Y.; Zhu, S.; Shao, J.; Yang, B. A New Type of 4176 Polymer Carbon Dots With High Quantum Yield: From Synthesis to 4177 Investigation on Fluorescence Mechanism. *Polymer* **2017**, *116*, 472– 4178 478.
- (270) Wang, W.; Lu, Y.; Yue, Z.; Liu, W.; Cao, Z. Ultrastable Core– 4180 Shell Structured Nanoparticles Directly Made From Zwitterionic 4181 Polymers. *Chem. Commun.* **2014**, *50*, 15030–15033.
- (271) Li, W.; Chu, K.; Liu, L. Zwitterionic Gel Coating Endows 4183 Gold Nanoparticles With Ultrastability. *Langmuir* **2019**, *35*, 1369– 4184 1378.
- (272) Li, W.; Liu, Q.; Liu, L. Antifouling Gold Surfaces Grafted 4186 With Aspartic Acid and Glutamic Acid Based Zwitterionic Polymer 4187 Brushes. *Langmuir* **2014**, *30*, 12619–12626.
- (273) Feng, S. S.; Li, W.; Shi, Q.; Li, Y. H.; Chen, J. C.; Ling, Y.; 4189 Asiri, A. M.; Zhao, D. Y. Synthesis of Nitrogen-Doped Hollow Carbon 4190 Nanospheres for CO₂ Capture. *Chem. Commun.* **2014**, *50*, 329–331.
- (274) Peng, L.; Hung, C. T.; Wang, S. W.; Zhang, X. M.; Zhu, X. H.; 4192 Zhao, Z. W.; Wang, C. Y.; Tang, Y.; Li, W.; Zhao, D. Y. Versatile 4193 Nanoemulsion Assembly Approach to Synthesize Functional Meso- 4194 porous Carbon Nanospheres With Tunable Pore Sizes and 4195 Architectures. *J. Am. Chem. Soc.* **2019**, *141*, 7073–7080.
- (275) White, R. J.; Yoshizawa, N.; Antonietti, M.; Titirici, M. M. A 4197 Sustainable Synthesis of Nitrogen-Doped Carbon Aerogels. *Green 4198 Chem.* **2011**, *13*, 2428–2434.
- (276) Rahmatika, A. M.; Yuan, W.; Arif, A. F.; Balgis, R.; Miyajima, 4200 K.; Anilkumar, G. M.; Okuyama, K.; Ogi, T. Energy-Efficient 4201 Templating Method for the Industrial Production of Porous Carbon 4202 Particles by a Spray Pyrolysis Process Using Poly(Methyl 4203 Methacrylate). *Ind. Eng. Chem. Res.* **2018**, *57*, 11335–11341.
- (277) Titirici, M. M.; White, R. J.; Brun, N.; Budarin, V. L.; Su, D. 4205 S.; del Monte, F.; Clark, J. H.; MacLachlan, M. J. Sustainable Carbon 4206 Materials. *Chem. Soc. Rev.* **2015**, *44*, 250–290.
- (278) Liu, D. Y.; Peng, X. X.; Wu, B. H.; Zheng, X. Y.; Chuong, T. 4208 T.; Li, J. L.; Sun, S. G.; Stucky, G. D. Uniform Concave Polystyrene- 4209 Carbon Core-Shell Nanospheres by a Swelling Induced Buckling 4210 Process. *J. Am. Chem. Soc.* **2015**, *137*, 9772–9775.
- (279) Zhao, T.; Zhu, X.; Hung, C.-T.; Wang, P.; Elzathary, A.; Al- 4212 Khalaf, A. A.; Hozzein, W. N.; Zhang, F.; Li, X.; Zhao, D. Spatial 4213 Isolation of Carbon and Silica in a Single Janus Mesoporous 4214 Nanoparticle With Tunable Amphiphilicity. *J. Am. Chem. Soc.* **2018**, 4215 *140*, 10009–10015.
- (280) Lee, J. H.; Oh, S. H.; Jeong, S. Y.; Kang, Y. C.; Cho, J. S. 4217 Rattle-Type Porous Sn/C Composite Fibers With Uniformly 4218 Distributed Nanovoids Containing Metallic Sn Nanoparticles for 4219 High-Performance Anode Materials in Lithium-Ion Batteries. *Nano- 4220 scale* **2018**, *10*, 21483–21491.
- (281) Chen, C. H.; Xie, L.; Wang, Y. Recent Advances in the 4222 Synthesis and Applications of Anisotropic Carbon and Silica-Based 4223 Nanoparticles. *Nano Res.* **2019**, *12*, 1267–1278.

- 4225 (282) Pei, F.; An, T. H.; Zang, J.; Zhao, X. J.; Fang, X. L.; Zheng, M. S.; Dong, Q. F.; Zheng, N. F. From Hollow Carbon Spheres to N-Doped Hollow Porous Carbon Bowls: Rational Design of Hollow Carbon Host for Li-S Batteries. *Adv. Energy Mater.* **2016**, *6*, 1502539.
- 4229 (283) Chen, C. H.; Wang, H. Y.; Han, C. L.; Deng, J.; Wang, J.; Li, M. M.; Tang, M. H.; Jin, H. Y.; Wang, Y. Asymmetric Flasklike Hollow Carbonaceous Nanoparticles Fabricated by the Synergistic Interaction Between Soft Template and Biomass. *J. Am. Chem. Soc.* **2017**, *139*, 2657–2663.
- 4234 (284) Frank, E.; Stuedle, L. M.; Ingildeev, D.; Sporr, J. M.; Buchmeiser, M. R. Carbon Fibers: Precursor Systems, Processing, Structure, and Properties. *Angew. Chem., Int. Ed.* **2014**, *53*, 5262–5298.
- 4238 (285) Li, X.; Lin, Z.-H.; Cheng, G.; Wen, X.; Liu, Y.; Niu, S.; Wang, Z. L. 3D Fiber-Based Hybrid Nanogenerator for Energy Harvesting and as a Self-Powered Pressure Sensor. *ACS Nano* **2014**, *8*, 10674–10681.
- 4242 (286) Saetia, K.; Schnorr, J. M.; Mannarino, M. M.; Kim, S. Y.; Rutledge, G. C.; Swager, T. M.; Hammond, P. T. Spray-Layer-by-Layer Carbon Nanotube/Electrospun Fiber Electrodes for Flexible Chemiresistive Sensor Applications. *Adv. Funct. Mater.* **2014**, *24*, 4246–4250.
- 4247 (287) Liu, Y.; Zhang, L.; Guo, Q.; Hou, H.; You, T. Enzyme-Free Ethanol Sensor Based on Electrospun Nickel Nanoparticle-Loaded Carbon Fiber Paste Electrode. *Anal. Chim. Acta* **2010**, *663*, 153–157.
- 4250 (288) Prasad, B. B.; Madhuri, R.; Tiwari, M. P.; Sharma, P. S. Imprinted Polymer–Carbon Consolidated Composite Fiber Sensor for Substrate-Selective Electrochemical Sensing of Folic Acid. *Biosens. Bioelectron.* **2010**, *25*, 2140–2148.
- 4254 (289) Sebastian, J.; Schehl, N.; Bouchard, M.; Boehle, M.; Li, L.; Lagounov, A.; Lafdi, K. Health Monitoring of Structural Composites With Embedded Carbon Nanotube Coated Glass Fiber Sensors. *Carbon* **2014**, *66*, 191–200.
- 4258 (290) Liao, Q.; Mohr, M.; Zhang, X.; Zhang, Z.; Zhang, Y.; Fecht, H.-J. Carbon Fiber–ZnO Nanowire Hybrid Structures for Flexible and Adaptable Strain Sensors. *Nanoscale* **2013**, *5*, 12350–12355.
- 4261 (291) Di, J.; Zhang, X.; Yong, Z.; Zhang, Y.; Li, D.; Li, R.; Li, Q. Carbon-Nanotube Fibers for Wearable Devices and Smart Textiles. *Adv. Mater.* **2016**, *28*, 10529–10538.
- 4264 (292) Guo, W.; Liu, C.; Zhao, F.; Sun, X.; Yang, Z.; Chen, T.; Chen, X.; Qiu, L.; Hu, X.; Peng, H. A Novel Electromechanical Actuation Mechanism of a Carbon Nanotube Fiber. *Adv. Mater.* **2012**, *24*, 5379–5384.
- 4268 (293) Lu, L.; Liu, J.; Hu, Y.; Zhang, Y.; Randriamahazaka, H.; Chen, W. Highly Stable Air Working Bimorph Actuator Based on a Graphene Nanosheet/Carbon Nanotube Hybrid Electrode. *Adv. Mater.* **2012**, *24*, 4317–4321.
- 4272 (294) Meng, F.; Zhang, X.; Li, R.; Zhao, J.; Xuan, X.; Wang, X.; Zou, J.; Li, Q. Electro-Induced Mechanical and Thermal Responses of Carbon Nanotube Fibers. *Adv. Mater.* **2014**, *26*, 2480–2485.
- 4275 (295) Chen, T.; Dai, L. Macroscopic Graphene Fibers Directly Assembled From Cvd-Grown Fiber-Shaped Hollow Graphene Tubes. *Angew. Chem., Int. Ed.* **2015**, *54*, 14947–14950.
- 4278 (296) Cheng, H.; Liu, J.; Zhao, Y.; Hu, C.; Zhang, Z.; Chen, N.; Jiang, L.; Qu, L. Graphene Fibers With Predetermined Deformation as Moisture-Triggered Actuators and Robots. *Angew. Chem., Int. Ed.* **2013**, *52*, 10482–10486.
- 4282 (297) Wang, H. G.; Yuan, S.; Ma, D. L.; Zhang, X. B.; Yan, J. M. Electrospun Materials for Lithium and Sodium Rechargeable Batteries: From Structure Evolution to Electrochemical Performance. *Energy Environ. Sci.* **2015**, *8*, 1660–1681.
- 4286 (298) Fu, Y.; Cai, X.; Wu, H.; Lv, Z.; Hou, S.; Peng, M.; Yu, X.; Zou, D. Fiber Supercapacitors Utilizing Pen Ink for Flexible/Wearable Energy Storage. *Adv. Mater.* **2012**, *24*, 5713–5718.
- 4289 (299) Cakici, M.; Kakarla, R. R.; Alonso-Marroquin, F. Advanced Electrochemical Energy Storage Supercapacitors Based on the Flexible Carbon Fiber Fabric-Coated With Uniform Coral-Like MnO₂ Structured Electrodes. *Chem. Eng. J.* **2017**, *309*, 151–158.
- (300) Liu, H.-J.; Wang, X.-M.; Cui, W.-J.; Dou, Y.-Q.; Zhao, D.-Y.; Xia, Y.-Y. Highly Ordered Mesoporous Carbon Nanofiber Arrays From a Crab Shell Biological Template and Its Application in Supercapacitors and Fuel Cells. *J. Mater. Chem.* **2010**, *20*, 4223–4230.
- (301) Cai, X.; Peng, M.; Yu, X.; Fu, Y.; Zou, D. Flexible Planar/Fiber-Architected Supercapacitors for Wearable Energy Storage. *J. Mater. Chem. C* **2014**, *2*, 1184–1200.
- (302) Wu, F.; Dong, R.; Bai, Y.; Li, Y.; Chen, G.; Wang, Z.; Wu, C. Phosphorus-Doped Hard Carbon Nanofibers Prepared by Electrospinning as an Anode in Sodium-Ion Batteries. *ACS Appl. Mater. Interfaces* **2018**, *10*, 21335–21342.
- (303) Shi, R. Y.; Han, C. P.; Xu, X. F.; Qin, X. Y.; Xu, L.; Li, H. F.; Li, J. Q.; Wong, C. P.; Li, B. H. Electrospun N-Doped Hierarchical Porous Carbon Nanofiber With Improved Degree of Graphitization for High-Performance Lithium Ion Capacitor. *Chem. - Eur. J.* **2018**, *24*, 10460–10467.
- (304) Yuan, J.; Márquez, A. G.; Reinacher, J.; Giordano, C.; Janek, J.; Antonietti, M. Nitrogen-Doped Carbon Fibers and Membranes by Carbonization of Electrospun Poly(Ionic Liquid)s. *Polym. Chem.* **2011**, *2*, 1654.
- (305) Zhang, S. B.; Wu, Q. L.; Tang, L.; Hu, Y. G.; Wang, M. Y.; Zhao, J. K.; Li, M.; Han, J. Y.; Liu, X.; Wang, H. Individual High-Quality N-Doped Carbon Nanotubes Embedded With Nonprecious Metal Nanoparticles Toward Electrochemical Reaction. *ACS Appl. Mater. Interfaces* **2018**, *10*, 39757–39767.
- (306) Lee, H.; Kim, B. J.; Kim, S. J.; Park, Y. K.; Jung, S. C. Enhanced Electrochemical Performance of Carbon Nanotube With Nitrogen and Iron Using Liquid Phase Plasma Process for Supercapacitor Applications. *Int. J. Mol. Sci.* **2018**, *19*, 3830.
- (307) Chen, Z.; Ye, S. J.; Evans, S. D.; Ge, Y. H.; Zhu, Z. F.; Tu, Y. F.; Yang, X. M. Confined Assembly of Hollow Carbon Spheres in Carbonaceous Nanotube: A Spheres-in-Tube Carbon Nanostructure With Hierarchical Porosity for High-Performance Supercapacitor. *Small* **2018**, *14*, 1704015.
- (308) Yin, F. X.; Ren, J.; Wu, G. Y.; Zhang, C. W.; Zhang, Y. G. Polypyrrole Nanowires With Ordered Large Mesopores: Synthesis, Characterization and Applications in Supercapacitor and Lithium/Sulfur Batteries. *Polymers* **2019**, *11*, 277.
- (309) Jones, C. W.; Koros, W. J. Carbon Molecular-Sieve Gas Separation Membranes: Preparation and Characterization Based on Polyimide Precursors. *Carbon* **1994**, *32*, 1419–1425.
- (310) Ismail, A. F.; David, L. I. B. A Review on the Latest Development of Carbon Membranes for Gas Separation. *J. Membr. Sci.* **2001**, *193*, 1–18.
- (311) Rodrigues, S. C.; Andrade, M.; Moffat, J.; Magalhaes, F. D.; Mendes, A. Carbon Membranes With Extremely High Separation Factors and Stability. *Energy Technol.* **2019**, *7*, 1801089.
- (312) Ye, Z.; Li, T.; Ma, G.; Dong, Y.; Zhou, X. Metal-Ion (Fe, V, CO, and Ni)-Doped MnO₂ Ultrathin Nanosheets Supported on Carbon Fiber Paper for the Oxygen Evolution Reaction. *Adv. Funct. Mater.* **2017**, *27*, 1704083.
- (313) Kong, D.; Wang, H.; Lu, Z.; Cui, Y. CoSe₂ Nanoparticles Grown on Carbon Fiber Paper: An Efficient and Stable Electrocatalyst for Hydrogen Evolution Reaction. *J. Am. Chem. Soc.* **2014**, *136*, 4897–4900.
- (314) Hou, D.; Zhou, W.; Liu, X.; Zhou, K.; Xie, J.; Li, G.; Chen, S. Pt Nanoparticles/MoS₂ Nanosheets/Carbon Fibers As Efficient Catalyst for the Hydrogen Evolution Reaction. *Electrochim. Acta* **2015**, *166*, 26–31.
- (315) Sawangphruk, M.; Krittayavathananon, A.; Chinwipas, N. Ultraporous Palladium on Flexible Graphene-Coated Carbon Fiber Paper as High-Performance Electro-Catalysts for the Electro-Oxidation of Ethanol. *J. Mater. Chem. A* **2013**, *1*, 1030–1034.
- (316) Wang, X.; Li, W.; Xiong, D.; Petrovykh, D. Y.; Liu, L. Bifunctional Nickel Phosphide Nanocatalysts Supported on Carbon Fiber Paper for Highly Efficient and Stable Overall Water Splitting. *Adv. Funct. Mater.* **2016**, *26*, 4067–4077.

- 4360 (317) Nyholm, L.; Nyström, G.; Mihranyan, A.; Strømme, M.
4361 Toward Flexible Polymer and Paper-Based Energy Storage Devices.
4362 *Adv. Mater.* **2011**, *23*, 3751–3769.
- 4363 (318) Yang, L.; Cheng, S.; Ding, Y.; Zhu, X.; Wang, Z. L.; Liu, M.
4364 Hierarchical Network Architectures of Carbon Fiber Paper Supported
4365 Cobalt Oxide Nanonet for High-Capacity Pseudocapacitors. *Nano*
4366 *Lett.* **2012**, *12*, 321–325.
- 4367 (319) Chmiola, J.; Largeot, C.; Taberna, P.-L.; Simon, P.; Gogotsi,
4368 Y. Monolithic Carbide-Derived Carbon Films for Micro-Super-
4369 capacitors. *Science* **2010**, *328*, 480.
- 4370 (320) Saufi, S. M.; Ismail, A. F. Fabrication of Carbon Membranes
4371 for Gas Separation—A Review. *Carbon* **2004**, *42*, 241–259.
- 4372 (321) Vu, D. Q.; Koros, W. J.; Miller, S. J. High Pressure CO₂/CH₄
4373 Separation Using Carbon Molecular Sieve Hollow Fiber Membranes.
4374 *Ind. Eng. Chem. Res.* **2002**, *41*, 367–380.
- 4375 (322) Zhang, C.; Wenz, G. B.; Williams, P. J.; Mayne, J. M.; Liu, G.;
4376 Koros, W. J. Purification of Aggressive Supercritical Natural Gas
4377 Using Carbon Molecular Sieve Hollow Fiber Membranes. *Ind. Eng.*
4378 *Chem. Res.* **2017**, *56*, 10482–10490.
- 4379 (323) Wei, G.; Yu, H.; Quan, X.; Chen, S.; Zhao, H.; Fan, X.
4380 Constructing All Carbon Nanotube Hollow Fiber Membranes With
4381 Improved Performance in Separation and Antifouling for Water
4382 Treatment. *Environ. Sci. Technol.* **2014**, *48*, 8062–8068.
- 4383 (324) Liu, Q.; Wang, Y.; Dai, L.; Yao, J. Scalable Fabrication of
4384 Nanoporous Carbon Fiber Films as Bifunctional Catalytic Electrodes
4385 for Flexible Zn-Air Batteries. *Adv. Mater.* **2016**, *28*, 3000–3006.
- 4386 (325) Men, Y.; Siebenbürger, M.; Qiu, X.; Antonietti, M.; Yuan, J.
4387 Low Fractions of Ionic Liquid or Poly(ionic Liquid) Can Activate
4388 Polysaccharide Biomass Into Shaped, Flexible and Fire-Retardant
4389 Porous Carbons. *J. Mater. Chem. A* **2013**, *1*, 11887.
- 4390 (326) Muench, F.; Seidl, T.; Rauber, M.; Peter, B.; Brotz, J.; Krause,
4391 M.; Trautmann, C.; Roth, C.; Katusic, S.; Ensinger, W. Hierarchically
4392 Porous Carbon Membranes Containing Designed Nanochannel
4393 Architectures Obtained by Pyrolysis of Ion-Track Etched Polyimide.
4394 *Mater. Chem. Phys.* **2014**, *148*, 846–853.
- 4395 (327) Reddy, A. L. M.; Gowda, S. R.; Shaijumon, M. M.; Ajayan, P.
4396 M. Hybrid Nanostructures for Energy Storage Applications. *Adv.*
4397 *Mater.* **2012**, *24*, 5045–5064.
- 4398 (328) Yoon, T.; Chae, C.; Sun, Y.-K.; Zhao, X.; Kung, H. H.; Lee, J.
4399 K. Bottom-Up in Situ Formation of Fe₃O₄ Nanocrystals in a Porous
4400 Carbon Foam for Lithium-Ion Battery Anodes. *J. Mater. Chem.* **2011**,
4401 *21*, 17325–17330.
- 4402 (329) Chen, M.; Liu, J.; Chao, D.; Wang, J.; Yin, J.; Lin, J.; Jin Fan,
4403 H.; Xiang Shen, Z. Porous α-Fe₂O₃ Nanorods Supported on Carbon
4404 Nanotubes-Graphene Foam as Superior Anode for Lithium Ion
4405 Batteries. *Nano Energy* **2014**, *9*, 364–372.
- 4406 (330) Wang, W.; Guo, S.; Penchev, M.; Ruiz, I.; Bozhilov, K. N.;
4407 Yan, D.; Ozkan, M.; Ozkan, C. S. Three Dimensional Few Layer
4408 Graphene and Carbon Nanotube Foam Architectures for High
4409 Fidelity Supercapacitors. *Nano Energy* **2013**, *2*, 294–303.
- 4410 (331) Kim, D.; Kim, D. W.; Buyukcakir, O.; Kim, M.-K.;
4411 Polychronopoulou, K.; Coskun, A. Highly Hydrophobic Zif-8/Carbon
4412 Nitride Foam With Hierarchical Porosity for Oil Capture and
4413 Chemical Fixation of CO₂. *Adv. Funct. Mater.* **2017**, *27*, 1700706.
- 4414 (332) Singh, A. K.; Lu, J.; Aga, R. S.; Yakobson, B. I. Hydrogen
4415 Storage Capacity of Carbon-Foams: Grand Canonical Monte Carlo
4416 Simulations. *J. Phys. Chem. C* **2011**, *115*, 2476–2482.
- 4417 (333) Dong, X.; Chen, J.; Ma, Y.; Wang, J.; Chan-Park, M. B.; Liu,
4418 X.; Wang, L.; Huang, W.; Chen, P. Superhydrophobic and
4419 Superoleophilic Hybrid Foam of Graphene and Carbon Nanotube
4420 for Selective Removal of Oils or Organic Solvents From the Surface of
4421 Water. *Chem. Commun.* **2012**, *48*, 10660–10662.
- 4422 (334) Lee, C.-G.; Jeon, J.-W.; Hwang, M.-J.; Ahn, K.-H.; Park, C.;
4423 Choi, J.-W.; Lee, S.-H. Lead and Copper Removal From Aqueous
4424 Solutions Using Carbon Foam Derived From Phenol Resin.
4425 *Chemosphere* **2015**, *130*, 59–65.
- 4426 (335) Lee, C.-G.; Lee, S.; Park, J.-A.; Park, C.; Lee, S. J.; Kim, S.-B.;
4427 An, B.; Yun, S.-T.; Lee, S.-H.; Choi, J.-W. Removal of Copper, Nickel
4428 and Chromium Mixtures From Metal Plating Wastewater by
Adsorption With Modified Carbon Foam. *Chemosphere* **2017**, *166*, 4429
203–211. 4430
- (336) Velasco, L. F.; Tsytsarski, B.; Petrova, B.; Budinova, T.;
4431 Petrov, N.; Parra, J. B.; Ania, C. O. Carbon Foams as Catalyst
4432 Supports for Phenol Photodegradation. *J. Hazard. Mater.* **2010**, *184*,
4433 843–848. 4434
- (337) Burke, D. M.; Morris, M. A.; Holmes, J. D. Chemical
4435 Oxidation of Mesoporous Carbon Foams for Lead Ion Adsorption.
4436 *Sep. Purif. Technol.* **2013**, *104*, 150–159. 4437
- (338) Yuan, Y.; Ding, Y.; Wang, C.; Xu, F.; Lin, Z.; Qin, Y.; Li, Y.;
4438 Yang, M.; He, X.; Peng, Q.; Li, Y. Multifunctional Stiff Carbon Foam
4439 Derived from Bread. *ACS Appl. Mater. Interfaces* **2016**, *8*, 16852–
4440 16861. 4441
- (339) Hao, G. P.; Li, W. C.; Qian, D.; Wang, G. H.; Zhang, W. P.;
4442 Zhang, T.; Wang, A. Q.; Schuth, F.; Bongard, H. J.; Lu, A. H.
4443 Structurally Designed Synthesis of Mechanically Stable Poly-
4444 (benzoxazine-co-Resol)-Based Porous Carbon Monoliths and Their
4445 Application As High-Performance CO₂ Capture Sorbents. *J. Am.*
4446 *Chem. Soc.* **2011**, *133*, 11378–11388. 4447
- (340) Chen, J.; Xu, J.; Zhou, S.; Zhao, N.; Wong, C.-P. Nitrogen-
4448 Doped Hierarchically Porous Carbon Foam: A Free-Standing
4449 Electrode and Mechanical Support for High-Performance Super-
4450 capacitors. *Nano Energy* **2016**, *25*, 193–202. 4451
- (341) Sakintuna, B.; Yurum, Y. Templated Porous Carbons: A
4452 Review Article. *Ind. Eng. Chem. Res.* **2005**, *44*, 2893–2902. 4453
- (342) Zbair, M.; Ainassaari, K.; El Assal, Z.; Ojala, S.; El Ouahedy,
4454 N.; Keiski, R. L.; Bensitel, M.; Brahm, R. Steam Activation of Waste
4455 Biomass: Highly Microporous Carbon, Optimization of Bisphenol A,
4456 and Diuron Adsorption by Response Surface Methodology. *Environ.*
4457 *Sci. Pollut. Res.* **2018**, *25*, 35657–35671. 4458
- (343) MolinaSabio, M.; Gonzalez, M. T.; RodriguezReinoso, F.;
4459 SepulvedaEscribano, A. Effect of Steam and Carbon Dioxide
4460 Activation in the Micropore Size Distribution of Activated Carbon.
4461 *Carbon* **1996**, *34*, 505–509. 4462
- (344) Wang, J. C.; Kaskel, S. KOH Activation of Carbon-Based
4463 Materials for Energy Storage. *J. Mater. Chem.* **2012**, *22*, 23710–23725. 4464
- (345) Gorka, J.; Jaroniec, M. Hierarchically Porous Phenolic Resin-
4465 Based Carbons Obtained by Block Copolymer-Colloidal Silica
4466 Templating and Post-Synthesis Activation With Carbon Dioxide
4467 and Water Vapor. *Carbon* **2011**, *49*, 154–160. 4468
- (346) Shao, Y. Y.; Wang, X. Q.; Engelhard, M.; Wang, C. M.; Dai, S.;
4469 Liu, J.; Yang, Z. G.; Lin, Y. H. Nitrogen-Doped Mesoporous Carbon
4470 for Energy Storage in Vanadium Redox Flow Batteries. *J. Power*
4471 *Sources* **2010**, *195*, 4375–4379. 4472
- (347) Jaouen, F.; Lefèvre, M.; Dodelet, J.-P.; Cai, M. Heat-Treated
4473 Fe/N/C Catalysts for O₂ Electroreduction: Are Active Sites Hosted in
4474 Micropores? *J. Phys. Chem. B* **2006**, *110*, 5553–5558. 4475
- (348) Zitolo, A.; Goellner, V.; Armel, V.; Sougrati, M. T.; Mineva,
4476 T.; Stievano, L.; Fonda, E.; Jaouen, F. Identification of Catalytic Sites
4477 for Oxygen Reduction in Iron- and Nitrogen-Doped Graphene
4478 Materials. *Nat. Mater.* **2015**, *14*, 937–942. 4479
- (349) Strickland, K.; Miner, E.; Jia, Q.; Tylus, U.; Ramaswamy, N.;
4480 Liang, W.; Sougrati, M. T.; Jaouen, F.; Mukerjee, S. Highly Active
4481 Oxygen Reduction Non-Platinum Group Metal Electrocatalyst
4482 Without Direct Metal-Nitrogen Coordination. *Nat. Commun.* **2015**,
4483 *6*, 7343. 4484
- (350) Wan, X.; Liu, X.; Li, Y.; Yu, R.; Zheng, L.; Yan, W.; Wang, H.;
4485 Xu, M.; Shui, J. Fe–N–C Electrocatalyst With Dense Active Sites and
4486 Efficient Mass Transport for High-Performance Proton Exchange
4487 Membrane Fuel Cells. *Nat. Catal.* **2019**, *2*, 259–268. 4488
- (351) Li, J.; Ghoshal, S.; Liang, W.; Sougrati, M.-T.; Jaouen, F.;
4489 Halevi, B.; McKinney, S.; McCool, G.; Ma, C.; Yuan, X.; Ma, Z.-F.;
4490 Mukerjee, S.; Jia, Q. Structural and Mechanistic Basis for the High
4491 Activity of Fe–N–C Catalysts Toward Oxygen Reduction. *Energy*
4492 *Environ. Sci.* **2016**, *9*, 2418–2432. 4493
- (352) Zhang, J.; Song, Y.; Kopeć, M.; Lee, J.; Wang, Z.; Liu, S.; Yan,
4494 J.; Yuan, R.; Kowalewski, T.; Bockstaller, M. R.; Matyjaszewski, K.
4495 Facile Aqueous Route to Nitrogen-Doped Mesoporous Carbons. *J.*
4496 *Am. Chem. Soc.* **2017**, *139*, 12931–12934. 4497

- 4498 (353) Ludwinowicz, J.; Jaroniec, M. Potassium Salt-Assisted
4499 Synthesis of Highly Microporous Carbon Spheres for CO₂
4500 Adsorption. *Carbon* **2015**, *82*, 297–303.
- 4501 (354) Su, S.; Lai, Q.; Liang, Y. Schiff-Base Polymer Derived
4502 Nitrogen-Rich Microporous Carbon Spheres Synthesized by Molten-
4503 Salt Route for High-Performance Supercapacitors. *RSC Adv.* **2015**, *5*,
4504 60956–60961.
- 4505 (355) Deng, X.; Zhao, B.; Zhu, L.; Shao, Z. Molten Salt Synthesis of
4506 Nitrogen-Doped Carbon With Hierarchical Pore Structures for Use as
4507 High-Performance Electrodes in Supercapacitors. *Carbon* **2015**, *93*,
4508 48–58.
- 4509 (356) Li, W.; Hu, S.; Luo, X.; Li, Z.; Sun, X.; Li, M.; Liu, F.; Yu, Y.
4510 Confined Amorphous Red Phosphorus in MOF-Derived N-Doped
4511 Microporous Carbon as a Superior Anode for Sodium-Ion Battery.
4512 *Adv. Mater.* **2017**, *29*, 1605820.
- 4513 (357) Yang, S. J.; Kim, T.; Im, J. H.; Kim, Y. S.; Lee, K.; Jung, H.;
4514 Park, C. R. MOF-Derived Hierarchically Porous Carbon With
4515 Exceptional Porosity and Hydrogen Storage Capacity. *Chem. Mater.*
4516 **2012**, *24*, 464–470.
- 4517 (358) Xiang, Z.; Cao, D.; Huang, L.; Shui, J.; Wang, M.; Dai, L.
4518 Nitrogen-Doped Holey Graphitic Carbon From 2D Covalent Organic
4519 Polymers for Oxygen Reduction. *Adv. Mater.* **2014**, *26*, 3315–3320.
- 4520 (359) Kim, G.; Yang, J.; Nakashima, N.; Shiraki, T. Highly
4521 Microporous Nitrogen-Doped Carbon Synthesized From Azine-
4522 Linked Covalent Organic Framework and Its Supercapacitor
4523 Function. *Chem. - Eur. J.* **2017**, *23*, 17504–17510.
- 4524 (360) Lan, X.; Li, Y.; Du, C.; She, T.; Li, Q.; Bai, G. Porous Carbon
4525 Nitride Frameworks Derived From Covalent Triazine Framework
4526 Anchored Ag Nanoparticles for Catalytic CO₂ Conversion. *Chem. -*
4527 *Eur. J.* **2019**, *25*, 8560–8569.
- 4528 (361) Lee, J. S.; Wang, X.; Luo, H.; Baker, G. A.; Dai, S. Facile
4529 Ionothermal Synthesis of Microporous and Mesoporous Carbons
4530 From Task Specific Ionic Liquids. *J. Am. Chem. Soc.* **2009**, *131*, 4596–
4531 4597.
- 4532 (362) Zhang, P.; Yuan, J.; Fellingner, T.-P.; Antonietti, M.; Li, H.;
4533 Wang, Y. Improving Hydrothermal Carbonization by Using Poly-
4534 (Ionic Liquid)s. *Angew. Chem., Int. Ed.* **2013**, *52*, 6028–6032.
- 4535 (363) Gong, J.; Lin, H.; Antonietti, M.; Yuan, J. Nitrogen-Doped
4536 Porous Carbon Nanosheets Derived From Poly(ionic Liquid)s:
4537 Hierarchical Pore Structures for Efficient CO₂ Capture and Dye
4538 Removal. *J. Mater. Chem. A* **2016**, *4*, 7313–7321.
- 4539 (364) Luo, W.; Zhao, T.; Li, Y.; Wei, J.; Xu, P.; Li, X.; Wang, Y.;
4540 Zhang, W.; Elzatahry, A. A.; Alghamdi, A.; Deng, Y.; Wang, L.; Jiang,
4541 W.; Liu, Y.; Kong, B.; Zhao, D. A Micelle Fusion–Aggregation
4542 Assembly Approach to Mesoporous Carbon Materials With Rich
4543 Active Sites for Ultrasensitive Ammonia Sensing. *J. Am. Chem. Soc.*
4544 **2016**, *138*, 12586–12595.
- 4545 (365) Liu, Y.; Wang, Z.; Teng, W.; Zhu, H.; Wang, J.; Elzatahry, A.
4546 A.; Al-Dahyan, D.; Li, W.; Deng, Y.; Zhao, D. A Template-Catalyzed
4547 in situ Polymerization and Co-Assembly Strategy for Rich Nitrogen-
4548 Doped Mesoporous Carbon. *J. Mater. Chem. A* **2018**, *6*, 3162–3170.
- 4549 (366) Chu, W. C.; Bastakoti, B. P.; Kaneti, Y. V.; Li, J. G.; Alamri, H.
4550 R.; Alothman, Z. A.; Yamauchi, Y.; Kuo, S. W. Tailored Design of
4551 Bicontinuous Gyroid Mesoporous Carbon and Nitrogen-Doped
4552 Carbon From Poly(ethylene Oxide-*b*-Caprolactone) Diblock Copoly-
4553 mers. *Chem. - Eur. J.* **2017**, *23*, 13734–13741.
- 4554 (367) Yuan, R.; Wang, H.; Sun, M.; Damodaran, K.; Gottlieb, E.;
4555 Kopeć, M.; Eckhart, K.; Li, S.; Whitacre, J.; Matyjaszewski, K.;
4556 Kowalewski, T. Well-Defined N/S Co-Doped Nanocarbons from
4557 Sulfurized PAN-*b*-PBA Block Copolymers: Structure and Super-
4558 capacitor Performance. *ACS Appl. Nano Mater.* **2019**, *2*, 2467–2474.
- 4559 (368) Nguyen, C. T.; Kim, D.-P. Direct Preparation of Mesoporous
4560 Carbon by Pyrolysis of Poly(Acrylonitrile-*b*-Methylmethacrylate)
4561 Diblock Copolymer. *J. Mater. Chem.* **2011**, *21*, 14226.
- 4562 (369) Zhou, Z.; Liu, G. Controlling the Pore Size of Mesoporous
4563 Carbon Thin Films Through Thermal and Solvent Annealing. *Small*
4564 **2017**, *13*, 1603107.
- 4565 (370) Aftabuzzaman, M.; Kim, C. K.; Kowalewski, T.;
4566 Matyjaszewski, K.; Kim, H. K. A Facile Route to Well-Dispersed Ru
Nanoparticles Embedded in Self-Templated Mesoporous Carbons for
High-Performance Supercapacitors. *J. Mater. Chem. A* **2019**, *7*, 4568
20208–20222.
- (371) Kim, C. K.; Zhou, H.; Kowalewski, T.; Matyjaszewski, K.;
Kim, H. K. Soft-Templated Tellurium-Doped Mesoporous Carbon as
a Pt-Free Electrocatalyst for High-Performance Dye-Sensitized Solar
Cells. *ACS Appl. Mater. Interfaces* **2019**, *11*, 2093–2102.
- (372) Lee, S. H.; Kim, J.; Chung, D. Y.; Yoo, J. M.; Lee, H. S.; Kim,
M. J.; Mun, B. S.; Kwon, S. G.; Sung, Y.-E.; Hyeon, T. Design
Principle of Fe–N–C Electrocatalysts: How to Optimize Multimodal
Porous Structures? *J. Am. Chem. Soc.* **2019**, *141*, 2035–2045.
- (373) Qiao, Y.; Han, R.; Pang, Y.; Lu, Z.; Zhao, J.; Cheng, X.;
Zhang, H.; Yang, Z.; Yang, S.; Liu, Y. 3D Well-Ordered Porous
Phosphorus Doped Carbon as an Anode for Sodium Storage: Design
Structure Design, Experimental and Computational Insights. *J. Mater.*
Chem. A **2019**, *7*, 11400–11407.
- (374) Fu, J.; Xu, Q.; Chen, J.; Chen, Z.; Huang, X.; Tang, X.
Controlled Fabrication of Uniform Hollow Core Porous Shell Carbon
Spheres by the Pyrolysis of Core/Shell Polystyrene/Cross-Linked
Polyphosphazene Composites. *Chem. Commun.* **2010**, *46*, 6563–
6565.
- (375) Meng, X.; Cui, H.; Dong, J.; Zheng, J.; Zhu, Y.; Wang, Z.;
Zhang, J.; Jia, S.; Zhao, J.; Zhu, Z. Synthesis and Electrocatalytic
Performance of Nitrogen-Doped Macroporous Carbons. *J. Mater.*
Chem. A **2013**, *1*, 9469–9476.
- (376) Liang, C.; Dai, S. Dual Phase Separation for Synthesis of
Bimodal Meso-/macroporous Carbon Monoliths. *Chem. Mater.* **2009**,
21, 2115–2124.